Processing and Properties of Nanostructured Zirconia Ceramics

By

Anish Paul

A Doctoral Thesis submitted in partial fulfilment of the requirements for the award of Doctor of Philosophy of Loughborough University

January 2009

Abstract

The term nanoceramics is well known in the ceramic field for at least two decades. Even though there are many reports that nanoceramics are superior in terms of mechanical and other properties, no comprehensive and conclusive study on the grain size dependent variation in mechanical properties. So this study was an attempt to study the property variation with grain size and yttria content for a well known ceramic, yttria stabilised zirconia.

High solids content but low viscosity YSZ nanosuspensions have been slip cast into ~52% dense, very homogeneous green bodies in sizes up to 60 mm in diameter. Sintering cycles have been optimised using both hybrid and conventional two-step heating to yield densities >99.5% of theoretical whilst retaining a mean grain size of <100 nm. The sintered samples have been characterised for hardness, toughness, strength, wear resistance and hydrothermal ageing resistance. The results have been compared with that of a submicron zirconia ceramic prepared using a commercial powder.

The strength of the nanoceramics has been found to be very similar to that of conventional submicron ceramics, viz. ~1GPa, although the fracture mechanism was different. Two toughness measurement approaches have been used, indentation and surface crack in flexure. The results indicate that the nano1.5YSZ ceramics may be best viewed as crack, or damage, initiation resistant rather than crack propagation resistant; indentation toughness measurements as high as 14.5 MPa $m^{1/2}$ were observed. Micro-Raman mapping was demonstrated to be a very effective technique to map the phase transformations in zirconia. The wear mechanism of nanozirconia has been observed to be different compared to that in conventional, submicron YSZ and the wear rates to be lower, particularly under wet conditions. In addition, and potentially most usefully, the nano3YSZ ceramics appear to be completely immune to hydrothermal ageing for up to 2 weeks at 245°C & 7 bar; conditions that see a conventional, commercial submicron ceramic disintegrate completely within 1 hour.

Keywords: Nanoceramics, zirconia, slip casting, two-step sintering, microwaves, hydrothermal ageing.

Acknowledgements

I would like to acknowledge Dr. B. Vaidhyanathan and Prof. Jon Binner for their valuable support, guidance and encouragement during the course of this work. I sincerely thank them for guiding me in the right direction.

I am indebted to all the people from LMCC, especially Mr. John Bates and Dr. David Ross for their co-operation concerning electron microscopy and X-ray diffraction. Many thanks to all the staff and students from Department of Materials and other departments for their help and support. Special thanks to all the members of the ceramic research group for helping me with my experiments.

I am grateful to MEL chemicals for providing the raw materials and Dr. Roger Morrel, NPL for conducting the standard strength and toughness measurements.

My sincere thanks go to Mr. Biju Cherian for sponsoring my studentship in UK. I also would like to acknowledge my family for their continuous support and motivation which helped me to stay focussed.

Anish Paul

Loughborough
04th January 2009

Table of Contents

List of Figures

List of Tables

Chapter 1

1 Introduction

Nanotechnology was first introduced in the famous lecture of Nobel Laureate Richard P. Feynman, "There's Plenty of Room at the Bottom," given in 1959 at the California Institute of Technology.[1] Nanotechnology deals with the production and application of physical, chemical and biological systems at scales ranging from a few nanometres up to 100 nanometres. It also deals with the integration of the resulting nanostructures into larger systems.[2]

Drexler[3] gave one of the earliest definitions of nanotechnology as "the control of matter based on molecule-by-molecule control of products and by-products through high-precision systems as well as the products and processes of molecular manufacturing, including molecular machinery." According to Whatmore and Corbett[4] the subject of nanotechnology includes "almost any materials or devices which are structured on the nanometre scale in order to perform functions or obtain characteristics which could not otherwise be achieved".

The scientific understanding related to nanotechnology is new. However, nanosized devices and objects have existed on earth as long as life. The exceptional mechanical performance of biomaterials, such as bones or mollusc shells, is due to the presence of nanocrystals of calcium compounds.[5] The nanocomposite material of the abalone shell consists of nanosized particles of calcium carbonate bound by a glue made of a carbohydrate protein-mix.[6] This type of composite nanostructure leads to high strength and toughness of the shell because of the interlocking of nanoblocks of calcium carbonate, which are responsible for crack arrest and energy dissipation.

There are already products available on the market which contain nanoparticles.[7] Sunscreens contain nanoparticles designed to give better protection from the harmful rays of the sun; there are fabrics with nanoparticles that make the fabric liquid and stain repellent. In medicine nanoceramics are already being used in drug delivery and as bone replacement agents. In the paint industry nanostructured molecules are used to preserve the integrity of the paint. Modern mobile phone batteries use nanotechnology

for longer battery life. At present the two dominant market sectors for nanotechnology appear to be information and communication technology (ICT) and medicine, although other niche applications include cosmetics, sunscreens, self-cleaning windows, ultra-strong lightweight materials, low-cost solar power generation, miniature fuel cell technology and environmental pollution monitoring and remediation.[8]

ICT applications include ultra-high density information storage – terabyte range, ultra-fast conventional computers, novel ultra-powerful "quantum computers", ultra-broadband communication systems, high-definition, low-energy consumption flat-screen display technologies and a new generation of fully integrated communication and information systems.[8]

Medical applications include diagnostics – "lab-on-a-chip"- technology for rapid identification of pathogens, patient monitoring – real-time sensing of physiological and biochemical parameters, "smart" drug delivery systems – providing swift and timely delivery of just the right amount of pharmaceutical product to where it is needed in the body, and targeted treatment of disease using "designer" nanoparticles which attach themselves selectively to specific sites, etc.[8]

There are two approaches to fabricating at the nano scale, top-down and bottom-up. In the top-down approach, the start is at a large scale which is then reduced in size to reach the nano level as in the preparation of microprocessors for computer industry. When nanoparticles are created using the bottom–up approach, the size and the shape of a particle can be controlled by the production conditions. These particles can also be considered as nanocrystals. The atoms within the particle are perfectly ordered, or crystalline. When the dimensions of a particulate material are decreased from micronsize to nanosize, significant changes in electronic conductivity, optical absorption, chemical reactivity and mechanical properties occur.

With decrease in size, more atoms are located on the surface of the particle.[9] Nanopowders have a remarkably high surface area because of the large fraction of atoms residing on the particle surface. This surface area imparts change of surface

energy and surface morphology. These factors alter the basic properties and the chemical reactivity of the nanomaterials.[2,6,10] The change in properties causes improved catalytic ability,[11] tuneable wavelength-sensing ability,[12] and better-designed pigments and paints with self-cleaning and self-healing features.[13,14]

Thus, in each and every field we can identify the use of nanomaterials and the influence of these materials in the miniaturisation of various products and the evolution of new products with better performance. Nanosized particles have been used to enhance the mechanical performance of plastics and rubbers[2,15,16] whilst nanoceramic cutting tools are harder and more ductile.[17,18,19] For example, ductile behaviour has been reported for nanophase ceramics such as titania and alumina processed by consolidation of ceramic nanoparticles.[19] New nanomaterials based on oxides of zirconium, silicon and germanium have demonstrated superplastic behaviour, undergoing 100–1000% elongation before failure.[19,20]

Some of the advantages expected in using nanoceramics include lower sintering temperature and lower processing time which could lead to increased production rates at reduced costs. The lower sintering temperatures will also enable co-sintering with metals for applications such as solid oxide fuel cells (SOFCs). Nanoceramics are also expected to yield better mechanical, thermal and physical properties. Mechanical properties such as hardness, fracture toughness, flexural strength etc. are expected to be different from their submicron sized counter parts. These property variations are predicted to be due to the increased number of grain boundaries in nanoceramics which could alter the behaviour of the material under loading.

The materials industry is very keen to manufacture products using nanoceramics because of the possible savings in production cost and/or improvement in performance. But there are some major obstacles at the present time. The first and foremost is the difficulty in keeping the nanostructure during sintering. It is difficult to control grain growth and in the case of many nanoceramics this is unavoidable. Hence the optimisation of sintering cycles for different nanoceramics is very essential. Secondly, the lack of data about the properties of the nanoceramics. Even though many researchers have reported the sintering of nanoceramics, only a very few were

successful in sintering them to full density keeping the grain size below 100 nm. Also in many cases the sample size was too small to make any meaningful property measurements.

The main focus of the present work is the mechanical property evaluation of nanozirconia ceramics. The market for zirconia ceramics is very high because of their properties such as chemical resistance, wear resistance etc. Zirconia is also finding applications in areas such as oxygen sensors, SOFCs etc. Thus the demand for zirconia is increasing and material scientists all over the world are trying to improve the properties of this material. In this work nanozirconia green bodies are sintered to full density using optimised sintering cycles. Microwave assisted sintering techniques have been employed to control grain growth during densification. Samples with sufficient size for making test specimens are made to make property measurements including hardness, wear resistance, flexural strength, toughness and ageing resistance. Once the properties are evaluated, it can be used either to modify the present zirconia products or to develop new products with improved performance. Thus the deliverables of the present work are quite significant and the impact could be high.

Chapter 2

2 Literature Review

2.1 Nanocrystalline ceramics

Nanocrystalline ceramics are those ceramics with mean grain sizes less than 100 nm. The current interest for manufacturing and studying nanocrystalline ceramics lies in the unique properties they are expected to possess. As the grain size becomes smaller and smaller, a larger and larger fraction of atoms reside on the grain boundaries and thus the behaviour of the nanocrystalline ceramics is often dominated by events at the grain boundaries.[21] For example nanocrystalline ceramics can deform plastically and extensively by grain boundary sliding.[22,23,24] Because of their many grain boundaries and short diffusional paths nanoceramics have also been used as a solid state bonding agent to join together other large grained commercial ceramics at moderate temperatures.[25] There are also indications that nanocrystalline ceramics can have extremely low thermal conductivity[26] and enhanced ionic and electronic conductivity.[27] Vickers hardness tests from several investigators also indicate that nanocrystalline ceramics are softer than large grained ceramics at room temperature and tend to crack less easily.[28,29]

Another great advantage with nanostructured ceramics is the energy savings resulting from the lower temperatures necessary for the sintering of nanoceramics. The free energies of nanocrystalline materials are higher compared to submicron or micron sized particles.[30] This additional free energy provides a higher driving force for sintering and grain growth and also modifies the equilibrium phases such as the stabilisation of the monoclinic phase in nanoyttria, which is normally stable under high pressure. Consider the equation for the densification rate (dL/Ldt) for all stages of sintering[31]

$$\frac{dL}{Ldt} = \frac{\gamma\Omega}{kT}\left(\frac{\lambda D_g \rho_g}{d^4} + \frac{D_b \rho_b}{d^3}\right) \qquad \text{Eqn. (2.1)}$$

where L is the thickness of the sample, γ is the surface energy, Ω is the atomic volume, λ is the grain boundary width, D_g and D_b are the grain boundary and bulk diffusivities, ρ_g and ρ_b are the grain boundary and bulk density and d is the particle size. According to the above equation, by decreasing the particle size by three orders of magnitude (i.e. from μm to nm) the densification rate could be increased by

12 orders of magnitude.[31] In nanocrystalline materials, in the absence of processing flaws, the size of the strength determining flaws will be much less compared to submicron or micron samples and hence they have the potential to show superior mechanical properties. The present study is mainly focused on nanocrystalline yttria stabilised zirconia ceramics, which will be discussed in some detail in the following sections.

2.2 Zirconia Ceramics

Zirconia (ZrO_2) is a refractory material. It has the highest toughness among all monolithic ceramics. It offers chemical and corrosion resistance to very high temperatures and has low thermal conductivity. It is ionically conductive above 600°C and is used in oxygen sensors and as susceptors (heater) in high temperature induction furnaces. Some of the key properties and typical applications of zirconia are listed in Table 2-1.

Table 2-1 Key properties and typical uses of zirconia.[32,33] The typical uses listed in the right hand side are not corresponding to the properties on the left

Key properties of ZrO_2	Typical uses of ZrO_2
Use temperatures up to 2400°C	Precision ball valve balls and seats
High density > 6 g cm^{-1}	High density ball and pebble mill grinding media
Low thermal conductivity (20% that of alumina)	Rollers and guides for metal tube forming
Chemical inertness	Thread and wire guides
Resistance to molten metals	Hot metal extrusion dies
Ionic electrical conduction	Deep well down-hole valves and seats
Wear resistance	Powder compacting dies
High fracture toughness > 8 MPa $m^{1/2}$	Marine pump seals and shaft guides
High hardness > 12 GPa	Oxygen sensors
Biocompatibility	Hip, knee and dental implants
	High temperature induction furnace susceptors
	Fuel cell membranes
	Electric furnace heaters over 2000°C in oxidizing atmospheres
	Thermal barrier coatings, Metrology components

Pure zirconia exists in three crystal phases at different temperature regimes. At very high temperatures (>2300°C) the material has a cubic structure; at intermediate temperatures (1170 to 2300°C) it has a tetragonal structure and at low temperatures (below 1170°C) the material transforms to the monoclinic structure.

The transformation from tetragonal to monoclinic is rapid and is accompanied by a 3 to 5 percent volume increase that causes extensive cracking in the material. This transformation is a reversible, athermal, martensitic transformation associated with a large temperature hysteresis (approx. 200°C) and involves a large shear strain of the order of 14-15%, Figure 2-1.

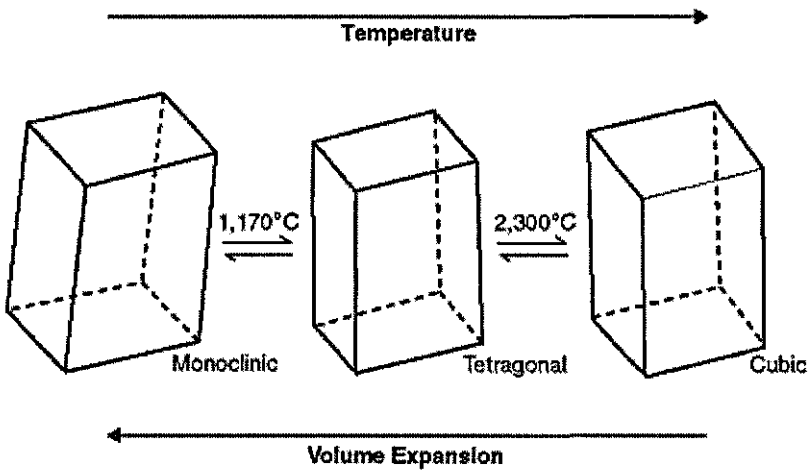

Figure 2-1 Phase transitions in zirconia.[34]

This behaviour destroys the mechanical properties of fabricated components during cooling and excludes pure submicron zirconia for any structural or mechanical applications. Several oxides which dissolve in the zirconia crystal structure can slow down or eliminate these crystal structure changes. Commonly used effective additives are MgO, CaO, and Y_2O_3. With sufficient amounts added, the high temperature cubic structure can be stabilized at room temperature. Cubic stabilized zirconia is a useful refractory and a technical ceramic material because it does not go through structure destructive phase transitions during heating and cooling.

2.2.1 Yttria stabilised zirconia ceramics (YSZ ceramics)

The controlled, stress induced volume expansion of the tetragonal to monoclinic phase change is used to produce very hard, high strength, tough varieties of zirconia

for mechanical and structural applications. There are several different mechanisms that lead to strengthening and toughness improvements in zirconia that contain tetragonal grains. These depend on the grain size, the thermal history and the kind and amount of stabilizing additive in the body. These variations lead to two strong, commercially available partially stabilized zirconia (PSZ) microstructures identified as TTZ (tetragonally toughened zirconia) and TZP (tetragonal zirconia polycrystal) ceramics.[32] The TTZ is a MgO partially stabilized zirconia often designated MgTTZ or MgPSZ consisting of uniformly dispersed tetragonal precipitates in larger cubic phase crystals. The second variety, TZP, is a pure tetragonal phase, very fine grain material stabilized with rare earth oxides, primarily yttria and less commonly ceria. They are often designated YTZP for the yttria stabilized product and CeTZP for the ceria stabilized product. The TZP material has found uses in cutting and wear resistant applications due to its outstanding hardness and toughness.

The phase diagram for the zirconia-yttria system for the zirconia rich portion is shown in Figure 2-2. 3 mol% yttria stabilised zirconia is most commonly used for mechanical applications as it provides enough stabilisation against transformation and is cost effective. The martensitic transformation from tetragonal phase to monoclinic phase can be induced by cooling or by external loading. Thermally induced transformation determines the amount of tetragonal phase which can be retained after thermal cycling and the stress enhanced transformation enhances the toughness of zirconia ceramics. The latter is known as transformation toughening. The tetragonal to monoclinic transformation is believed to take place in two different stages. In the first, the lattice structure undergoes a transformation from tetragonal to monoclinic by shearing displacement of zirconium ions and in the second oxygen ions undergoes a diffusional migration to the oxygen sites present in the monoclinic lattice.

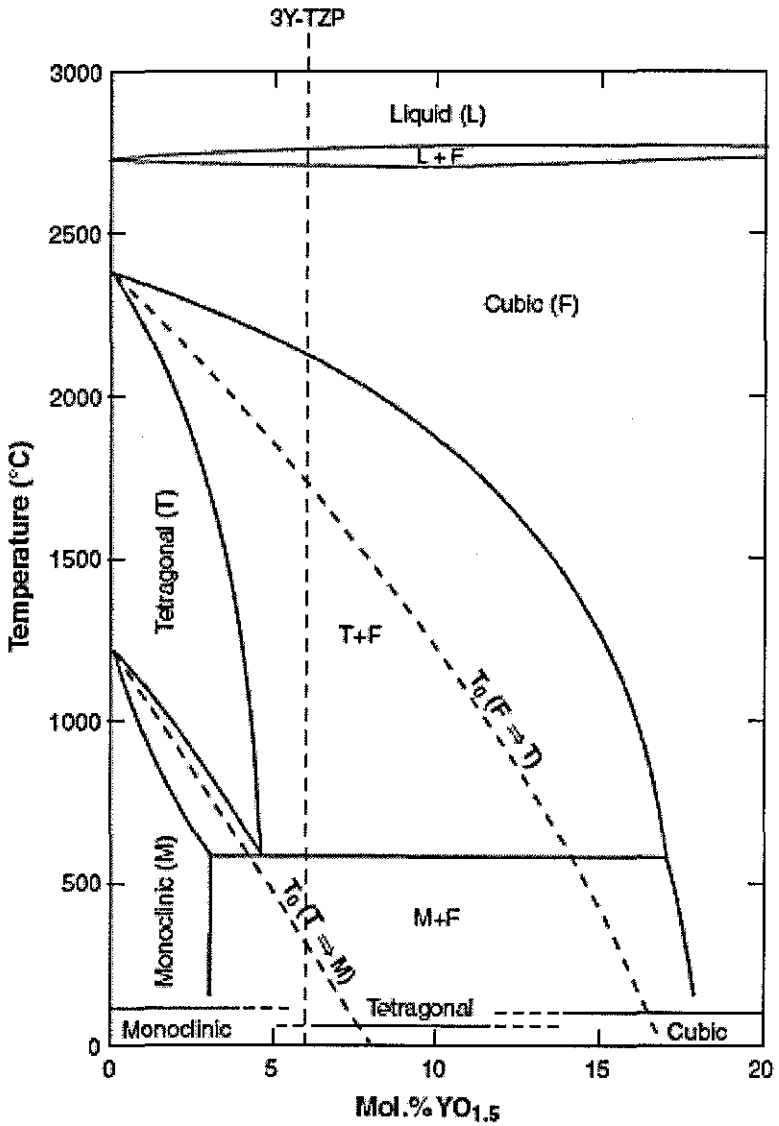

Figure 2-2 ZrO_2-Y_2O_3 phase diagram.[35]

Transformation toughening is responsible for the high toughness of zirconia ceramics. The transformable tetragonal phase present in a zirconia ceramic will transform to the stable monoclinic phase in the tensile stress field around a propagating crack, Figure 2-3. The volume increase associated with the transformation generates a net compressive stress around the crack tip, minimising or preventing the crack propagation.

The total free energy change per unit volume required for constrained transformation can be expressed as

$$\Delta G_{t\rightarrow m} = -\Delta F_{CH} + \Delta Ue + \Delta Us - \Delta Ui$$
$$= -\Delta F_{CH} + \Delta S - \Delta Ui \qquad \text{Eqn. (2.2)}$$

where ΔF_{CH} is the chemical free energy change associated with the tetragonal to monoclinic transformation, ΔUe is the strain free energy change, ΔUs is the change in surface free energy and ΔUi is the interaction energy density, ΔS is the sum of the changes in surface and strain free energy.

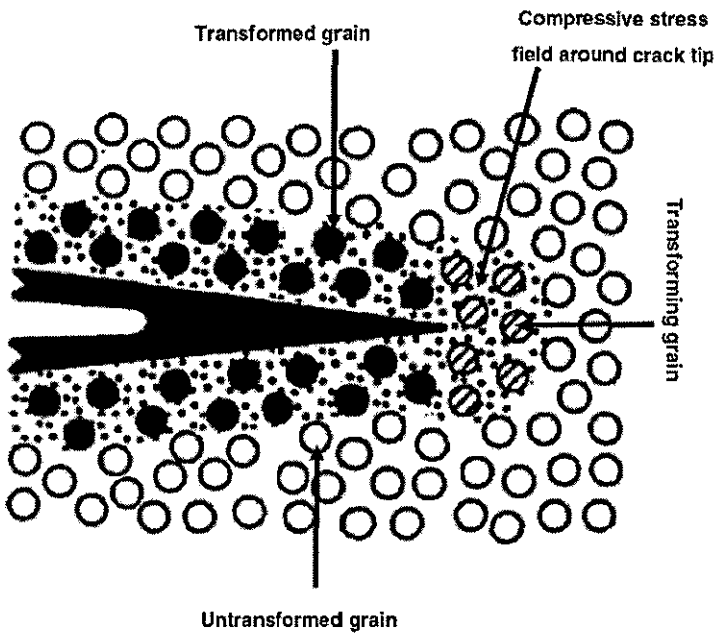

Figure 2-3 Schematic illustration of the transformation toughening in YSZ.[36]

There are three approaches to increase the total free energy change and the t-ZrO_2 phase. They are:

1. decreasing the chemical free energy change by alloying with a stabilising dopant oxide such as yttria;
2. increasing the strain free energy change by dispersing the tetragonal phase in a constraining elastic matrix such as alumina (ZTA);
3. decreasing the tetragonal grain size.

Reducing the tetragonal grain size can be used effectively to increase the stabilisation of zirconia ceramics. The martensitic transformation in zirconia is nucleation controlled and its kinetics is not significantly affected by the growth process. This nucleation is heterogeneous and is triggered by the generation or activation of certain nucleating defects, such as dislocations, within the metastable phase by external stresses.[37,38] As the grain size decreases, the chance for finding such a defect in a grain decreases further. So, as the grain size decreases, the stability against transformation increases. Conventionally zirconia based products are fabricated starting with

submicron or micron sized starting powder. If nanoparticles of yttria stabilized zirconia could be produced, and if the nanosized crystallites could be retained throughout the powder processing steps, superior phase homogeneity and low-temperature sinterability can be achieved. Nanocrystalline-sintered YSZ would be expected to have improved mechanical, thermal, electrical, catalytic, and optical properties as compared with YSZ produced by conventional ceramic processing routes.[39,40]

2.2.2 Preparation of YSZ nanoceramics

There are a large number of techniques reported for the synthesis of nanozirconia powders and their subsequent processing. The synthesis techniques include hydro-thermal synthesis,[41] mixed-organic inorganic co-precipitation,[40] laser evaporation and condensation,[42] nitrate-citrate route,[43,44] precipitation synthesis,[45,46,47] microwave assisted methods,[48] solvothermal methods,[39] ultrasonic spray pyrolysis,[49] flame spray pyrolysis,[50] solid-state synthesis[51] etc. Among all these powders prepared using various techniques, only a few have been sintered to high density whilst retaining the grain size. It is not possible to discuss all the techniques used for the preparation of nanozirconia considering the numerous reported methods. Hence a few synthesis methods are discussed below where the prepared powder has been subsequently sintered to greater than at least 90% density.

Maca et al.[45] conducted studies on the sintering of pure nanozirconia, 1.5YSZ and 3YSZ, prepared by precipitation synthesis. Green bodies were prepared by cold isostatic pressing; but after sintering at 1100°C they were able to achieve a density of only 90% of the theoretical density (TD). The preparation of a 94% dense YSZ with 50 nm average grain size has been reported in literature; the nanopowder prepared using a solvothermal method.[39] A nitrate-citrate combustion route[43] has been reported for the preparation of nanozirconia powders with crystallite size of the order of 10 nm. Pellets were prepared by uniaxial pressing which were subsequently sintered at 1400-1500°C, to yield a density of 97% with 0.4 μm average grain size. The density was very low considering the higher temperature used for sintering and the final grain size was also found to be larger.

Zych et al.[41] reported the preparation of nanozirconia green bodies by filter pressing of a zirconia powder with a particle size of about 8 nm, prepared using a co-precipitation method. The sintering of the green bodies was carried out at 1200°C to achieve 99.9% of theoretical. The results were compared with samples prepared using commercial powder (Tosoh Co.) with similar starting density and composition and found that the shrinkage of the former started at temperatures as low as 200°C compared to the latter, Figure 2-4. Shrinkage of the submicron powder started at about 1000°C, and at 1200°C it reached only 8%, corresponding to about 60% of theoretical density, whilst at this temperature the nanopowders shrinkage terminated, and the sample density was about 99.9% of theoretical with grains less than 150 nm in size.

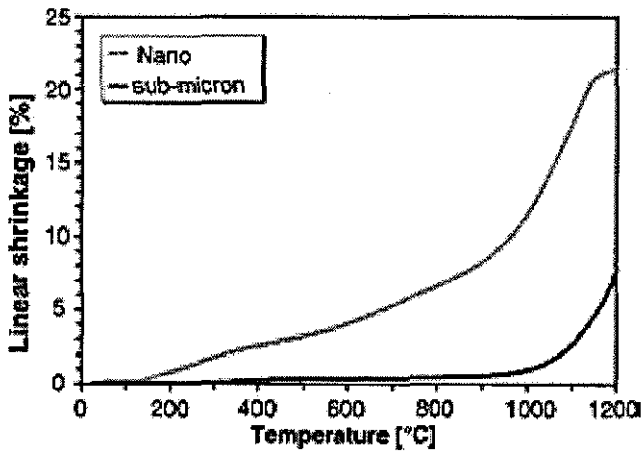

Figure 2-4 Linear shrinkage of nano and sub-micron samples during sintering[41]

Duran et al.[40] reported the sintering of ~9 nm 3Y-TZP powders prepared by a mixed organic-inorganic precursors co-precipitation method. Fully dense nanoscale ceramics with an average grain size below 95 nm were obtained after sintering at 1200°C for 20 min or at 1150°C for 4 h.

2.3 Properties of nanoceramics

Nanocrystalline materials can exhibit increased strength/hardness[52,53] improved toughness, reduced elastic modulus and ductility, enhanced diffusivity,[54] higher specific heat, enhanced thermal expansion coefficient (CTE), better conductivity[55,56] and superior soft magnetic properties in comparison with conventional polycrystalline materials.

Ceramics are generally brittle materials, but nanocrystalline ceramics have the attractive ability to exhibit superplasticity at strain rates considerably higher than their microcrystalline counterparts. Superplasticity was reported in fine grained tetragonal zirconia partially stabilised with 3 mol% yttria in the year 1986, Figure 2-5.[57]

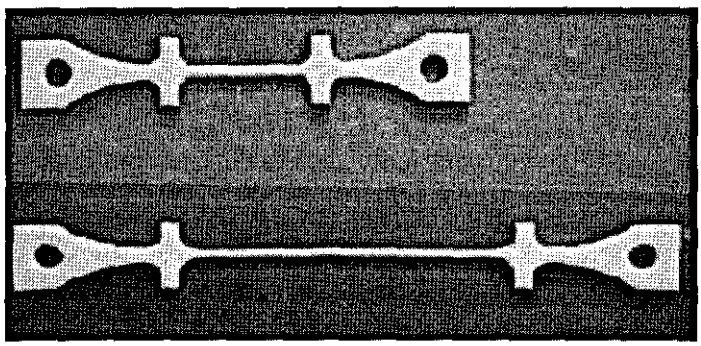

Figure 2-5 First demonstration of superplastic elongation of Y_2O_3 stabilised ZrO_2 polycrystals (Y- TZP). Specimens before and after deformation are shown.[57]

Other ceramic materials which displayed superplasticity include; single-phase ceramics such as alumina,[58] silicon nitride,[59,60] silicon carbide,[61] hydroxyapatite[62] and $YBa_2Cu_3O_{7-x}$,[63] polyphase ceramics such as zirconia/alumina,[64] zirconia/mullite,[65] and silicon nitride/silicon carbide with other mixed phases.[66] The essential requirement for useful superplasticity is a fine grain size. Winnubst et al.[67] reported that the deformation strain rate of nanocrystalline Y-TZP increased by a factor of 4 when the grain size decreased from 200 to 100 nm. Nanocrystalline materials tend to exhibit much reduced ductility, due in part to a low work hardening rate leading to early strain localisation and failure and also due to a reduced ability of the materials to accommodate the progression of cracks by extensive plastic deformation. A ductility study of nanocrystalline zirconia - based ceramics at low temperature showed that the maximum elongation of about 60% could be achieved with ZrO_2 + 10 wt.% Y_2O_3 + 12 wt.% Al_2O_3 composite ceramic at 1250°C.[68]

A conductivity study in nanocrystalline YSZ carried out by Mondal et al.[55] showed that the specific grain boundary conductivity of the nanocrystalline samples was 1-2 orders of magnitude higher than that of the microcrystalline samples. Transparency has also been observed for nanoceramics; this is mainly reported for neodymium (Nd) doped yttrium aluminium garnate (YAG) ceramics.[69] Low temperature, high pressure preparation of $MgAl_2O_4$ transparent ceramics has also been reported in literature.[70]

One of the interesting phenomena observed for yttria stabilised nanozirconia ceramics is the lower amount of stabilisers required to achieve the same degree of stabilisation as for conventional submicron versions.[71] This could result in different properties for nanoceramics compared to their submicron sized counterparts as well as potential reduction in the cost of these materials. According to Garvie,[72] pure zirconia can be stabilised in the tetragonal phase without any additives at room temperature if the grain size of the tetragonal grains in the sintered microstructure is below a critical grain size limit, he suggested a value of 30 nm. He experimentally demonstrated that the specific surface area of nanocrystalline ZrO_2 is very significantly enhanced below the critical grain size of 30 nm and that such nanocrystallites possess excess energy compared to a single, large crystal. Based on these observations he proposed that the stabilisation of the metastable tetragonal phase below 30 nm, at room temperature, is due to both enhanced specific surface area and excess energy below this critical size.

There are number of other factors also that could influence the critical grain size and the room temperature stabilisation of nanozirconia. In their review on room temperature stabilisation of zirconia, Shukla and Seal,[73] explained the effect of the various parameters including the roles of (i) interfacial energy, (ii) strain energy, (iii) external hydrostatic pressure, (iv) internal hydrostatic pressure, (v) structural similarities, (vi) surface coatings, (vii) water vapour, (viii) anions and (ix) oxygen ion vacancies. Considering the influence of all the above factors, they came to the conclusion that in the case of nanocrystalline ZrO_2, the tetragonal phase can be stabilised at room temperature in an isolated, single, strain free nanoparticle below a critical size of 10 nm. The critical size increases to 33 nm in the case of agglomerated nanopowders, which is similar to the size reported by Garvie.[72] This grain size dependent stabilisation and the potential for superior properties generated the main interest in the present work.

2.4 Mechanical property variation with grain size, density and yttria content

Hardness, fracture toughness and bending strength are important properties that affect the performance of structural materials. These properties help to characterize the

ability of ceramic materials to resist deformation as well as crack initiation and propagation.

2.4.1 Hardness

The hardness of a material is defined as the resistance to plastic deformation when indented. The principle of indentation consists of applying a given load and, subsequently, measuring the dimensions of the residual impression left in the material once the indenter has been withdrawn. The hardness of the material is then defined as the ratio between the indentation load and a parameter representative of the area of the residual impression, depending on the shape of the indenter and the method employed for the hardness calculation. The Vickers hardness number (VHN) generally used is then calculated using the formula:

$$VHN = \frac{P}{A_{TAC}} = \frac{P}{d^2/2 \cdot \sin\left(\psi/2\right)} \left(= 1.8544 \frac{P}{d^2}\right) \qquad \text{Eqn. (2.3)}$$

where VHN is expressed in MPa, with P the applied load in N and d the diagonal of the indent in mm. ψ is the angle between the two opposite sides of the indenter, 136° for a pyramidal indenter and A_{TAC} represents the true area of contact.

There are a large number of reports about the hardness of zirconia and nanocrystalline zirconia. Medvedovski and Sarkar[74] reported a hardness value of 12 GPa for PSZ. Cottom and Mayo[75] reported the hardness of nanocrystalline 3YSZ ceramics. Samples with densities ranging from 90.4% to 98.7% of theoretical density and grain sizes from 55 nm to 160 nm were tested by Vickers indentation. The hardness increased with density, with the maximum hardness similar to those reported by Medvedovski and Sarkar.[74] No grain size dependent variation in hardness was observed. Chaim and Hefetz[76] also investigated the effect of grain size on hardness of nanocrystalline 3YSZ ceramic with grain sizes ranging between 23 to 130 nm. There was no correlation between hardness and grain size; the former increased with final density with reported hardness values <8 GPa.

Bravo-Leon et al.[77] studied the hardness of 0, 1.0 and 1.5 mol% nanozirconia ceramics over a wide range of densities (89-100%) and grain sizes (60-100 nm). A

linear increase in hardness with density was reported. The 1.5 mol% had a higher hardness than the 0 and 1.0 mol% at a given density, although, the values were lower than those reported for nano3YSZ.[75] The maximum hardness values were ~11 GPa for the 1.5 mol% YSZ and ~9.5 GPa for the 1.0 mol% YSZ. A moderate increase in hardness with grain size was also observed. Hardness of 1.5, 2.0 2.7 and 3.0 mol% yttria stabilised nano zirconia ceramics prepared by wet routes has also been reported in literature.[78] For 3YSZ, the highest hardness of 11.7 GPa was obtained for a sample with an average grain size of 112 nm and 99.8 % relative density. The Vickers hardness versus relative density for the various compositions is shown in Figure 2-6. It can be seen that the hardness increased with density, up to a certain value and then decreased. Only the 2Y-TZP ceramic reached the highest average hardness at full density with a value of 13.5 GPa. The highest average hardness of 13.65 GPa was demonstrated by the 2.5Y-TZP ceramic (99.2% theoretical density).

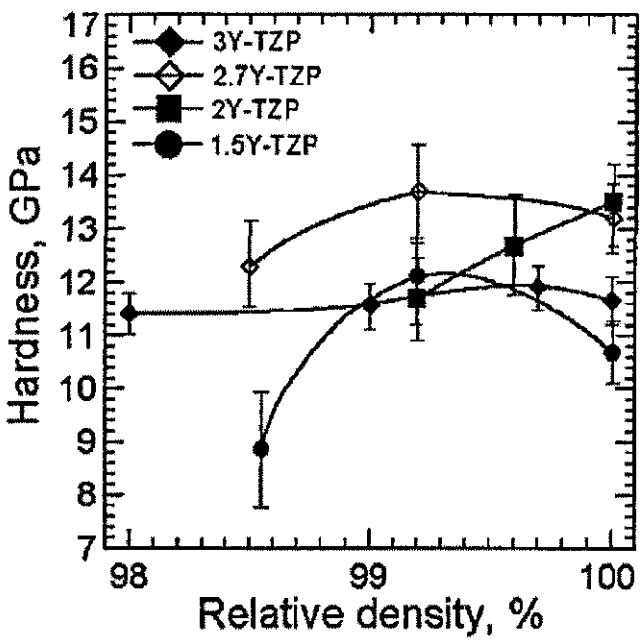

Figure 2-6 Vickers hardness versus relative density for fully tetragonal Y-TZP ceramics with 1.5 to 3 mol% yttria content[78]

2.4.2 Toughness

The application of the Vickers indentation fracture toughness test to brittle materials has become wide spread because (i) it can be used on small samples of materials not amenable to other fracture toughness tests, (ii) specimen preparation is relatively simple requiring only the provision of a polished, reflective plane surface, (iii) the Vickers diamond indenter used to produce the hardness indentation is a standard item

used on a dedicated hardness tester or on a universal testing machine, (iv) in many instances the crack lengths can be measured optically without undue difficulty, and (v) it is both quick and cost effective.[79]

Some of these advantages are offset by a number of complications such as (i) the accuracy to which the crack length can be measured (and hence to which the fracture toughness can be calculated), (ii) all the indentation fracture models given in the literature assume that either one or other of the two idealised crack systems (Palmqvist or median) is formed during the Vickers indentation test which may or may not be the case for the material in question, (iii) the diversity of indentation fracture toughness equations reported in the literature, and (iv) the often reported discrepancy between the indentation fracture toughness of a material and its fracture toughness as measured by conventional methods, such as the single edge notched beam (SENB) test.[79]

Ponton and Rawling[79] calculated the indentation toughness of a range of materials including three different grades of zirconia. These values were then compared with the toughness values determined by conventional three point bending single edge notched beam plane strain fracture toughness tests. The indentation toughness values were found to be different from the SENB toughness values in most of the cases. They also reviewed the relative merits of the 19 standardised Vickers indentation fracture toughness equations reported for the determination of indentation toughness and carried out studies on various materials.[79,80]

Cook and Pharr[81] reported that there are five main types of cracks generated in the surface of brittle materials depending on its properties as shown in Figure 2-7. In their studies on YSZ,[81] a discrete initiation for the primary radial cracks was not observed but the cracks were initiated from the indentation corners and propagated out of the planes perpendicular to the surface. Kaliszewski et al.[82] have also studied the development of indentation induced cracks with increasing indent load in 3 and 4 mol% Y_2O_3 stabilised ZrO_2 ceramics. The cracks formed as radial or Palmqvist cracks at low loads, assumed a "kidney" shape at intermediate loads, and finally formed median (half-penny) cracks at high loads. In the 3 mol% material, about half of the transformable material transformed to the monoclinic phase in the compressed

zone under the indent, whereas in the 4 mol% material only 6% transformation was observed. In a second part of the study,[83] the indentation induced cracks were grown in a four-point bend test and the toughness of 3 and 4 mol% Y_2O_3 stabilised ZrO_2 ceramics was determined. The reported plateau values were 5 MPa $m^{1/2}$ for 3 mol% zirconia and 3.1 MPa $m^{1/2}$ for 4 mol% zirconia. Medvedovski and Sarkar[74] reported a much higher indentation toughness values of 9-10 MPa $m^{1/2}$ for a PSZ.

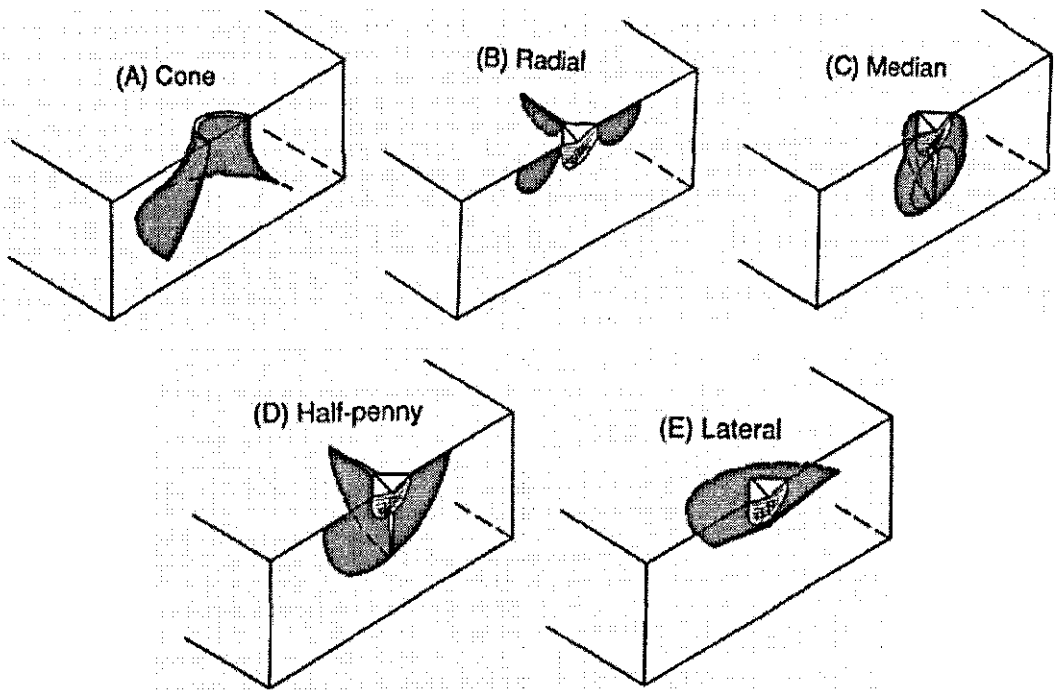

Figure 2-7 Isometric sections of idealized crack morphologies observed at indentation contacts: (A) cone crack, (B) radial cracks and associated contact impression and plastic deformation zone, (C) median cracks (The full circle indicates the extent just after initiation, and the truncated circle the possible extent on continued loading), (D) half-penny cracks, and (E) lateral crack.[81]

Wang et al.[84] analysed TZP ceramics containing 2.0, 2.5 and 3.0 mol% Y_2O_3 with different grain sizes from 0.5 to 2.0 μm and determined toughness by both single edge notched beam and indentation. Indentation toughness showed a maximum at a particular grain size for each of the compositions. The relevant grain sizes for materials containing 2.0, 2.5 and 3.0 mol% Y_2O_3 were 0.87, 1.34 and 1.46 μm respectively. The SENB toughness as a function of grain size also displayed similar trends showing peaks at similar grain sizes, however, the toughness values were higher. Basu et al.[85] compared the toughness of various YSZ compositions prepared by a mixing route with Tosoh samples for the same density and yttria content. The overall yttria content was varied from 1.5 mol% to 2.5 mol%. The samples prepared

by the mixing route were found to have higher toughness compared to the Tosoh samples for the same density and yttria content. Maximum fracture toughness (10.3 MPa $m^{1/2}$) was observed for 2.0 mol% yttria sample prepared by the mixing route which was higher than that of the commercial 2.0 mol% Tosoh (5.9 MPa $m^{1/2}$) and 3.0 mol% Tosoh (2.5 MPa $m^{1/2}$).

Cottom and Mayo[75] measured the indentation toughness of nanocrystalline 3Y-ZrO_2 ceramics, calculated using the equation proposed by Anstis et al.[86] The indentation toughness were found to be independent of grain size and reported to be in the range 2.25 – 4.25 MPa $m^{1/2}$. These values were much lower than that observed for a sample with micron grain size (8.2 MPa $m^{1/2}$) measured by the same authors.

Bravo-Leon et al.[77] reported the toughness of 0, 1.0 and 1.5 mol% nanozirconia ceramics with densities ranging from 89-100% and grain sizes from 60-100 nm. The toughness was calculated using the equation suggested by Niihara et al.[87,88] for the Palmqvist type of cracks. The fracture toughness increased strongly with increasing grain size up to a maximum value of 16-17 MPa $m^{1/2}$ for both the 1.0 and 1.5 mol% compositions, Figure 2-8.

The maximum toughness was obtained at a grain size of 90 nm for 1.0 mol% composition and 110 nm for 1.5 mol% composition. The maximum toughness reported for undoped monoclinic material was 2.6 MPa $m^{1/2}$. These toughness values are similar to those reported by Vasylkiv et al. for samples with similar yttria content and grain size prepared by wet processing,[78] however, the results are not directly comparable with those reported by Cottom and Mayo[75] as different equations were used to calculate the toughness values.

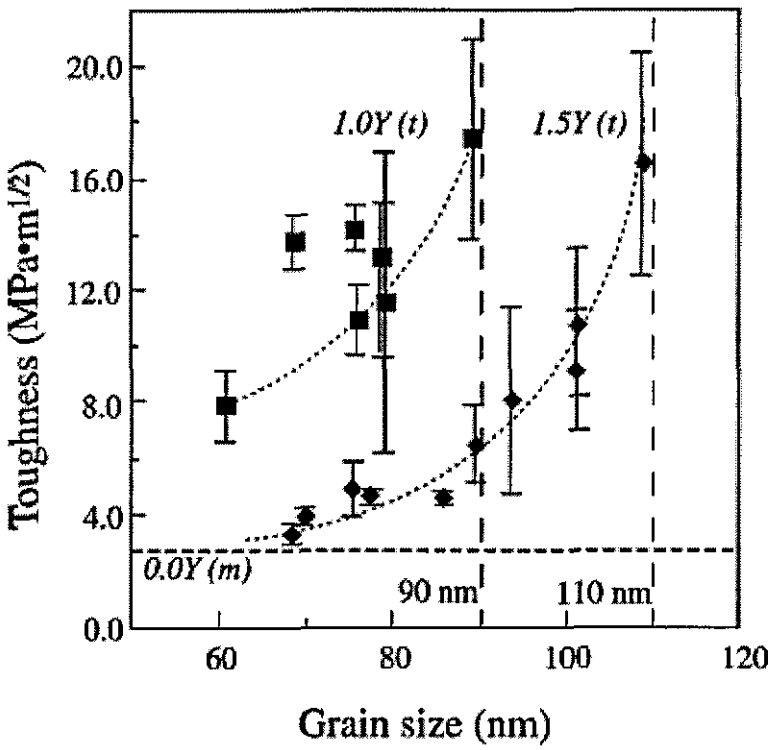

Figure 2-8 Toughness vs. grain size for the fully tetragonal samples 1.0Y and 1.5Y. Both sets of data follow a similar trend, reaching maximum values around 16–17 MPa $m^{1/2}$ when the grain size has a critical value: 90 nm for 1.0Y and 110 nm for 1.5Y.

A similar study has been reported for 2Y-TZP with grain size from 150 to 500 nm and density more than 97%.[89] A linear increase in fracture toughness was observed for the samples with grain size. The plateau values of toughness in air increased from 3.1 MPa $m^{1/2}$ for a grain size of 150 nm up to 5.4 MPa $m^{1/2}$ for a grain size of 300 nm. For the 500 nm grain size specimen the value dropped to 4.3 MPa $m^{1/2}$.The fracture toughness of monoclinic zirconia has also been reported in literature.[90] Samples were sintered to densities up to 92.2% with grain size of approximately 150 nm. Fracture toughness was measured using the SCF technique. The reported value for toughness was 2.06 MPa $m^{1/2}$ and this value was slightly lower than that reported for monoclinic zirconia with 82 nm grain size (2.6 MPa $m^{1/2}$).[77]

2.4.3 Strength

Uniaxial strength is another important property of engineering ceramics and is commonly determined using a flexural strength test method. Quinn and Morrell[91] carried out a review on flexural strength from a design point of view. Monolithic engineering ceramics are brittle and failure occurs by the catastrophic propagation of

a crack like defect when subjected to a sufficiently high stress; the defect size in engineering ceramics is typically of the order of 5 to 200 μm in size. This small size makes them difficult to detect and to control. The largest defect will vary from specimen to specimen and hence the strength of nominally identical specimens can have a considerable spread.

Quinn and Morrell[91,92] draw a number of recommendations for obtaining reliable results as listed below:

1. Flexural testing must be carefully conducted by skilled personnel, preferably by a standard method, to obtain reliable accurate results;
2. Flexural specimens are sensitive to machining damage, and specimen preparation should be done by competent, experienced professionals to careful specifications. Short-cut practices are not acceptable;
3. The flexural bar material (average microstructure, density, porosity, etc) must accurately represent the component material;
4. The flexure bar defects must accurately represent the defects that will cause failure in the component. Defects must be properly characterised;
5. The reliability of any design extrapolation is likely to be best when the test bar most closely relates to the component in terms of size, stress rate, and defect distribution;
6. Fractography to characterize failure origins is essential and 100% fractography is strongly recommended;
7. Multiple flaw populations seriously complicate design. Extrapolation of flexure data should be done only over a narrow size range if multiple flaw populations are present;
8. The flexure specimens must contain a representative number of strength-limiting defects;
9. When these flexural data are used in design, very close quality control should be placed;
10. Flexure testing by itself is not recommended for quantitative creep analysis.

There are not many reports on the strength values of nanozirconia ceramics. Wang et al.[84] reported maximum strength values in the range 1000-1100 MPa for zirconia

samples with 2.0, 2.5 and 3.0 mol% yttria content with different grain size. The fracture strength of materials containing 3.0 mol% Y_2O_3 peaked at 1.4 μm, slightly higher than that (1.22 μm) of the materials containing 2.5 mol% yttria. A fall in the fracture strength at grain sizes of 1.86, 2.0 and 2.2 μm for TZP-2, 2.5 and 3.0 mol% Y_2O_3 respectively, corresponded to the critical grain size for each of the compositions at which spontaneous transformation occurred on cooling. The relationship between the amount of yttria and the fracture strength was also dependent on the grain size of the material. When the grain size was less than 1 μm (i.e., 0.76 and 0.95 μm) the fracture strength decreased significantly with increasing amount of yttria from 2 to 3 mol%. The 1.02 μm grain size material showed a slight decrease in the fracture strength with increasing yttria content. In contrast, for 2.5 mol% material, the strength was maximum at a grain size of 1.20 μm. Basu et al.[85] evaluated the strength of yttria doped zirconia ceramics prepared by a mixing route. The flexural strength values reported for these materials were 1007 MPa, 1085 MPa and 1269 MPa respectively for 3.0 mol% Tosoh, 2.5 mol% sample prepared by mixing route and 2.0 mol% samples prepared my mixing route.

In a recent paper Eichler et al.[93] reported the mechanical properties of submicrometer 3Y-TZP with grain sizes in the range 110-480 nm. Biaxial fracture strength of these samples was studied before and after hydrothermal ageing at 200°C for 6 h. It is interesting to note that the range of grain size reported in this study was less than that (0.5-2.0 μm) reported by Wang et al.[84] Fracture strength was tested using flat ball on a three-ball geometry. The test specimen thickness was 0.8 mm, and the density of the samples tested range from 92 to 98% of theoretical density. The biaxial fracture strength increased from 580 MPa for a mean gain size of 0.11 μm up to 700 MPa for a mean grain size of 0.38 μm. A further increase in grain size to 0.48 μm was found to decrease the fracture strength to 660 MPa. On hydrothermal ageing the fracture strength reduced to ~400 MPa for the 110 and 210 nm mean grain size samples.

2.4.4 Wear properties of zirconia ceramics

The wear properties of zirconia ceramics have been extensively reported in the literature.[94,95,96,97,98,99] Wear resistance is a material property and hence hardness, strength, fracture toughness, thermal conductivity, thermal expansion and microstructure (grain size and porosity) all influence the wear properties of a material.

Fisher et al.[94] analysed the wear properties of three zirconia ceramics with different yttria content (and hence different toughness values) viz. 3, 4 and 6 mol% and found that the wear resistance was proportional to the fourth power of toughness. Lee et al.[95] studied the wear characteristics of 4.7 wt% yttria doped zirconia in detail and generated three dimensional wear maps under dry and lubricated conditions. Water, paraffin oil and formulated oil were all used as lubricants.

The wear regions were identified as a function of load, speed and lubrication environment. Under dry sliding, wear generally increased as the load was increased. Also the predominant wear mechanism changed from plastic deformation at low speeds to brittle fracture at high loads. At fixed load, the wear rate increased when the load was low, and then decreased gently as the speed was increased. Yang also observed similar results.[97] Under dry-sliding conditions wear is controlled by a number of mechanisms including, plastic deformation, brittle fracture, and thermal-shock induced fracture - depending on speed and load.

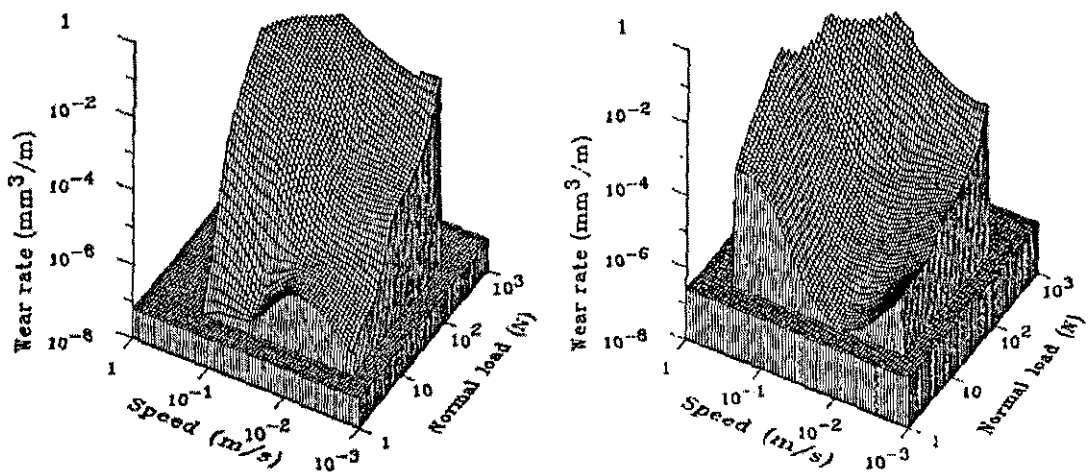

Figure 2-9 Wear maps for Y-TZP under various lubrication conditions: left, in dry air, and right, in water, after Lee et al.[95]

The effect of load was more pronounced under wet conditions. At low loads, wear decreased as the load was increased. It dropped to a minimum at about 0.05 m/s, and then increased rapidly. At high loads wear increased with speed. This increased wear rate was reported to be due to the combination of thermal cracks and cracking from hydrolysis. The presence of monoclinic phase after wear test has been reported by

Sanchez et al.[100] after both dry and wet wear tests on 3 mol% TZP with 1.2 μm mean grain size.

The effect of porosity on friction and wear of Y-TZP with a 180 nm mean grain size has also been reported in literature[96]. The wear resistance decreased by a factor of 5 as the porosity increased from 1.5 to 7.0 vol%. Plastic deformation and microcracking were identified as the basic wear mechanisms for materials of this grain size. Unlike the findings of Lee et al.,[94] irreversible phase transformation to monoclinic zirconia was also observed during wear tests.

He et al.[101] investigated the effect of grain size on wear properties for 5.7 and 3 mol% yttria containing zirconia with mean grain sizes ranging from 0.18 μm to 1.50 μm. All the samples reached a stationary value for the coefficient of friction after running for approximately 3.3 h on the wear tester. The friction coefficient was higher for the samples with grain size ≤0.7 μm and a lower friction coefficient was measured for samples with larger grain size. The wear morphology was also found to be quite different depending on the grain size. For the 0.18 μm mean grain size sample, the wear morphologies indicated plastic deformation, microcracking, microcutting or microploughing and adhesion of wear debris, Figure 2-10 a. The specimens with grain sizes in the range 0.9 to 1.5 μm showed a pronounced surface roughness after the wear test. They also showed a displacement of the surface layer and delamination, Figure 2-10 b. Fracture at the subsurface was also observed, which was mainly of the intergranular type and pits were also developed due to grain pullout. The main difference was the absence of microcracking because of the surface transformation from tetragonal to monoclinic resulting in volume increase.

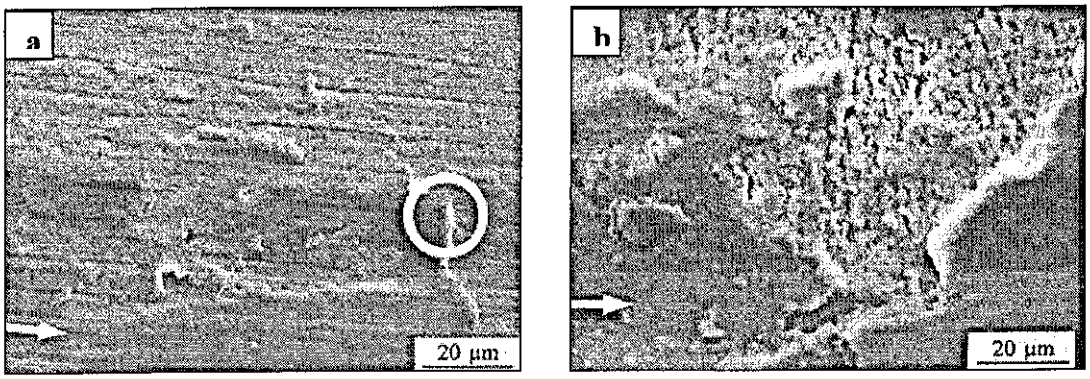

Figure 2-10 Grain size dependent wear morphologies: (a) 0.18 μm mean grain size sample indicating plastic deformation, (b), 1.50 μm mean grain size sample indicating grain pullout and delamination.[101]

The wear properties of samples prepared by colloidal processing have also been reported in the literature.[97] A range of 3Y-TZP samples with mean grain sizes of 0.40 μm, 0.45 μm, 0.60 μm, 0.70 μm, 0.81μm and 1.20 μm were prepared by wet processing. The wear rate was found to increase with increase in grain size. The samples with mean grain sizes above 0.7 μm underwent phase transformation from tetragonal to monoclinic after wear testing. The authors reported that the critical grain size for phase transformation was between 0.5 and 0.7 μm which was lower than that reported by Zum Gahr et al.[102] The wear morphology showed plastic deformation and redeposition of wear debris. Maximum wear resistance was obtained for samples with highest fracture toughness and hardness.

Basu et al.[98,99] observed that both the wear volume and the coefficient of friction increased with increasing toughness and the wear resistance decreased with increasing tetragonal grain size. Raman spectra studies on the worn surfaces indicated a phase transformation of tetragonal to monoclinic and this resulted in extensive microcracking. The spark plasma sintered nano samples[99] with >99% theoretical density and 70-80 nm grain size, a higher hardness and wear resistance was observed, compared to conventionally sintered samples prepared using similar starting powder. Grain pullout was also observed for the nano samples.

2.4.5 Hydrothermal degradation of zirconia ceramics

Zirconia stands out from other ceramics because of its superior mechanical properties, but it is very sensitive to the surrounding environment, especially in the presence of water/moisture and at elevated temperatures. In the presence of moisture zirconia

undergoes a phase transformation, transforming from the tetragonal phase to the monoclinic phase, which seriously deteriorates the properties. Kobayashi et al.[103] was the first to report this ageing transformation in zirconia, which is very deleterious in applications such as biomedical implants, cutting tools for microsurgery, optical ferrules, pump parts and valve parts used in applications such as oil rigs.

One of the major application areas that have been significantly affected by the hydrothermal degradation of zirconia is the biomedical industry. This is especially important in the case of zirconia femoral head components of total hip prostheses and the FDA warned surgeons against steam sterilisation of zirconia ceramic heads in 1997[104,105] and in 2001 recalled all the zirconia heads manufactured by the French manufacturer Saint Gobain.[106] Recently there were a number of reviews about the use of zirconia in biomedical applications.[36,107,108,109,120] The ageing of biomedical zirconia is discussed in detail below.

Thompson and Rawlings[110] studied the mechanical properties of zirconia toughened alumina and three other grades of tetragonal zirconia polycrystals after ageing for 19 months in Ringer's solution at simulated body temperature. They have observed a significant reduction in strength for ZTA and ZrO_2. XRD detected the transformation of the tetragonal surface layer to monoclinic and the amount of conversion increased with ageing time.

Haraguchi et al.[111] was the first one to report two cases of surface deterioration and roughening of zirconia ceramic femoral head associated with phase transformation after total hip arthroplasty. They have analysed two zirconia femoral heads retrieved after three and six years and found that the monoclinic content rose from 1% to about 30% on the surface of the heads. SEM analysis of the heads revealed numerous craters indicating extraction of zirconia particles from the surface as shown in Figure 2-11. Surface roughness increased from an initial value of 0.006 μm up to 0.12 μm. The monoclinic content was found to be similar all over the surface of the head while the surface roughness varied. Clarke et al.[108] also conducted an extensive research on retrieved zirconia femoral heads. The Y-TZP ball retrieved at 8 years was found to have more than 70% transformed monoclinic phase and developed very high surface roughness whereas another ball retrieved after 10 years showed very high surface

finish and minimal phase transformation. This illustrated the variability of zirconia heads with regard to low temperature degradation (LTD) and the dependence on processing variables.

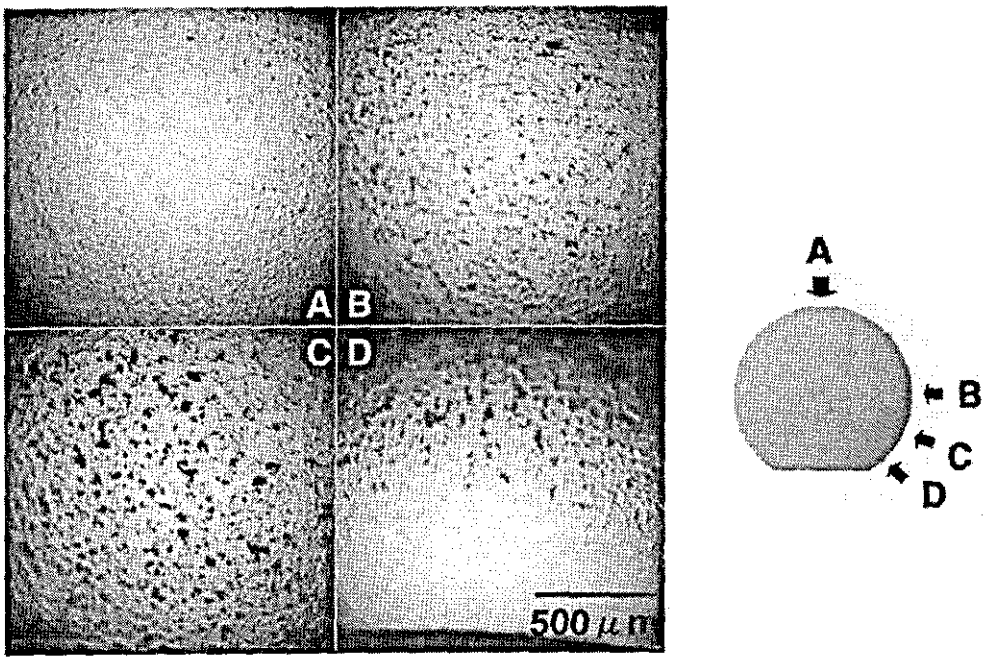

Figure 2-11 Photomicrographs of the retrieved zirconia head. Diagram showing A) the pole of the head, B) at the equator of the head, C) 5 mm below the equator and D) the lower border of the head. The distribution of the craters varied with the site. The surface near the pole (A) was relatively smooth while that near the equator was rough (C). The arrows on the diagram indicate the sites of observation. From Haraguchi et al.[111]

The following factors were reported to be characteristic of the degradation transformation:[112,113]

- The degradation process is most intensive at a temperature of 200 – 300°C and is time dependent;
- The degradation is caused by the tetragonal-monoclinic phase transformation, which is accompanied by micro and macro-cracking;
- Water and water vapour enhances the transformation;
- The transformation proceeds from the grain boundaries to the grain centre and from the surface of a component into the bulk, with the degradation depth increasing with the time of ageing;
- Finer grain sizes and higher stabiliser content retard the transformation.

In a review of the environmental degradation of zirconia ceramics, Lawson[114] also discussed the various aspects of the degradation, concluding that the most important variables were (i) material variables including grain size, stabiliser content and composition, and (ii) test variable including ageing temperature and test environment. Some of these factors will be discussed in the following sections with reference to the studies performed by different researchers.

There are at least three mechanisms reported for the ageing of zirconia with no single mechanism currently accepted by everyone. The most important mechanisms are discussed below.

Sato et al.[115] conducted hydrothermal ageing experiments for submicron samples with different yttria contents and proposed that water vapour reacted with Zr-O-Zr bonds to form Zr-OH bonds, leading to degradation, as shown schematically in Figure 2-12.

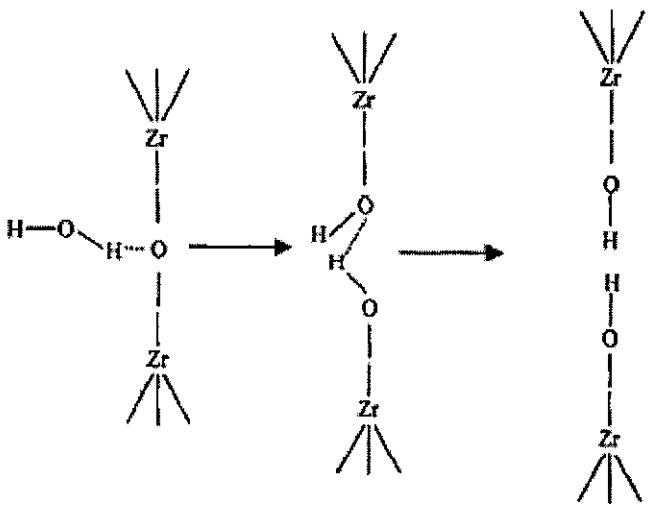

Figure 2-12 Proposed mechanism by Sato for the hydrothermal degradation of zirconia.[115]

Lange et al.[116] investigated the phenomenon at temperatures between 150°C and 400°C with respect to the gaseous ageing environment and the Y_2O_3 and SiO_2 content of the material. TEM of the samples after ageing showed that water vapour reacted with yttrium in the zirconia to produce clusters of small crystallites of α-$Y(OH)_3$. They hypothesised that this reaction produced a monoclinic nucleus on the surface of an exposed tetragonal grain. If the transformed grain was greater than a critical size, it produced a microcrack which exposed subsurface tetragonal grains to the ageing phenomenon and resulted in catastrophic degradation. They also suggested that the

degradation could be avoided by keeping the grain size below the critical value required for microcracking.

According to Yoshimura et al.[112,113] the dissociation of H_2O at the zirconia surface and the formation of Zr-OH or Y-OH bonds resulted in lattice strain at the surface, promoting the tetragonal to monoclinic transformation. IR spectroscopy studies showed the introduction of OH^- ions by the hydrothermal ageing. They proposed the following steps in the degradation mechanism of Y-TZP by water:

- The chemical adsorption of H_2O at the surface;
- The formation of Zr-OH and/or Y-OH at the surface, at which point stressed sites were created;
- The accumulation of the stresses by the migration of OH- at the surface and in the lattice to prepare nucleating defects;
- The nucleation of the monoclinic phase in the tetragonal grains; then the t-m transformation yields micro and macro-cracking.

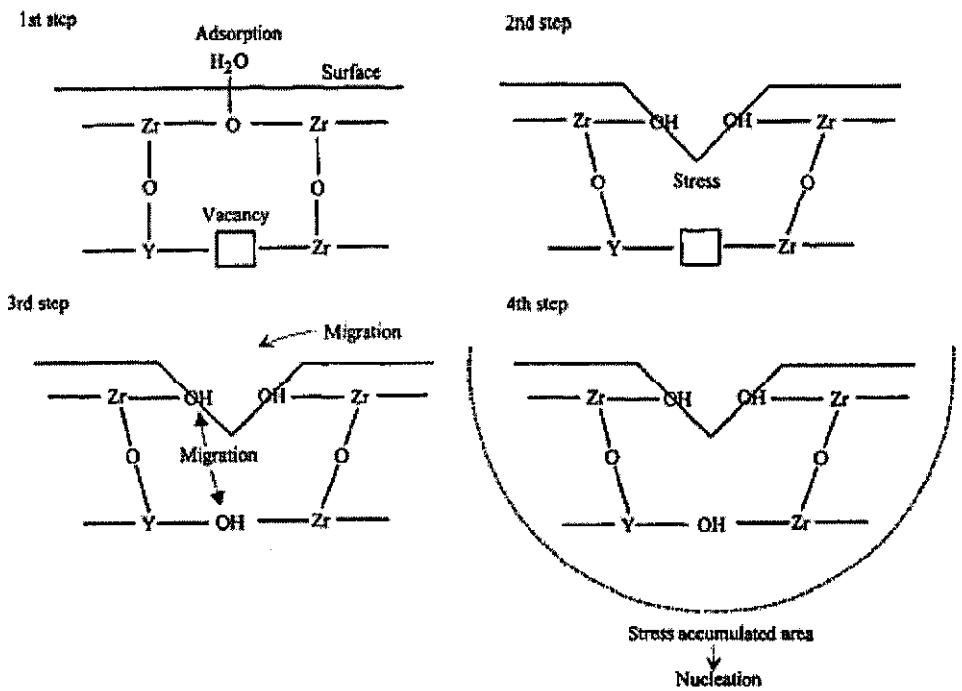

Figure 2-13 Various steps involved in the hydrothermal degradation of zirconia according to Yoshimura et al.[112,113]

Hernandez et al.[117] proposed that the reaction of OH^- ions with the more active Y_2O_3 to form an oxyhydroxide, YO(OH), species was the key process responsible for the

degradation of yttria stabilised zirconia. Guo[118] presented a similar mechanism based on the chemical adsorption of H_2O on ZrO_2 surface and the reaction to form OH^- ions.

The mechanisms proposed by Sato[115] and Yoshimura[112,113] failed to explain the effects of grain size and yttria content. The mechanisms proposed by Lange[116] and Hernandez[117] can explain the effect of dopant level, but they cannot explain the effect of grain size. The mechanism proposed by Guo[118] can explain the effects of both dopant level and grain size.

The effect of grain size on hydrothermal degradation has also been reported in literature.[93,119] Eichler et al.[93] studied the hydrothermal degradation of 3Y-TZP with mean grain sizes in the range 110-480 nm at 200°C and 16 bar pressure for 6 h in an autoclave. For the 110 and 210 nm mean grain size batches, the mean strength decreased by 8% and 14% respectively. For the 110 nm mean grain size samples, the monoclinic content was reported to be 11% whilst for the 210 nm mean grain size, the degradation was more severe reaching a maximum of 90% monoclinic at the surface and the depth of transformation was also higher compared to the 110 nm samples. For even larger grain sizes, the monoclinic phase content was more than 97% at the surface. Saldana et al.[119] prepared samples by Hipping at 1400, 1500 and 1600°C and performed ageing studies in air and in water at different temperatures. No transformation was observed in air and the transformation in water after 8 h ageing was found to be minimal for the samples Hipped at the lowest temperature. They suggested that fully dense materials with mean grain sizes <0.36 μm had got superior ageing resistance and considered this as the critical grain size for low temperature degradation resistance.

Chevalier[120] recently illustrated schematically the various events taking place during the hydrothermal degradation of zirconia Figure 2-14.

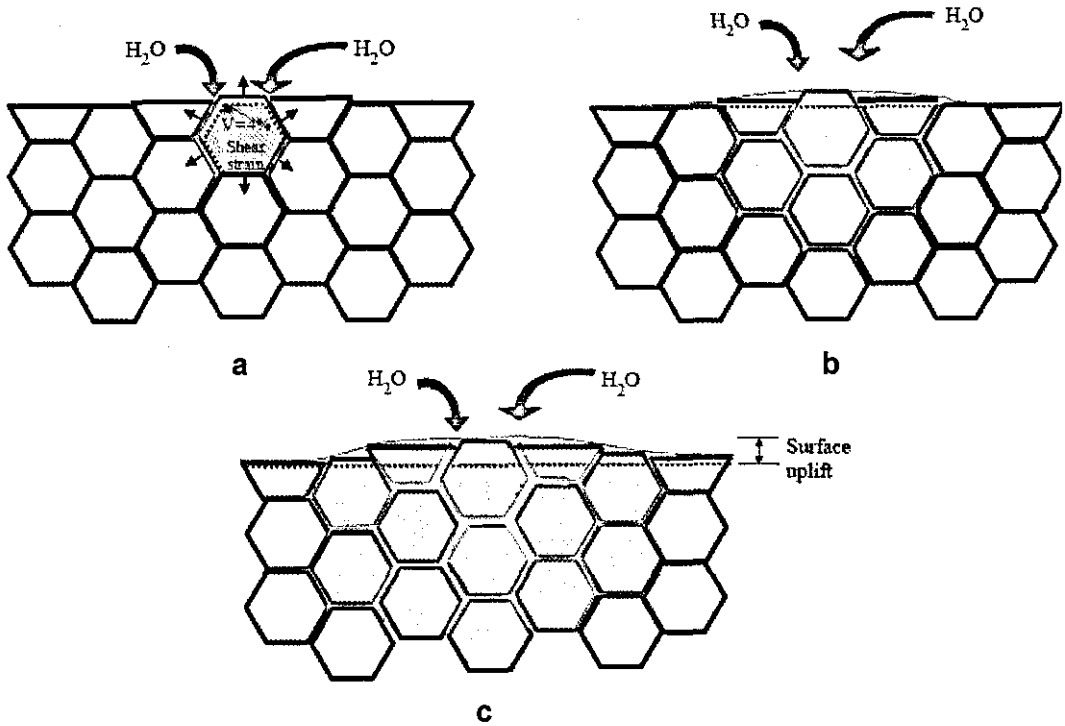

Figure 2-14 Schematic of the ageing process occurring in a cross section according to Chevalier, showing the transformation from one grain to its neighbours. (a) Nucleation on a particular grain at the surface, leading to microcracking and stresses to the neighbours. (b) Growth of the transformed zone, (c) Leading to extensive microcracking and surface roughening. Transformed grains are gray; the red path represents the penetration of water due to microcracking around the transformed grains.[120]

2.5 Issues related to the fabrication of nanoceramics from nanocrystalline powders

So far the potential advantages for nanoceramics have been discussed with main focus on nanozirconia, but there are at least four major obstacles to the preparation of nanoceramics by the compaction and sintering of ultrafine starting powders.[21] They are:

- The production of sufficient quantities of nanocrystalline powder;
- The control of agglomeration in the nanocrystalline powder;
- The compaction of the ultrafine particles to achieve flawless dense packing before sintering and
- The minimisation of grain growth during sintering.

The first three will be discussed below and the fourth one will be discussed in Section 2.11.

2.5.1 *Production of sufficient quantities of ultrafine powder*

In the early years the production of ultrafine powder was a major hurdle in the preparation of nanoceramics. In 1984 Gleiter et al.[121] reported a "gas phase condensation" technique for the preparation of iron nanoparticles with less than 10 nm particle size. Later the technique has been used for the preparation of ceramic nanoparticles also. ZnO[122] and MgO[123] were prepared by direct evaporation and condensation of high vapour pressure ceramics. Due to the simplicity of the process the technique gained popularity and other oxide ceramics such as TiO_2,[124,125] Al_2O_3[123] etc. were also prepared. Techniques that have been scaled-up for the commercial production of nanopowders include gas condensation, combustion synthesis, thermochemical synthesis, chemical precipitation and sol-gel processing. Because of these techniques, a large number of reasonably good quality nanopowders are available now.

2.5.2 Control of agglomeration in nanocrystalline powders

Agglomeration is a natural property of nanoparticles. In nanocrystalline powders, the crystallites are bonded together to form larger units or agglomerates. Hard agglomerates hinder the progress of pore elimination and prevent different nanoparticles from uniform mixing

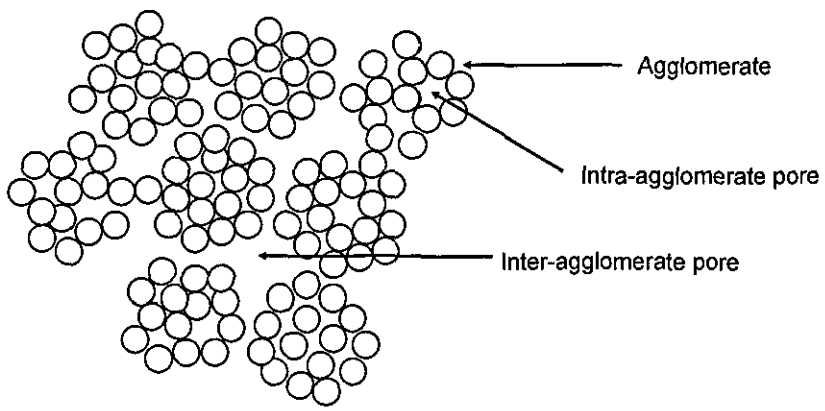

Figure 2-15 Schematic representation of agglomerates in powders.

In the case of agglomeration, the presence of both intra-agglomerate and inter-agglomerate pores in the agglomerated powder will lead to two separate peaks in the pore size distribution curve, one corresponding to the small intra-agglomerate pores

and the other to the inter-agglomerate pores. Pressureless sintering is very sensitive to the agglomeration of nanoparticles because the driving force, shrinkage and shrinkage rate inside agglomerates differ from those in between agglomerates. This leads to internal stresses, and appearance and stabilisation of large pores or microcracks. The size of such a defect is determined by the density, strength and size of the agglomerate. The presence of agglomerates is therefore extremely deleterious to the sintering of nanocrystalline particles to a solid with mean grain sizes <100 nm.

The larger the agglomerate size, the higher will be the sintering temperature. The latter resulting from the necessity of eliminating large inter-agglomerate pores during densification.[126,127,128,129] In the sintering of an agglomerated powder, the small intra-agglomerate pores present will disappear first, partway through the sintering process, as shown in Figure 2-16. At this point the widely spaced large inter-agglomerate pores are the only pores present to pin grain boundaries and control grain growth, so the grain size can easily grow to the agglomerate size. Note that the inter-agglomerate pores remained even after heating at higher temperatures. These high sintering temperatures promote grain growth.

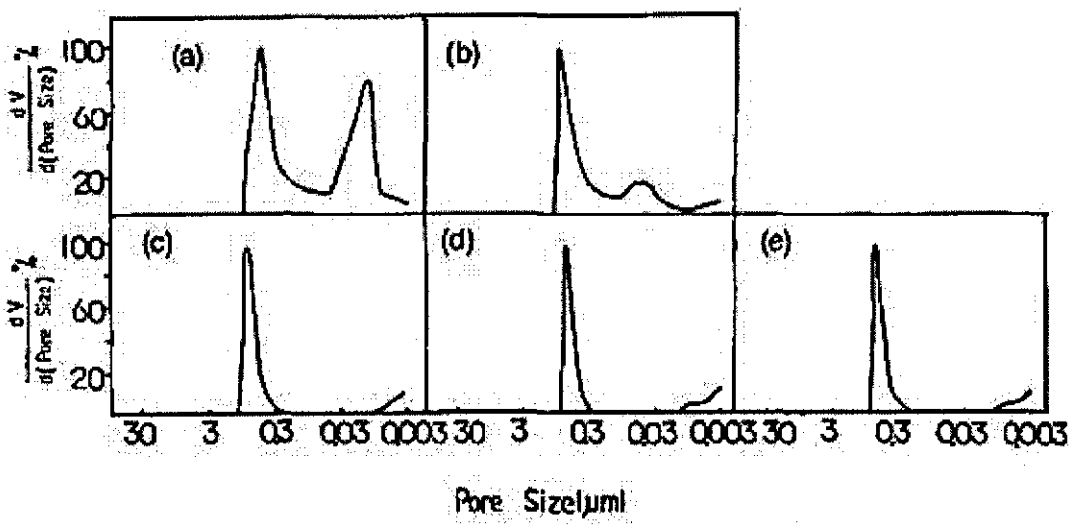

Figure 2-16 Pore size distributions of bodies up to (a) 1000°C, (b) 1250°C (c) 1400°C (d) 1600°C and (d) 1800°C (Compacts formed at 100 MPa. Constant heating rate for all bodies).[126]

2.5.3 Green forming - Dry routes

The preparation of green bodies with higher green density and uniform density distribution are critical for the preparation of nanoceramics; the uniformity and homogeneity of green bodies affects the densification and grain growth as described

above. In addition to agglomeration, nanoparticles have got a large number of particle-particle point contacts per unit volume compared with a submicron powder. Each of these point contacts represents a source of frictional resistance to the compaction of the powder and thus the total frictional resistance to compaction can be much greater.[128] Consequently, for a given applied stress during compaction, there tends to be less particle-particle sliding and particle rearrangement than for a conventional submicrometer powder. In some cases the surface roughness of the die is higher than the particle diameter resulting in high friction coefficients.

The different techniques reported to compact nanocrystalline powders into green bodies are discussed below.

2.5.3.1 Cold uniaxial pressing

Here the powder confined in a die is compacted by uniaxial pressing at room temperature. Even with submicrometer sized powders, however, uniaxial pressing results in density gradients and residual stresses throughout the thickness of the green body and these are much more severe with non free-flowing nanopowders. Cold compaction pressures used to consolidate nanocrystalline powders are often extremely large, 1-9 GPa.[124,125,130] When using such high pressures, the specimen size is limited to small diameters (<1 cm).

2.5.3.2 Pressing with powerful ultrasonic action

Here intensive mechanical ultrasonic vibrations are applied during consolidation to decrease the negative effect of die wall friction. The friction forces are mainly acting on the die walls and because of the powerful ultrasonic action, the powder particles will become detached from the die walls periodically, reducing the friction forces. The ultrasonic action also decreases the interparticle friction forces resulting in higher green densities.[131]

2.5.3.3 Collector pressing

In collector pressing, the direction of the die wall friction is redistributed to eliminate the effects of die wall friction which causes density gradients. This is achieved by moving the parts of the die in various directions relative to the powder compact. It can reduce the density gradients along the axis of a green compact by as much as 60% compared to uniaxial pressing.[131]

2.5.3.4 Cold isostatic pressing

In this process the powder is shaped at a low pressure (typically by uniaxial pressing), then encapsulated in a deformable, leak proof membrane (rubber, latex or polymer), and immersed in a liquid that is subsequently pressurised. The liquid evenly distributes the stress along all the surfaces of the powder compact and hence the density gradients will be smaller compared to uniaxial pressing and better particle packing is achieved. However, the process is typically limited to maximum pressures of ~550 MPa, too low for pressing agglomerated nanoparticles. Consequently, the process is often used as a preliminary compaction procedure, to produce green bodies that are ultimately consolidated by hot isostatic pressing or sinter-forging.

2.5.4 Green forming - Wet routes

2.5.4.1 Colloidal processing of ceramics

The main steps in colloidal processing are the preparation of the suspension, consolidation of the suspension into the desired component shape and the removal of the solvent phase. Colloidal processing has been shown to produce low defect densities and uniform microstructures from submicrometer ceramic powders. The main benefit of colloidal processing compared to the common powder processing is that in colloidal processing the ceramic particle packing is controlled by the particle size and not by the granule size and hence it can produce near-perfect green bodies.[132,133]

Colloidal stability is governed by the total interparticle potential energy, V_{total}, which can be expressed as[132]

$$V_{total} = V_{vdw}+V_{elect}+V_{steric}+V_{structural} \qquad \text{Eqn. (2.4)}$$

where V_{vdw} is the attractive potential energy due to long range van der Waals interactions between particles, V_{elect} is the repulsive potential energy resulting from electrostatic interactions between like charged particle surfaces, V_{steric} is the repulsive potential energy resulting from steric interactions between particle surfaces coated with adsorbed polymeric species, and $V_{structural}$ is the potential energy resulting from the presence of non-adsorbed species in solution that may either increase or decrease suspension stability. The various types of stabilisation are schematically illustrated in Figure 2-17.

There are a large number of techniques available to prepare ceramic green bodies from a colloidal suspension, which can be classified into different groups. Consolidation via; (1) fluid removal including pressure filtration, slip casting, osmotic consolidation, tape casting and robocasting, (2) particle flow including sedimentation, centrifugation and electrophoretic deposition and (3) gelation including aqueous injection moulding, gel casting and direct coagulation casting. Out of all these methods only slip casting will be discussed in some detail below as it is more relevant for the present work.

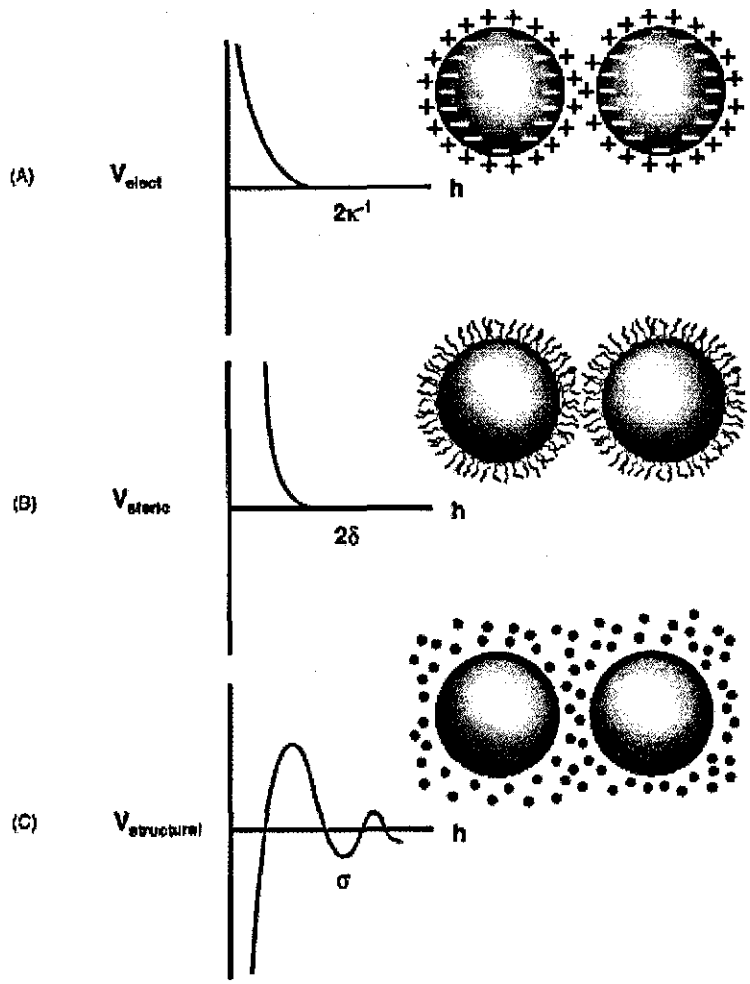

Figure 2-17 Schematic illustration of the interaction potential energy and relevant length scales for (A) electrostatic, (B) steric, and (C) structural contributions, where k^{-1} is the effective double-layer thickness, δ the adlayer thickness, and σ the characteristic size of species resulting in ordering within the interparticle gap. From Lewis.[132]

2.5.4.2 Slip casting

Slip casting consists of making a slurry of the green body constituents, then casting this in a porous mould, typically of (naturally porous) plaster. It can be considered as a low pressure filtration method where capillary suction provides the driving force for liquid removal and formation of a cast body as shown in Figure 2-18.

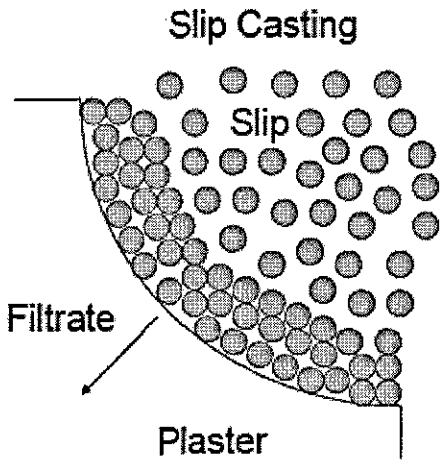

Figure 2-18 Liquid removal during slip casting.[134]

During slip casting, the majority of the liquid vehicle is removed to yield a saturated ceramic body that is subsequently dried, binder removed and sintered. The fluid flows into the mould via capillary driven transport. As much of the slurry liquid at or near the mould surface is absorbed in the pores in the mould, a layer of solid is formed by the interlocking solid particles in the region near the mould surface. As the process continues, this solid layer increases so long as the mould pores continue to absorb slurry liquid. Slip casting is a slow process since the casting rate decreases parabolically with the thickness of the cast layer.

There are two important factors to be considered while slip casting. The first is the slurry, usually known as a slip. For reasonable shelf life and uniformity of the resultant green body, stable slips are important. The following factors are to be considered while preparing a proper slip for casting, the volume fraction of the ceramic in the slurry, particle size, particle shape, particle surface charges, and the degree of dispersion.[135] The particle size distribution is another important factor as it influences the packing in the green body and hence the green density. The particle surface condition is critical in slip casting as it affects the state of dispersion of the

slurry. A good dispersion with high solid content is preferred in slip casting as it can lead to high green density and low pore volume. Ultrasonication is found to improve dispersion and hence the quality of the green body.[135]

Proper mould preparation is the second critical factor in slip casting. The moulds are usually prepared using plaster of Paris and the amount of water used in the preparation of the moulds will control the porosity of the mould and hence the ability of the mould to absorb water from the slip. 70 to 80 wt% water is normally used in the preparation of moulds. A detailed description of the mechanics of slip casting process can be found in Rahaman.[136]

Out of all the slip casting variants, drain casting and solid casting are commonly used as shown in Figure 2-19.

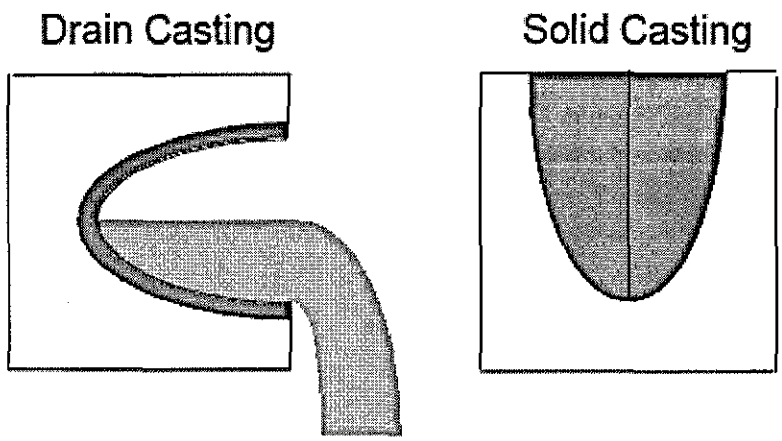

Figure 2-19 Drain casting and solid casting of ceramics.[134]

In drain casting when the desired thickness is reached, the excess slip is poured out or drained from the mould. Solid casting is identical, but slip is continuously added until a solid body has been achieved.[135] The major limitation of slip casting is the long time required to cast articles in the mould. Its also labour intensive, requires a large inventory of moulds and requires more floor space compared to dry pressing. The ability to obtain a better particle packing and a resulting narrow pore size distribution offsets some of these disadvantages,[137] however.

2.6 Colloidal processing of zirconia

Colloidal processing has been used widely for the processing of zirconia ceramics in general with a large number of publications on the processing of submicron zirconia

powders,[138,139,140,141] however, there are only a very few reports for the processing of nanopowders.

Shojai et al.[138] prepared stable aqueous suspension of 3YSZ powder using both electrostatic and electrosteric stabilisation. They found that the zirconia particle surface was positively charged at pH < isoelectric point (IEP) and electrostatic stabilisation was reported to be efficient at acidic pH < 4 where zeta potential was >40 mV, however the stability of the suspension was very sensitive to slight changes in pH, and this was easily caused by the dissolution of yttria in 3YSZ, which is highly basic. For electrostatic stabilisation an ammonium salt of polymethacrylic acid (PMMA-NH_3) was used. Fengqiu et al.[139] also used polymethacrylic acid for the stabilisation of zirconia. They have also studied the effect of polyethylene imine (PEI) and diammonium citrate (DAC). Wang et al.[140] studied the dispersion stability of 8YSZ with polyacrylic acid (PAA) as the dispersing agent. They have analysed the influence of the pH value, solid loading, temperature and the amount and molecular weight of PAA on the dispersion stability. The preparation of 78 and 83 wt% 8YSZ slip using ammonium polyacrylate and its slip casting has also been reported in literature.[141]

The stabilisation of nanozirconia particles in water is more complex because of the small particle size and the resultant large surface area and surface energy. The development of green nanostructured ceramics by wet forming routes requires very strict control of the colloidal forces involved in order to overcome the strong tendency toward agglomeration. The surface properties of nanozirconia particles with PEI have been reported in the literature.[142] Duran et al.[143] also studied the stabilisation of nanozirconia in water using PEI as the dispersant. Suspensions were prepared with different amounts of dispersant at different pH values and then slip cast to prepare green bodies. They found that the amount of PEI adsorbed increased steeply with increase in pH. Synthesis of nanozirconia powder, its dispersion in water, slip casting and sintering has been reported by Vasylkiv et al.[78] Ammonium polycarboxylate was used as the dispersant and ultrasonication was used to break the agglomerates. Suspensions with solid content up to 30 vol% were prepared and after slip casting, the green density obtained was about 46% of theoretical which was increased to 52% on subsequent cold isostatic pressing. The use of ammonium polyacrylate as a dispersant

for nanozirconia has also been reported in literature.[144] Jachimska et al.[145] used polysodium 4-styrenesulfonate as a dispersant, but the result was poor. The rheological properties of highly filled (20 vol%) nanozirconia suspension in water and water-1-2 propanediol mix with respect to various dispersants has also been reported in literature.[146]

Chera et al.[147] compared seven commercially available dispersants for the preparation of concentrated aqueous suspensions of nanoalumina and nanozirconia.
Table 2-2 lists the various dispersants used and Figure 2-20 shows the zeta potential values obtained for nanozirconia with the various dispersants.

Table 2-2 Surfactants used by Chera et al.[147]

Surfactant	Producer	Chemical characteristic
Tiron	Aldrich, USA	a low molecular weight aromatic di-sufonic acid, anion active
Aluminon	Aldrich, USA	a low molecular weight aromatic tri-carboxylic acid, anion active
Tri-ammonium citrate	Merck, Germany	a low molecular weight aliphatic tri-carboxylic acid, anion active
Atsurf 3315	ICI, UK	a modified polycarboxylic acid, anion-active
Atsurf 3222	ICI, UK	polyalkylene amine derivative, cation-active
PAA	Aldrich, USA	polyacrylic acid, Mw 1200, polyelectrolyte, anion-active
KD 7	Uniqem, UK	polyacrylic acid-based copolymer (PAA – polyethylenglycol), anion- active

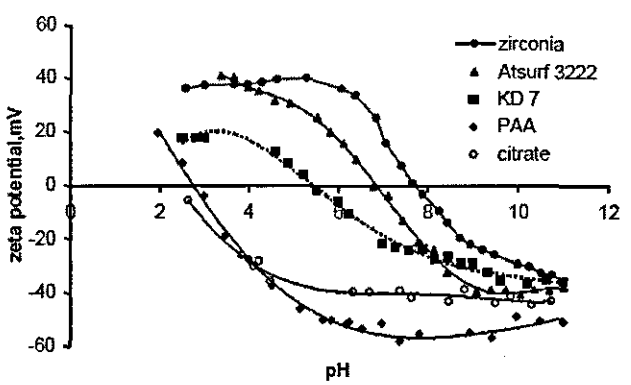

Figure 2-20 Zeta potential versus pH in (a) alumina and (b) zirconia aqueous suspensions with and without dispersants.[147]

The maximum solid content achieved was 74 wt% for alumina with atsurf 3315 and 72.7 wt% for zirconia with atsurf 3222. No mention was given about the long term stability, viscosity or further processing of the suspensions into solid bodies

Santacruz et al.[148,149] developed a multiultrasound process involving more than one dispersant to prepare very stable, high solid content, low viscosity nanozirconia suspensions. They were able to prepare up to 28 vol% (70 wt%) suspensions with less than 0.05 Pa s viscosity which were stable for more than 15 days. They studied a number of systems consisting of different dispersants including PEI, tetramethyl ammonium hydroxide (TMAH) and ammonium polyacrylate (Dispex A40) and TMAH and TAC. Both Dispex A40 and TAC were found to be effective in the basic pH and the TMAH-TAC system was reported to be the best.

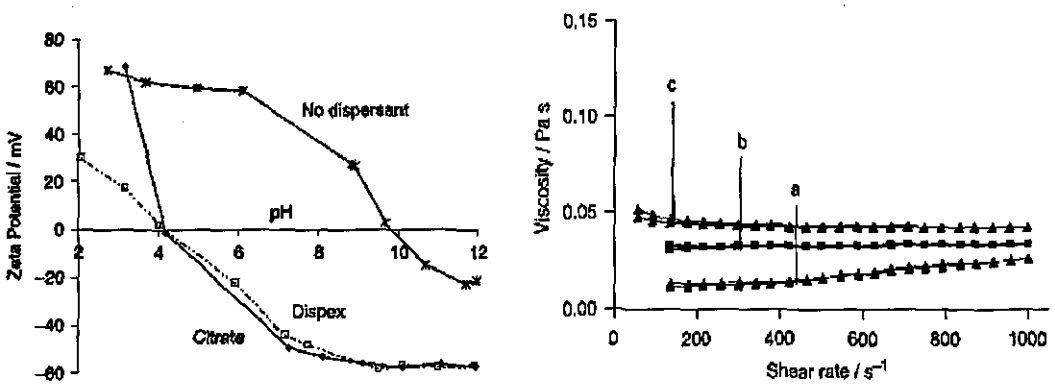

Figure 2-21 Zeta potential as a function of pH for the diluted nanosuspension without dispersant, with 2.5 wt% Dispex A40 or TAC. Figure on the right shows the viscosity curves for the nanosuspensions: (a) 24.0 vol% using TMAH and TAC after a 6 min. ultrasound, (b) 19.0 vol% prepared using TMAH and Dispex A40 after multiultrasound, (c) 28.0 vol% using TMAH and TAC after multiultrasound treatments[148]

The destabilisation of TMAH-Dispex A40 system on multiultrasound for longer periods of time was suggested to be due to the breaking of the Dispex A40 chain, since it is longer than TAC.

2.7 Sintering

Sintering is a processing technique used to produce density-controlled materials and components from metal and/or ceramic powders by the application of thermal energy. In ceramic sintering, the dried and debinded green body is converted to a useful body by the application of thermal energy. A number of diffusion mechanisms are involved

during sintering, which together produce the required increase in density and changes in mechanical and other properties of the material. Through this diffusion, ions move into vacancies within the crystal lattice, resulting in a net transport of empty space from the bulk of the material to the surface causing an eventual reduction in volume.

2.7.1 Categories of sintering

Sintering processes can be generally divided into solid state sintering and liquid phase sintering.[150] Solid state sintering occurs when the powder compact is densified wholly in a solid state at the sintering temperature, whilst liquid phase sintering occurs when a liquid phase is present in the powder compact at the sintering temperature. Figure 2-22 illustrates the two cases in a schematic phase diagram. At temperature T_1, solid state sintering occurs in an A-B powder compact with composition X_1, while at temperature T_3, liquid phase sintering occurs in the same powder compact.

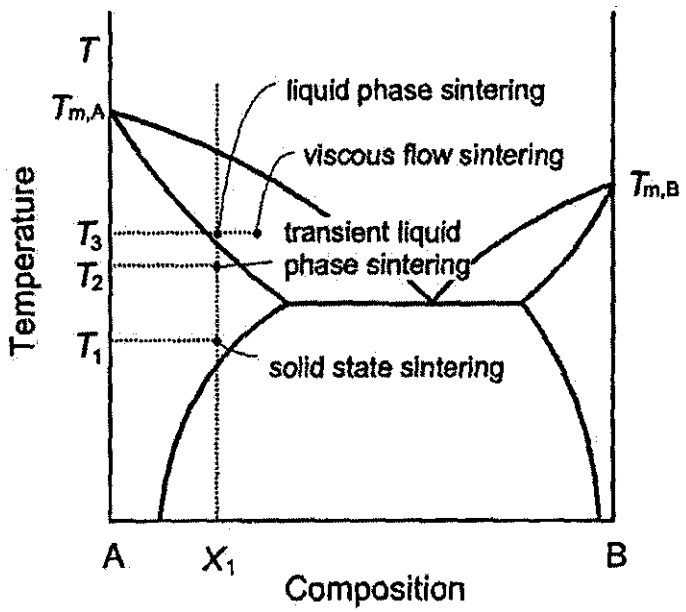

Figure 2-22 Illustration of various types of sintering.[150]

In addition to solid state and liquid phase sintering, other types of sintering such as transient liquid phase sintering and viscous flow sintering can be utilised. Viscous flow sintering occurs when the volume fraction of liquid is sufficiently high that the full densification of the compact can be achieved by a viscous flow, without having any grain shape change during the final stages of densification. Transient liquid phase sintering is a combination of liquid phase sintering and solid phase sintering. In this case a liquid phase forms in the early stages of sintering, but the liquid disappears as

sintering proceeds and densification is completed in the solid state. Figure 2-23 shows a comparison of the microstructures obtained by solid state and liquid phase sintering.

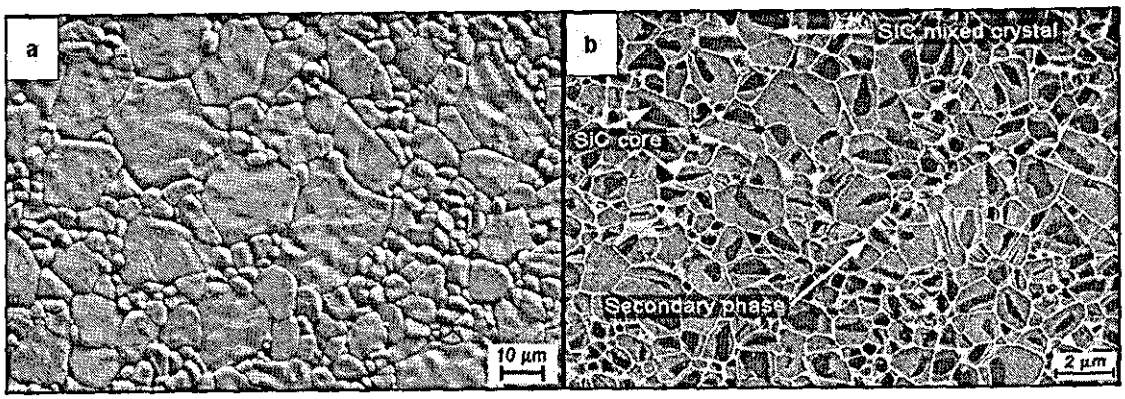

Figure 2-23 Typical microstructures observed during (a) Solid state sintering (Al_2O_3) (b) Liquid state sintering (SiC).[151]

2.7.2 Driving forces for sintering

The main driving force for sintering is the reduction of the total surface interfacial energy. For a powder compact this is expressed as γA, where γ is the interfacial energy and A specific surface area of the compact. The reduction of the total energy can be expressed as[150]

$$\Delta(\gamma A) = \Delta\gamma A + \gamma\Delta A \qquad \text{Eqn. (2.5)}$$

Here the change in interfacial energy ($\Delta\gamma$) is due to densification and the change in interfacial area (ΔA) is due to grain coarsening.

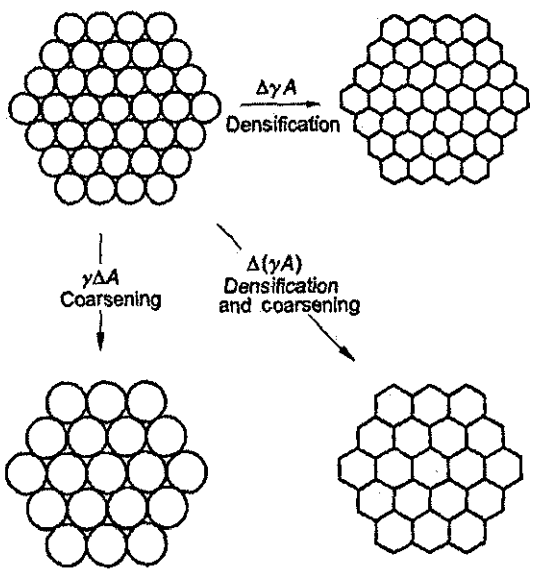

Figure 2-24 Basic phenomena occurring during sintering.[150]

For solid state sintering, $\Delta\gamma$ is related to the replacement of solid/vapour interfaces by solid/solid interfaces. As schematically shown in Figure 2-24, the reduction in total interfacial energy occurs via densification and grain growth, the basic phenomena of sintering.

2.8 Solid state sintering models and densification

Solid state sintering is usually divided into three overlapping stages – initial, intermediate and final. Figure 2-25 schematically depicts the typical densification curve of a compact through these stages over sintering time.

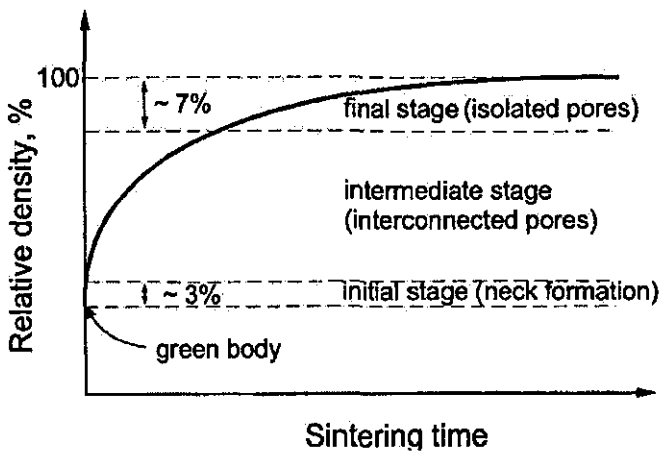

Figure 2-25 Densification curve of a compact showing the various stages of sintering.[150]

The initial stage is characterised by the formation of necks between particles and its contribution to compact shrinkage is limited to 2-3% at most. During the intermediate stage, considerable densification occurs before isolation of the pores. The final stage involves densification from the isolated pore state to the final densification.

2.9 Effect of sintering variables on sintering kinetics

The variables that affect the sinterability and final microstructure can be divided into two categories: material variables and process variables. Material variables include the chemical composition of the powder compact, powder particle size, size distribution and shape, degree of powder agglomeration, etc. These variables influence the powder compressibility and sinterability (densification and grain growth). In the case of compacts containing more than two kinds of powders, the homogeneity of the powder mixture is also of prime importance. The other variables involved in sintering are mostly processing variables, such as temperature, time,

atmosphere, pressure, heating and cooling rate. Some of the important variables are discussed in detail below.

2.9.1 Effect of particle size

Herring's scaling law can be used to explain the effect of particle size on sintering. Consider two particles with size a_1 and a_2 where $a_2 = \lambda a_1$. The powders are assumed to have similar shapes and are sintered under the same experimental conditions and by the same mechanism. Then the scaling law predicts the relation between the relative periods of time t_2 and t_1 required to get the same degree of sintering as[150]

$$t_2 = (\lambda)^{\alpha} t_1 \qquad \text{Eqn. (2.6)}$$

where α is an exponent and the value of α varies with the type of diffusion. For example $\alpha = 4$ for grain boundary diffusion, 2 for vapour diffusion and 3 for lattice diffusion.

In addition to particle size, the particle size distribution, the particle shape and particle structure and the particle packing all affect the sintering behaviour of green samples.

2.9.2 Effect of temperature

Sintering is a thermally activated process and the variables such as diffusivity, viscosity etc. varies with temperature. Generally ln t is proportional to 1/T, where t is the sintering time to get a given degree of sintering.[150] This general relation varies depending on the sintering mechanism, for example in the case of lattice diffusion ln(t/T) is proportional to 1/T.

2.9.3 Effect of pressure

In pressureless sintering the driving force for sintering is derived from the capillary pressure difference due to curvature difference. When an external pressure is applied, the total sintering pressure will become the sum of the capillary and external pressures. Densification rate always increases with increased pressure.[150]

2.9.4 Effect of chemical composition

The chemical composition can affect the diffusivity of the atoms and the atom mobility and hence can affect the rate of sintering and the sintering temperature.

Chemical modification is achieved by adding sintering aids, to initiate the sintering at a lower temperature, increase the sintering rate and also to achieve higher density.[150]

2.10 Grain growth

The average size of grains increases in the final stages of sintering in polycrystalline materials. The grain boundary is a region with a complex structure with thickness in the range 0.5 to 1.0 nm between two grains (crystalline domains). The atoms in the grain boundary have a higher energy than those in the bulk of the grains. The reduction in the grain boundary area and hence the energy associated with the grain boundaries provides the driving force for grain growth. Grain growth can be divided into two: normal and abnormal (or exaggerated) grain growth. Over the years many studies have been made on recrystallisation and grain growth. From these studies a number of rules about grain growth have been formulated. These rules are:[152]

1. Grain growth occurs by grain boundary migration and not by the coalescence of neighbouring grains as do water droplets;
2. Grain boundary migration is discontinuous or jerky and its direction may suddenly change;
3. One grain may grow into a neighbouring grain on one side while it is being consumed from another side;
4. The rate of consumption of a grain frequently becomes more rapid as the grain is about to disappear;
5. A curved grain boundary usually migrates towards its centre of curvature;
6. When grain boundaries in a single phase meet at angles other than 120 degrees, the grain included by the more acute angle will be consumed so that the angles approach 120 degrees.

These have been the basis of a number of theories that attempt to describe grain growth in terms of more fundamental characteristics such as driving forces and mechanisms of grain boundary migration.

2.10.1 Normal grain growth

Burke and Turnbull proposed a model for the migration of a grain boundary due to atom transport under a driving force caused by the difference in surface curvature as

shown in Figure 2-26 and Figure 2-27.[153] Because of the pressure of the surface curvature, the boundary tends to migrate toward its centre of curvature so that the grain boundary area and its energy can be reduced. A conceptual idea of the change in free energy associated with the diffusion of an atom from one grain to the next is shown in Figure 2-26.

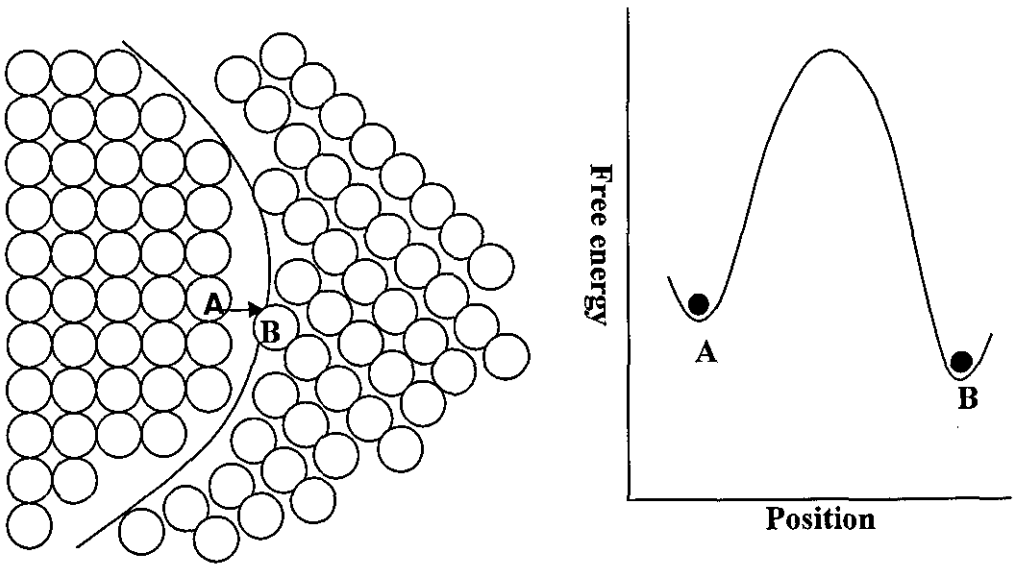

Figure 2-26 The movement of an atom from one side of the grain boundary to the other involves a change of Gibbs free energy. When an atom moves from position A to position B, the free energy will decrease, so it is a possible direction for an atom on the boundary to move and the boundary will move in the opposite direction.

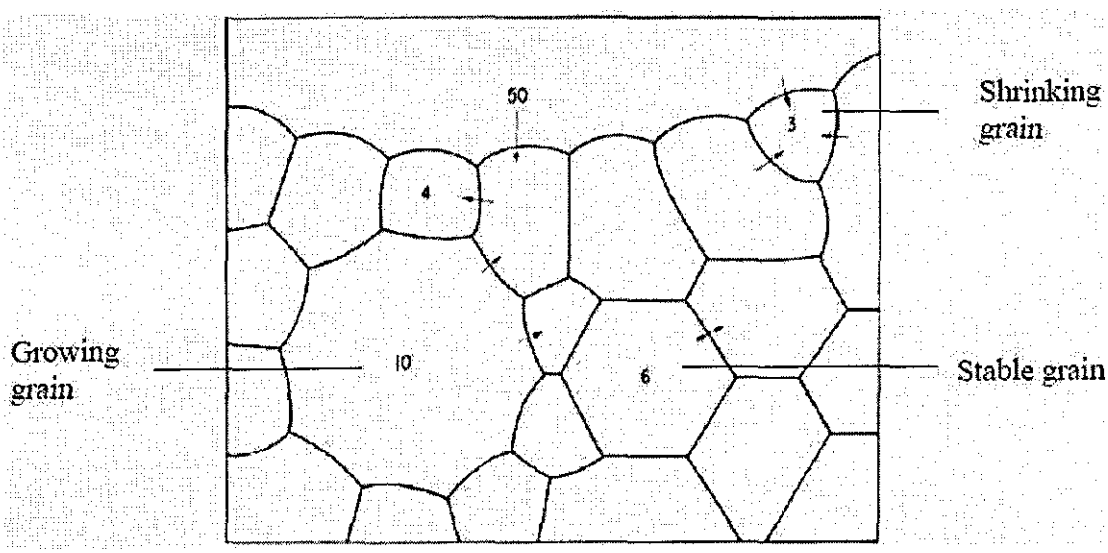

Figure 2-27 Schematic illustration of grain boundary movement.[153]

Due to the pressure of the surface curvature, the boundary tends to migrate toward its centre of the curvature, as this reduces the grain boundary area and hence its energy.

For a pure material, the velocity of grain boundary migration, v_{gb}, is given by the product of the grain boundary mobility, M_{gb}, and the force

$$v_{gb} = M_{gb} F_{gb} \qquad \text{Eqn. (2.7)}$$

where F_{gb} is the driving force

The pressure difference across the boundary is given by the equation of Young and Laplace[154]

$$\Delta p = \gamma_{gb}\left(\frac{1}{r_1}+\frac{1}{r_2}\right) \qquad \text{Eqn. (2.8)}$$

where r_1 and r_2 are the principal radii of curvature of the boundary. Assuming that the radii of the boundary is proportional to G, then[154]

$$\left(\frac{1}{r_1}+\frac{1}{r_2}\right) = \frac{\alpha}{G} \qquad \text{Eqn. (2.9)}$$

where α is a geometrical constant that depends on the shape of boundary and G is the average grain size. The driving force for atomic diffusion across the boundary can be taken as the gradient in the chemical potential[154]:

$$F_{gb} = \frac{d\mu}{dx} = \frac{d(\Omega\Delta p)}{dx} = \left(\frac{1}{\delta_{gb}}\right)\left(\frac{\gamma_{gb}\Omega\alpha}{G}\right) \qquad \text{Eqn. (2.10)}$$

where Ω is the atomic volume and $dx = \delta_{gb}$ is the width of the grain boundary. The flux of atoms across the boundary is[154]

$$J = \frac{D_{gb}}{\Omega kT}\frac{d\mu}{dx} = \frac{D_{gb}}{\Omega kT}\frac{\gamma_{gb}\Omega\alpha}{\delta_{gb}G} \qquad \text{Eqn. (2.11)}$$

where D_{gb} is the diffusion coefficient for atomic motion across the grain boundary. The boundary velocity becomes[154]

$$v_{gb} \approx \frac{dG}{dt} = \Omega J = \frac{D_{gb}}{kT}\left(\frac{\Omega}{\delta_{gb}}\right)\left(\frac{\gamma_{gb}\alpha}{G}\right) \qquad \text{Eqn. (2.12)}$$

The driving force is taken as the pressure difference across the boundary, $\gamma_{gb}\alpha/G$, and

$$v_{gb} \approx \frac{dG}{dt} = M_{gb} F_{gb} = \frac{D_{gb}}{kT}\left(\frac{\Omega}{\delta_{gb}}\right)\left(\frac{\gamma_{gb}\alpha}{G}\right)$$

so M_{gb} should be D_{gb}/kT.

The equation of v_{gb} may be integrated to yield[154,155,156,157]

$$G^2 - G_o^2 = \frac{2\alpha M_{gb}\gamma_{gb}\Omega}{\delta_{gb}}t = Kt \qquad \text{Eqn. (2.13)}$$

where K is $\dfrac{2\alpha M_{gb}\gamma_{gb}\Omega}{\delta_{gb}}$

Experimental measurement of normal grain growth in metals and ceramics has shown that parabolic growth is rarely obeyed. This means that Eq. 2.25 needs to be improved. For this reason, it is expressed by[154,155,156,157]

$$G^n - G_0^n = Kt, \qquad \text{Eqn. (2.14)}$$

where n is an integer. This equation can also account for impurity drag by various rate determining diffusion steps and pore drag by various rate determining steps.

2.10.2 Abnormal grain growth

Certain ceramic materials after sintering at sufficient temperature for a long enough period of time show some large grains distributed in a matrix of fine grains. These large grains are referred to as abnormal grains and develop as a result of abnormal or runaway grain growth in which the large grains have a much faster growth rate than the fine-grained matrix. The faster growth rate is normally explained in terms of the greater driving force for growth of a large grain in a fine-grained matrix relative to that for a small grain in the same matrix.

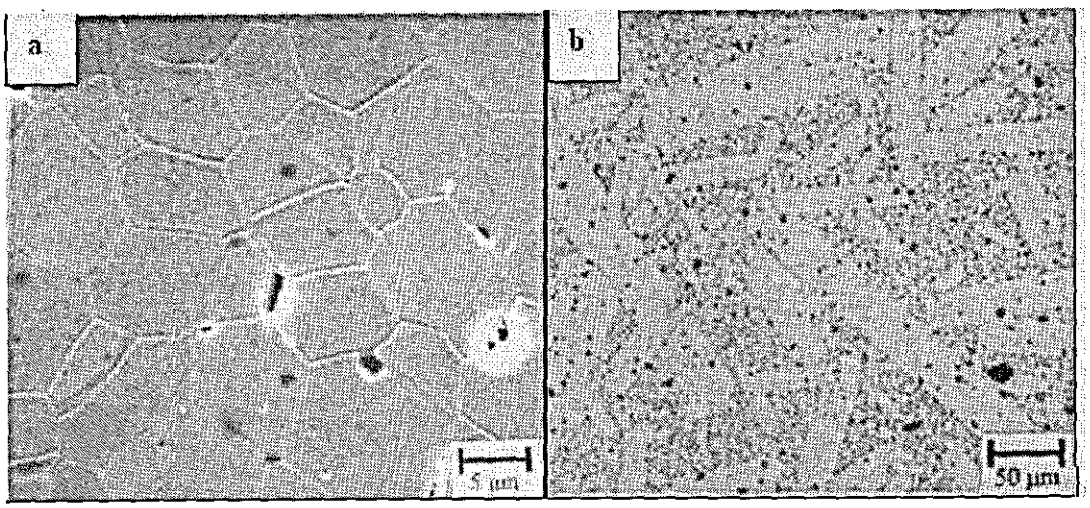

Figure 2-28 (a) Normal grain growth (pure Al_2O_3) (b) and abnormal grain growth in the presence of a liquid phase (0.05% anorthite).[158]

2.11 Minimising grain growth and maximising densification during sintering of ultrafine particles

As described in Section 2.10, final stage sintering is always accompanied by grain growth and is the biggest challenge in the preparation of nanoceramics. Studies on nanopowder consolidation have shown similar densification phenomena as in conventional powders.[30] The specific features of sintering small powders are related to a high tendency to agglomerate, significant interparticle friction, high reactivity and

associated contamination, rapid sintering, and grain coarsening. Densification of nanopowders takes place at temperatures well below those of larger grained powders, up to several hundred degrees lower. The onset of sintering in nanopowders may be as low as ~0.2 Tm as compared to about 0.5 Tm for their conventional counterparts.[159] There are various techniques to control grain growth and some of them are discussed below.

2.11.1 Rapid rate pressureless sintering

As discussed in the previous section there are generally two mechanisms operative in sintering. One, at lower temperatures, is controlled by surface diffusion and results in neck formation between particles but little actual densification and some grain growth. At higher temperatures sintering occurs by grain boundary or lattice diffusion.[159] Most of the densification occurs during this second stage. In rapid sintering, the heating schedule is manipulated to enhance the densification rate relative to the coarsening rate. To achieve this one should pass through the surface diffusion regime as quickly as possible and proceed directly to temperatures where more useful densification mechanisms are operative. Thus rapid heating prevents the amount of grain growth and also prevents the early grain growth from suppressing the densification kinetics later on. This technique is useful in systems where the activation energy for densification is higher than that of coarsening, and hence the rate of densification is higher than that of coarsening at higher temperatures.

Nanocrystalline ceramics are ideal for rapid rate sintering because of their large surface areas. This technique has been used with success for the sintering of Al_2O_3,[160] $BaTiO_3$,[161] Al_2O_3-TiC and ZrO_2[21] ceramics. Materials with lower thermal conductivity can result in thermal gradients at high heating rates leading to non-uniform densification and cracking.

2.11.2 Hot pressing

Hot uniaxial pressing has been used to consolidate nanocrystalline ceramics. Here pressure and temperature are applied simultaneously to a sample contained typically in a graphite die; the pressures used span a large range, typically 25 MPa to 50 MPa. The application of pressure at the sintering temperature accelerates the kinetics of densification by increasing the contact stress between particles and by rearranging

particle positions to improve packing.[162] The energy available for densification is increased by a factor of about 20 by application of pressure during sintering; this can reduce the sintering temperature, usually resulting in less grain growth than would occur with pressureless sintering. This technique can only be used for samples with simple shapes and has been reported for the sintering of metals, intermetallic compounds[159] and nanoceramics.[163]

2.11.3 Hot isostatic pressing (HIPing)

In hot isostatic pressing, pressure is applied simultaneously from multiple directions whilst heating the sample resulting in a more uniform pressure distribution in the sample. HIP densification involves relatively long times and grain growth is more likely to occur than in hot pressing, however grain sizes <100 nm have been reported by this method.[159] This is achieved by sintering the samples under very high pressure (2 to 5 GPa) for a relatively shorter period of time (30 min).[164] The equipment cost is very high for this technique and it is limited to samples with simple geometries.

2.11.4 Sinter forging

The most attractive benefit of sinter forging is its ability to densify green compacts with large inter-agglomerate pores. In sinter forging a uniaxial pressure is applied, but unlike hot pressing or HIPing the sample is not confined by the die walls. Hence the sample is free to move in the lateral direction.[165] This shear deformation can lead to the elimination of large pores as shown in Figure 2-29. The stress levels required for sinter forging are also lower than in hot pressing or HIPing. This method has been used extensively to achieve nanoceramic particle consolidation for ceramics such as ZrO_2, Al_2O_3,[166]TiO_2 and ZrO_2 toughened Al_2O_3.[159]

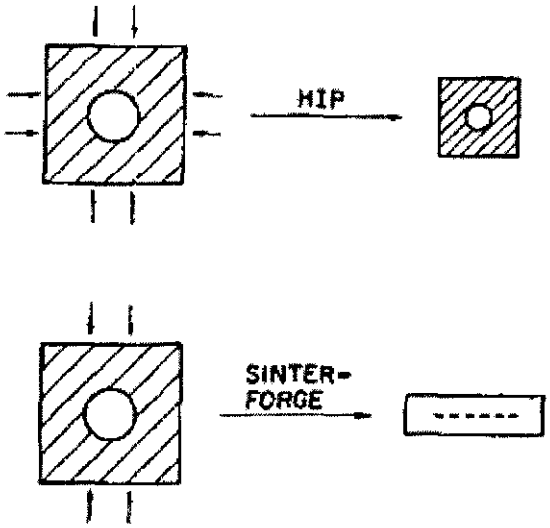

Figure 2-29 Schematic showing how shear deformation can lead to the breakdown of large pores.[167]

2.11.5 Ultrahigh pressure sintering

Here the pressures applied during sintering are very high; values up to 5-7 GPa have been achieved using belt-type and piston-anvil devices and cubic anvil cells. This high pressure, in combination with lower sintering temperatures, can be used to sinter nanoceramics. This technique has been reported for the sintering of 200 nm grain size SiC ceramics by applying 980 MPa pressure at 1600°C for 1 h.[168]

2.11.6 Shock compaction

In shock compaction high velocity compressive waves are used to compact and sinter ceramic powders simultaneously. The shock wave induces high pressure and at the same time causes localised heating of the particle surfaces due to friction between adjacent rubbing particles. As a result of their small size, nanocrystalline particles allow this surface heating to be transferred quickly to the core of the particles, thereby allowing the entire particle to be at elevated temperature before the shock wave has completely passed through the particle.[21,159]

2.11.7 Field assisted sintering techniques (FAST)

FAST techniques utilise the effect of an electric field on the particle surface and the resulting enhanced mass transport. Spark plasma sintering (SPS) or pulse electro-discharge consolidation where a powder compact is subjected to one or more arc

discharges before or during pressure assisted sintering can significantly reduce sintering temperature and time.[159] The key characteristics of SPS are:

1. The generation of local electric discharge and its effect on heat and mass transport;
2. The combined effect of external fields such as force and electric field on the densification and phase formation in a particulate system;
3. Influence of electric current in the near surface layers of conductors and semiconductors as well as insulators;
4. Rapid and uniform heating/cooling throughout the sample which gives the possibility to avoid thermal gradients.

2.11.8 Two-step sintering

Two-step sintering is relatively a new sintering technique for the production of advanced ceramics. This technique was first reported as a method for the preparation of nanostructured ceramics by Chen et al.[169,170] for the sintering of nanostructured yttria (Y_2O_3) ceramics. In their work they heated the green compacts to a high temperature, T_1, for a very short time and then cooled it down to a lower temperature, T_2, and held at that temperature for sufficient time so that complete densification was achieved. The main advantage of this technique was that it can be used effectively for the preparation of nanostructured ceramics. In addition to Y_2O_3, this technique has been used successfully for the sintering of silicon carbide (SiC),[171] barium titanate ($BaTiO_3$),[172,173,174] zinc oxide (ZnO),[175,176] Ni-Cu- Zn ferrite,[173] PbTiO3 based ceramics,[177] and ZrO_2[178] nanoceramics and also for nano[179] and submicrometer alumina.[180]

In the two-step sintering of yttria,[169] the green samples were initially heated to 1250 or 1310°C for a very short time and then cooled down and held at 1150°C for 20 h to achieve full density. No grain growth was reported during the second stage of heating as shown in Figure 2-30. To succeed in two-step sintering, a sufficiently high density (>70% of TD for Y_2O_3) is required after the first step.

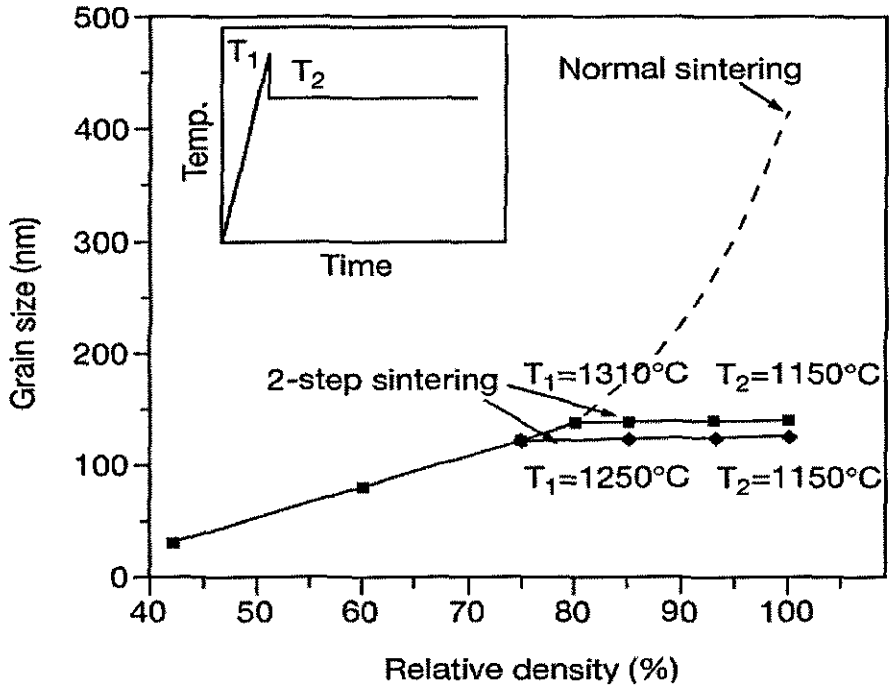

Figure 2-30 Grain size of Y_2O_3 in two step sintering[169] (Heating schedule shown in inset). Note that the grain size remains approx. constant in the second sintering step.

The lack of grain growth in second-step sintering has important implications for kinetics. Chen et al. claimed that during the second-step sintering, the microstructure was frozen and hence the sintering kinetics was slower. Yet the slower kinetics was sufficient for reaching full density, while providing the benefit of suppressing the grain growth. Suppression of grain growth, but not densification, is consistent with a grain boundary network pinned by triple-point junctions which have higher activation energy for migration than grain boundaries. Thus the feasibility of densification without grain growth relies on the suppression of grain-boundary migration while keeping grain-boundary diffusion active.

Chen et al.[169,170] have also suggested that there is a kinetic window for second stage sintering and that it has a characteristic shape spanning a wider temperature range with increasing grain size as in Figure 2-31. At higher temperatures, above the kinetic window, grain growth occurs, for which the driving force diminishes as the grain size increases. At lower temperatures below the kinetic window, diffusion manifests long transients and eventually comes to exhaustion, especially at smaller grain size.

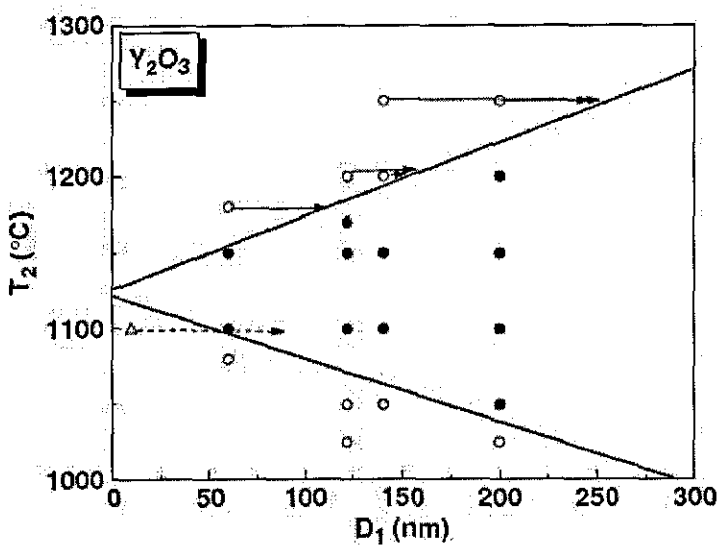

Figure 2-31 Kinetic window for the second stage sintering of Y_2O_3.[169] Solid symbols are reaching full density without grain growth. Data above the upper boundary had grain growth. Data below the lower boundary did not fully densify. Triangle represents a one-step sintering experiment at the temperature shown.

They also observed that fully dense samples did not resist grain growth indefinitely at T_2, the grain size was found to increase after a long incubation time. The effect of magnesium (Mg) and niobium (Nb) doping on the second stage of sintering was also studied and a shift in the kinetic window was observed with doping. Mg shifted the kinetic window towards lower temperature reflecting enhanced kinetics whereas Nb shifted it towards higher values, indicating depressed kinetics.

In the two-step sintering of $BaTiO_3$ reported by Kim et al.,[172] grain growth progressed during the second step whilst density significantly increased. The authors were not able to maintain the nanostructure and the average grain size of the dense ceramics was around 1000 nm. But Wang et al.,[173] were able to retain the nanostructure after the two-step sintering of nanoBaTiO3 with final grain sizes as low as 70 nm and densities >96% of theoretical. Polotai et al.[181] reported a combination of rate controlled sintering and two-step sintering for the preparation of fully dense nanoBaTiO$_3$ ceramics with ~100 nm grain size.

In the case of Ni-Cu-Zn ferrite ceramics,[173] a grain size of 200 nm was reported after two-stage sintering with a starting powder with average particle size of 10 nm. Duran et al.[175] employed a two-step sintering cycle to prepare nano zinc oxide samples with submicrometer grain size starting with ~10 nm nanopowders. They were not able to

retain the nanostructure and the mean grain size reached ~500 nm, but no grain growth was reported during the second stage. Mazaheri et al.,[176] used three different two-step sintering regimes for nano zinc oxide and the sintering time was varied. They observed that if the first and second step temperatures were higher than optimum, sintering and grain growth proceeds as in conventional single step sintering. If the second step temperature was lower, grain growth occurred with minimal or no densification. Hence according to Mazaheri et al. identification of suitable temperature levels for the first and second step are critical in two-step sintering to obtain samples with high density and minimal grain growth; but even with their optimised two-step sintering cycles they have observed a grain growth from 280 nm to 680 nm during the second stage of sintering for nanoZnO.

Lee et al.,[171] reported the two-step sintering of ultrafine β-SiC powders containing 7 wt% Al_2O_3, 2 wt% Y_2O_3 and 1 wt% CaO. The authors observed that the grain size of the conventionally sintered specimens increased continuously with densification whilst zero-time sintered samples showed a slightly finer grain size at a given density. In the case of two-step sintered specimens the rate of grain growth reduced significantly in the second step of sintering and grain growth usually occurring during the final stage of densification was largely absent with this technique.

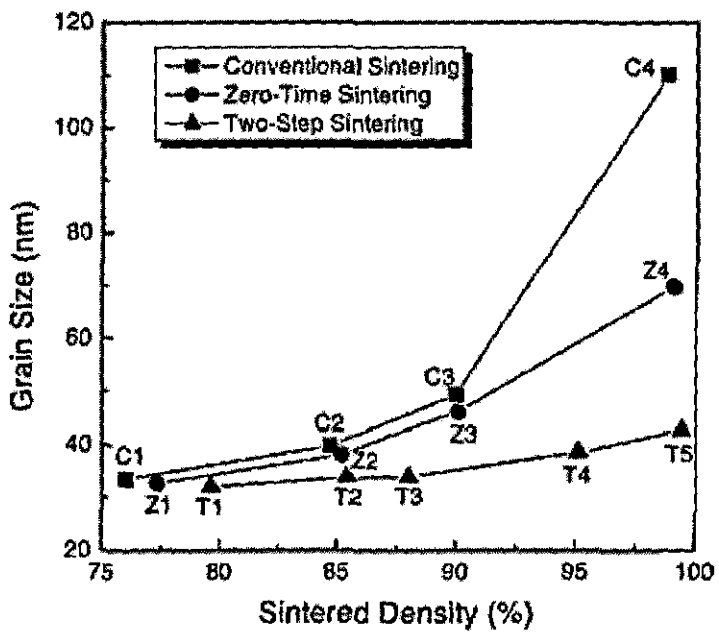

Figure 2-32 Grain size-density trajectories of the SiC specimens sintered by various methods.[171]

Yu et al.[178] employed two-stage sintering for the densification of nanoYSZ processed by powder injection moulding. They used a range of temperature combinations for the sintering and identified 1350°C as the lowest temperature limit for activating the sintering and 900°C as the second stage temperature.

The ability of two-step sintering to prevent grain growth has been investigated for submicrometer alumina[180] and the grain growth was found to be lower for two-step sintering, but even in the second stage, there was some grain growth. The authors observed that more than 92% TD after first step was necessary to achieve higher densification after second stage. The technique has also been used for the sintering of fine grain (1-x)$BiScO_3$-x$PbTiO_3$ ceramics.[177] The authors observed that in addition to minimising the grain growth, two-step sintering required lower sintering temperatures, hence minimising the loss of volatile elements such as lead.

Based on the above discussions on two step sintering, the following advantages can be listed:

- it can be an effective technique to prepare fully dense nanostructured ceramics;
- sophisticated and expensive equipment is not required;
- it can be used for a variety of ceramics;
- better control over densification and grain growth can be achieved as both the first and second step temperature can be varied.

One critical step involved in two-step sintering is the identification of the kinetic window for various materials.

2.12 Microwave Processing of Ceramics

2.12.1 Microwave fundamentals

Microwaves are a form of electromagnetic energy. They cover a broad spectrum of frequencies, usually considered to range from 300 MHz to 300 GHz, Figure 2-33. They, like all other electromagnetic radiation, have an electric component as well as a magnetic component. The microwave portion of the electromagnetic spectrum is

characterised by wavelengths between 1 mm and 1 m, as shown in Figure 2-33. Most of the industrial microwave units use a specific, fixed frequency of 2.45 GHz.

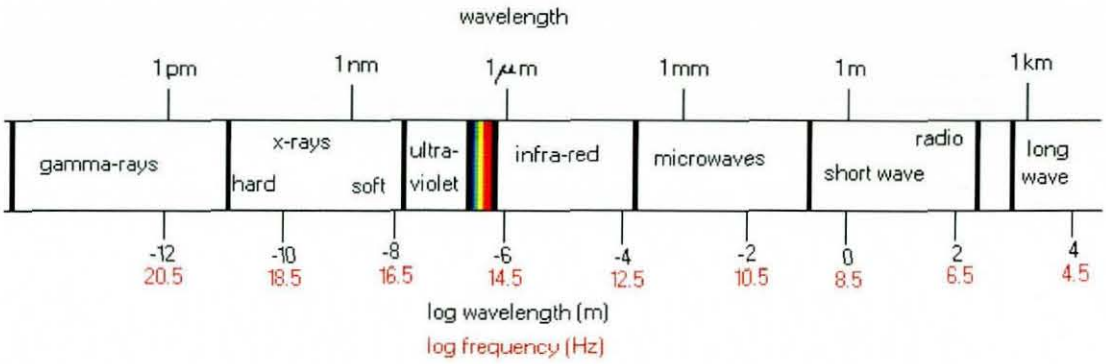

Figure 2-33 The electromagnetic spectrum.

Microwaves travel in the same manner as light waves; they also change direction when travelling from one dielectric material into another; they are reflected by metallic objects, absorbed by some dielectric materials, and transmitted without significant absorption through other dielectric materials. Microwaves travel in free space at the speed of light (Figure 2-34). The free space wavelength λ_0 is related to the frequency by the equation:

$$\lambda_0 = c/f \qquad \text{Eqn. (2.15)}$$

Where λ_0 is the free space wavelength, c is the speed of light and f is frequency.

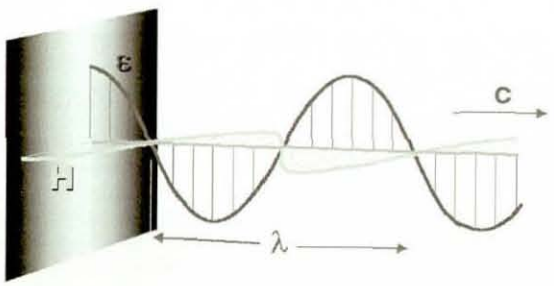

Figure 2-34 The propagation of the plane wave.

There are several reasons for the interest in microwave processing over conventional processing methods including (1) potentially significant reduction in manufacturing costs due to energy savings and shorter processing times, (2) improved product uniformity and yields, (3) improved or unique microstructure and properties, and (4) synthesis of new materials.[182]

2.12.2 Microwave heating

For conventional heating, heat enters the sample through its surface and propagates inside due to heat transfer processes - mainly thermal conduction. The temperature inside the sample is therefore always lower than on the surface, with an exception of the case when a constant temperature is maintained. The heat transfer process takes a certain time (longer for larger samples), which limits the heating rate.

A distinguishing feature of microwave heating is its volumetric nature, where heat is generated internally within the material instead of originating from external heating sources. This results in volumetric heating and the heating rate is limited only by the power of the microwave source for a given material. The thermal gradients and heat flow are from the inside of the material towards its surface. Therefore, the temperature inside the sample is always higher than on the surface. This microwave specific temperature distribution is known as an "inverse temperature profile". Consequently, microwave processing makes it possible to heat samples very rapidly and can be effective in removing volatiles (e.g. binders) from thick sections. It can also reduce the thermal stresses that cause cracking during processing. All these together can lead to significant energy savings and a reduction in process time.[182,183]

The heating effect of microwaves usually arises from the interaction of the electric field component of the wave with charged dipoles in the material. When microwaves penetrate and propagate through a dielectric material, the internal electric fields generated within the affected volume induce translational motions of free or bound charges and rotate charge complexes such as dipoles. The resistance of these induced motions cause losses and attenuates the electric field and volumetric heating results.[182] Two major effects, polarization and conduction, are responsible for the heating. There are several mechanisms which are responsible for polarization, including: electronic, ionic, molecular (dipolar) and interfacial (space-charge) polarization. Therefore, for a dielectric material the net polarization, P, of the dielectric material is determined by the sum of the contributions from each mechanism, given by

$$P = P_e + P_i + P_m + P_s \qquad \text{Eqn. (2.16)}$$

where P_e is electronic polarization, P_i is ionic polarization, P_m is molecular (dipole) polarization and P_s is interfacial (space-charge) polarization.

A measure of polarization of a material to an external electric field is the dielectric permittivity, ε. If the external electric field is alternating (ac), the dielectric response of the material follows it, generally with some lag behind the field changes. To describe this phenomenon quantitatively a complex dielectric permittivity that depends on the field frequency, ω, is formally introduced.[183]

$$\varepsilon(\omega) = \varepsilon'(\omega) + i\varepsilon''(\omega) \qquad \text{Eqn. (2.17)}$$

The lag will be larger if the imaginary part of the permittivity is greater. The change of polarization, i.e. the redistribution of internal charges, is accompanied by the motion of electric charge, i.e. by the electric ac current, which generates heat inside the material. The effective high-frequency conductivity, σ, can be introduced in order to characterize the power of heating, similar to the case of a dc current. The power of heating per unit volume, which equals the absorbed microwave power, is

$$W = \sigma E^2 \qquad \text{Eqn. (2.18)}$$

where E is electric field strength inside the material. The effective high-frequency conductivity is linked to the imaginary part of the dielectric permittivity, $\sigma = \omega\varepsilon_0\varepsilon''$, where ε_0 is a constant called the permittivity of free space. Because of absorption, the electromagnetic fields decrease as the wave passes through the material. The dissipation of electromagnetic energy is commonly characterized by the so-called loss factor, $\tan\delta = \varepsilon''/\varepsilon'$. The attenuation of the electromagnetic wave can also be characterized by a penetration depth (or skin depth),[183] on which the field strength is reduced by a factor of e = 2.71828

$$l = \frac{c}{\omega}\sqrt{\frac{2\left[1+\sqrt{1+(\tan\delta)^2}\right]}{\varepsilon'(\tan\delta)^2}} \qquad \text{Eqn. (2.19)}$$

where c is the velocity of light. When the electromagnetic wave is incident (from air or vacuum) onto a plane surface of material, it is partly reflected from the surface and partly penetrates into the material.

For a normal incidence of the electromagnetic wave on a plane boundary between material and vacuum, the fraction of reflected power (reflection coefficient) is[183]

$$R = \frac{1-\sqrt{2\varepsilon'\left[1+\sqrt{1+(\tan\delta)^2}\right]+\varepsilon'\sqrt{1+(\tan\delta)^2}}}{1+\sqrt{2\varepsilon'\left[1+\sqrt{1+(\tan\delta)^2}\right]+\varepsilon'\sqrt{1+(\tan\delta)^2}}} \qquad \text{Eqn. (2.20)}$$

Many of the heating processes that use electromagnetic energy can be characterized by the two parameters, l and R.

In the microwave frequency range the absorption properties of non-metallic materials vary greatly. In general tan δ initially rises slowly with temperature, until some critical point is reached, beyond which tan δ rises rapidly. The loss factor, tan δ, varies at room temperature from 10^{-4}–10^{-3} (for example in pure alumina and silicon nitride) up to 1 and higher (in carbides, borides, some oxides, and intermetallic compounds). Correspondingly, the penetration depth varies from metres to fractions of a millimetre. Thus knowledge of the dielectric properties of materials, as well as their dependence on frequency, temperature, chemical composition, and microstructure is of paramount importance for the intelligent/efficient use of microwave energy for high-temperature processing.[182,183]

At elevated temperatures, microwave absorption in most materials grows sharply, primarily due to the onset of another absorption mechanism. This is characteristic for both solids with ionic (Al_2O_3, ZrO_2) and covalent (Si_3N_4, AlN) bonding. A sharp increase in the microwave loss starts at temperatures of about 0.4–0.5 Tm (where Tm is the absolute melting temperature of the material). In this temperature range the bonds between ions in ionic crystals start to break and the electrons in covalent materials begin to populate the conduction bands. As tan δ increases with temperature, the material begins to absorb microwave energy more efficiently, which further increases the temperature. This causes tan δ to rise even faster, resulting in an exponential increase in temperature. This sharp increase in microwave absorption with temperature can cause a thermal instability, commonly known as a 'thermal runaway',[182] which can cause undesirable hot spots within a material. It can also be used to heat small samples at rapid rates however. Thermal runaway can be prevented or controlled by regulating or pulsing the microwave power level or by designing the microwave system and applicator to deposit the microwave energy within the material or product in a prescribed manner.[182]

2.12.3 Applicators

Microwave processing of samples enclosed in a thermal insulation arrangement is usually performed in a closed chamber with metal walls, called an applicator. The

metal walls of the applicator return the radiation reflected from the sample or transmitted through it back to the sample, Figure 2-35. The resonator increases the microwave field strength in its volume due to multiple passes of the electromagnetic waves through each point.

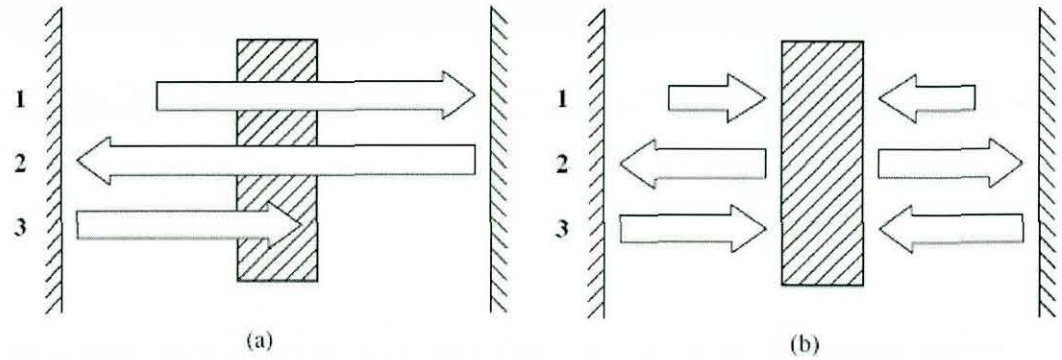

Figure 2-35 Illustration of resonant cavity operation. (a) Case of a low-loss sample: 1, incident radiation; 2 and 3 radiation returned to the sample after reflection from resonator walls. (b) Case of a high loss sample: 1, incident radiation; 2, radiation reflected from the sample; 3, radiation returned to the sample after reflection from resonator walls.[183]

2.12.3.1 Single-mode cavities

The essential characteristic of single-mode cavities is the deliberate creation of a standing wave pattern inside the cavity. The dimensions of the cavity must be carefully controlled such that it is related to the characteristic wavelength of the microwave in a systematic way. For 2.45 GHz microwaves, the length of a single full wave is 12.2 cm in air. A single mode cavity for 2.45 GHz microwaves must be dimensioned such that a whole number multiple of the full or half wavelength fits inside the confines of the cavity. Figure 2-36 shows a schematic of the wave pattern in a single-mode applicator.

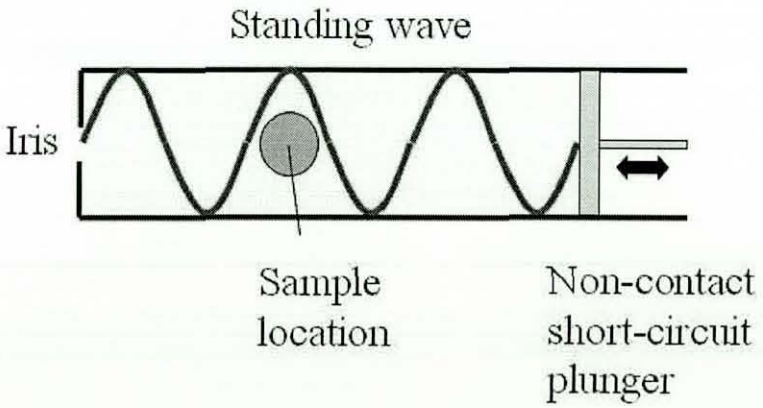

Figure 2-36 Schematic showing the wave pattern in a single mode applicator.

There are specific positions inside the single-mode cavity where items to be heated must be placed. The intensity of the electric field is greatest at the peaks of the standing wave, and goes to zero at the nodes of the standing wave. There will be no heating at the nodes unless the material undergoes magnetic heating. This limits the physical dimensions of an object that can be placed in a single-mode cavity and be heated effectively.

2.12.3.2 Multimode cavities

In multimode cavities, there is the deliberate avoidance and/or disruption of any standing wave pattern inside the cavity. This can be achieved in number of ways. First, the dimensions of the cavity must be carefully controlled to avoid whole-number multiples of the microwave full or half wavelength. Second, some means must be employed to physically disrupt any standing waves that may form as a consequence of items placed in the cavity. This can be done with a mechanical mode stirrer, typically a periodically moving metal vane that continuously changes the instantaneous field pattern inside the cavity. The shape and movement of the mode stirrer should be such that the microwave field is continuously stirred, and therefore the field intensity is homogeneous in all directions and all locations throughout the entire cavity. A third option is to use a turn table or a similar device to move the work piece through the fields. The ratio of the work piece volume to that of the cavity (filling factor) also affects the heating efficiency of the cavity. Very small work pieces tend to be heated less effectively than larger ones.[182,183] A uniform electric field distribution can be created inside a cavity by keeping at least one of its dimensions 100 times greater than the wavelength of the incident microwave radiation.

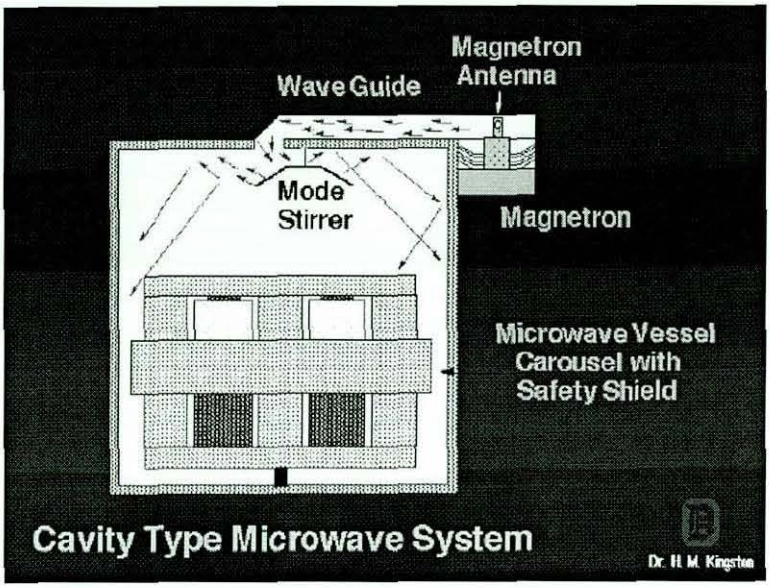

Figure 2-37 Typical multimode cavity.

Advantages include: any microwave absorbing material placed anywhere in the cavity can be heated; there is no specific position inside the cavity where items to be heated must be placed. As the field in the multimode cavity is continuously re-homogenised, nothing placed in the cavity will permanently affect the distribution of the field intensity, so there are no limitations on the size and shape of the objects placed inside the cavity. Multiple objects can be processed simultaneously and scale-up is also possible.

2.12.4 Advantages of microwave high temperature processing

Bykov et al.[183] in their classic review 'High temperature microwave processing of materials' summarised the advantages and disadvantages of microwave processing.

2.12.4.1 Reduced energy consumption and process time

The main advantage of microwave heating is its volumetric nature due to the direct deposition of energy on the work piece. This eliminates the need for spending energy on heating the walls of the furnace or reactor and its components. As a result, the use of microwave methods can significantly reduce energy consumption, especially in high-temperature processes, since heat losses grow dramatically with an increase in the process temperature. The volumetric nature of energy deposition also accelerates heating, which reduces the time needed to complete a process.

2.12.4.2 Rapid and controllable heating

Microwaves can be used to heat materials rapidly. This can also be utilised in the sintering of nanostructured ceramics and composite materials. At different stages of sintering, different diffusion processes, viz. surface, grain boundary, and bulk diffusion, determine the mass transport. Inhibition of surface diffusion at the initial stage of densification is favourable for sintering. An increase in the rate of heating at the onset of densification can reduce the formation of a rigid neck structure between the grains. At the intermediate and final stages of sintering high rates of microwave heating help overcome grain growth, resulting in ceramic materials with a fine microstructure, which in turn enhances their mechanical properties.[183]

2.12.4.3 Inverse temperature profile

Microwave heating results in an inverse temperature distribution within the body. This helps to keep the initial porous structure open to a higher average value of density.[184] It helps to remove binders and other organics relatively easily compared to conventional heating. Also this effect contributes both to the acceleration of densification under microwave heating and achieving a higher final density. This inverse temperature profile is also useful in processes like reaction bonding of silicon nitride (RBSN) ceramics[185] and the fabrication of SiC based composites by vapour phase infiltration with methyltrichlorosilane.[186]

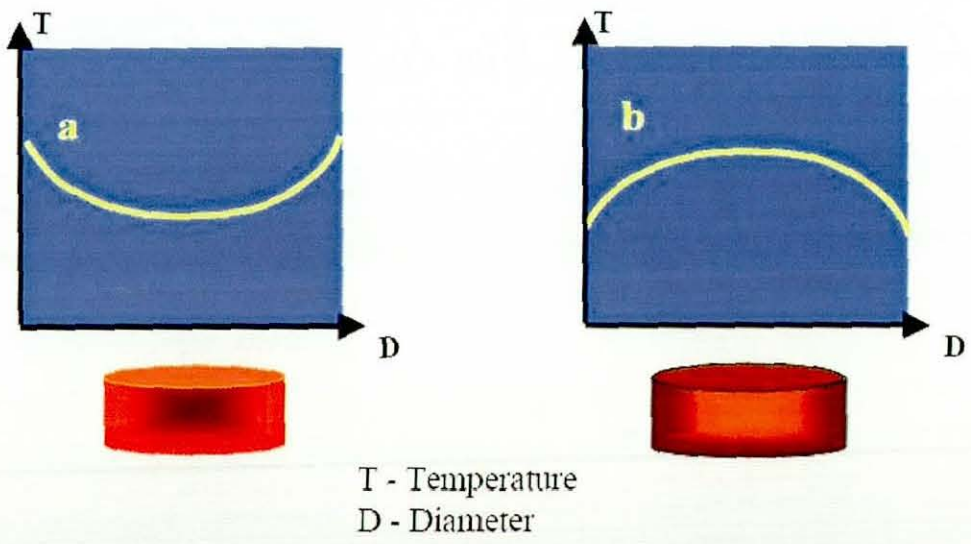

Figure 2-38 Schematic diagram of temperature profiles during (a) conventional and (b) microwave heating.[187]

2.12.4.4 Selectivity

The dependence of the deposited microwave power upon the absorption properties of materials opens the way to the implementation of selective heating of materials. Sometimes this is a disadvantage as it leads to non-uniform heating or thermal gradients, but it can be used with advantage in the processing of composite materials, e.g. a ceramic matrix impregnated with a metal-organic precursor.

2.12.5 Limitations of microwave processing

There are a number of limitations associated with the microwave processing of materials. One of them is inaccurate or incomplete temperature measurements.[188] Thermocouple sensors generally measure the temperature of the thermocouple head, which may be close to the temperature of the material at the point which the head touches, but it can still differ substantially from the temperature in most other points of the material. The reasons are heat losses via the thermocouple, microwave absorption in the thermocouple, etc. Thermocouples can also lead to local field distortion and/or enhancement and in some cases to the ability to heat otherwise microwave transparent materials.[189] Pyrometers measure temperatures on the surface of the material but these are different from those in the bulk. Hence one of the best techniques in terms of accuracy, if not practicality in commercial environments, is the use of optical fibre thermocouples.[187,190]

Another problem experienced is the difficulty to implement a microwave heating process with a uniform temperature distribution in the material undergoing processing. Temperature gradients are a fundamental attribute of microwave volumetric heating and the effects caused by them contribute to differences in the process flow. Possible mechanisms of temperature gradients are, for example, thermo-elastic stresses[191] and thermal diffusion.[192]

2.12.6 Microwave sintering of ceramics

During the last couple of decades, various structural ceramics and composites have been sintered successfully by microwave heating (MW heating). These include alumina[193,194] and alumina based composites,[195,196] aluminium nitride,[197] zirconia,[198,199,200,201,202,203,204] zinc oxide, barium titanate[205], silicon nitride,[206,207,208,209,210] silicon carbide-based ceramics,[211] ytrria[198] and sialon.[212]

Microwave sintering of partially stabilised and fully stabilised ZrO_2 using microwaves with a SiC susceptor have been reported by a number of authors.[213,214,215,216] Wilson et al.[213] sintered partially stabilised zirconia to fairly low final densities (95-98% of TD) using microwaves with SiC susceptors. A susceptor is a material used for its ability to absorb electromagnetic energy. Microwave sintering of yttria stabilised zirconia without susceptor has also been reported in literature.[198] From a comparison of the mechanical properties the authors reported slightly better bending strength, flexural strength and hardness with the microwave sintered samples. Microwave heating behaviour of zirconia doped with 3, 5, and 8 mol% yttria and 10 mol% ceria were compared by Moeller et al.[217] and they reported similar time-temperature profiles for all these compositions. Sharma et al.[218] sintered lead-zirconate-titanate (PZT) using microwaves and studied the dielectric properties and hardness. Microwave sintering studies on barium strontium titanate[219] indicated that high density, and improved microstructure and dielectric properties can be achieved with microwaves. The Curie temperature was also higher for microwave sintered material. Wang et. al.[190] compared the microwave sintering of Al_2O_3 – a low microwave absorbing material, partially stabilised ZrO_2 – a moderate microwave absorber, and ZnO – a very good microwave absorber, and found that the degree of enhancement caused by microwaves increases according to their ability to absorb microwaves in a microwave field. Experiments were also done using nanozirconia and nanoalumina. Xie et al.[220] reported much finer grain size and improved flexural strength and breakdown strength after the microwave processing Al_2O_3, Ce-Y-ZrO_2 and lead based ferroelectrics in 2.45 GHz microwave furnace.

Although these experiments show a potentially bright future for microwave sintering, this technique is still in its initial stages. One of the problems that is often encountered in microwave sintering is the lack of "room-temperature coupling".[221] Microwave heating is a process in which the materials couple with microwaves, absorb the electromagnetic energy volumetrically, and transform it into heat. The parameter determining the coupling property is the dielectric loss factor, according to which materials can be classified as transparent (low loss insulator), opaque (conductor) or absorbing (high loss insulator). At room temperature, SiC shows a high loss factor and therefore couples well with the microwaves, whereas most ceramics such as

Al_2O_3, ZrO_2 and Si_3N_4 have a low loss factor or are transparent. One solution for the heating of low loss materials is the use of hybrid heating.

2.13 Hybrid sintering

Hybrid sintering is a relatively new sintering technique in which the thermal energy necessary for sintering is supplied from two or more different sources or two or more types of energy. For example, a combination of radiant energy and microwave power or a combination of laser and microwaves.[222] Radiant-microwave hybrid heating can be used successfully for the sintering of low loss materials where the application of pure microwave heating is difficult. A better control over the heating rate and a more uniform temperature distribution can also be achieved with hybrid heating.

Wroe and Rowley[223] investigated the advantages of hybrid heating for the sintering of partially stabilised zirconia in a hybrid furnace, which allowed the simultaneous application of microwave and radiant energy. They reported enhanced sintering and lower sintering temperatures for the hybrid heating. The total shrinkage was also higher in hybrid sintering, leading to an increased final density. They also found that the densification was enhanced as the proportion of microwave power was increased.

Wang et al.,[187,190] conducted extensive hybrid sintering studies using submicron and micron ZnO, nano and submicron 3YSZ, submicron 10YSZ and nano Al_2O_3. These materials were selected because of their difference in dielectric properties, and hence their ability to absorb microwaves. The samples were sintered using radiant/microwave hybrid heating and different microwave power levels - 200, 400, 600, 800 and 1000 W – but identical time-temperature profiles. They found that the use of microwaves resulted in enhanced densification. Higher microwave power levels and finer particle sizes resulted in greater enhancement; which indicated the advantages with hybrid heating. Lorenz[224] also observed similar results in the hybrid sintering of submicron ZnO. The effects of microwaves were very evident from the microstructures; Figure 2-39.

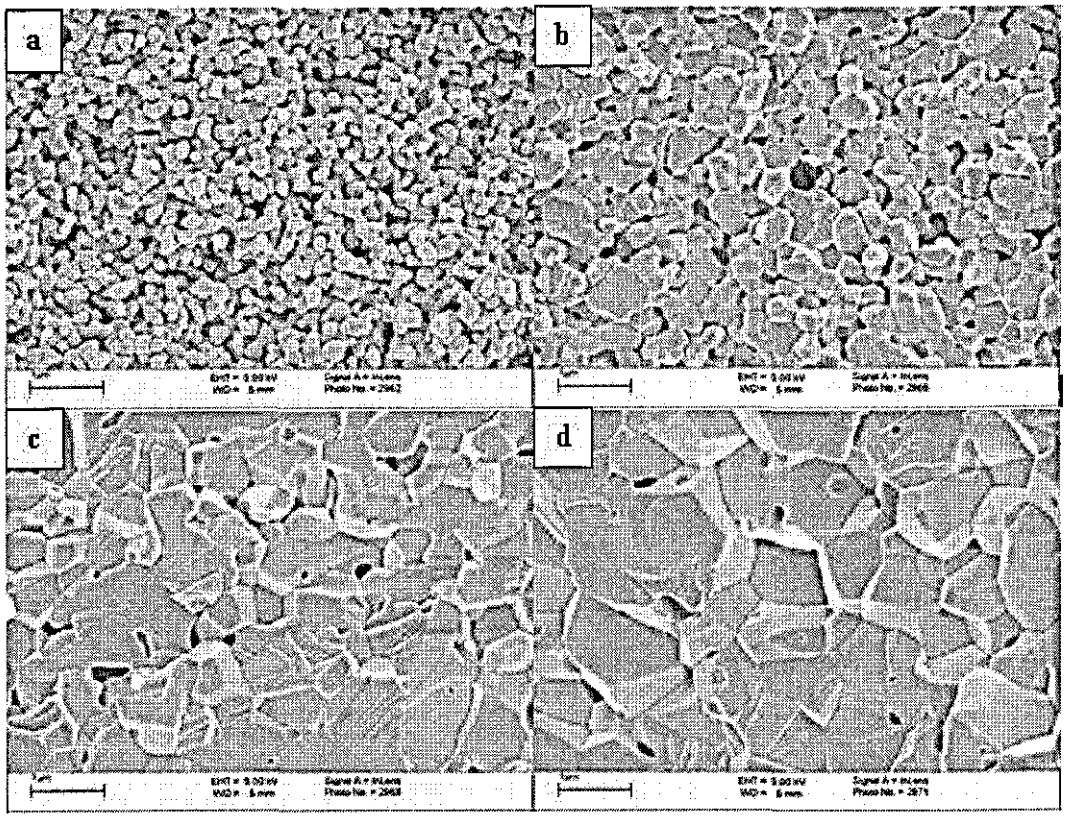

Figure 2-39 Submicron ZnO sintered at 700°C[224] (a) pure conventional, (b) Hybrid with 600 W, (c) Hybrid with 800 W, (d) Hybrid with 1000 W. Note: All samples sintered using the same time-temperature profile.

Danko et al.[225] reported that microwave hybrid heating produces β-SiC more effectively than conventional oven heating starting with preceramic polymers. Thus there are a large number of reports indicating the benefits of hybrid heating for the sintering of advanced ceramics.

2.14 Objectives of the present work

Even though there are many reports on the preparation of nanozirconia ceramics, a well organised study to find the properties of the material as a function of grain size and yttria content is missing in the literature. As described in Section 2.4, there are only a few published papers which described some of the properties of nanoceramics, such as superplasticity and transparency. No one has reported a thorough study on the mechanical and hydrothermal ageing properties of genuine nanostructured zirconia ceramics.

The mechanical properties are very important from the design and product manufacturing point of view. It is evident that lower sintering temperatures are

sufficient for the sintering of nanomaterials, which can result in considerable energy savings in large scale manufacturing. Also a lower amount of stabilisers are expected to be sufficient in the case of nanozirconia ceramics, to achieve similar stabilization when compared with the submicron grained zirconia ceramics. This should result in cost reduction when considering the cost of stabilisers, such as yttria; although, this needs to be balanced with the increased production cost of the nanopowders.

The main objectives of the present work can be listed as below:

1. Sintering of nanozirconia using a novel microwave assisted, hybrid, two-step sintering cycle to full density (> 99%TD) with minimal grain growth;
2. Determination of hardness, fracture toughness and flexural strength of the sintered nanoceramics as a function of average grain size and the amount of stabiliser (yttria);
3. Comparison of the wear properties of nanozirconia ceramics with submicron zirconia;
4. Analysis of the hydrothermal ageing resistance of nanozirconia and comparison with submicron zirconia to study the overstabilisation of nanozirconia due to the reduced grain size effect;
5. Optimisation of grain size, density and yttria content to improve performance for specific applications based on the requirements.

Chapter 3

3 Experimental

3.1 Materials used

Zirconia nanosuspensions containing different amounts of yttria, viz. 0, 1.5, 2, and 3 mol% were provided by MEL Chemicals, UK. A benchmark, submicron 3YSZ zirconia powder (Grade Tosoh 3YSB-C) was obtained from Tosoh Corporation (Tosoh Europe, Amsterdam, Netherlands). According to the manufacturer, the crystallite size of the Tosoh powder is 37 nm, loss of ignition is 5.4 wt% and Y_2O_3 content is 5.2 wt%. The following naming convention, Table 3-1, has been used to label these samples throughout the thesis.

Table 3-1 Sample codes used for different yttria-zirconia compositions

Code	Sample
Nano0YSZ	Nanozirconia with 0 mol% yttria
Nano1.5YSZ	Nanozirconia with 1.5 mol% yttria
Nano2YSZ	Nanozirconia with 2 mol% yttria
Nano3YSZ	Nanozirconia with 3 mol% yttria
Benchmark Tosoh or (submicron 3YSZ)	Submicron zirconia with 3 mol% yttria

With respect to the other chemicals used, tetramethyl ammonium hydroxide (TMAH) was procured from Aldrich Chemicals Ltd., Dorset, UK. Tri-ammonium citrate (TAC) from Fisher Scientific UK Ltd., Loughborough, UK, was used as a dispersant. Other chemicals such as HCl, NaOH, acetone and ethyl alcohol were also obtained from Fisher Scientific. Plaster of Paris was obtained from Lafarge Prestia (Millecast, Lafarge Prestia, Mériel, France).

3.2 Characterisation of suspensions/powders and their processing

The as received materials were characterised using a variety of techniques, each of which is discussed below.

3.2.1 Determination of solid content of the suspension

About 25 g of suspension was weighed accurately into a petridish, which had been previously heated to remove any moisture. The suspension was then heated at 60°C for 24 hr to remove the volatiles and the weight obtained after complete drying was noted. The dried zirconia sample was placed in a silica crucible and was further heated in a conventional furnace at a rate of 5°C per minute up to 700°C and held at that temperature for 2 h to burn off all the organics. It was then cooled to room temperature and the percentage solid content was calculated based on the initial weight of suspension taken for drying.

3.2.2 Zeta potential measurements

The electrokinetic behaviour of the various yttria containing suspensions were characterised using an AcoustoSizer II (Colloidal Dynamics, Sydney, Australia). This equipment facilitates automatic measurement of zeta potential over a wide range of pH from 2 to 13. Dilute suspensions with 5 wt% zirconia were used; pH modifying agents were dosed in small quantities to achieve any desired value. 0.1 M HCl/NaOH solutions were used for decreasing/increasing the pH respectively. An equilibration time of 180 seconds was used to ensure that the pH modifier was mixed homogeneously within the system before every zeta potential measurement at the different pH values.

As a general practice, the pH was initially taken in increments of 1 pH point to the nearest extreme and then traced back to the other extreme pH again in steps of 1 pH point, with the zeta potential measurements being made at each step.

3.2.3 Preparation of powder from nanozirconia suspensions

The nanozirconia suspensions were taken in a glass tray and dried at 60°C for 24 h in an air oven to yield the solids. The solid mass obtained after drying was micronized in a McCrone micronising mill (McCrone Scientific, London, UK) using zirconia as the grinding media for 4 min.

3.2.4 Concentration of the as received suspension

The as received suspensions were concentrated to up to 70 wt % solid content using a patented technique developed at Loughborough University.[149] This was achieved by

modifying the pH of the as received suspensions from the initial value of 2-3 to 11.5 via the addition of sufficient quantities of TMAH, followed by the addition of TAC as the dispersant. Typically 3 wt% of TAC based on the solids content of the suspension was used. The suspension with these additives was then heated to 65°C in a water bath under continuous stirring. During the concentration process, the suspension was subjected to ultrasound treatment at regular intervals using a Soniprep 150 ultrasonicator (MSE scientific instruments, Manchester, UK) to break the agglomerates. During the initial stages of concentration ultrasonic treatment was done every 2h and once the solid content was above 40wt% it was applied every hour. During ultrasound treatment, the amplitude was set at 14 μm and the power was 75 W.

The Soniprep 150 transmitted sound energy to the medium through high frequency vibration at the tip of an interchangeable probe. The effect of this was to create many micro-cavities in the dispersion medium. The rapid alternation of positive and negative pressure produced by the sound waves travelling through the liquid caused these minute gas filled bubbles to disintegrate implosively during the rarefaction phase of the sound pressure wave. This produced intense local shock waves in which the pressure may have reached several thousand atmospheres and rapid microstreaming of the liquid will have occurred around the point of collapse. The intense localised shear gradients so generated combined, in part, with the transient regions of high pressure, resulted in the agglomerate-disruptive capabilities of this instrument.

The solid content of the suspension after concentration was determined as described in Section 3.2.1

3.2.5 Viscosity measurements

The viscosity of the as received suspensions and the concentrated suspensions were measured using an Anton Paar RheolabQC viscometer (Anton Paar GmbH, Österreich, Austria) from 10 s^{-1} to 1000 s^{-1} shear rate. All the measurements were done at room temperature.

3.3 Preparation of green bodies

Green bodies were prepared by both dry and wet routes. At the start of the project the samples were mainly prepared using a dry pressing route and based on the initial results the focus was later shifted to slip casting.

3.3.1 Dry pressing

Green compacts were dry pressed using a Lloyds mechanical testing machine (L10000 Tensometer, Lloyds Instruments, Fareham, UK) in a single-action, hardened steel die with a diameter of 10 mm. Before every pressing, the die and the punch wall were thoroughly cleaned, polished and washed with acetone. About 1 g of powder was used for every pellet. The ram speed was 1 mm min^{-1} and was held at the consolidation pressure of 480 MPa for 1 min. The pellets were slowly ejected from the die and used for further processing.

Pellets were also pressed using the benchmark Tosoh 3YSZ powder by applying a much reduced pressure of 160 MPa. This pressure was sufficient for the submicron powder as it contained 5 wt% organic binders. Benchmark samples were also pressed in disc form and as rectangular blocks for machining test specimens.

After the initial sintering studies and optical microscopy analysis it was found that the dry pressed nanosamples contained hard agglomerates that were difficult to break even at 480 MPa pressure. Hence the focus was shifted to the preparation of green bodies using wet routes such as slip casting.

3.3.2 Slip casting

The preparation of the slip casting mould was found to be critical after the initial experiments. Initially, circular or rectangular cavities were machined into cast plaster of Paris (PoP) moulds. The surface finish obtained from machining was not good enough and hence lead to cracking of the cast samples. In order to prepare moulds with better surface finish, inserts were prepared using polyvinyl chloride (PVC) blocks around which the PoP/water slurry was poured. The slurry was allowed to harden for 1 h after which the PVC block was removed from the mould and the latter was allowed to dry in an air oven at 60°C for 24 h. After drying, the mould was cleaned using an air jet and visually inspected for any defects; if any were present the

mould was rejected. Initially the cavity size was 15 mm dia. x 20 mm depth, subsequently the cavity size was increased to 60 mm dia. x 25 mm depth.

The suspension to be slip cast was exposed to ultrasound for 3 min prior to casting, keeping it in a water bath to prevent undesirable heating during the process. The required amount of suspension was weighed into a plastic weigh boat and transferred slowly into the cavity without creating any air bubbles in the suspension during transfer. The PoP mould with the cast sample was left under atmospheric conditions for up to 72 h to remove water from the suspension. After the initial drying the samples were removed from the cavity and placed on a Teflon sheet for further drying, the latter being used to facilitate easy shrinkage of the samples with minimal resistance. The solid content of the suspension, its viscosity and the amount of organics used were all found to affect the quality of the slip cast bodies.

3.3.3 Binder removal

Even though no binders were added externally during the preparation of pellets and slip cast bodies, there were organics present in all the samples coming from the TMAH and TAC used during the concentration of the suspensions. So it was essential to remove these organics using a slow heating cycle. The binder removal cycle was designed based on the TGA of the additives used during the sample preparation. The samples were heated at a heating rate of 0.5°C per minute keeping them at 100°C, 200°C, 300°C and 400°C for 30 min each and finally at 700°C for 2 h. The samples were then cooled down to room temperature using the cooling rate of 0.5°C per minute. After binder removal the samples were visually inspected for any defects/cracks.

3.3.4 Measurement of green density

The green density of the dry pressed compacts was calculated from the weight of the sample (measured to ±0.001 g) and the dimensions of the compact (measured to ±0.01 mm). The dimensions were measured at at least three locations across the sample and averaged out for calculations.

The green density of the slip cast bodies was measured after binder removal using the Archimedes principle in mercury. The green density was calculated from:

$$\text{Green density, } \rho = \frac{M_s \cdot \rho_l}{M_s + M_l} \qquad \text{Eqn. (3.1)}$$

Where M_s is the weight of the sample in air, M_l weight of sample in mercury and ρ_l is the specific gravity of mercury at the measurement temperature.

3.4 Sintering of green bodies

Sintering experiments were carried out using both a conventional box furnace and a hybrid microwave furnace. The conventional box furnace was manufactured by Carbolite UK Ltd. and consisted of SiC heating and the temperature was controlled using a Eurotherm 902 controller (Eurotherm UK Ltd., West Sussex, UK) connected to a thermocouple inside the furnace chamber.

The hybrid furnace was more sophisticated, consisting of a magnetron, waveguide, cooling system, circulator, microwave tuner, reflective power monitor and hybrid microwave cavity (applicator) as shown in Figure 3-1.

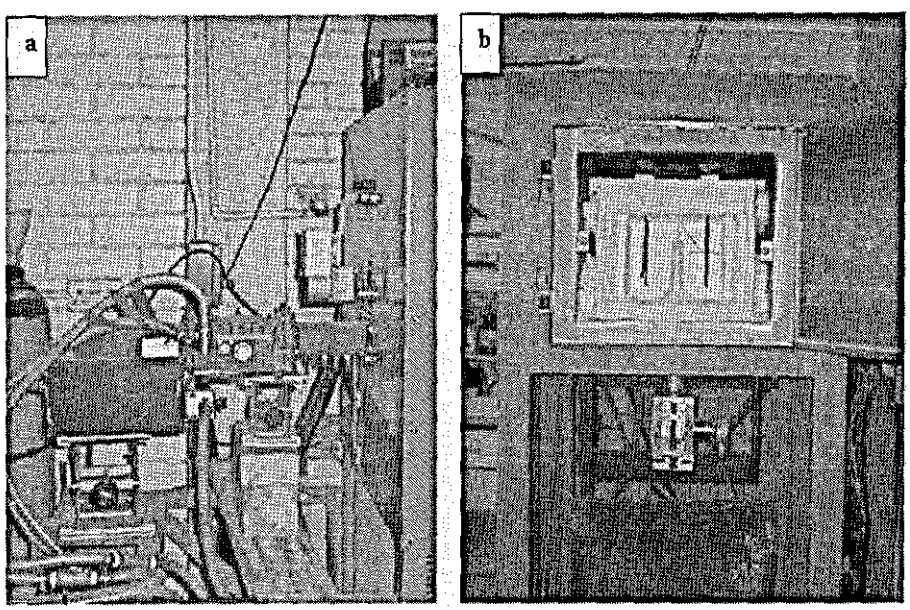

Figure 3-1 (a) The microwave unit, wave guide and mode stirrer of the hybrid furnace. (b) Applicator of the hybrid furnace showing the dilatometer, heating elements and optical fibre thermometer.

The applicator consisted of a rectangular metallic box, a mode stirrer and alumina fibre insulation materials. Six molybdenum disilicide ($MoSi_2$) heating elements were used to provide the radiant heating. The magnetron could supply up to 2 kW microwave power at a frequency of 2.45 GHz. The conventional heating was

controlled by a Eurotherm 902 controller whereas the microwave power was adjusted manually. The furnace was specially designed to allow both microwave and conventional heating sources to operate simultaneously.

Two optical fibre thermometers (OFTs), (Accufiber Model M10 and M100, Luxtron Corp, Santa Clara, California, USA) were used to record the temperature of the sample, one from the top and one from the side, of the applicator.

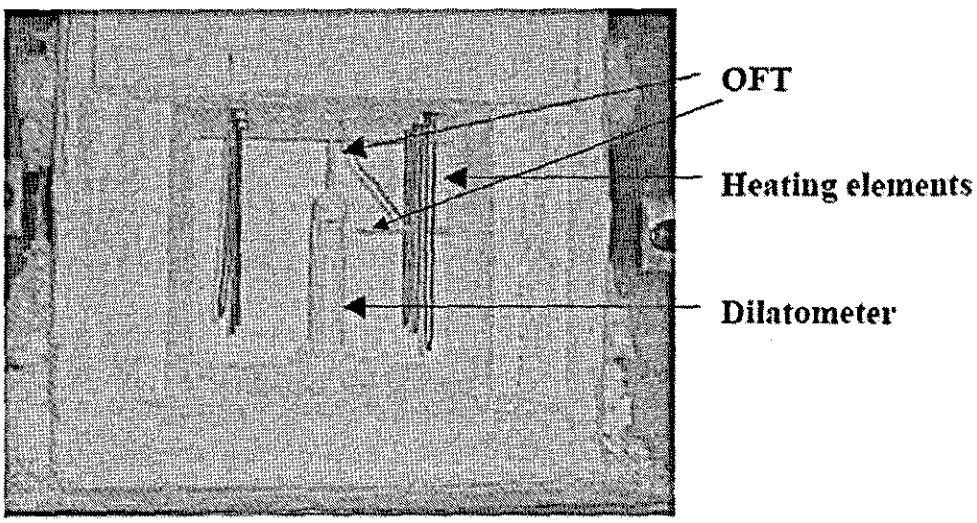

Figure 3-2 Heating chamber of the hybrid furnace showing OFTs and heating elements.

OFTs can be used in a non-contact or contact mode. In the former, the system consists of a narrow diameter sapphire rod that acts as a light pipe to gather the radiation from the target and transmit it to a photo detector in the electronics unit. The photo detector converts the light energy into an electrical signal which is digitised and converted into a temperature value using Planck's radiation equation. It requires knowledge of the emissivity of the material. In the contact mode, the same sapphire light pipe has a very thin (less than 10 μm) coating of a refractory precious metal at the end that turns it into a black body. The temperature of the latter is then sensed by the instrument, removing the need to know the target's emissivity. The black body tip can interact with the microwave field if the latter is too intense, however for multimode applicators, such as used in the current work, this is not a problem. In the present work the temperature from the top OFT (M100) was used to control the heating or cooling. In addition to these two OFTs, there was a chromal-constantan thermocouple inside the applicator. This was used as a safety thermocouple to protect the equipment

if the OFTs fail and was located well away from the sample to avoid local perturbation of the microwave field.

In order to optimise the sintering conditions the initial sintering experiments were carried out using the nano3YSZ samples prepared by dry pressing. Dry pressed samples were chosen because of their higher green density, which is an essential requirement for two-step sintering. The initial trials were carried out using the hybrid furnace. The green bodies were sintered using single step and two-step cycles in conventional and hybrid heating modes at a heating rate of 20°C per minute. For single step sintering the temperature was varied from 1000°C to 1150°C and sintering time from 0.1 min to 180 min. When two-step sintering was used, the first step temperature, T_1, was kept constant at 1150°C based on the single step heating trials and T_2 was varied from 1000°C to 1050°C to achieve optimal densification. The time at the second stage was also varied from 180 min to 300 min. Initial hybrid sintering trials were conducted at 600 W microwave power level.

In order to determine the effect of microwaves on the densification and grain growth, samples were sintered using the same time-temperature profile but with different microwave power levels from 0 W to 1000 W. As it was not possible to measure the amount of microwave power absorbed by the sample, the amount of radiant power input was recorded in order to find whether the contribution of microwaves was greater at higher power levels. The idea behind this was that if the sample absorbed more microwaves for heating itself, then the furnace would use less conventional power, which would be reflected in the conventional power requirements.

With the hybrid sintering experiments of the dry pressed nano3YSZ it was found that the maximum density was limited by the presence of hard agglomerates in the green body, which were detrimental to densification and the properties of the body after sintering. Hence the focus was shifted to the sintering of slip cast bodies. There were a few difficulties in directly transferring the sintering conditions of the dry pressed samples to slip cast samples. The major differences arose from the differences in sample mass and green density. The sample size of the slip cast samples was much larger and hence the microwave absorption, which is dependent of the sample mass, was different from that of dry pressed samples. The lower green density of the slip

cast samples also meant that they needed higher temperatures/longer times to reach the same density as that of the dry pressed samples. Initially hybrid sintering experiments of the slip cast samples were performed using heating cycles similar to that employed for the dry pressed samples at different power levels. The heating rate was also lowered from 20°C to 15°C and then to 10°C per minute.

As the density obtained after hybrid two-step sintering was unsatisfactory it was decided to use conventional two-step sintering at a reduced heating rate. The slip cast samples were sintered at 1000°C, 1050°C, 1100°C, 1150°C, 1200°C, 1250°C, 1300°C, 1400°C and 1500°C for 10 h. The samples were also sintered at 1050°C, 1075°C, 1100°C, 1125°C and 1150°C for 0.1 min. in order to mimic the first stage heating. This was necessary to design an optimal two-step sintering schedule. The heating rate was kept constant at 10°C per minute compared to 20°C min^{-1} in hybrid heating for all the conventional sintering experiments to minimise any possible thermal gradients within the large sample. The density and grain size were determined after sintering. At higher temperatures desintering or bloating was observed, which resulted in lower final densities. Based on the results of these single step sintering experiments, it was decided to use two different levels of temperature as the first step temperature, 1100°C and 1150°C for the two-step sintering of nano3YSZ. The second step temperature was varied from 900°C to 1050°C and the time at these temperatures from 180 min. to 1800 min. to obtain samples with full density.

Based on the sintering experiments on nano3YSZ, the same optimised sintering cycle was initially used for the sintering of nano2YSZ and nano1.5YSZ bodies prepared by slip casting. Since it was observed that the sinterability of the nano2YSZ and nano1.5YSZ were different from that of the nano3YSZ, necessary modifications were performed to achieve maximum density with minimum grain growth.

Undoped 0YSZ samples were also sintered using both single step and two-step sintering cycles in an attempt to prepare fully dense monoclinic zirconia ceramics. A range of sintering temperatures and sintering times were examined. Also the samples were sintered both above and below the monoclinic to tetragonal transformation temperature. When the temperature was close to the phase transformation temperature (>1135°C) the samples were found to be shattered due to the slow reverse phase

transformation. When the sintering temperature was below 1135°C, the sample was found to retain its integrity.

Tosoh samples were sintered for comparison at 1500°C, at a heating/cooling rate of 2°C min^{-1} holding at the maximum temperature for 2 h.

3.4.1 Sintered Density Measurements

The density of the sintered samples was measured using the Archimedes principle with distilled water as the displacing medium utilizing the proper density correction for the temperature of the medium.

$$\text{Density of sample,} \quad \rho = \frac{M_s . \rho_l}{M_s - M_l} \qquad \text{Eqn. (3.2)}$$

Where, *Ms,* mass of sample in air, M_l, mass of sample in water, and ρ_l is the density of the liquid at measuring temperature.

3.5 Property Measurements

The samples after sintering were subjected to a number of tests to determine the properties. The sample preparation and testing procedures used are described below

3.5.1 Mounting and polishing of sintered pellets

For polishing, the sintered samples were mounted in epoxy resin (Epofix, Struers Ltd., Solihull, UK) and polished using a semi-automatic polishing machine (TegraPol-25, Struers Ltd. UK) with a rotating sample holder (TegraForce-5, Struers Ltd., Solihull, UK) and an automatic feeding system for the polishing media (TegraDoser-5, Struers Ltd., Solihull, UK). In a typical polishing cycle, the properly mounted samples were initially plane ground using an MD-Piano220 polishing disc (grit size 220), followed by fine grinding using MD-Piano600 (grit size 600) and MD-Piano1200 (grit size 1200), followed by polishing using a diamond paste containing 3 μm size particles. The final polishing was done using 0.04 μm colloidal silica suspension (OP-S, Struers Ltd., Solihull, UK). Between each polishing step the samples were removed from the specimen holder and cleaned with deionised water and dried with a heat gun. After the final polishing the sample was subjected to ultrasound for 2 min. in a beaker containing deionised water, sprayed with ethanol and dried using a heat gun to get a surface free from contamination and remains of the polishing media. The samples

were then removed from epoxy resin by heating them in an air oven at 150°C for 10 min.

3.5.2 Etching of the ceramics

The polished samples were etched to reveal the microstructure. Initially chemical etching was used to expose the grains using a mixture of hydrofluoric acid (18 ml), concentrated nitric acid (90 ml) and water (90 ml). Based on the preliminary work, the optimum etching time was found to be 5 min. Necessary care was taken while using the hydrofluoric acid. The etching was carried out in a fume cupboard.

After analysing the chemically etched samples using FEGSEM, it was found that though it is possible to observe the grains, it was very difficult to perform accurate grain size measurements using a linear intercept method. Hence thermal etching was investigated; the temperature was selected such that it was 100°C lower than that of the sintering temperature in the case of single stage sintered samples and for two-step sintered samples the thermal etching was performed at the second step temperature. The etching time was kept short, 6 min., to prevent any possible grain growth during thermal etching in both cases. The grain size of the samples were compared after chemical etching and thermal etching to make sure that there was no grain growth during thermal etching; 6 min. being sufficient to improve the grain/grain boundary contrast allowing accurate determination of grain size.

3.5.3 Vickers hardness measurements

Before the final oxide polishing the microhardness and indentation toughness of the samples were determined. After the polishing with diamond slurry the samples were removed from the specimen holder, subjected to ultrasound for 2 min. in water, sprayed with ethanol and dried using a heat gun.

The Vickers micro indentation hardness of the samples was determined as per ASTM E 384, using Mitutoyo HM-124 micro hardness tester (Mitutoyo Corporation, Kawasaki, Japan). A square-based pyramidal-shaped diamond indenter with face angles of 136° was used to find the hardness and a load of 1 kg was applied for 15 sec. After the removal of the load the length of the diagonals of the indentation on

the samples were measured with the help of a microscope and the Vickers hardness of the samples were calculated using the formula,

Vickers hardness HV (GPa) = $0.0018544 \times P/d^2$ Eqn. (3.3)

where:

P = force, N, and

d = length of the long diagonal of the indentation, mm

3.5.4 Indentation toughness measurements

The indentation toughness of the samples was determined using a Mitutoyo AVK-C2 hardness tester (Mitutoyo Corporation, Kawasaki, Japan). The indents on the samples were created using a Vickers pyramidal indenter by applying a 10 kg load for 15 sec. This load was found to be sufficient to generate cracks for most of the samples. After indenting the sample, the diagonal length and the length of the cracks were recorded. For certain samples, 10 kg load was not enough to generate cracks and hence the load was increased to 20 kg and then to 30 kg. The indentation toughness was calculated using the formula suggested by Anstis et al.[86]

$$K_{Ic} = 0.016 \left(\frac{E}{H}\right)^{1/2} \frac{P}{C^{3/2}} \qquad \text{Eqn. (3.4)}$$

Where E is the Young's modulus of the material, H is the Vickers hardness, P the indentation load and c the crack length. The value of E is assumed to be 210 GPa for all the YSZ samples

The indentation toughness was also calculated using various other formulas such as the ones proposed by Lankford[226] and that suggested by Niihara[87,88] for radial and Palmqvist type of cracks. Even though all the formulas showed the same trend, the values obtained using the Anstis method are reported for easy comparison.

After indenting the sample, micro-Raman spectra were recorded in and around the indent to qualitatively determine the amount of transformed crystal phases. Also micro-Raman mapping was performed to spatially determine the distribution of the transformed crystalline phases.

3.5.5 Strength and toughness measurements

Strength and toughness measurements were carried out at National Physical Laboratories (NPL, UK). Test-pieces from the slip cast and sintered disc samples were rough-cut by hand using a diamond saw, avoiding visible cracks. The following samples were selected for strength measurements: nano3YSZ and nano1.5YSZ with full density and maximum indentation toughness and the submicron benchmark sample with full density.

The samples were ground into rectangular section test-pieces 2.5 mm x 2 mm x 25 mm in the NPL workshops using a 320 grit wheel for final finishing and grinding parallel to the test-piece length. Chamfers were applied to all four long edges in accordance with the guidelines in ASTM C 1161-02c for size A specimens using a flat lap and 500 grit SiC paper. The inner and outer spans were 6.7 mm and 20 mm respectively.

The sample bars were tested using an Instron 4505 machine with United Kingdom Accreditation Service (UKAS) accredited load cell calibration. A monoblock design of semi-articulating four-point flexural strength jig was employed with 2.5 mm diameter tungsten carbide rollers. The design allowed free movement of the support rollers during loading. Tests were conducted at a cross-head displacement rate of 0.2 mm/min. Peak force at fracture was captured and nominal flexural strength computed using the following equation.

$$S = \frac{3PL}{4bd^2} \qquad \text{Eqn. (3.5)}$$

where:

P = break force,

L = outer support span,

b = specimen width, and

d = specimen thickness

Exactly 10 samples were tested for each composition and the mean was calculated. The fractured samples were analysed using FEGSEM and micro-Raman spectroscopy.

The toughness of the samples was also measured at NPL as per ASTM C 1421-01b in the surface crack in flexure (SCF) mode. The tests were carried out using the standard flexural strength test specimens and a standard set of conditions were used for all the samples. The procedure used was:

- Placed three HV40 indentations along the centre-line of the test-piece separated by about 1 mm using a standard Vickers machine. The test-piece was canted sideways at 5° and tilted lengthwise at 2° (to make the pre-crack more obvious). Three indentations were used to cover the problem of variability in the degree of cracking induced;
- Removed the indentation to a depth of about 100 μm (this was less than recommended by the standards, but avoided completely removing the pre-cracks) using a 320 grit diamond lap. The test-pieces were held in the jaws a tool-maker's clamp and finger loaded. There were some problems with procedure – it proved difficult to ensure that the test-pieces remained parallel-faced. After this, the edges of the face were re-chamfered to minimise the risks of edge failure;
- Fractured the samples using the 20 mm/6.7 mm test jig at 0.2 mm/min. and recorded peak force;
- Measured the cross-sectional dimensions of the test-piece at the point of fracture with a calibrated micrometer;
- Photographed the pre-cracks and any subcritical crack growth on both halves of the fractured test-piece at a calibrated magnification; determined the pre-crack and/or subcritical crack growth boundary, measured the wide (2c) and depth (a) either from paper images or a computer screen;
- Computed the fracture toughness in accordance with the standard equation given below using an Excel spreadsheet.

$$K_{Isc} = Y\left[\frac{3P_{\max}[S_o - S_i]10^{-6}}{2BW^2}\right]\sqrt{a} \qquad \text{Eqn. (3.6)}$$

where:

K_{Isc} = the fracture toughness using the surface crack in flexure method (MPa $m^{1/2}$)

Y = the stress intensity factor coefficient (dimensionless)

P_{max} = the maximum force (break force, N)

S_0 = the outer span (m)

S_i = the inner span (m)

B = the side to side dimension of the test specimen perpendicular to the crack length (m)

W = the top to bottom dimension of the test specimen parallel to the crack length (m)

a = crack depth (m)

c = the crack half width (m)

The stress intensity shape factor coefficients were calculated for both the deepest point of the pre-crack periphery, Y_d, and for the point at the surface, Y_s, were calculated and the greater value of these two were taken as Y to calculate the toughness of the material.

3.5.6 Measurement of wear properties

Both dry and wet wear testing was carried out using a linearly reciprocating ball-on-flat sliding wear tester as per ASTM G 133-05. The test set up was similar to the one shown in Figure 3-3 schematically.

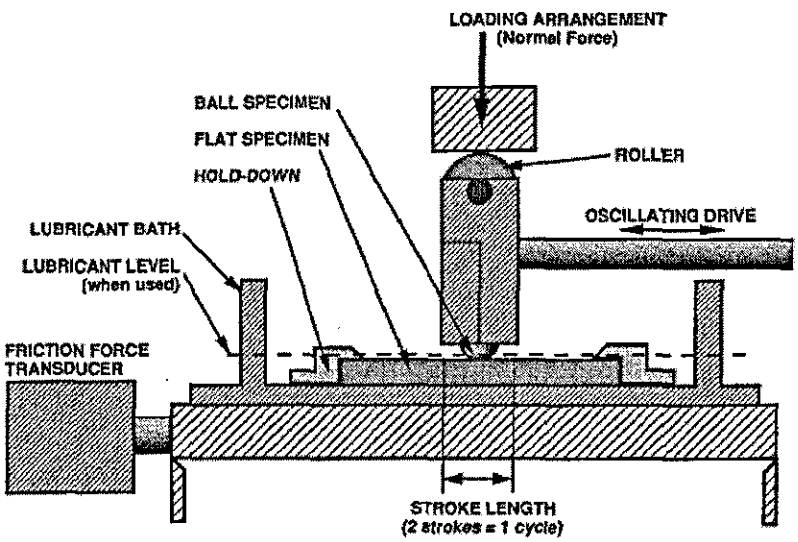

Figure 3-3 Ball-on-a flat reciprocating wear test – Schematic (From ASTM G 133-05).

The samples were mounted in epoxy resin and polished to a fine surface finish, ~30 nm Ra (average surface roughness parameter) measured using a Talysurf CLI 2000 system (Taylor Hobson Ltd. Leicester, UK). 12 mm diameter tungsten carbide–cobalt balls (5-7% cobalt) were used as the ball with a constant 20 N load being applied. The total number of cycles was 100,000 with a 2.5 cm stroke length, equivalent to a total sliding distance of 5 km. After wear testing, the samples were cleaned using ultrasound in distilled water, followed by acetone and then methanol and the weight loss of each sample and the respective ball (a fresh ball was used for each test) was measured and the wear volume calculated. The wear scar on the zirconia specimens was analysed using FEGSEM, XRD and micro-Raman spectroscopy. When the wear testing was carried out under water, the samples were thoroughly dried before recording the weights.

3.6 Hydrothermal ageing experiments

Hydrothermal ageing studies were conducted to evaluate the hydrothermal degradation resistance of the various zirconia ceramics. Ageing experiments were performed for a number of different samples viz. submicron 3YSZ, nano3YSZ, nano2YSZ and nano1.5YSZ. The ageing experiments were performed using an autoclave, with a PTFE liner, containing deionised water with the temperature and pressure being varied. The initial ageing studies were performed at 140°C temperature and 4 bar pressure, these conditions being selected as they are close to the conditions used for the hydrothermal ageing studies of biomedical grade zirconia ceramics.[227] The ageing temperature was increased to 150°C, then to 200°C and up to 250°C for selected samples, with ageing periods up to 14 days. The aged samples were characterised using XRD, micro-Raman, FEGSEM and the hardness was also measured.

3.7 Other characterisation techniques

A number of other characterisation techniques were also employed in the present study for the investigation of various zirconia powders, green bodies and the sintered samples and each is discussed below.

3.7.1 Thermogravimetric analysis (TGA)

Thermogravimetric analysis was performed on the as-received suspension, the concentrated suspension, TMAH, TAC and Tosoh 3YSZ. The samples were heated to 700°C at a heating rate of 5°C per minute and weight loss was monitored. This information was useful in designing the binder removal cycle for the green bodies.

3.7.2 X-ray diffraction studies

X-ray diffraction patterns of the various nanozirconia and submicron zirconia powders was recorded using a Bruker D8 model diffractometer (model D8 diffractometer, Bruker AXS GmbH, Karlsruhe, Germany) with a quarter-circle eulerian cradle, which is a non-destructive tool to analyse the crystalline phases and basic structure of the materials.

Testing conditions:

1. CuKα radiation with a wave length of 1.5406 Å was used.
2. All the samples were analyzed at a step size of 0.02° increment in 2θ with a step time of 1 sec.
3. XRD patterns were recorded from 20° to 80° 2θ range

The volume fraction of the monoclinic phase, Vm, in various zirconia samples was determined by the method of Toraya[228]

$$V_m = \frac{1.311X_m}{1+0.311X_m} \qquad \text{Eqn. (3.7)}$$

$$X_m = \frac{I_{(\bar{1}11)m} + I_{(111)m}}{I_{(111)t} + I_{(\bar{1}11)m} + I_{(111)m}} \qquad \text{Eqn. (3.8)}$$

where Xm is the integrated intensity ratio and the subscripts 'm' and 't' represent the monoclinic and tetragonal phases respectively. The integrated intensity values were calculated using the refinement technique with the help of DiffracPlus and Topas software. A fundamental parameters approach was employed for the refinement.

High temperature XRD patterns were recorded for the nano0YSZ, nano1.5YSZ, nano2YSZ, nano3YSZ and Tosoh powder to determine the various phases present at different temperatures. This experiment was conducted to investigate any particle size

dependent variation in t→m phase transformation temperature for nanozirconia. High temperature XRD patterns were recorded from 25° to 35° 2θ and from 70° to 80° 2θ at room temperature, 500°C, 600°C, 700°C, 800°C, 900°C, 1000°C, 1100°C, 1200°C and after cooling down to 500°C.

The XRD patterns of the various sintered samples were recorded to identify the phases present after sintering.

3.7.3 High temperature differential scanning calorimetry (High temperature DSC)

High temperature differential scanning calorimetry was performed to investigate further into the grain size dependant phase transformation of various zirconia ceramics and also to find whether there was any shift in the phase transformation temperature. About 5 mg of the sample to be analysed was placed on an alumina pan and heated at a rate of 5°C per minute up to 1200°C and cooled down to room temperature under a constant flow of nitrogen gas. An empty alumina pan was used as the reference material. The difference in heat flow was monitored to identify any transition in the material under investigation. High temperature DSC studies were performed for all the nanopowders and the benchmark Tosoh powder.

3.7.4 Field emission gun scanning electron microscopy (FEGSEM)

The agglomerate morphology, shape and primary particle size of the various zirconia powders were analysed using Leo 1530VP field emission gun scanning electron microscope (Leo 1530VP FEGSEM, LEO Elektronenskopie GmbH, Oberkochen, Germany) at different magnifications. The nanopowder was dispersed in alcohol and sprayed on to conducting carbon film mounted on aluminium stubs. The samples were sputter coated prior to analysis with gold to make them conductive and also to prevent them from charging. For the submicron sample, the powder was placed directly onto the stub to find the morphology of the agglomerates. The in lens detector was used to record the images at 5 kV accelerating voltage and a working distance of 5 mm was used.

The microstructure of the sintered specimens was observed by FEGSEM on polished and etched surfaces. The surface to be analysed was coated with a thin layer of gold with the help of an ion sputter coater.

The grain size was determined using the linear intercept method (ASTM E 112-96). The two dimensional grain size was converted to three dimensional using a conversion factor of 1.56.[75] At least three micrographs and a total of 300 grains were evaluated to determine the grain size for each sintering batch. The method measures the mean grain size from the number of grains (intercepts) or grain boundaries (intersections) that intersect one or more lines of known length superimposed on a field of view or micrograph. The mean grain size was calculated by the equation,

$$D = \frac{L \times A_1}{M \times N} \qquad \text{Eqn. (3.9)}$$

where D is the equivalent mean grain diameter, L is the length of superimposed lines, A_1 is the shape correction factor, 1.56, M is magnification (dimensionless) and N is the quantity of intercepts or intersections.

3.7.5 Transmission electron microscopy (TEM)

Transmission electron microscopy (TEM) was used as a very useful tool to find the particle size of the powder. A JEOL JEM 2000FX (JEOL Ltd. Tokyo, Japan) transmission electron microscope was used for the study. The TEM also gave an idea about the shape of the particles and the nature of any agglomerates and their size. TEM was also used to observe very thin samples of sintered bodies prepared using focused ion beam as discussed in Section 3.7.6. The samples were analysed for porosity and grain size.

3.7.6 Focused ion beam (FIB) and high resolution TEM (HRTEM)

A Dual Beam Nanolab 600 FEI FIB, which combines a focused ion beam microscope and FEGSEM, was used for preparing TEM and HRTEM specimens from representative samples to look for porosity and also to observe the integrity of the grain boundaries.

For preparing the sample from a ceramic, a thin layer of Pt was deposited on the surface to protect the sample area. Then a gallium ion beam was used to remove

material from both sides of the sample area. Then a U shaped cut was made on the sample and it was removed and attached to the TEM grid by Pt deposition using a micromanipulator. Then the final thinning was carried out.

A Philips Tecnai F 20 HRTEM microscope (Birmingham University, UK) was used to record the HRTEM images.

3.7.7 Optical microscopy

Optical microscopy (ReichertJung MeF3 optical microscope), was used as a powerful tool to identify the presence of agglomerates in the sintered and polished samples. It was also used to check the surface finish of the samples before property measurements. The equipment enabled images to be taken in the bright field mode, dark field mode or in the polarised light mode.

Bright field images of the indentation induced images were also recorded to measure the crack lengths with higher accuracy. Polarised light imaging with a differential interference scattering (Nomarski scattering) mode was used to record the stress fields around indentation-induced cracks in the sample.

3.7.8 Measurement of surface roughness

The surface finish of the various samples was measured using a Talysurf CLI 2000 system (Taylor Hobson UK Ltd.). The measurements were carried out in the noncontact mode using a CLA 3000 induction gauge. From a 2D map of a 250 μm x 250 μm representative area, line profiles were generated to calculate the average surface roughness parameter. The surface finish of submicron and nanosamples were measured. For the submicron sample, the surface roughness was measured on the as-sintered sample and the sample after polishing. For the nanosample, both dry pressed and slip cast samples were analysed. For the slip cast nanosample, the as-sintered and sintered and polished surfaces were both analysed.

3.7.9 Micro-Raman spectroscopic studies

The micro-Raman study was performed using a Horiba Yvon Raman LabramHR spectrometer (Horiba Jobin Yvon SAS, Villeneuve d'Ascq, France). It was equipped with a liquid nitrogen cooled CCD detector and two objective lenses, x10 and x50

magnification. The optical microscope of the micro-Raman device was connected to a video monitor that allowed selection of specific areas on the sample surface to record the Raman spectrum. The movement of the sample stage was controlled using a computer. The spectroscope was equipped with argon (wavelength 514 nm) and helium-neon (wavelength 632.8 nm) lasers; the He-Ne laser was used in the present study to excite the sample with the laser power being 20 mW. The spectrum integration time was 15 s and the average of two spectra was taken from every data point. When micro-Raman spectra were recorded the samples were excited with laser for 60 s and the average of two spectra were taken every time and the spectra were collected from 100 cm^{-1} to 800 cm^{-1}. When mapping was performed the spectrum was collected from 100 cm^{-1} to 350 cm^{-1} to save time. This range was selected as it was enough to cover the most important peaks corresponding to the monoclinic and tetragonal phases. The spectra of a fully monoclinic and fully tetragonal and a cubic sample were also recorded to compare the results. The spot size of data collection was less than 1 μm. The sample was positioned below the microscope by a computer controlled stepping motor.

Micro-Raman spectra were recorded for samples after sintering, after indentation toughness measurements, after wear testing and after the hydrothermal ageing studies.

Chapter 4

4 Results and Discussions

4.1 Solid content of the suspensions

The as-received solid contents of the various zirconia suspensions used in the experiments are summarised in Table 4-1. The solid content was determined experimentally and the yttria content was obtained from the manufacturer's data. Any variation in solid content and yttria additives were beyond our control and entirely dependent on the supplier.

Table 4-1 Yttria content and solid content of the as-received suspensions.

Suspension code	Yttria content (Manufacturer data / mol%)	Solid content at 700°C / wt.%
Nano0YSZ	0	25.1 ± 0.4
Nano1.5YSZ	1.5	18.4 ± 0.3
Nano2YSZ	2.0	24.0 ± 0.3
Nano3YSZ	3.0	25.5 ± 0.2

4.2 Zeta potential

The zeta potential of the various nanozirconia suspensions are shown in Figure 4-1. The IEP were 8.5, 9.22, 9.21 and 8.87 respectively for the nano0YSZ, nano1.5YSZ, nano2YSZ and nano3YSZ. The zeta potential was above 30 mV for all suspensions above a pH of ~10.2 and hence they can be considered stable above this value. The suspensions were even more stable in the acidic region, but it was decided to conduct further processing in the basic region to prevent yttria dissolution under acidic conditions.[138]

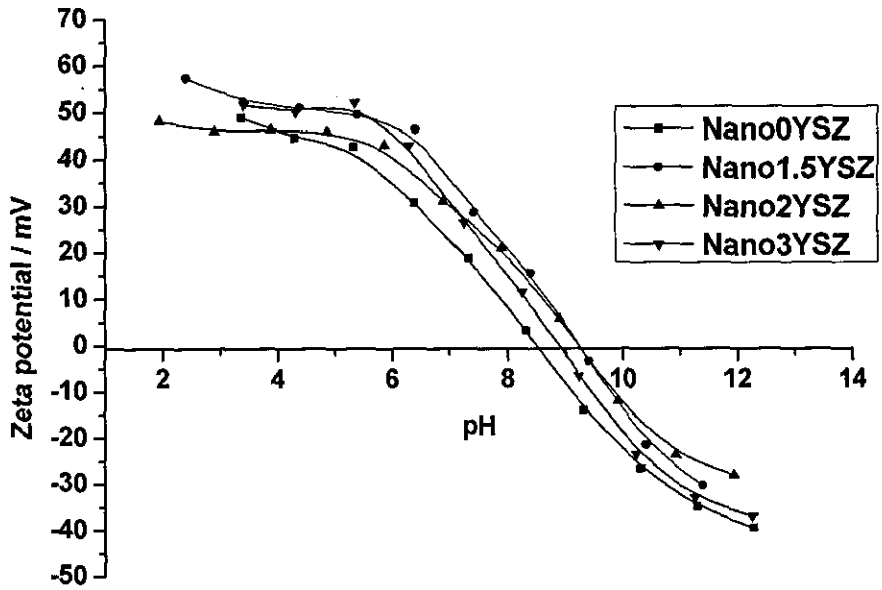

Figure 4-1 Zeta potential of as-received nanozirconia suspensions.

4.3 Viscosity

Representative viscosity vs. shear rate curves for the as-received and concentrated nano3YSZ zirconia suspensions are given in Figure 4-2; the solid content of the latter was ~58 wt%. As expected, the viscosity of the concentrated suspension was higher than that of the as-received suspension, but was still very low (<0.02 Pa s), enabling subsequent processing. A slight increase in viscosity with shear rate was also observed for this particular suspension.

Before concentration, the pH of the as received suspension was changed to basic pH, by the addition of TMAH, to prevent yttria dissolution. Further concentration was carried out by the addition of TAC as a dispersant, which is more effective in the basic pH range. The chemical structure of TMAH and TAC are shown in Figure 4-3.

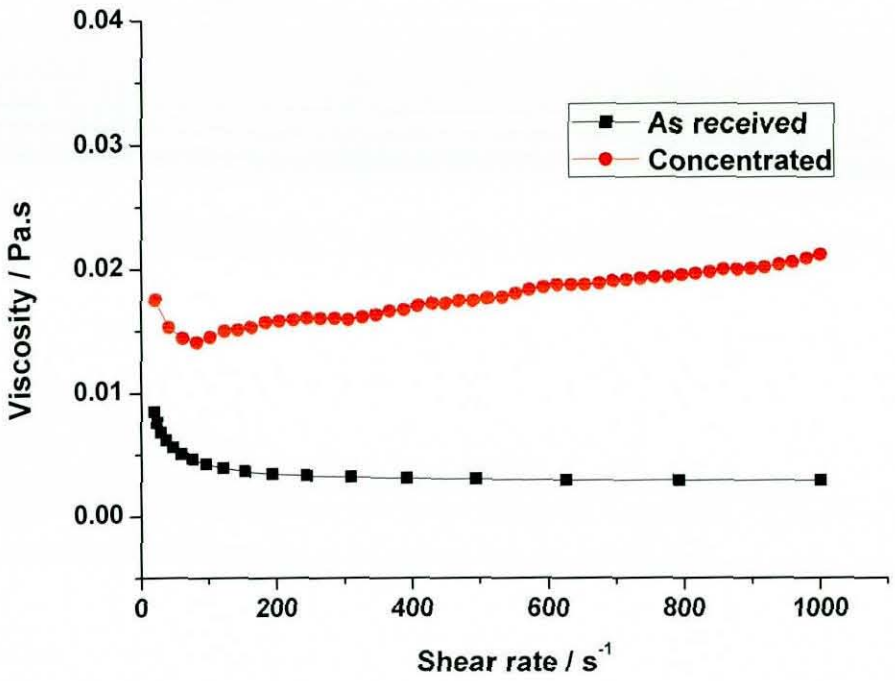

Figure 4-2 Viscosity data for the as-received and concentrated nano3YSZ suspensions.

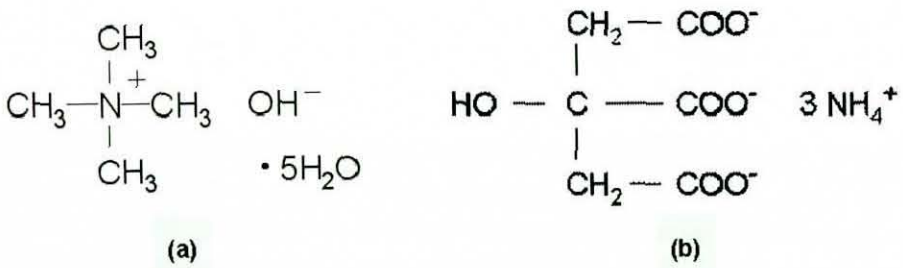

Figure 4-3 Chemical structure of (a) TMAH and (b) TAC.

TMAH does not release any H^+ ions, but change the balance of OH^- and H^+ ions by changing the pH. Electrostatic potential is strongly dependent on the balance between positively and negatively charged ions in the liquid medium and hence when changing the pH through the addition of TMAH, the electrostatic potential of the suspension also changes. When TAC was added to the pH modified zirconia suspension, it adsorbed electrostatically on the zirconia particles stabilising them within the aqueous dispersion medium. The adsorption of TAC changed both the zeta potential and the viscosity of the suspension.[148,149]

4.4 Powder characterisation

4.4.1 FEGSEM results

Figure 4-4 shows micrographs of the oven-dried nano3YSZ powder after micronising.

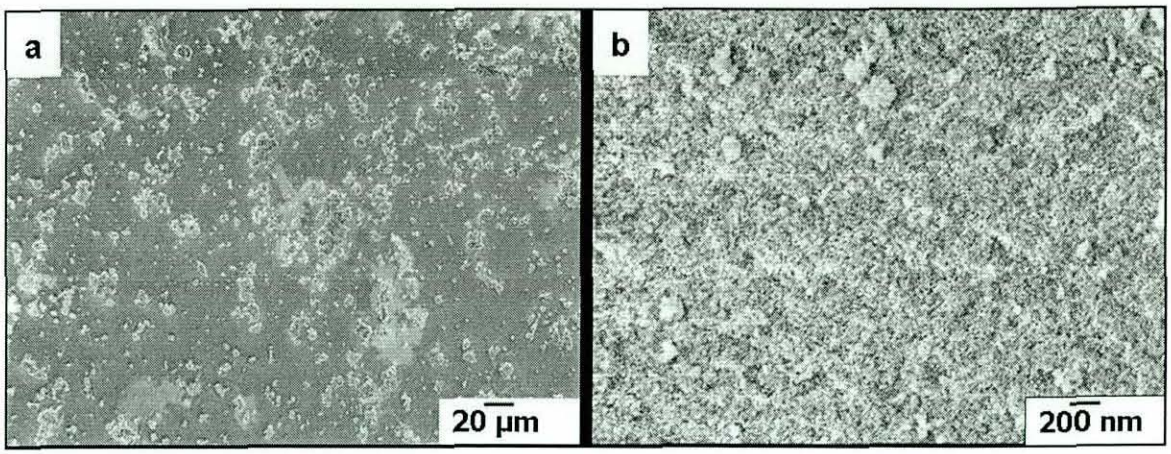

Figure 4-4 FEGSEM image of zirconia powder after micronisation (a) low magnification (b) higher magnification.

From Figure 4-4 it can be seen that the dried powder is highly agglomerated. At higher magnification the individual crystallites can be identified. Micronising is an energy intensive process and the micronising time can be controlled to obtain more uniformity between different batches.

The FEGSEM images of the Tosoh powder are given in Figure 4-5. At low magnification it shows the spray dried agglomerates with the characteristic dimples from the spray drying process.

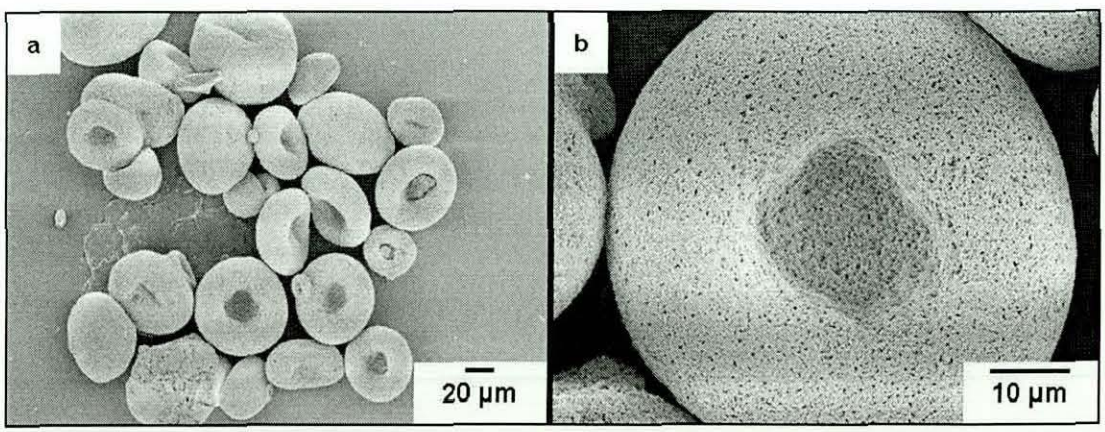

Figure 4-5 FEGSEM images of Tosoh powder (a) low magnification and (b) high magnification of one of the agglomerates.

4.4.2 TEM studies

TEM images of oven-dried powders were taken at different magnifications as shown in Figure 4-6.

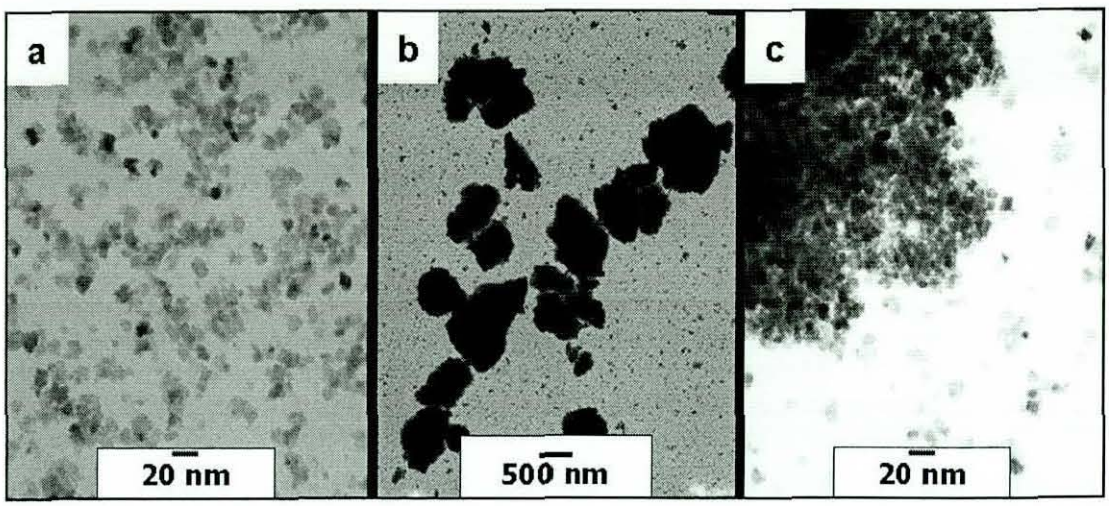

Figure 4-6 TEM images of oven-dried nanozirconia powder micronized using McCrone micronising mill. (a) individual crystallites (b) agglomerates and (c) higher magnification image of one of the agglomerates showing the aggregation of individual crystallites.

From the images it is very clear that the individual crystallites were very small, of the order of ~20 nm. The powder also contained large agglomerates of about 500 – 800 nm size. On a closer look at the agglomerates the individual crystallites are very clearly visible.

4.4.3 XRD

The X-ray diffraction patterns of the various nanozirconia powders are shown in Figure 4-7.

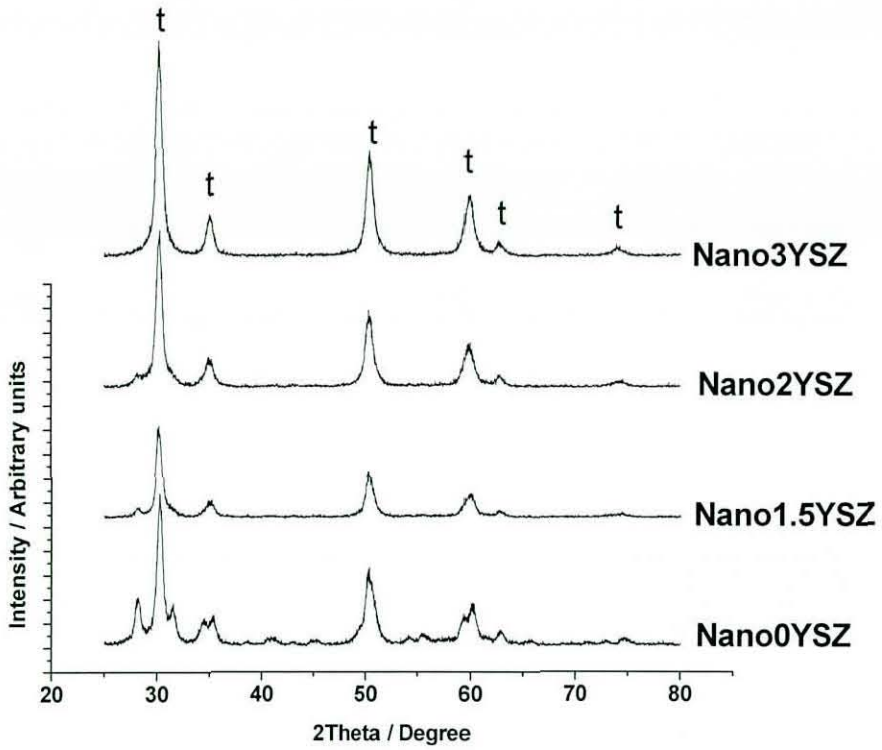

Figure 4-7 XRD pattern of the various nanozirconia powders. All the unmarked peaks correspond to monoclinic zirconia.

The nano3YSZ contained only the tetragonal phase, whilst the nano2YSZ contained 25.4 vol% monoclinic, the nano1.5YSZ contained 32.3 vol% monoclinic phase and the nano0YSZ contained 45.8 vol% monoclinic phase. It is interesting to note that the major phase in the nano0YSZ was still tetragonal zirconia; pure monoclinic phase was expected for zirconia without any stabilising additives at room temperature. The presence of the tetragonal phase is attributed to the self-stabilisation of the zirconia as a result of the ultrafine particle size. In order to investigate this further, the nano0YSZ powder was heated to 1000°C for 1 h to increase the particle size; the XRD pattern recorded is shown in Figure 4-8. This shows the presence of only the monoclinic phase as expected, confirming that the presence of the tetragonal phase in the original nano0YSZ at room temperature was due to the fine particle size.

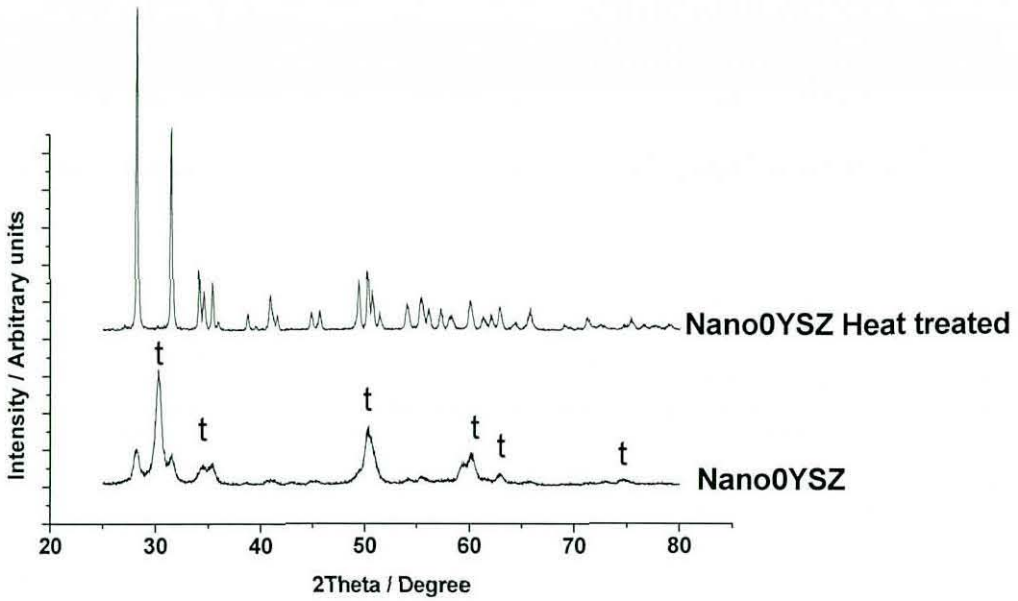

Figure 4-8 XRD pattern of nano0YSZ before and after heat treatment at 1000°C. Unmarked peaks correspond to the monoclinic phase.

The microstructure of the nano0YSZ after heat treatment is shown in Figure 4-9; it can be observed that the grain size is larger than the critical value for self-stabilisation. This could be used with advantage for the preparation of fully sintered monoclinic zirconia ceramics, something that will feature later in this thesis.

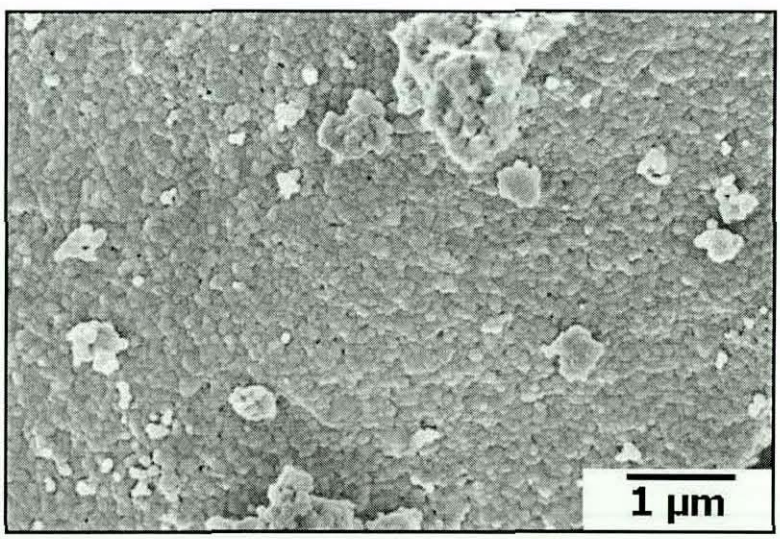

Figure 4-9 FEG-SEM image of nano0YSZ powder after heat treatment at 1000°C.

The XRD pattern of the Tosoh benchmark powder is compared with that of the nano3YSZ in Figure 4-10. It was concluded that the former contained 29.7 vol% monoclinic at room temperature whereas the nano3YSZ showed no monoclinic phase, clearly indicating overstabilisation in the case of the latter. The amount of monoclinic phase in the Tosoh powder was less than the monoclinic content of the nano1.5YSZ but more than that of the nano2YSZ indicating crudely the approximate extent of the degree of overstabilisation.

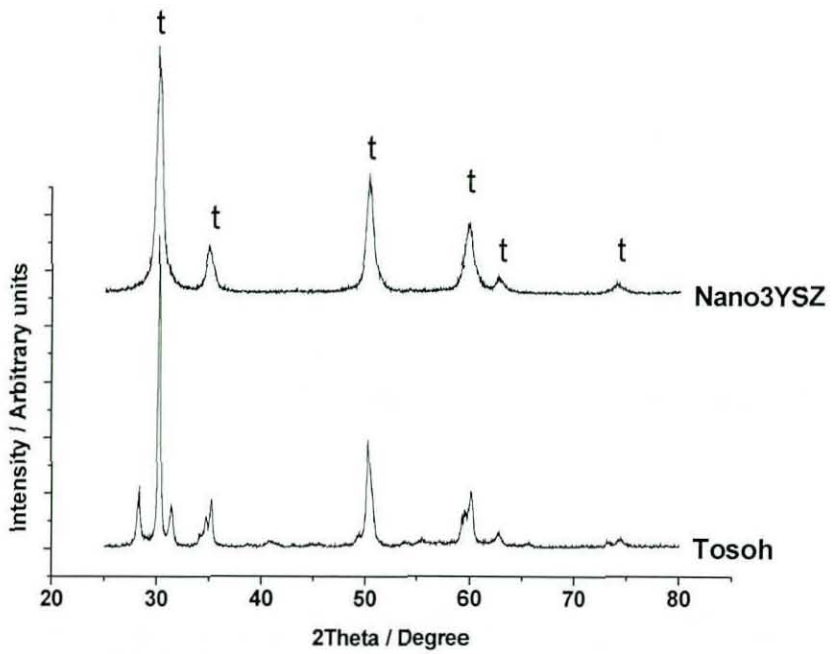

Figure 4-10 XRD pattern of the nano3YSZ and Tosoh powders. Unmarked peaks correspond to the monoclinic phase.

4.4.4 High temperature XRD and high temperature DSC studies

From the room temperature XRD patterns it was observed that the phase stability of the nanozirconia was affected by the crystallite size which is in line with what is reported in literature.[229,230] Representative high temperature XRD patterns for the Tosoh, nano3YSZ and nano0YSZ powders are shown in Figure 4-11 a, b and c.

a

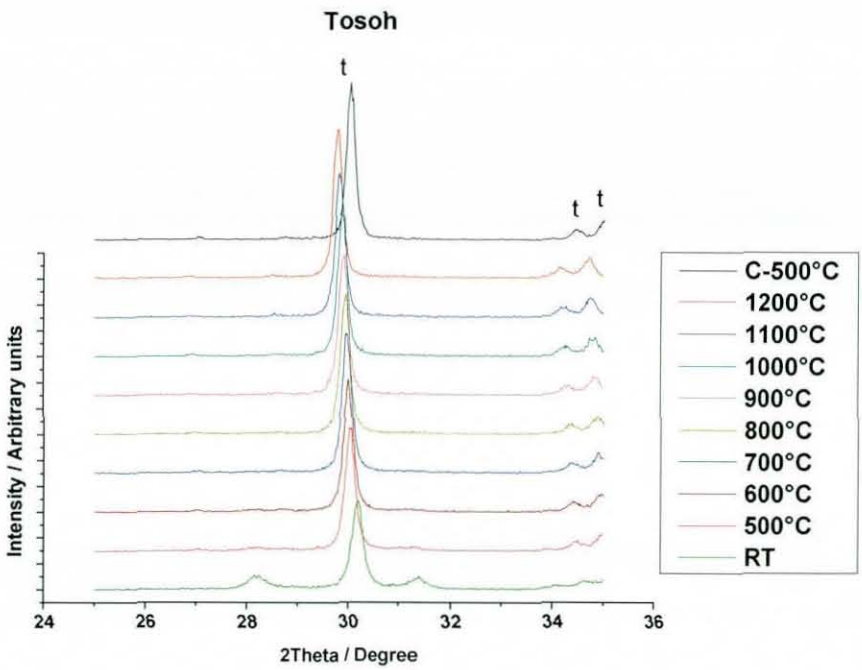
Tosoh
t
t t
Intensity / Arbitrary units
2Theta / Degree
24
26
28
30
32
34
36
C-500°C
1200°C
1100°C
1000°C
900°C
800°C
700°C
600°C
500°C
RT

b

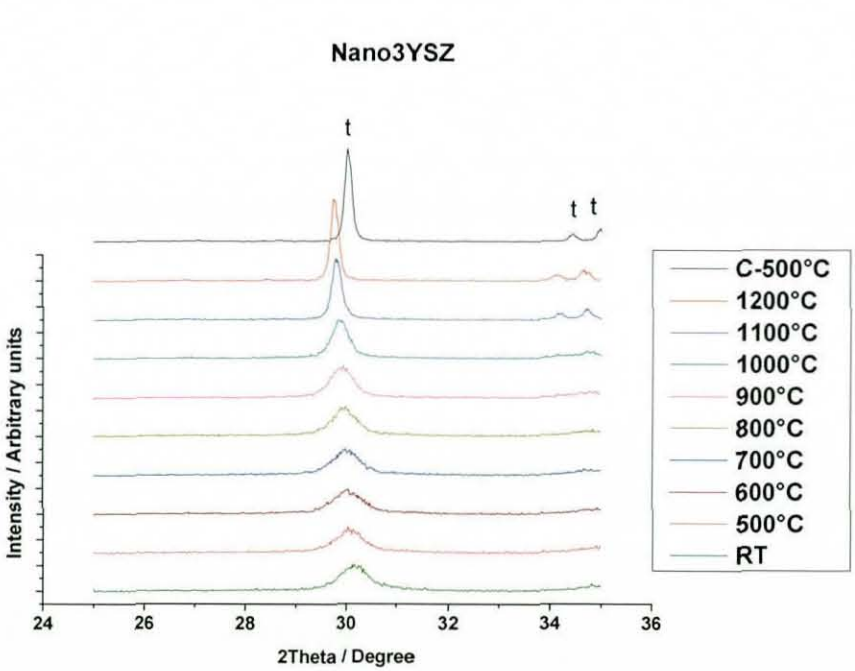
Nano3YSZ
t
t t
Intensity / Arbitrary units
2Theta / Degree
24
26
28
30
32
34
36
C-500°C
1200°C
1100°C
1000°C
900°C
800°C
700°C
600°C
500°C
RT

c

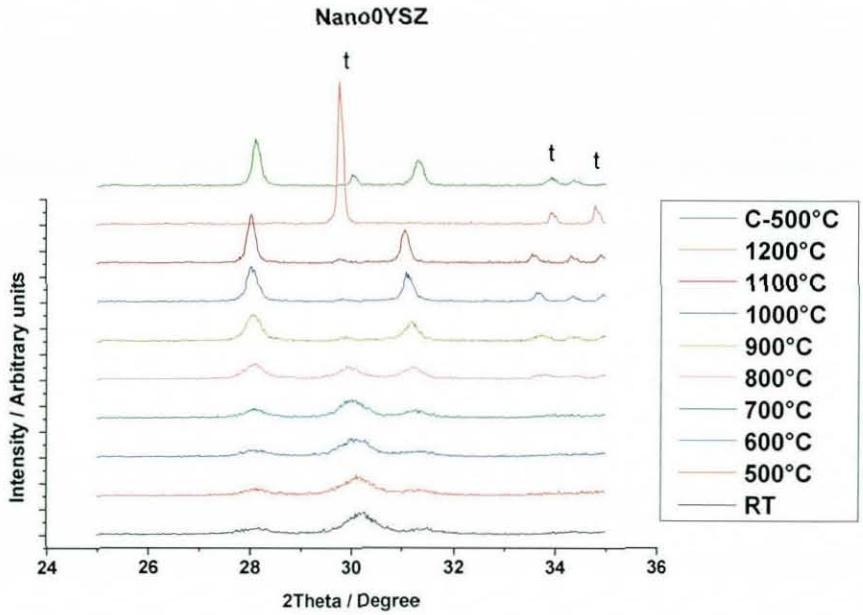

Figure 4-11 High temperature XRD patterns of (a) the benchmark Tosoh powder, (b) the nano3YSZ powder and (c) the nano0YSZ powder. Unmarked peaks correspond to the monoclinic phase.

The amount of monoclinic and tetragonal phases present at the different temperatures were calculated by refinement using the fundamental parameters approach and are summarised in Table 4-2. At this point it is important to note that the results are not very accurate for monoclinic contents lower than 5%.

Table 4-2 Monoclinic content calculated from high temperature XRD of the different powders.

Temperature / °C	Monoclinic content / vol% ± 1%				
	nano0YSZ	nano1.5YSZ	nano2YSZ	nano3YSZ	Tosoh
RT	45.8	32.3	25.4	0	29.7
500	48.7	31.4	21.2	0	8.1
600	48.1	31.5	25.0	0	6.4
700	56.0	28.8	19.1	0	4.3
800	72.6	28.1	16.0	0	3.9
900	92.0	24.7	15.4	0	4.3
1000	95.9	14.4	8.5	0	3.2
1100	95.6	3.8	0	0	2.8
1200	0	0	0	0	2.6
C-500	88.6	0	0	0	2.8

From the table it can be observed that for nano0YSZ the monoclinic content increased with temperature because of the increase in particle size. For all other samples the monoclinic content decreased with temperature due to the crystallisation, and hence the resulting increase in intensity of the tetragonal phase. Above the phase transformation temperature no monoclinic phase was detected for any of the nano samples, but a very small fraction of monoclinic phase was observed for the submicron sample and it was retained even after cooling back to 500°C. Nano0YSZ underwent phase transformation on cooling down from 1200°C to 500°C whereas all other nano samples retained the tetragonal phase on cooling.

From the high temperature XRD results it can be concluded that if nano2YSZ and/or nano3YSZ can be heated to a temperature above 1100°C, fully tetragonal bodies can be prepared. Nano1.5YSZ and Tosoh samples may contain small amounts of monoclinic and nano0YSZ will contain mainly monoclinic phase after sintering at ~1100°C. This provides a means of sintering monoclinic zirconia ceramics without going through the phase transformation temperature limit.

With respect to the high temperature DSC results an exothermic peak at ~1152°C corresponding to the monoclinic to tetragonal phase transformation was observed for the nano0YSZ and a reverse transformation was observed at ~967°C. These results are in agreement with the high temperature XRD results. No transformation was observed for any other samples up to 1170°C. The reverse phase transformation of nano0YSZ involved a hysteresis of approx. 200°C.

4.4.5 TGA studies

The TGA of the starting nanozirconia suspension and the two organics used for processing, viz TAC and TMAH, are shown in Figure 4-12.

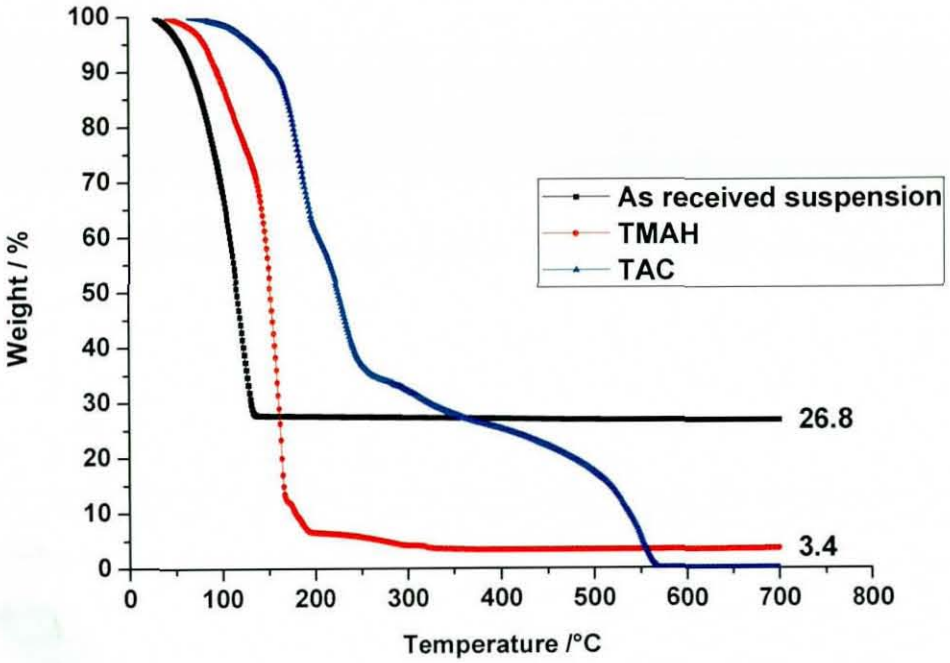

Figure 4-12 TGA of as-received suspension, TMAH and TAC.

From the figure it can be observed that most of the weight loss for the nanosuspension occurred below 100°C, this is due to the evaporation of water. There was less than 1% weight loss from 140°C to 700°C, possibly due to the presence of any unreacted precursors. The weight loss of TMAH can be divided into two regions. The region below 200°C where the material loses ~93% of its weight and one above 200°C where the weight loss was ~3.6%. The decomposition of TAC can also be divided into two regions, one below 275°C and one above that. No residue was left after 575°C. The final solids left after 700°C was 26.8% for the as-received suspension and 3.4% for TMAH whereas no residue was left for TAC.

The TGA of a concentrated nano3YSZ suspension and the benchmark Tosoh powder are shown in Figure 4-13.

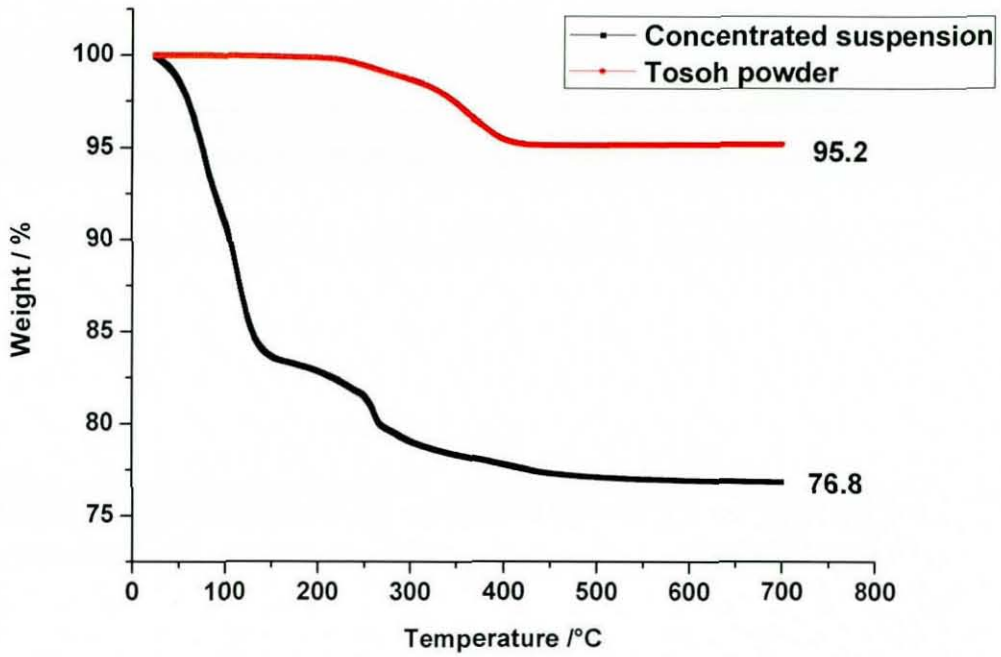

Figure 4-13 TGA of concentrated nano3YSZ suspension and benchmark Tosoh powder.

From the TGA of the concentrated suspension, three separate regions can be identified, one due to the evaporation of water and the other two corresponding to the decomposition of TMAH and TAC. The final solid content for this particular suspension was 76.8%. For the Tosoh powder a final solid content of 95.2% was obtained. The weight loss was due to the presence of binder in the powder and is in agreement with the manufacturers data.

4.5 Preparation and characterisation of green bodies

Preparation of defect free green bodies with sufficient size and green density was one of the biggest challenges in the present project. The green density of the pellets pressed at 480 MPa was found to be around 56.5 ± 0.4% of theoretical density. The pressure applied during dry pressing was well above that commonly used in industry for preparing green bodies, which is in the 150-200 MPa range. The requirement for higher pressure also prevented the preparation of samples with more than 10 mm diameter using the available facilities. The use of binders was tried and was not successful. The commercial Tosoh powder was pressed at 160 MPa and reached a green density similar to that of nanopowder dry pressed at 480 MPa.

Because of the difficulties with dry pressing, it was decided to prepare green bodies using wet routes. Wet processing is a relatively simple process for preparing green bodies using conventional ceramic powder suspensions. But this was not the case for nanosuspensions because of the high surface area of nanopowders and their higher surface energies. Also nanopowders can easily clog the pores present in the PoP mould after a few casting cycles. Wet processing required the optimisation of a large number of parameters including the solid content of the suspension, its viscosity, the amount of organics used for suspension preparation, drying conditions, mould preparation and even the selection of the proper grade of PoP. The best green bodies were obtained with a 55 wt% suspension. Higher solid contents were found to cause sample cracking, Figure 4-14. The extent of cracking increased with increasing solid content. The suspension was too thick with solid content above 70 wt% making it unsuitable for slip casting. Suspensions with <50 wt% solid content resulted in green bodies with <50% theoretical density. Vasylkiv et al.,[78] also observed similar cracking during the slip casting of nanozirconia suspensions. According to them the optimum solid content was 20 vol% (60 wt%).

Humidity drying was also investigated to slow down the drying rate with high solid content suspensions. This was partially successful. But the drying time increased up to 14 days making the process very slow.

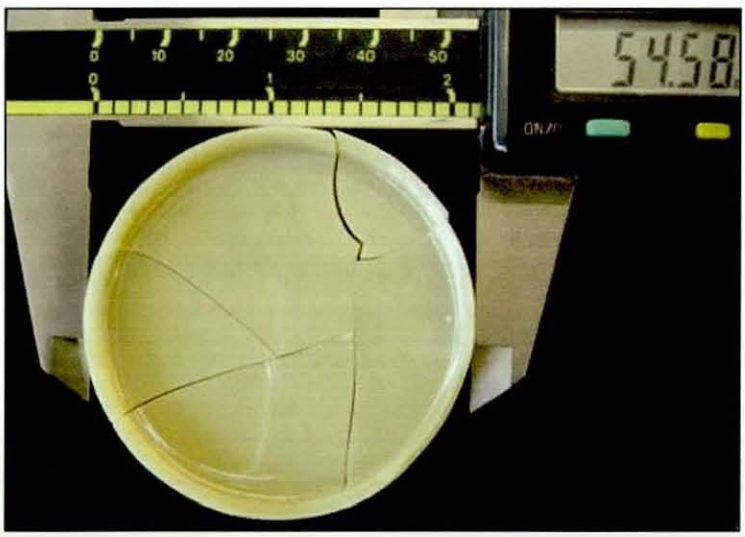

Figure 4-14 Sample cracking during drying was a major problem with slip casting

The slip cast samples were dried at room temperature followed by binder removal at 700°C. The green density of the slip cast samples prepared using the 55 wt% suspension was measured in mercury after binder removal and was found to be 52.1 ± 0.5%, which was less than that of the dry pressed samples. Images of the green bodies before and after binder removal are given in Figure 4-15 and Figure 4-16 respectively.

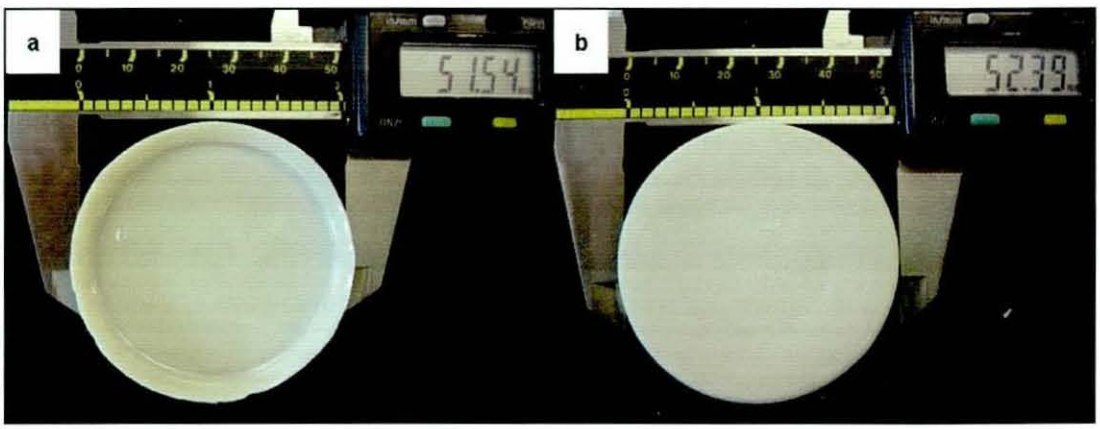

Figure 4-15 Photograph of a nano3YSZ green body prepared by slip casting before binder removal (a) top surface and (b) bottom surface.

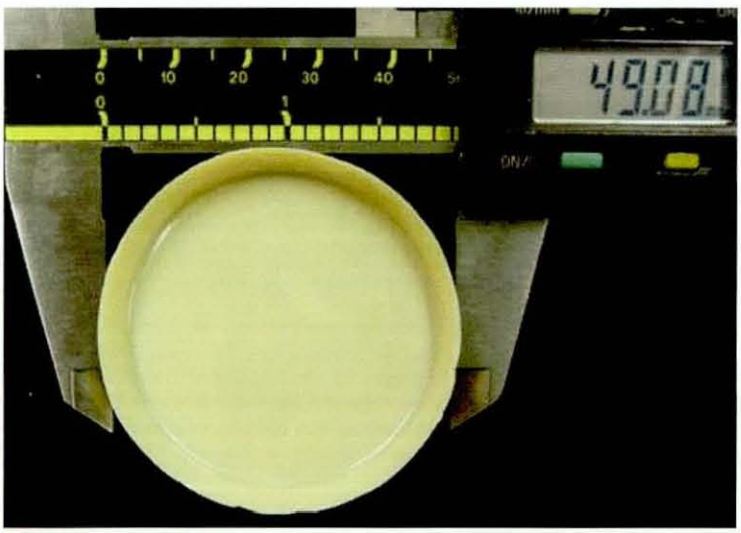

Figure 4-16 Photograph of a nano3YSZ slip cast body after binder removal but before sintering.

The FEGSEM images of the green bodies prepared by both dry pressing and slip casting were recorded and are shown in Figure 4-17.

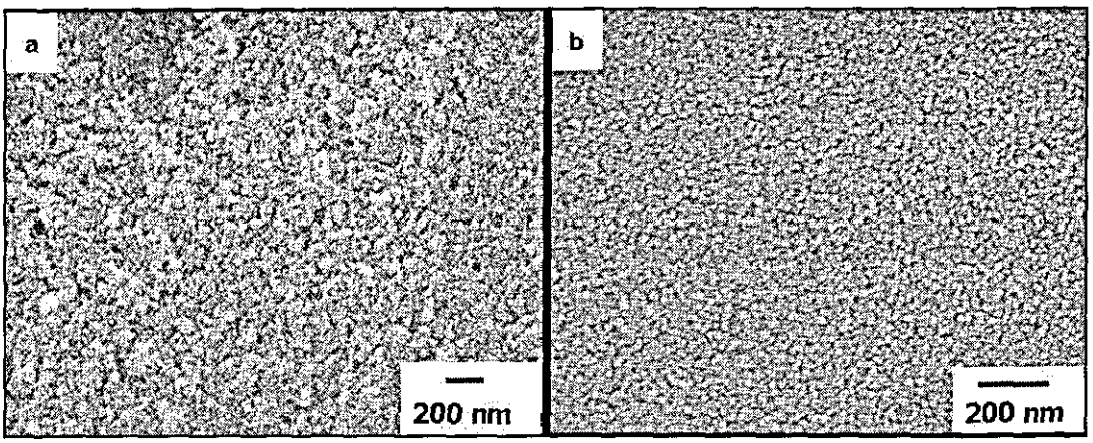

Figure 4-17 FEGSEM images of the fracture surface of nano3YSZ green bodies (a) dry pressed (b) slip cast.

The green microstructure was more uniform in the case of the slip cast green bodies. This is due to the proper dispersion of nano particles in the suspension and also due to the absence of hard agglomerates.

4.6 Sintering experiments

Most of the sintering cycle optimisation experiments were conducted with nano3YSZ samples. The sintering experiments are divided into two sections; in the first the results of the hybrid sintering experiments of the dry pressed and slip cast samples are discussed whilst in the second the results of the conventional sintering experiments are discussed. The sintering properties of the dry pressed and slip cast samples were found to be quite different; especially in the case of two-step sintering, this was probably due to the lower green density of the slip cast samples.

4.6.1 Hybrid sintering of dry and wet processed nano3YSZ samples

The densities of the dry pressed samples sintered using single step sintering cycles within the hybrid furnace are summarised in Table 4-3. To avoid the effect of heating rate on density and grain growth, both conventional and hybrid heating trials were conducted at a constant heating rate of 20°C/min.

In the table CSS stands for "conventional single step" followed by the sintering temperature (°C) and time (h). D stands for dry pressed samples. Similarly HSS stands for "hybrid single step". The preface number in the sample code gives the yttria content (%). The code also gives an idea of the microwave power used (in Watts). Similarly in the coming sections CTS indicates "conventional two-step" and HTS

represents "hybrid two-step" and the code also gives an indication of the first and second step temperatures.

Table 4-3 Density and grain size after single step sintering using the hybrid furnace

Sample code	Temperature / °C	Time / min.	MW power / W	Density / % theor.	Avg. gs / nm
3CSS 1050-3D	1050	180	0	91.2	55
3CSS 1100-3D	1100	180	0	97.2	132
3CSS 1150-3D	1150	180	0	97.7	174
3HSS 1000-3-600D	1000	180	600	91.5	52
3HSS 1050-3-600D	1050	180	600	97.2	97
3CSS 1150-0.1D	1150	0.1	0	~ 69.4	34
3HSS 1150-0.1-600D	1150	0.1	600	~74.4	40

The samples sintered at 1050°C for 3 h using a conventional sintering cycle yielded a fairly low final density (91.2%). In order to achieve higher density the temperature was increased to 1100°C, then to 1150°C, and a maximum density of 97.7% was obtained at the latter. With hybrid heating 97.2% density was obtained at 1050°C, matching the density obtained at 1100°C using conventional heating. The difference in density between the samples sintered at 1050°C using similar time-temperature profile, but with and without microwaves was approximately 6.0%. At 1000°C hybrid heating resulted in a density of only 91.5% and hence no conventional sintering was done. The higher density obtained with hybrid heating clearly depicts the "microwave effect" in the sintering of zirconia, a result that has been observed previously.[187,190,231,232]

Green samples were also heated to 1150°C for a very short time (0.1 min.), using both conventional and hybrid heating and rapidly cooled. This was to mimic the first step in the two-step sintering cycle. Hybrid heating resulted in an approx. 5.0% higher density after these short heating runs. All the hybrid heating experiments discussed so far were done using a constant microwave power of 600 W.

Figure 4-18 (a) represents the microstructure of 3HSS 1150-0.1-600D, which was heated for 0.1 min. at 1150°C with 600 W microwaves. The average grain size was very small, ~40 nm. Figure 4-18 (b) and (c) compares the microstructure of two samples sintered using the same time-temperature profile, but with and without microwaves. MW assisted heating resulted in increased densification (less porosity). The densities of samples (c) and (d) in Figure 4-18 were similar even with a 50°C difference in temperature, but the grain sizes were 97 and 132 nm respectively. This is because a lower temperature was sufficient to achieve higher densification with hybrid heating and this lower temperature resulted in less grain growth. Hence hybrid heating can be employed successfully to prepare high density samples with finer grain size compared to conventional sintering.

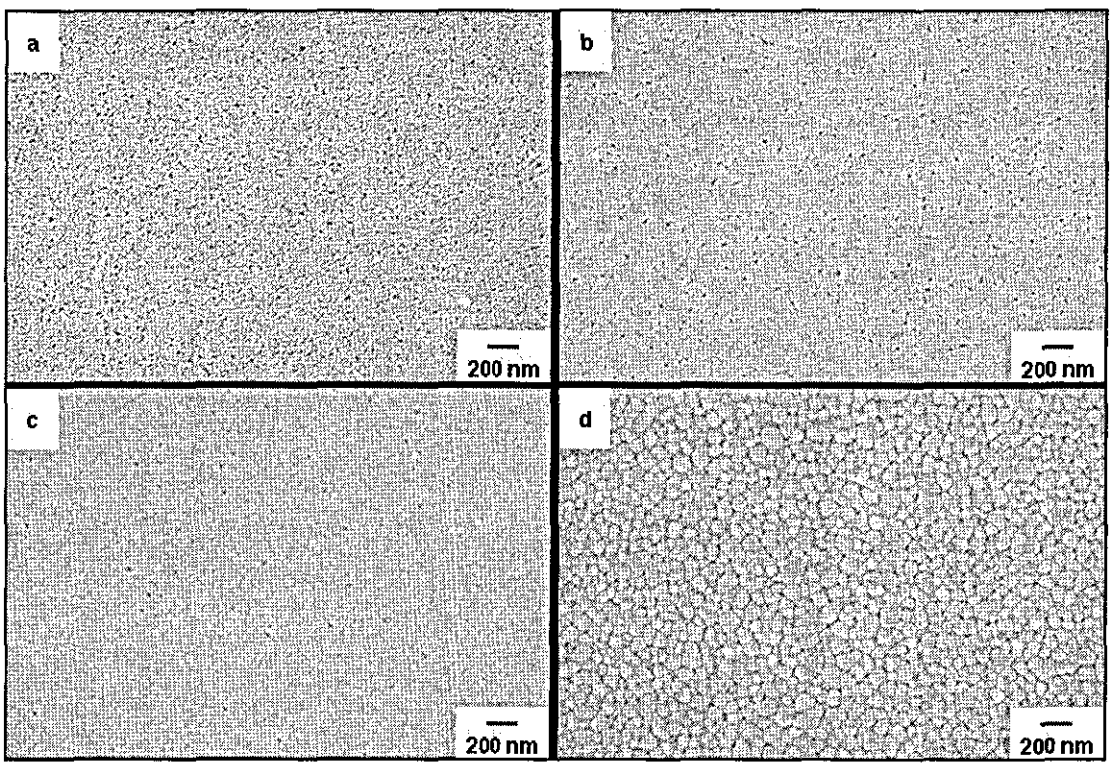

Figure 4-18 Representative microstructures after single step sintering in hybrid furnace (a) 3HSS 1150-0.1-600D, (b) 3CSS 1050-3D (c) 3HSS 1050-3-600D (d) 3CSS 1100-3D.

The densities of the samples sintered using various two-step sintering cycles are summarised in Table 4-4. The sintering schedules were designed based on the above single-step sintering experiments and previous experiments carried out at Loughborough University for the sintering of nanozirconia.[231,232] The first step temperature (T_1) was kept constant at 1150°C and the second step temperature (T_2)

was varied from 1000°C to 1050°C and the time at the second step (t_2) was varied from 3 h to 5h.

Table 4-4 Density and grain size after two step sintering using the hybrid furnace

Sample code	T_1 / °C	T_2 / °C	t_2 / h	MW power / W	Density / %theor.	Avg. gs / nm
3CTS 1150-1000-3D	1150	1000	3	0	91.1	51
3CTS 1150-1025-3D	1150	1025	3	0	91.8	54
3CTS 1150-1050-3D	1150	1050	3	0	94.1	63
3HTS 1150-1000-3-600D	1150	1000	3	600	93.6	58
3HTS 1150-1000-5-600D	1150	1000	5	600	95.5	63
3HTS 1150-1025-3-600D	1150	1025	3	600	96.5	65
3HTS 1150-1050-3-600D	1150	1050	3	600	97.5	74
3HTS 1150-1050-5-600D	1150	1050	5	600	97.9	80

With conventional two-step sintering with T_2 = 1000°C the density was only 91.1% of the theoretical density, but with the application of microwave power and increased sintering time the density increased and a maximum density of 95.5% was obtained when the samples were sintered for 5 h with 600 W microwaves. This was still too low and hence it was concluded that 1000°C for T_2 was insufficient to produce fully sintered pellets, i.e. 1000°C falls below the kinetic window for two-step sintering to proceed to full densification.[169,170,171]

In order to increase the final density, the second step temperature was increased to 1025°C; the density values were higher than those when T_2 was 1000°C but still too low, so T_2 was increased to 1050°C. From Table 4-4 it may be observed that hybrid sintering using 600 W of microwave power and T_1= 1150°C and T_2 = 1050°C yielded densities in excess of 97% of theoretical. According to Chen et al.,[169] the second sintering step proceeds via a frozen microstructure and hence has a slower kinetics. They said that this was sufficient for reaching full density, whilst providing the benefit of suppressing the grain growth. Unlike the results reported by Chen et al., however, a degree of grain growth occurred during the second stage of sintering in the present study, although the rate of grain growth was much lower compared to single step sintering and the final grain size was also considerably lower compared to CSS

and HSS. This is in agreement with the results reported for the two-step sintering of nano SiC[171], nanoZnO[176] and submicron Al_2O_3,[180] all of which resulted in grain growth during second stage of sintering. For nanoZnO[176] the grain size increased from 280 nm to 680 nm during the second sintering stage.

Representative microstructures of two samples after HTS are given in Figure 4-19, the second step temperatures were 1000°C and 1050°C respectively. The figure illustrates the higher densification achieved at the higher T_2.

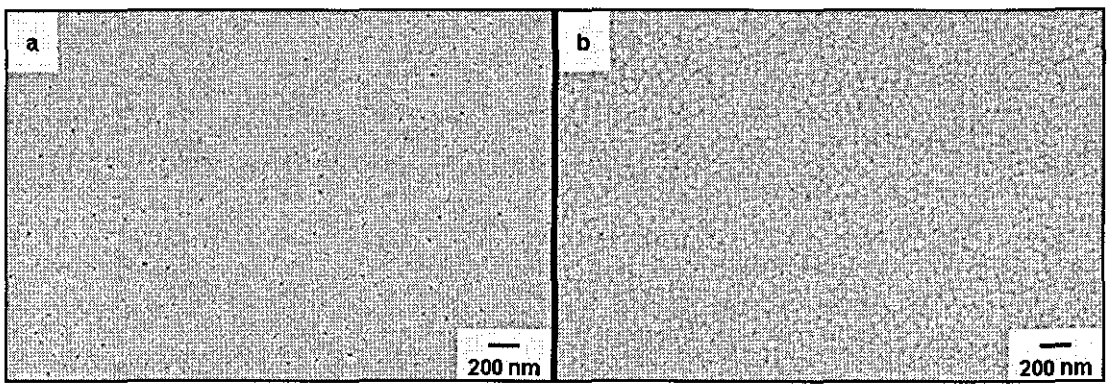

Figure 4-19 Representative microstructures of samples after hybrid two step sintering (a) 3HTS 1150-1000-3-600D and (b) 3HTS 1150-1050-3-600D.

To find the effect of microwaves on the densification and grain growth, samples were sintered using the same time-temperature profile but with different microwave power levels. As it was not possible to directly measure the amount of microwave power absorbed by the sample, the amount of radiant power input was recorded in order to find whether the contribution of microwaves was greater at higher power levels. As the microwave power input increased, the amount of conventional power used decreased; this indicated that the fraction of microwave power used for heating up the sample increased with microwave power input. The density and mean grain size were both found to increase with increasing microwave power, though the increase in density was minimal above 600 W, possibly because the sample has reached its maximum density for the conditions used whilst the mean grain size increased slightly and consistently with increase in microwave power.

Table 4-5 Hybrid sintering experiments with different amount of microwave power.

Sample code	T_1 / °C	T_2 / °C	t_2 / h	MW power / W	%TD	Avg. gs / nm
3CTS 1150-1050-3D	1150	1050	3	0	94.1	63
3HTS 1150-1050-3-200D				200	95.3	68
3HTS 1150-1050-3-400D				400	96.6	71
3HTS 1150-1050-3-600D				600	97.5	74
3HTS 1150-1050-3-800D				800	97.7	76
3HTS 1150-1050-3-1000D				1000	97.7	80

Representative FEGSEM images of the samples sintered using different amounts of microwave power are shown in Figure 4-20, it can be observed that the porosity decreased with increasing microwave power. This increased densification is clearly due to the influence of microwaves as every other parameter was kept the same.

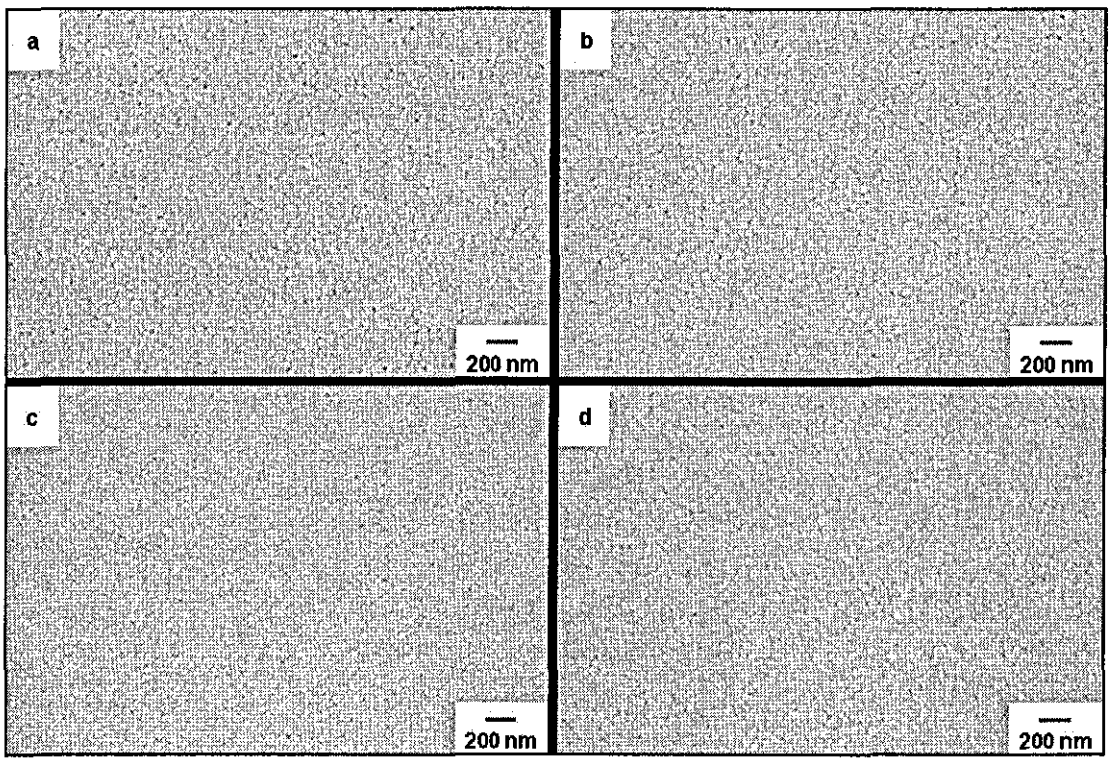

Figure 4-20 FEGSEM images of dry pressed samples sintered using the same time-temperature profile, but with different amount of microwave power (a) 0 W (b) 400 W (c) 800 W and (d) 1000 W.

The maximum density achieved for dry pressed samples, even with 1000W microwave power, was found to be less than 98%. This was due to the presence of

hard agglomerates in the green bodies. Whilst the pores within the agglomerates will have been eliminated at an early stage during sintering, it is well known that it is very difficult to eliminate inter-agglomerate pores without the application of high temperatures, external pressure or extended sintering times. The presence of hard agglomerates was identified on polished surfaces of sintered samples under the optical microscope. Hence the green body preparation technique was changed to slip casting. Slip casting, if done properly using a well dispersed suspension can yield green bodies with uniform microstructure free from agglomerates. It is a pressureless process and hence the green density of the slip cast bodies was found to be ~5% lower than that of the dry pressed bodies.

The sintering of the slip cast bodies was initially performed using the optimised sintering cycle used for dry pressed bodies, i.e. 1150°C first step temperature, 1050°C second step temperature and 600 W microwave power. But the densities obtained were unsatisfactory and hence the sintering cycle was modified as summarised in Table 4-6 where R10 and R15 indicates heating rates of 10 and 15°C min^{-1} respectively.

Table 4-6 Summary of the hybrid sintering experiments using slip cast 3YSZ samples

Sample code	T_1 / °C	T_2 / °C	Heating rate / °C min^{-1}	MW power / W	Density / %theor.	Avg. gs / nm
3HTS 1150-1050-3-0	1150	1050	20	0	87.1	80
3HTS 1150-1050-3-200				200	89.0	87
3HTS 1150-1050-3-400				400	90.8	91
3HTS 1150-1050-3-600				600	94.0	95
3HTS 1150-1050-3-800				800	95.5	97
3HTS 1150-1050-3-1000				1000	96.4	101
3HTS 1150-1050-3-600R15			15	600	97.0	104
3HTS 1150-1050-3-600R10			10	600	99.2	120
3HSS 1150-0.1-600		-	20	600	77.5	56
3HSS 1150-0.1-600R10		-	10	600	95.8	92

Figure 4-21 shows the microstructure of samples sintered using different amounts of microwave power using the same time-temperature profile, all the samples were

heated at a constant rate of 20°C min^{-1}. Similar to the dry pressed samples, the density increased with increasing microwave power, reaching a maximum of 96.4% at 1000 W microwave power. This density is approximately 10% higher than that of the sample sintered without microwaves and is similar to that of the dry pressed samples sintered using the same conditions even though the green density was ~5% lower for the slip cast bodies. This increased densification is due to a more uniform particle packing and particle orientation in the case of slip cast bodies and the resulting increased sinteractivity.

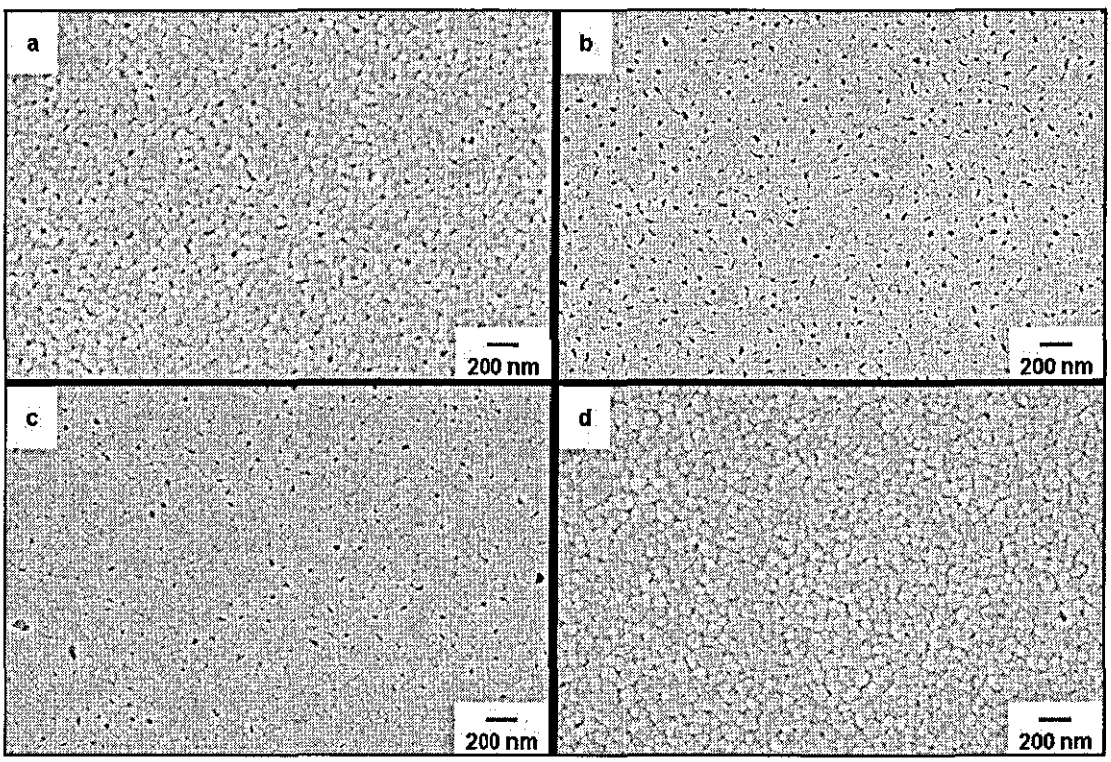

Figure 4-21 FEGSEM images of slip cast samples after hybrid sintering using different amount of microwave power (a) 3HTS 1150-1050-3-0 (b) 3HTS 1150-1050-3-200 (c) 3HTS 1150-1050-3-600 and (d) 3HTS 1150-1050-3-1000.

As the final density was low after hybrid sintering at a heating rate of 20°C min^{-1}, samples were sintered at slower heating rates, of 15°C min^{-1} and then 10°C min^{-1}. Figure 4-22 compares the microstructure of two samples heated to the first stage at 20°C min^{-1} and 10°C min^{-1} respectively using 600 W of microwave power; the densities were 77.5% and 95.8%. The density and grain size after the first stage is a critical factor is determining the final density.

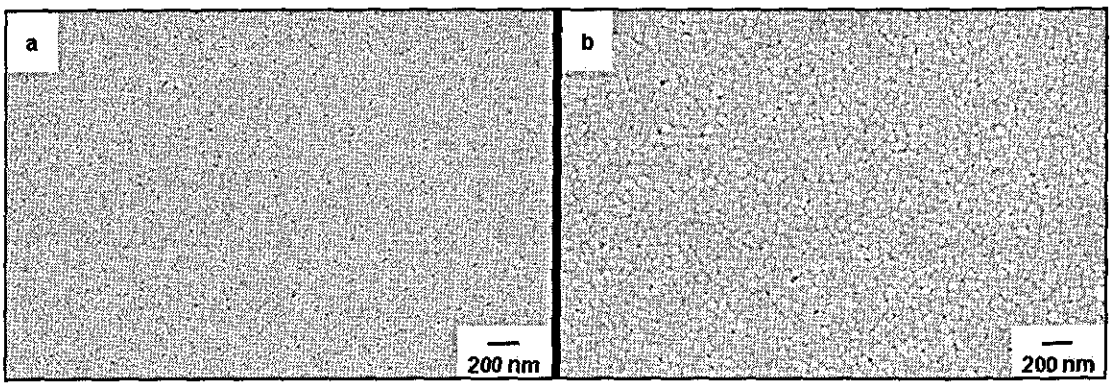

Figure 4-22 FEGSEM images of slip cast samples after first stage heating (a) 3HSS 1150-0.1-600 and (b) 3HSS 1150-0.1-600R10.

In Figure 4-23, the final microstructures of two samples sintered using the full hybrid two-step sintering cycle (HTS) at 10 and 15°C min^{-1} heating rates are shown. Compared to Figure 4-21 (c), where the sample was sintered at similar temperatures but at 20°C min^{-1}, the samples showed increased densification and grain growth.

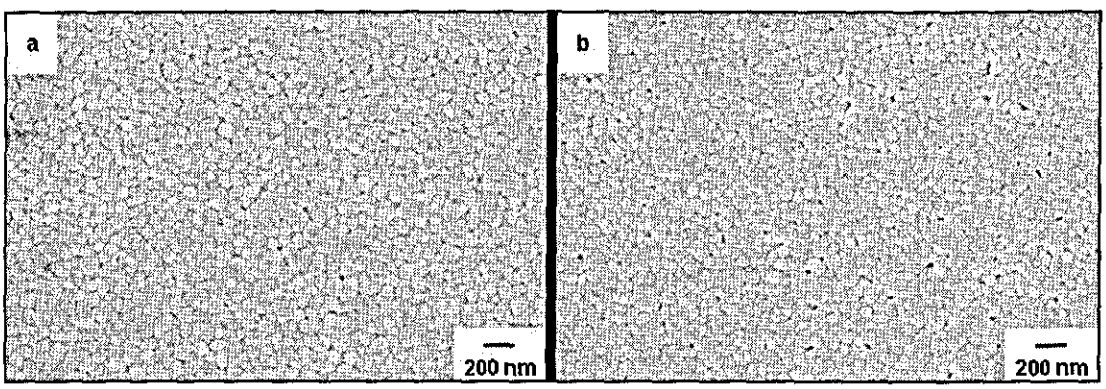

Figure 4-23 FEGSEM images of slip cast samples after hybrid sintering at two different heating rates (a) 3HTS 1150-1050-3-600R10 and (b) 3HTS 1150-1050-3-600R15.

The density increased from 94.0% to 97.0% and then to 99.2% as the heating rate decreased from 20°C min^{-1} to 15°C min^{-1} and then to 10°C min^{-1}. The final density achieved was much higher than that reached with dry pressed samples and this is believed to be due to the absence of agglomerates in the slip cast samples. The grain size, however, is also increased from 95 nm to 104 nm and then to 120 nm respectively as the heating rate was changed. So part of the advantage with hybrid heating was lost as the heating rate was reduced.

4.6.2 Conventional sintering of nano3YSZ slip cast samples

From the hybrid sintering experiments, it was found that the density obtained after MW assisted heating was always higher compared to conventional heating and the grain size was always finer, irrespective of whether single or two-step heating was used. The maximum density obtained after hybrid sintering was limited for the dry pressed samples by the presence of the agglomerates and for the slip cast samples by the lower starting density. When a slow heating rate was employed for the hybrid sintering cycles the final average grain size was more than 100 nm.

Zych et al.[41] reported a bimodal pore size distribution for nanozirconia green bodies prepared by dry pressing whereas a mono-modal pore size distribution was observed for the wet processed samples with similar green densities. The large pores in the dry pressed bodies corresponded to the inter-agglomerate porosity and the smaller ones to the intra-agglomerate pores. The presence of open porosity was reported for dry pressed samples, even at 97% TD. For low green density samples like those that were slip cast in the present study, the number of contact points between the particles will be reduced, in turn decreasing the number of matter transport paths and hence reducing the degree of densification expected. According to Gao et al.,[233] a 12% decrease in green density causes a 50% reduction in the number of matter transport paths. According to Trunec and Maca[234] after compacting nanozirconia at different compaction pressures, the maximum pore size decreased to 4.5 nm after compaction at 1000 MPa compared to 9 nm at 300 MPa; the green densities were 57% and 42% respectively. As a result of the reduced pore size and increased density, lower temperatures were found to be sufficient for reaching higher density. Hence for our samples with reduced density (and possibly bigger pore size), it was decided to sinter the samples using conventional heating with a longer hold period during the second stage. As a result of the absence of microwaves during heating, the heating rate had, of necessity, to be slow to avoid thermal stresses, potentially leading to greater grain growth.

There were a number of reasons to shift the focus from hybrid two-step sintering, despite all its advantages, to conventional two-step sintering, those are listed below:

1) The variation in microwave absorption with yttria content. A variation in dielectric loss factor has been reported for zirconia with different yttria content.[235,236] So again the microwave power needs to be adjusted when samples with different yttria content are prepared;
2) The need to increase the sample dimensions, to prepare samples big enough for mechanical property evaluation, and the necessity to sinter a large number of samples in a single run. The microwave absorption properties of materials vary with sample mass and hence the hybrid heating cycles needs to be adjusted for sample mass;
3) Conventional sintering provides better flexibility to vary the grain size for a sample with known green density, mass and yttria content – one of the main objectives of the present work;
4) The lower green density of the slip cast green bodies and the resulting grain growth after hybrid two-step sintering at reduced heating rates;
5) It is not possible to do binder removal and sintering in a single step for the slip cast samples using a hybrid heating cycle as the heating rates for binder removal are required to be very slow;

The density and grain size of the samples after the various single step heating experiments were measured and are summarised in Table 4-7. It can be observed that during conventional single step sintering, the density increased with temperature, reached a maximum and then decreased. This decrease in density at higher temperature is known as desintering or bloating and has been reported for nanoceramics before.[93,176,237] The maximum density was reached at 1100°C for 10 h. The grain size was found to increase with sintering temperature and time as expected.

Table 4-7 Summary of the conventional single step sintering experiments using slip cast 3YSZ samples.

Sample code	Sintering temperature / °C	Time	Density / %theor.	Avg. gs / nm
3CSS-1000-10	1000	10 h	89.1	53
3CSS-1050-10	1050		98.7	105
3CSS-1100-10	1100		99.7	128
3CSS-1150-10	1150		99.1	170
3CSS-1200-10	1200		98.9	220
3CSS-1300-10	1300		97.3	303
3CSS-1400-10	1400		95.0	344
3CSS-1500-10	1500		90.6	512
3CSS-1100-30	1100	30 h	99.1	141
3CSS-1050-0.1	1050	0.1 min.	84.1	49
3CSS-1075-0.1	1075		87.2	58
3CSS-1100-0.1	1100		89.9	66
3CSS-1125-0.1	1125		92.5	72
3CSS-1150-0.1	1150		95.6	80

Representative microstructures of the samples after the single step sintering trials are given in Figure 4-24. Figure 4-24 (a) and (b) shows the presence of porosity due to lack of densification and (f) shows porosity due to desintering. No visible porosity was observed for (c), (d) and (e) but the grain sizes varied as given in Table 4-7.

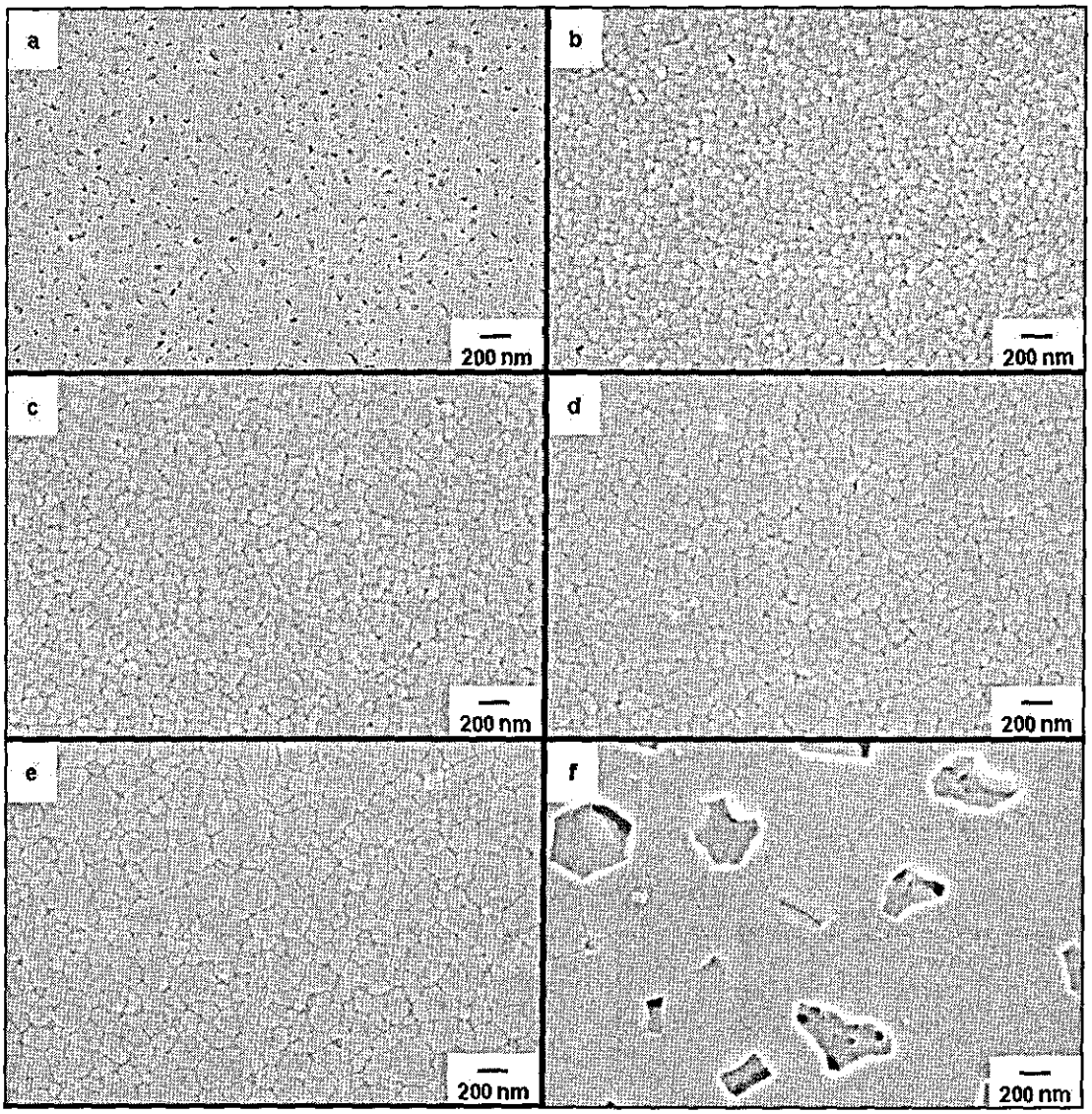

Figure 4-24 FEGSEM images of nano3YSZ samples sintered using conventional single step sintering (a) 3CSS 1000-10 (b) 3CSS 1050-10 (c) 3CSS 1100-10 (d) 3CSS 1150-10 (e) 3CSS 1200-10 and (f) 3CSS 1500-10.

The microstructure of the 3 CSS 1100-30 is shown in Figure 4-25 (a), for comparison the microstructure of the submicron benchmark zirconia sintered at 1500°C using the sintering cycle recommended by the manufacturer is shown in Figure 4-25 (b). The average grain size of the Tosoh sample was ~ 520 nm.

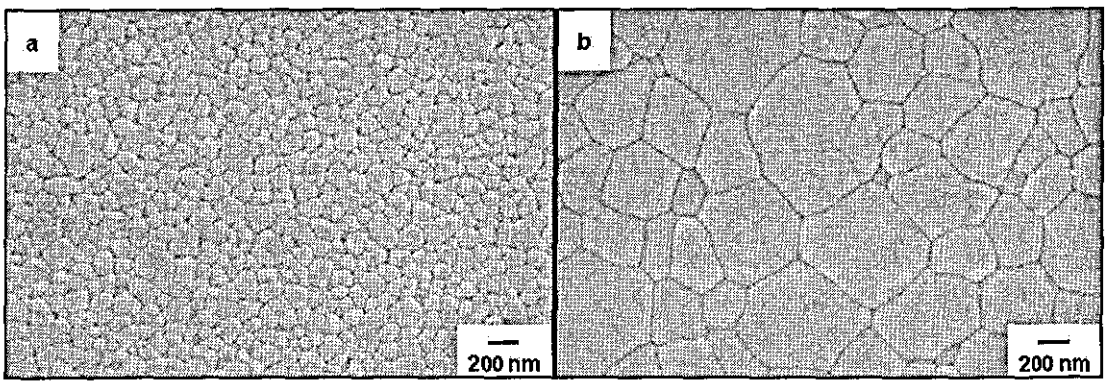

Figure 4-25 FEGSEM images (a) 3CSS 1100-30 and (b) the benchmark Tosoh sample.

Comparing Figure 4-24 (f) and Figure 4-25 (b) indicates very clearly how much lower the optimum sintering temperature is for nanoceramics.

The microstructures of the samples after the short term sintering experiments designed to elucidate T_1, are given in Figure 4-26 and the density and grain size data are given in Table 4-7. It may be observed that the density and grain size reached around 95% of theoretical at 1150°C for 0.1 min., resulting in 1100°C and 1150°C being selected as T_1. T_2 was then varied from 900°C to 1050°C to obtain samples with different density and mean grain size. The time at the second stage was also varied in an attempt to obtain maximum density with minimum grain growth. The results of the various two-step sintering experiments with T_1 = 1100°C are summarised in Table 4-8.

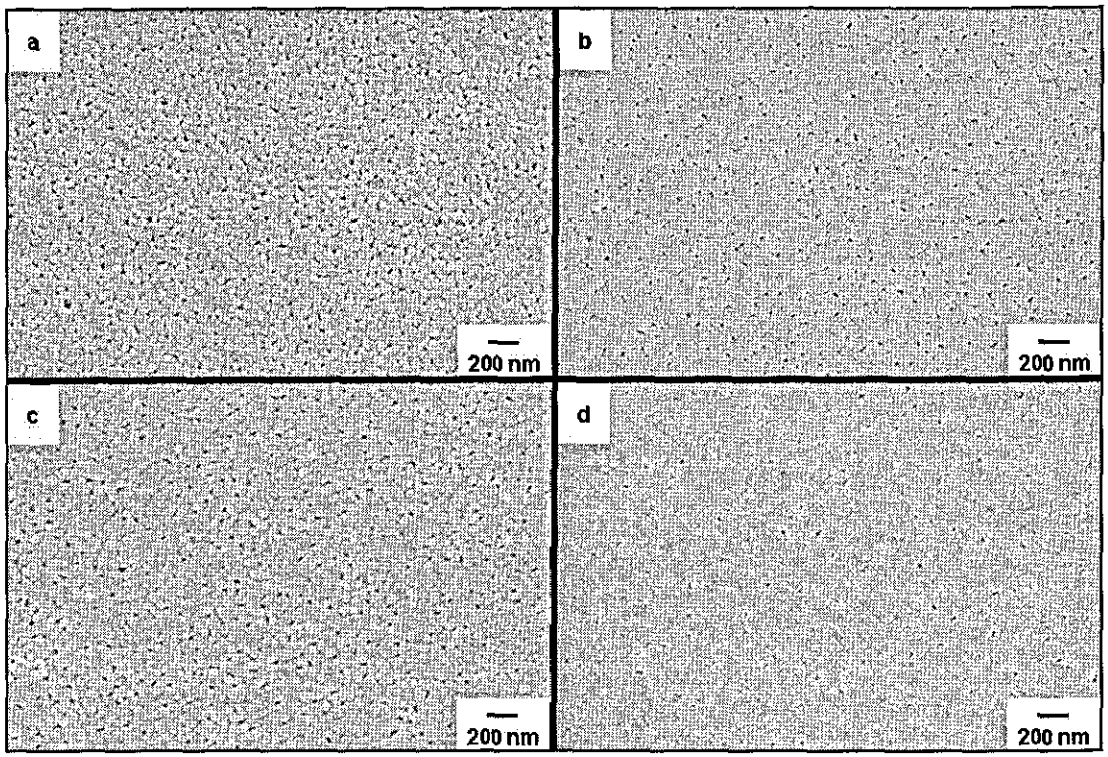

Figure 4-26 Microstructure of nano3YSZ samples after short term heating (a) 3CSS 1075-0.1 (b) 3CSS 1100-0.1 (c) 3CSS 1125-0.1 and (d) 3CSS 1150-0.1.

Table 4-8 Results of the two-step sintering experiments with T_1 = 1100°C.

T_1 / °C	T_2 / °C	Time at T_2 / h	Density / %theor.	Avg. gs / nm
1100	950	10	90.2	70
		15	92.6	74
	1000	10	95.7	75
		15	95.9	77
		30	95.9	84

Since the density and mean grain size after 0.1 min. at 1100°C were 89.9% and 66 nm respectively, it can be observed that very little extra densification has occurred when T_2 was 950°C. Increasing T_2 to 1000°C, and the time up to 30 h, resulted in little improvement. According to Chen et al.,[169,170] a density of approx. 75% after the first stage was sufficient to prepare nanoY_2O_3 samples with full density after second step sintering, provided the second step temperature was high enough. Based on the above sintering trials, this was clearly not the case for nanozirconia. From our experiments it can be observed that even >89% density after the first stage was not sufficient to produce bodies with >99% of theoretical density after CTS. Representative

microstructures of the samples sintered with T_1 = 1100°C and T_2 = 1000°C are shown in Figure 4-27.

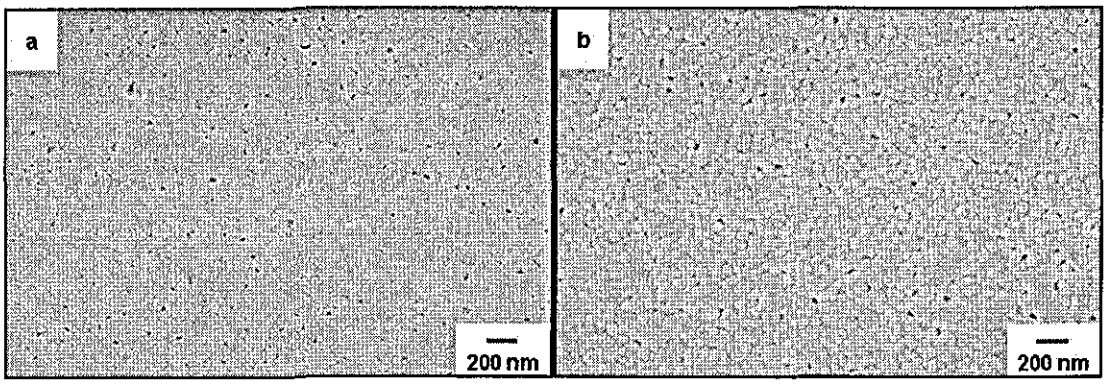

Figure 4-27 Microstructure of slip cast nano3YSZ after two-step sintering (a) 3CSS 1100-1000-10 and (b) 3CSS 1100-1000-30.

It was decided to increase T_1 to achieve a higher initial density; the results with T_1 = 1150°C are summarised in Table 4-9.

Table 4-9 Results of the two-step sintering experiments of nano3YSZ with T_1 = 1150°C.

T_1 / °C	T_2 / °C	Time at T_2 / h	Density / %theor.	Avg. gs / nm
1150	900	10	97.7	83
	950	3	98.1	85
		5	98.3	86
		10	98.4	87
		15	98.3	87
	1000	3	98.2	88
		5	98.6	90
		10	98.7	92
		15	98.9	95
	1050	5	99.3	93
		10	99.4	95

It may be observed that densities >98% of theoretical could be achieved with T_2 values ≥950°C, however, in order to achieve more than 99.0% of theoretical density, T_2 needed to be 1050°C. Representative microstructures of the samples sintered for 10 h at the different T_2s are given in Figure 4-28.

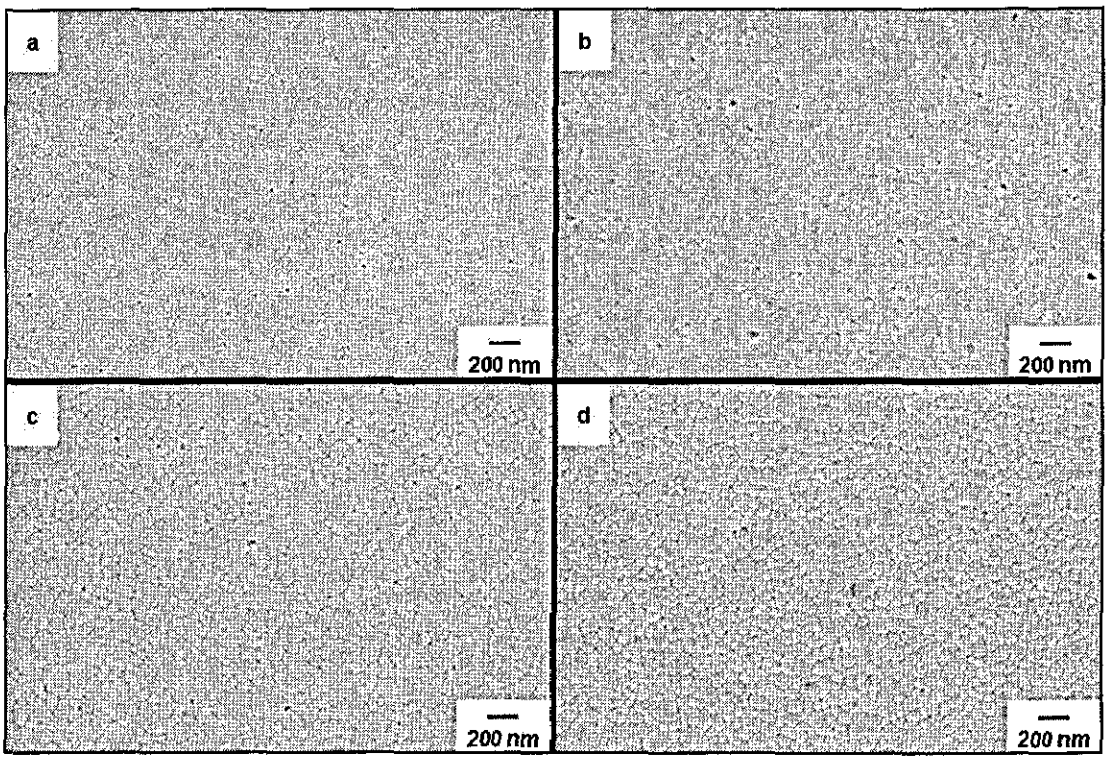

Figure 4-28 Microstructure of slip cast nano3YSZ after two-step sintering (a) 3CTS 1150-900-10 (b) 3CTS 1150-950-10 (c) 3CTS 1150-1000-10 and (d) 3CTS 1150-1050-10.

It may be observed that, as expected, the porosity decreased with increase in T_2 and the grain size increased. Sample 3CTS 1150-1050-10 sample was free from any visible porosity and had an average grain size of ~95 nm. These sintering conditions were therefore adopted for the sintering of slip cast nano3YSZ.

Based on the above two-step sintering experiments, the density of the samples should be more than 95% after the first stage of sintering in a conventional two-step heating cycle for nano3YSZ to obtain samples with >99% density and <100 nm final average grain size. According to Van De Graaf et al.[238] the grain growth of zirconia accelerates strongly above 95% density during conventional single stage sintering. So it is ideal to keep the density close to 95% after the first stage, to limit the grain size to a minimum. They also reported that the region 1100°C < T < 1200°C is a region of abnormal grain growth for nanozirconia and hence suggested minimisation of the holding time in this range to achieve high densities and small grain sizes. In the present study, the nano3YSZ samples were held at 1150°C for 0.1 min., a very short period of time, to reach sufficient densification with minimum grain growth in the

first step and in the second step the temperature was kept below 1100°C, above which the abnormal grain growth was reported.

4.6.3 Conventional sintering of nano2YSZ and nano1.5YSZ slip cast samples

After optimising the sintering cycle for the slip cast nano3YSZ samples, it was decided to apply the same conditions for the sintering of slip cast nano2YSZ samples as the green densities were similar, however, after measuring the density and grain size it was found that they were both higher than that for the nano3YSZ samples sintered using the same conditions. This led to the assumption that lower sintering temperatures were sufficient for the sintering of samples with lower yttria content, a conclusion also drawn by Vasylkiv et al.[78] for the sintering of nano3YSZ and nano2YSZ. They assumed that the better densification of the nano2YSZ samples was due to achieving a better green microstructure. The results of various experiments designed to optimise the sintering of the slip cast nano2YSZ samples are summarised in Table 4-10.

Table 4-10 Summary of the sintering experiments conducted for nano2YSZ.

Sample code	T_1 / °C	T_2 / °C	Time	Density / %theor.	Avg. gs / nm
2CSS 1050-10	1050	-	10 h	99.1	118
2CSS 1100-10	1100			99.6	149
2CSS 1150-10	1150			99.4	214
2CSS 1200-10	1200			99.3	248
2CSS 1300-10	1300			98.4	335
2CSS 1050-0.1	1050		0.1 min.	87.6	66
2CSS 1075-0.1	1075			90.9	72
2CSS 1100-0.1	1100			93.2	81
2CSS 1125-0.1	1125			95.8	84
2CTS 1150-1050-5	1150	1050	5 h	99.5	113
2CTS 1150-1000-10	1150	1000	10 h	99.8	108
2CTS 1150-1000-5	1150	1000	5 h	99.7	102
2CTS 1125-1000-10	1125	1000	10 h	99.3	96
2CTS 1100-1000-30	1100	1000	30 h	99.1	100

From the results, the best conditions were found to be T_1 = 1125°C and T_2 = 1000°C for 10 h. Similarly to obtain maximum density in a single step sintering cycle, 1100°C for 10 h is recommended for nano2YSZ.

The results for equivalent experiments performed for the slip cast nano1.5YSZ samples are summarised in Table 4-11, with the best conditions observed to be T_1 = 1075°C and T_2 = 1000°C for 10 h. For a conventional single stage sintering, a 10 h hold at 1100°C is suggested.

Table 4-11 Summary of the sintering experiments conducted for nano1.5YSZ.

Sample code	T_1 / °C	T_2 / °C	Time	Density / %theor.	Avg. gs / nm
1.5CSS 1100-10	1100	-	10 h	99.8	169
1.5CSS 1100-20	1100		20 h	99.8	190
1.5CSS 1125-10	1125		10 h	99.8	194
1.5CSS 1250-10	1250		10 h	93.9	342
1.5CSS 1050-0.1	1050		0.1 min	88.8	71
1.5CSS 1075-0.1	1075			92.6	77
1.5CSS 1100-0.1	1100			95.3	85
1.5CTS 1150-1000-10	1150	1000	10 h	99.9	139
1.5CTS 1100-1000-10	1100			99.7	113
1.5CTS 1075-1000-10	1075			99.6	89
1.5CTS 1050-1000-10	1050			96.5	81

Representative microstructures of the samples sintered using the best conditions are given in Figure 4-29,Figure 4-30 and Figure 4-31 respectively, for the first stage of sintering, single step sintering and two-step sintering.

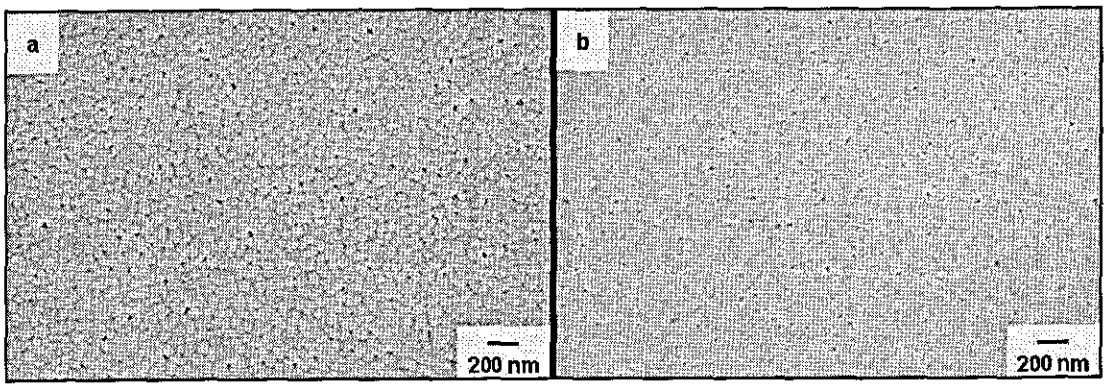

Figure 4-29 Microstructure of nano2YSZ and nano1.5YSZ after the first step of heating (a) 2CSS 1125-0.1 and (b) 1.5CSS 1075-0.1.

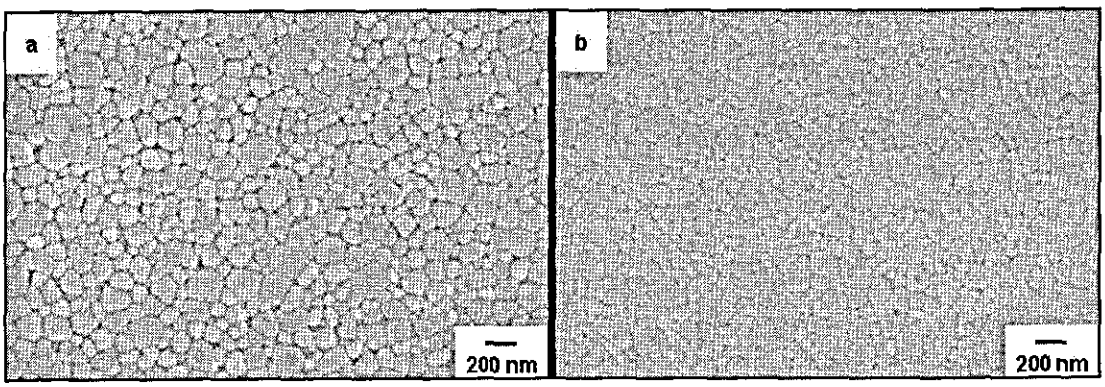

Figure 4-30 Microstructure of nano2YSZ and nano1.5YSZ after optimum single step sintering (a) 2CSS 1100-10 and (b) 1.5CSS 1100-10.

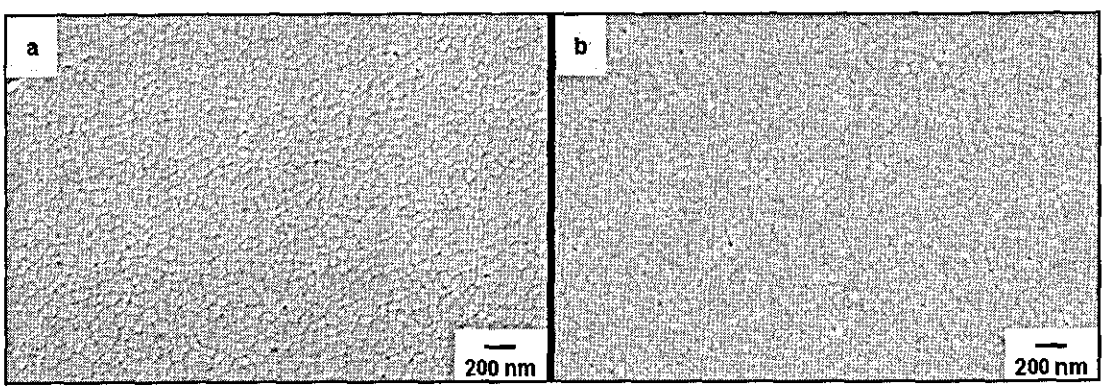

Figure 4-31 Microstructure of nano2YSZ and nano1.5YSZ after optimum two-step sintering (a) 2CTS 1125-1000-10 and (b) 1.5CTS 1075-1000-10.

The results suggest that the density achieved by the nano2YSZ and nano1.5YSZ samples was higher than that achieved by the nano3YSZ for the same sintering conditions, whilst a higher density after the first stage is needed for nano2YSZ compared to nano1.5YSZ if >99% density is to be achieved after the second sintering step.

From Figure 4-30 it may be observed that the grain sizes follow bimodal distributions; similar finding has also been reported by Zum Gahr et al.[102] Comparison of Figure 4-30 and Figure 4-31 show that the grain size is finer and the grain size distribution is more uniform when samples are sintered using CTS compared to CSS.

As a footnote, in the previous section on the sintering of dry pressed samples, it was observed that the presence of agglomerates was detrimental to densification, preventing the samples from reaching higher densities. This can also be a problem with slip casting if the suspension contains residual agglomerates that become trapped in the green body. Figure 4-32 shows the presence of abnormal grain growth and porosity that arose when a batch of nanosuspension was concentrated improperly.

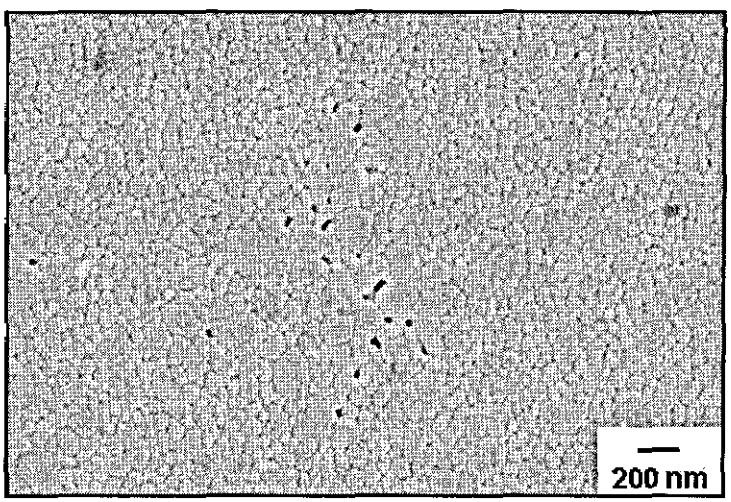

Figure 4-32 Effect of agglomerates on densification.

Representative images of the top and bottom surfaces of a slip cast sample after optimal processing and sintering are shown in Figure 4-33; no cracking was observed on any of the surfaces. The average diameter of this sample was more than 40 mm and thickness was ~4.5 mm. This was sufficient to machine test specimens for mechanical property measurements. The as-sintered surface finish was very good with the top surface showing a particularly smooth shiny finish; the surface roughness parameter was measured to be ~8 nm, using Talysurf.

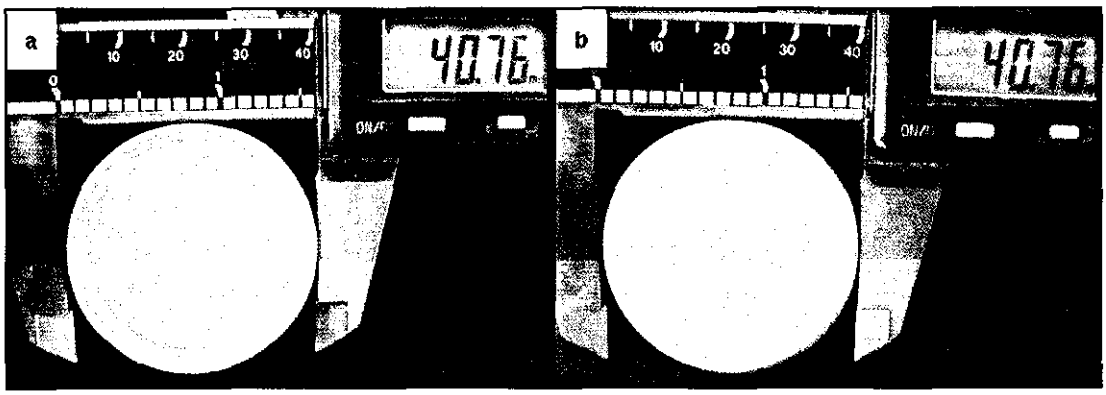

Figure 4-33 Images of a slip cast nanozirconia sample after sintering (a) top surface and (b) bottom surface.

4.6.4 Sintering of 0YSZ samples

Based on the sintering experiments described above, it has been observed that lower sintering temperatures are required for the sintering of nanozirconia ceramics compared to their submicron counterparts. In addition the sintering temperatures were found to decrease with decreasing yttria content and, with two-step sintering, required T_1 was always below the phase transformation temperature of zirconia. This suggested that it might be possible to prepare dense, pure ZrO_2 ceramics. In view of these ideas, a variety of sintering experiments, both single step and two-step, were performed using slip cast nano0YSZ samples; the sintering cycles used and the densities obtained are summarised in Table 4-12. It should be noted that the sintering temperatures were always below the tetragonal to monoclinic phase transformation temperature determined from high temperature DSC.

The samples sintered at temperatures ≥1135°C using CSS all shattered, possibly due to a slow phase transformation taking place close to the actual phase transformation temperature of 0YSZ (~1152°C from high temperature DSC). The maximum density obtained was 98.4% at 1130°C. It was not possible to prepare crack-free samples above this temperature.

The results of the various two-step sintering experiments are also summarised in Table 4-12. The first step temperature was either 1100°C or 1150°C for all the samples. None of the samples were cracked even with T_1 very close to the phase transformation temperature, though the time at this temperature was just 0.1 min. The

maximum density obtained after two-step sintering was less than that obtained after single step sintering, with a maximum density of only 96.4%.

Table 4-12 Summary of the sintering experiments conducted for nano0YSZ

Sample code	T_1 / °C	T_2 / °C	Time / h	Density / %TD
0CSS 1050-10	1050	-	10	93.9
0CSS 1100-10	1100			97.4
0CSS 1125-10	1125			98.1
0CSS 1130-10	1130			98.4
0CSS 1135-10	1135			Shattered
0CSS 1150-10	1150			Shattered
0CSS 1100-30	1100		30	97.7
0CTS 1100-950-10	1100	950	10	89.8
0CTS 1100-950-15			15	88.3
0CTS 1100-1000-10		1000	10	89.6
0CTS 1100-1000-15			15	90.5
0CTS 1150-950-3	1150	950	3	93.2
0CTS 1150-950-10			10	95.5
0CTS 1150-950-15			15	95.6
0CTS 1150-1000-3		1000	3	94.2
0CTS 1150-1000-5			5	95.9
0CTS 1150-1000-10			10	96.0
0CTS 1150-1050-5		1050	5	96.4

Representative microstructures of nano0YSZ after single step and two-step sintering cycles are shown in Figure 4-34. Abnormal grain growth was observed after single step sintering and unsatisfactory densities were obtained after two-step sintering.

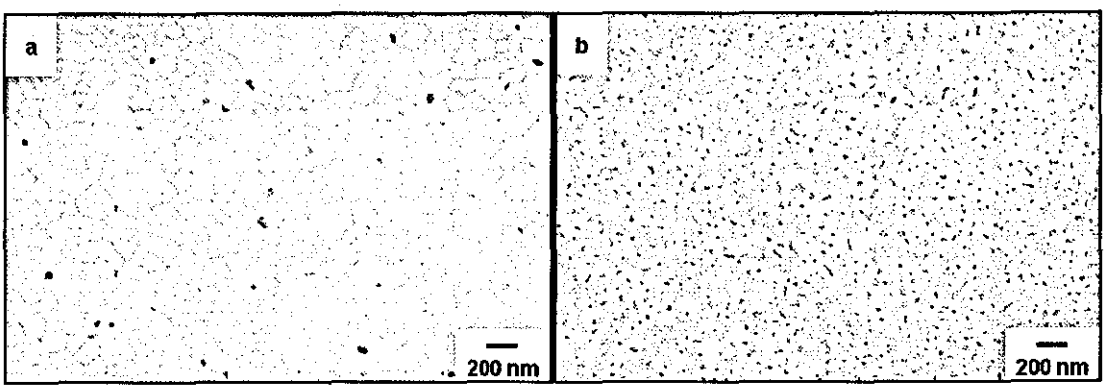

Figure 4-34 Representative microstructures of nano0YSZ samples after single step and two-step sintering (a) 0CSS 1125-10 and (b) 0CTS 1150-1000-10.

4.6.5 Variation in grain size and density

Although the mean grain sizes have already been reported, this section looks at the values, and particularly the trends, for the different materials and sintering conditions investigated. Figure 4-35 provides a comparison of mean grain size versus density after single step and two-step sintering cycles, both with and without microwaves, for the dry pressed green bodies.

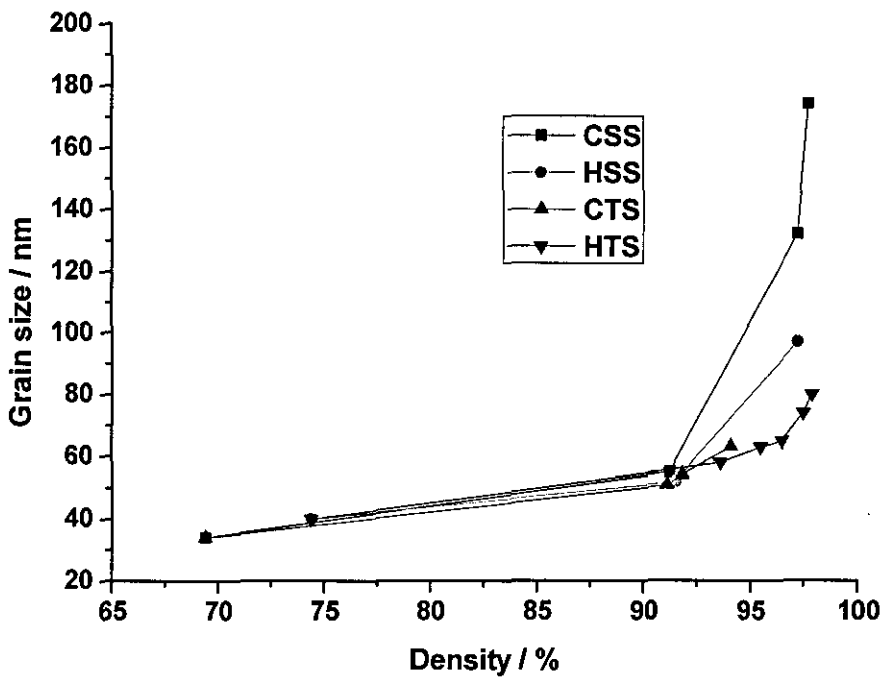

Figure 4-35 Variation in grain size with density for dry pressed 3YSZ samples. CSS-conventional single step, HSS- hybrid single step, CTS-conventional two-step and HTS-hybrid two-step.

It may be observed that the hybrid sintered samples resulted in reduced grain size for the same sintering temperatures, irrespective of whether it was single step sintering or two-step sintering. This is believed to be a combined effect of the increased heating rate and the reduced sintering time required to obtain the same density in a hybrid sintering cycle. Due to the volumetric nature of the hybrid heating, 20°C min^{-1} could be used without risking any damage to the sample from thermal stresses.[231,239,240]

All the hybrid heating results shown in Figure 4-35 were obtained after heating at a constant microwave power of 600 W. In order to find the effect of using different microwave power levels on density and grain size, slip cast samples were sintered at different microwave power levels using the same time-temperature profile (T_1 = 1150°C for 0.1 min and T_2 = 1050°C for 3 h). The variation in density and grain size with microwave power for the slip cast nano3YSZ samples are plotted in Figure 4-36.

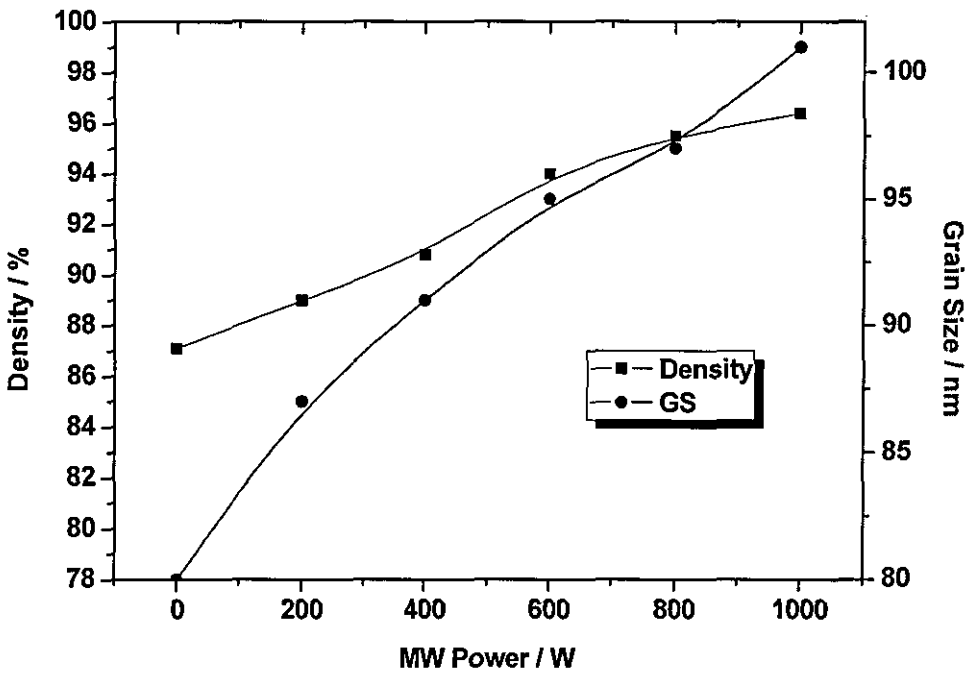

Figure 4-36 Variation in density and grain size with microwave power for slip cast samples of nano3YSZ.

Both parameters were found to increase with increasing microwave power, illustrating the effect of microwaves on sintering. Whilst there is some indication that the effect of the microwaves reduced above 600 W of microwave power; the grain size showed an approximately linear increase with microwave power, probably due to the increase in densification. Wroe and Rowley[223] also reported higher densities with microwave heating after the sintering of submicron zirconia pellets. They conducted pure conventional, hybrid and hybrid with microwaves switched on at high temperature - sintering runs and observed higher density when hybrid heating was used compared to conventional heating. Interestingly the densities obtained when microwaves were switched on in the later stages of sintering were similar to full hybrid runs. They attributed this difference to the different sintering mechanisms existing at lower and higher temperatures. At lower sintering temperatures, surface diffusion is the dominant mechanism whereas at higher temperatures volume diffusion and grain boundary diffusion control sintering. According to them, microwaves are more effective at higher temperature resulting in slightly higher density. Lorenz[224] also reported an increase in density and grain size with microwave power after sintering ZnO at different MW power levels.

The results of the conventional heating experiments are discussed below, with the results from the first stage of heating being compared first. The variation in density for the slip cast samples with different yttria content after the first stage of sintering are shown in Figure 4-37. The density was consistently higher for the lower yttria content bodies for the same temperature, indicating a difference in densification rate depending on the yttria content. This can be explained by the results reported by Matsui et al.[241] on the sintering of fine zirconia powders containing 3 and 8 mol% yttria. They observed that the shrinkage onset temperature for the 3YSZ was ~930°C compared to ~950°C for the 8YSZ samples; in addition the shrinkage rate of the latter was lower at any given temperature.

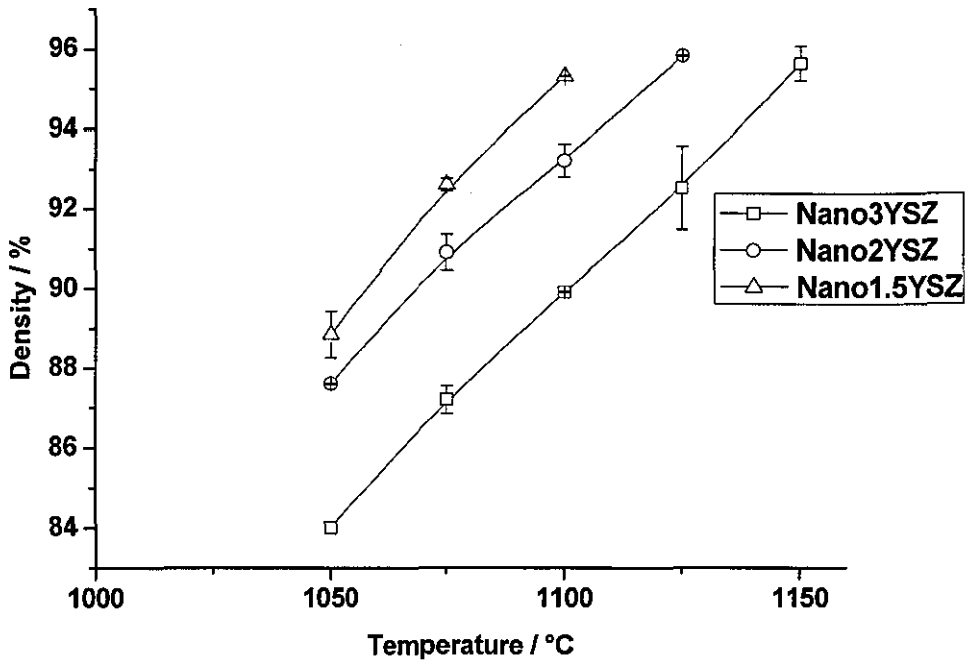

Figure 4-37 Variation in density with temperature after holding for 0.1 min at T_1 as a function of yttria content.

According to Matsui et al. the decrease in densification with increasing Y_2O_3 levels occurs because of an increasing activation energy for sintering during the initial stage of sintering. Luo et al.[242] also reported that higher firing temperatures are required for higher yttria concentrations after sintering zirconia with 3.0, 4.8, 5.7, 6.6, 7.5, 8.4, 10.2 and 12.0 mol% yttria.

The grain size showed a similar trend with yttria content as shown in Figure 4-38, though there was little difference between the nano1.5YSZ and nano2YSZ compositions.

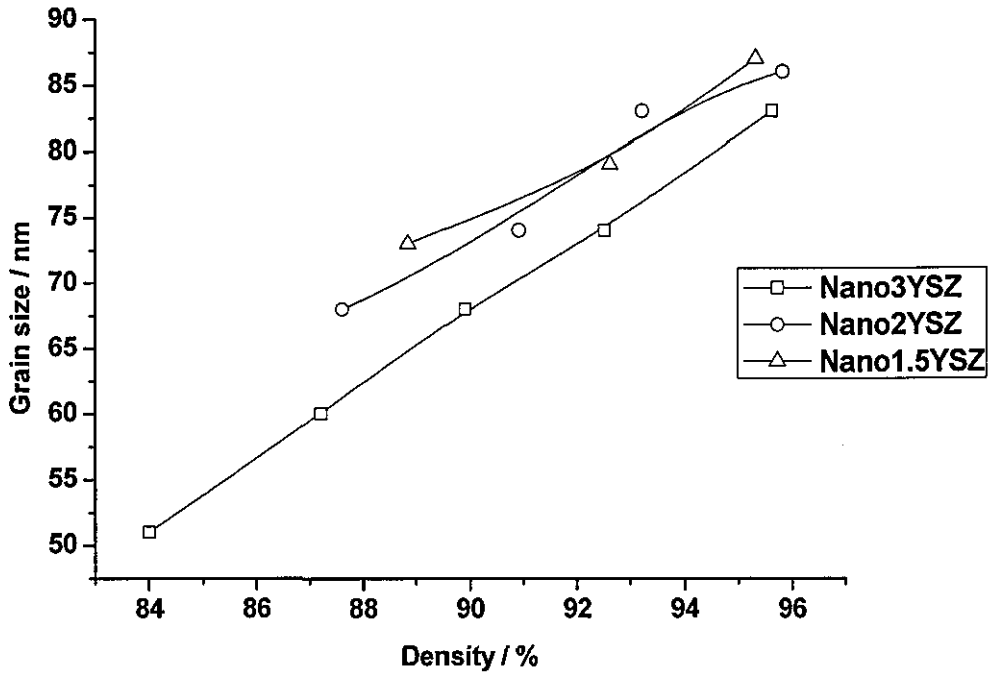

Figure 4-38 Variation in grain size with density after short term heating.

The density vs. grain size for the slip cast samples after conventional single and two-step sintering are summarised in Figure 4-39. The data for samples, where desintering was observed, are not included in these plots. Compared with the dry pressed samples with similar density, one major difference observed is the larger grain size for the slip cast samples, this is believed to be a result of the lower starting density for the slip cast samples. The latter means that increased sintering temperatures and time were required to reach equivalent densification leading to greater grain growth.

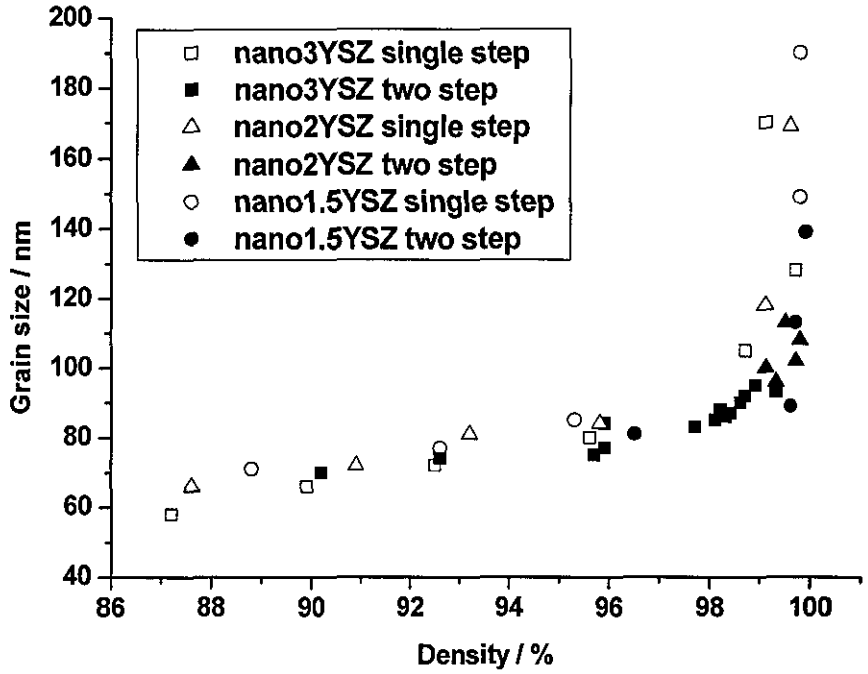

Figure 4-39 Variation in grain size with density for slip cast samples with different yttria content using conventional single and two-step sintering.

The optimum sintering conditions for the various samples using conventional single and two-step heating are summarised in Table 4-13.

Table 4-13 Optimum sintering conditions for the slip cast samples with different yttria content.

Sample	Sintering schedule	T_1 / °C	T_2 / °C	Time / h	Density / %theor.	Avg. gs / nm
Nano3YSZ	Single step	1100	-	10	99.7	128
Nano2YSZ		1100	-	10	99.6	149
Nano1.5YSZ		1100	-	10	99.8	169
Nano3YSZ	Two-step	1150	1050	10	99.4	95
Nano2YSZ		1125	1000	10	99.3	96
Nano1.5YSZ		1075	1000	10	99.6	89

Comparing the grain size after CSS and CTS sintering, it can be observed that there is grain growth during the second stage of sintering, but at a reduced rate. Similar results were reported by Mazaheri et al.[176] for the sintering of nanoZnO, and Bodisova et al.[180] for the sintering of alumina and the data is also consistent with the results reported from our group for the two-step sintering of ZrO_2.[231,239,240] So unlike the

results reported by Chen at al.,[169,170] the microstructure is not completely frozen during the second stage of sintering. But because of the lower sintering temperatures during the second stage, the sintering kinetics is very slow and hence the grain growth rate is also very low.

All the optimised two-step sintering cycles in the present study use temperatures much lower than those reported by Yu et al.,[178] for the two-step sintering of nanozirconia prepared by powder injection moulding. They have reported 1350°C for T_1 and 900°C for T_2 as optimum, but the density obtained was lower (<98%) and the grain size was higher.

A major difference in the sintering cycles between that reported by Chen et al.[169,170] for the sintering of Y_2O_3 and the optimum sintering cycles from the present work is the difference in the density required after the first stage of sintering to bring about complete densification. The goal of the first stage of two-step sintering is to produce a uniform pore microstructure while minimising grain growth. Different groups reported different intermediate density values after the first stage of sintering for different materials. Chen et al.[169,170] reported that a value of >75 % after first stage was sufficient for full densification of Y_2O_3. Values of 78%[176] and 80-90%[175] were reported for ZnO, 78%[173] and 89%[172] for $BaTiO_3$, >85% for SiC,[171] >90% for (1-x) $BiScO_3$-x$PbTiO_3$,[177] and >92% for Al_2O_3.[180] Of all these samples a final sintered density of >99.0 % has only been reported for Y_2O_3, SiC and ZnO whilst grain growth was reported for the latter two in the second stage. The lower final density could be due to the acceptance of a lower density after the first stage of sintering. In the present study, an intermediate density of ~95% was required for the nano2YSZ and nano3YSZ and ~92% density was required for the nano1.5YSZ to yield samples with >99% density. A small amount of grain growth was also observed during the second stage in line with the results reported for SiC,[171] ZnO[176] and Al_2O_3.[180]

The success of two-step sintering depends on the separation of grain boundary migration and grain boundary diffusion. The activation energy for the latter is lower than that of grain boundary migration, so by careful selection of T_2, grain boundary diffusion is kept active whilst grain boundary migration is prevented. According to Chen et al.,[170] the densification rate during the second stage of sintering can be

calculated using Herring's scaling law.[243,244] According to this equation the densification rate is given by

$$\frac{d\rho}{\rho\, dt} = F(\rho)\frac{3\gamma\Omega}{KT}\frac{\delta D}{G^4} \qquad \text{Eqn. (4.1)}$$

where

ρ	=	relative density
t	=	time
γ	=	surface energy
Ω	=	atomic volume
D	=	the grain boundary diffusivity
k	=	Boltzmann constant
T	=	the absolute temperature
G	=	the mean grain diameter
δ	=	the width of the grain boundary and
F (ρ)	=	an unspecified function of density ρ

During the second stage of sintering, the only parameter undergoing changes is the density, provided there is no grain growth. Hence during this stage F(ρ) changes with density and is the major factor deciding the densification rate. Typically, at $\rho > 0.7$, F(ρ) is a gradually decreasing function of ρ. This decrease in F(ρ) is assigned to an increase in diffusion distance at higher density.

If the sintering temperature is below the kinetic window during the second stage of sintering, densification will proceed for a while and then become exhausted. As an example, consider 3CTS 1100-1000-3 in the present study, the intermediate density was 89.9% after the first stage and the final density reached was only 95.7%. This exhaustion of densification is attributed to the exhaustion of grain boundary diffusion as the second step temperature was insufficient to provide the required energy.

In the present study, the grain size was found to increase slowly during the second stage of sintering. The isothermal grain growth behaviour can be described with kinetic growth equations of the general form

$$G^n - G_0^n = kt \qquad \text{Eqn. (4.2)}$$

where n is a constant characteristic for a given grain growth mechanism, G and G_0 the actual size and starting grain size for a certain grain growth stage respectively, k is a kinetic constant and t the time. This equation is true for two-step sintering also, as the second step sintering proceeds under isothermal conditions. Hence the grain size after the first stage of sintering, G_0, is a critical factor deciding the final grain size at the end of two-step sintering. G_0 should be kept as low as possible to prepare samples with a lower final grain size. Thus further grain size reduction can be achieved by increasing the green density. The increased green density will enable the first stage sintering to be carried out at lower temperatures leading to finer grain size.

4.7 Characterisation of sintered samples

The sintered samples were characterised using a variety of techniques. The density and FEGSEM images of the samples were already discussed above. The samples were also characterised using TEM, XRD, micro-Raman spectroscopy and the properties were evaluated. These results are discussed below.

4.7.1 TEM and HRTEM

A fully dense nano3YSZ sample was selected for TEM and HRTEM analysis. The TEM sample was prepared using focused ion beam milling.

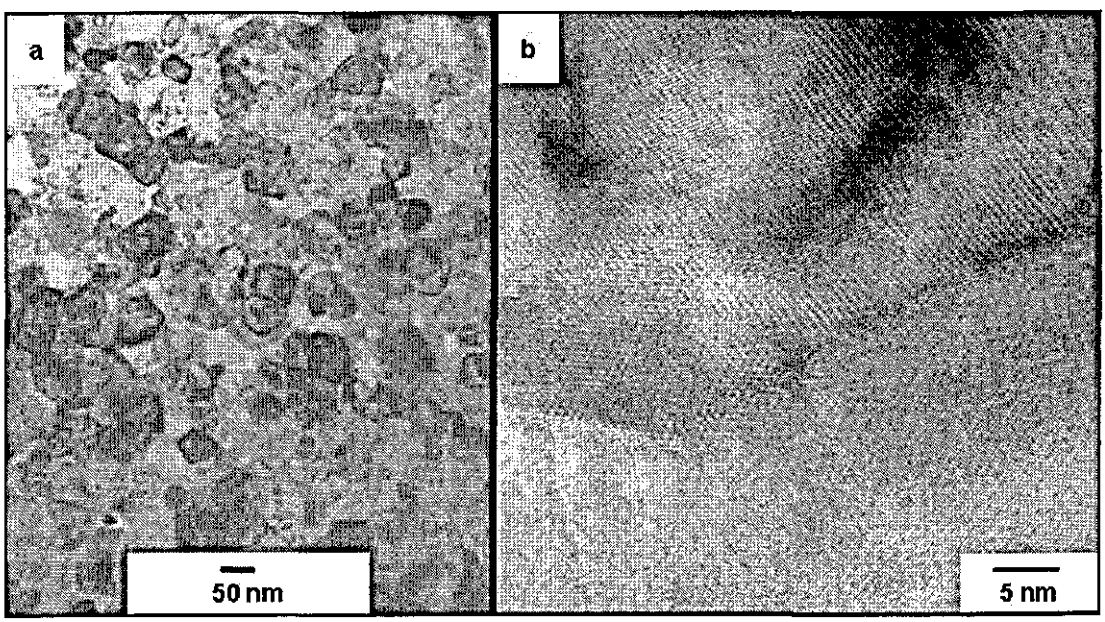

Figure 4-40 (a) TEM and (b) HRTEM images of a fully dense nano3YSZ sample.

From Figure 4-40 (a), it can be observed that the grains retained the nanostructure. No visible porosity was observed for the sample. From the HRTEM image it can be

observed that the individual grains are fused together and there were no defects or amorphous regions at the grain boundaries, indicating better densification. This is not always the case in the sintering of nanoceramics, as pointed out by Ragulya,[245] especially when pressure assisted processing techniques are used. In pressure assisted sintering, lattice adjustments in adjacent grains occur due to their shift or rotation, hence many grain boundaries represent a mechanical contact rather than a crystalline lattice and can contribute to strength reductions as shown in Figure 4-41. In pressureless sintering, as in the present situation, the grain boundaries are not forced together by just mechanical contact and hence will not degrade the properties.

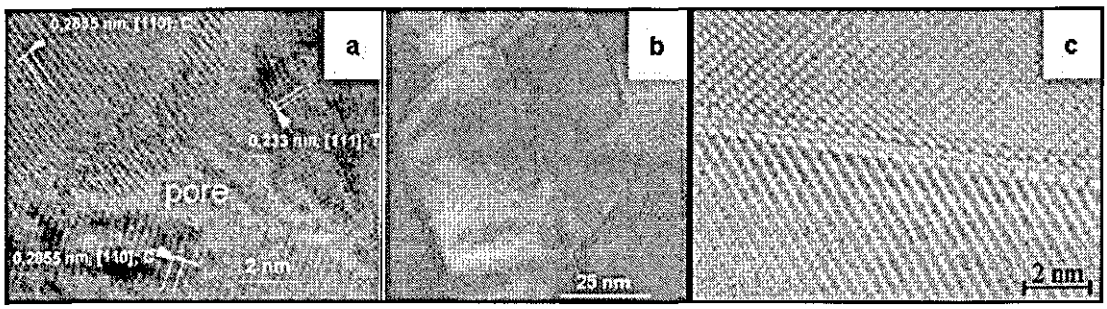

Figure 4-41 HRTEM images of nano $BaTiO_3$ ceramics sintered under high pressure (a) micropores (b) and (c) grain boundaries from Ragulya.[245]

4.7.2 XRD

The XRD pattern of the sintered nano1.5YSZ, nano2YSZ, nano3YSZ and benchmark samples are shown in Figure 4-42.

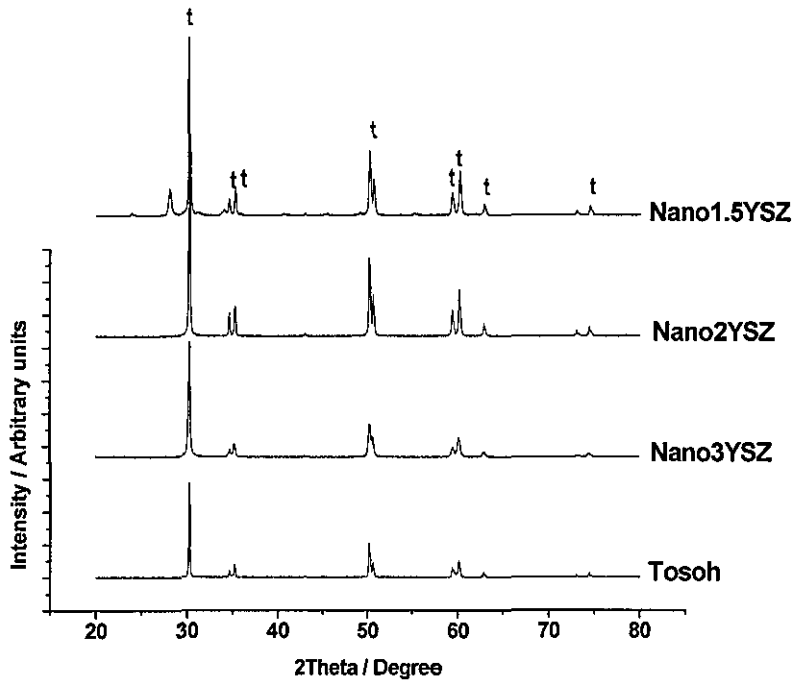

Figure 4-42 XRD patterns of the samples after sintering. nano1.5YSZ, nano2YSZ, nano3YSZ and Tosoh. t = tetragonal zirconia and all the unmarked peaks corresponds to monoclinic zirconia.

From the XRD patterns it can be observed that there is no monoclinic content present in nano2YSZ, nano3YSZ or Tosoh after sintering. Nano1.5YSZ contained 36.6 vol% monoclinic after sintering.

4.7.3 Micro-Raman spectroscopy

The micro-Raman spectra of the as-sintered samples are recorded in Figure 4-43 and Figure 4-44.

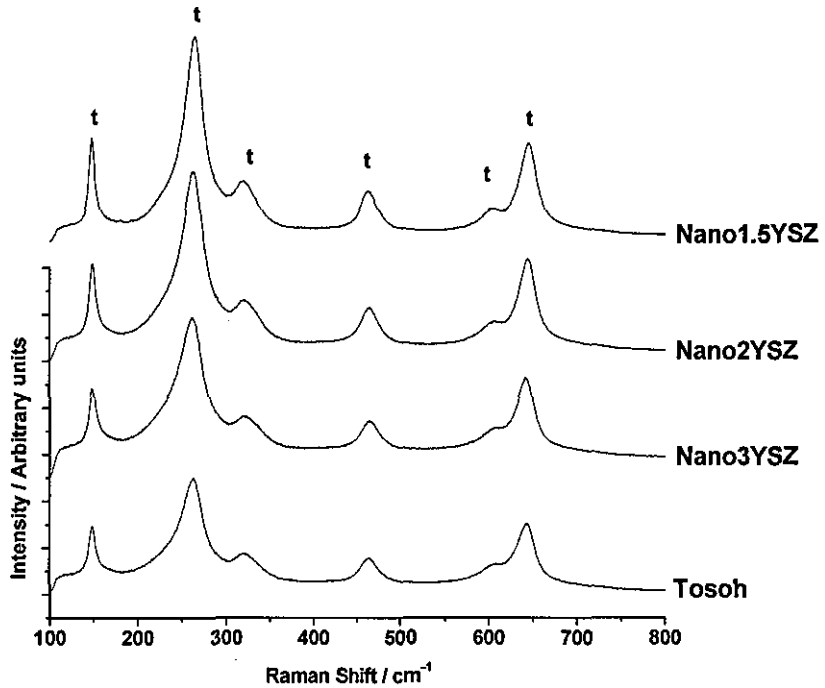

Figure 4-43 Micro-Raman spectra of the samples after sintering; nano1.5YSZ, nano2YSZ, nano3YSZ and the Tosoh benchmark.

All the peaks marked't' correspond to tetragonal zirconia and all the unmarked peaks corresponds to monoclinic zirconia. According to Keramidas et al.,[246] after factor-group analysis there are 18 Raman peaks corresponding to monoclinic zirconia and 6 peaks corresponding to tetragonal zirconia. The most important peaks corresponding to the tetragonal phase are those at 148 cm^{-1} and 264 cm^{-1} and those corresponding to monoclinic zirconia are at 181 cm^{-1} and 192 cm^{-1}. The peak at 476 cm^{-1} is common to both monoclinic and tetragonal.

The nano2YSZ, nano3YSZ and Tosoh benchmark samples show all the peaks corresponding to the tetragonal phase; whilst the peaks corresponding to the monoclinic phase in nano1.5YSZ are very small. From a comparison of the XRD with micro-Raman, it can be observed that XRD detected the presence of the monoclinic phase in nano1.5YSZ better than micro-Raman. In XRD the signal is collected from a thin layer on the surface of the specimen whereas in micro-Raman the laser beam can penetrate deeper into the sample. Fillit et al.[247] reported the detection of monoclinic zirconia up to a penetration depth of ~15 μm using CuKα radiation for an Al_2O_3+15% ZrO_2 material. The presence of monoclinic zirconia was reported on the surface for the as sintered and polished samples. According to Pezzotti and Porporati[248] the Raman penetration depth is dependent on the optics used and for 3YSZ it may vary

from

5 μm to ~40 μm depending on the laser power and the pinhole aperture, when used in the confocal configuration. Thus the Raman scattered signals are collected from a point well within the sample. The surface of the prepared zirconia samples are less constrained during sintering and subsequent sample preparation and hence there is a chance for the surface layer to transform to the monoclinic phase, especially for samples with low yttria content such as the 1.5YSZ from the present study. This could be the reason for the increase in intensity of the monoclinic peaks in XRD and the decrease in intensity of the monoclinic peaks in micro-Raman.

The micro-Raman spectrum of a 0YSZ sample is shown in Figure 4-44.

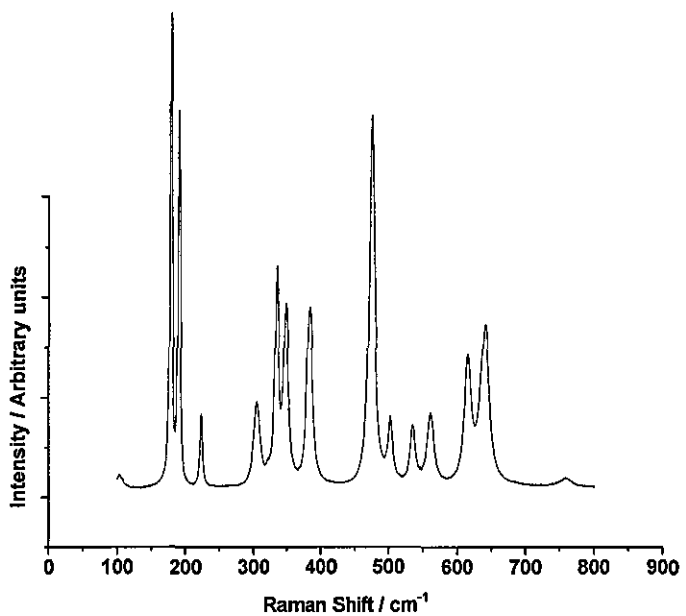

Figure 4-44 Micro-Raman spectrum of 0CSS 1100-10. All the peaks correspond to monoclinic zirconia.

0YSZ shows all the Raman peaks corresponding to monoclinic zirconia and no peaks corresponding to tetragonal zirconia. From the XRD pattern of the same sample it was found that it contains 12.1 vol% tetragonal phase. The absence of tetragonal peaks is because the Raman doublet at 181 cm^{-1} and 192 cm^{-1} for the monoclinic peaks are ~30 times stronger than the 264 cm^{-1} band for the tetragonal phase. This increase in intensity of the monoclinic peaks hides the tetragonal peaks.[249]

4.8 Hardness and toughness variation

The Vickers micro-indentation hardness was plotted against density for the various samples in Figure 4-45. Each data point is the average of at least 10 indents and all the indents were created by applying 1 kg (9.81 N) load.

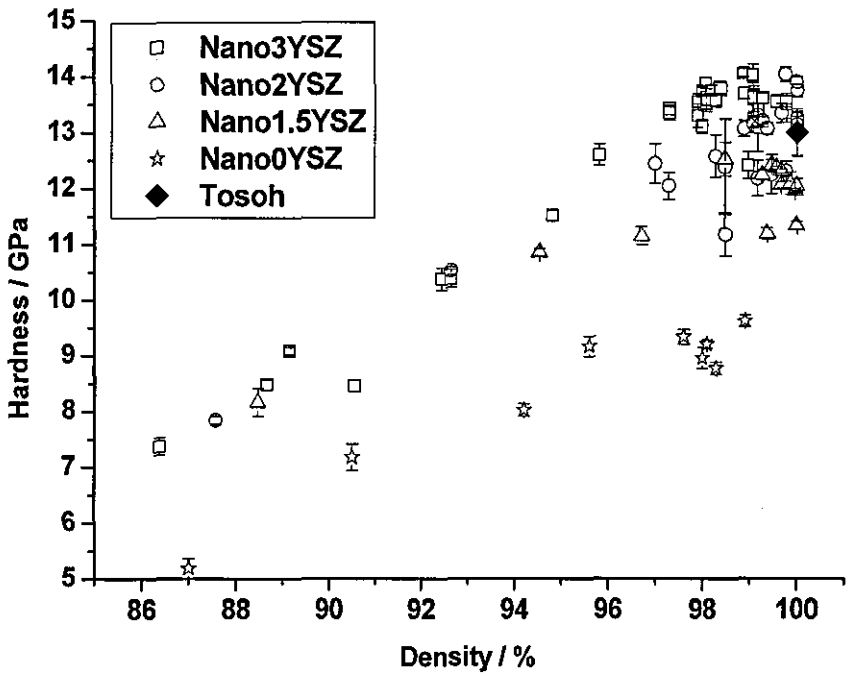

Figure 4-45 Variation in hardness with density.

The hardness increases with density almost linearly for each set of samples with a slight decrease in hardness observed very close to the maximum density. A linear increase in hardness with density has also been reported by Cottom and Mayo[75] for nano and submicron 3YSZ and by Bravo-Leon et al.,[77] for nano 0YSZ, 1YSZ and 1.5YSZ. Vasylkiv et al.[78] reported a slight decrease in hardness for nanozirconia samples when the density reached >99.5%. As the density increases the grain size also increases. Also, the transformability of the grains may increase with increase in grain size, due to the reason of easy nucleation of m zirconia near triple points or grain boundaries.[37,38] So when the samples with lager grain size are indented with the Vicker's indenter t-ZrO_2 grains tend to be easier to transform, and the material displays less resistance to the plastic deformation. This could be the reason for the slight decrease in hardness for samples with more than 98% density.

Comparing the hardness values of the samples with different yttria content, the maximum value of hardness was observed for the nano3YSZ sample (14.1 GPa) followed by nano2YSZ (14.0GPa) and nano1.5YSZ (12.5 GPa). A different trend in hardness has been reported in the literature for 1.5, 2.0 2.7 and 3.0 mol% yttria containing nanoceramics, with minimum hardness occurring for the 3.0 mol% nanoYSZ.[78] In contrast a higher hardness has been reported for a nano zirconia containing 1.5 mol% yttria compared to a sample with 1.0 mol% yttria,[77] similar to the trend observed in the present study. The hardness of nano0YSZ samples was much lower compared to all other samples and is similar to the values reported in literature for fully dense 100% monoclinic zirconia.[77]

Compared to the hardness of the benchmark Tosoh sample (13.0 GPa), both the nano3YSZ and nano2YSZ showed a higher hardness whilst the nano1.5YSZ showed a lower hardness. This is different from what was reported by Cottom and Mayo[75] for nano3YSZ and Tosoh samples. They reported similar hardness values for both ceramics with slightly higher hardness for the Tosoh sample. The maximum hardness values obtained for the nano3YSZ and nano1.5YSZ samples are higher than those reported in literature for zirconia ceramics[43] and nanozirconia ceramics[77,78] with similar yttria contents.

The variation in toughness with density is plotted in Figure 4-46 for the different zirconias. Note, however, that for samples showing similar densities, their grain sizes and pore sizes could have been quite different. In addition, whilst the majority of the toughness measurements were carried out using a 10 kg indentation load, for the nano1.5YSZ a 30 kg load had to be used to achieve indentation cracks. No correction was made to the measured toughness values for this variation in load used.

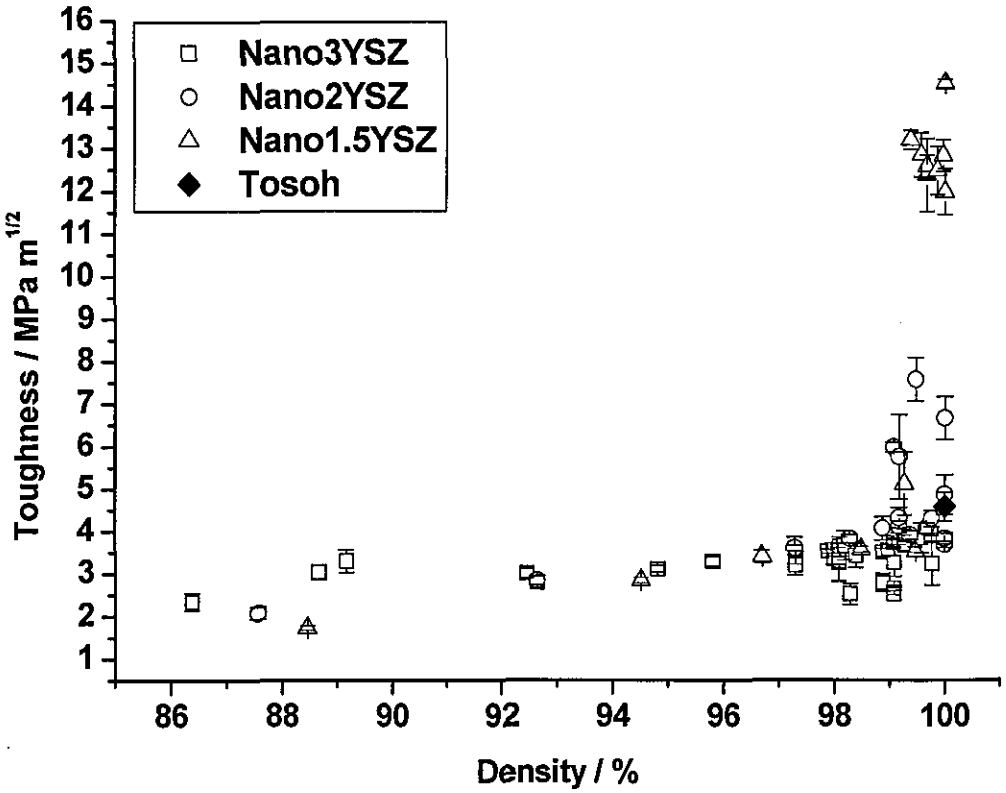

Figure 4-46 Variation in indentation toughness with density for different zirconias investigated.

From Figure 4-46 it can be seen how important it is to obtain a high density; there is no consistent difference in toughness below about 99% of theoretical density. Above this value it can be observed that whilst the toughness of the nano3YSZ sample is lower than that of the benchmark submicron ceramic, both the nano 2- and 1.5 YSZ are apparently significantly much tougher with the latter showing indentation toughness values up to nearly 15 MPa $m^{1/2}$. The toughness values of nano3YSZ from the present study are similar to the results reported in literature for nano and submicron 3YSZ samples.[75] The maximum toughness obtained for the nano0YSZ sample was 2.4 MPa $m^{1/2}$, similar to the values reported in literature.[77,90]

According to McMeeking et al.,[250] the toughness increment due to stress induced phase transformation can be expressed as

$$K_{Ic} = K^{m}_{Ic} + \eta\, Vf\, \Delta V\, E\, (h)^{1/2} / (1-\nu) \qquad \text{Eqn. (4.3)}$$

where K_{Ic} and K^{m}_{Ic} are the actual fracture toughness and the fracture toughness of the matrix without transformation toughening respectively, η is a constant, V_f is the

fraction of transformed tetragonal phase, ΔV is the volume expansion due to transformation, E is the Young's modulus, h is the half width of the transformation zone and v is the Poisson constant. The amount of transformable tetragonal phase is less for the nano3YSZ compared to the Tosoh sample and hence a lower toughness is observed. For the 0YSZ $K_{Ic} = K^{m}_{Ic}$ as $Vf \sim 0$. The value of Vf is minimum for nano3YSZ and maximum for nano1.5YSZ out of all other samples studied. Similarly as observed later from the micro-Raman spectroscopic results presented later, the size of the transformation zone is maximum for the nano1.5YSZ compared to all other samples contributing to increased toughness for these samples.

The variation in hardness with grain size for samples with at least 97.5 % density is plotted in Figure 4-47. It may be observed that there is a decrease in hardness with grain size. This decrease in hardness is due to the increased transformability of the grains with bigger grain size. Ghosh et al.[251] identified similar trends for 8YSZ samples and this effect was attributed to the better effectiveness of the grain boundary as an obstacle to plastic deformation when the grain size was finer. For the same grain size, nano1.5YSZ has always a lower hardness compared to nano2YSZ and nano3YSZ has the maximum hardness. The variation in hardness in the 80 – 160 nm range is very little however. The maximum hardness is observed for all three compositions in the 105-110 nm mean grain size range. A similar result has been reported for nano3YSZ with maximum hardness being at 112 nm; even though the absolute value of hardness was lower (11.7 GPa).

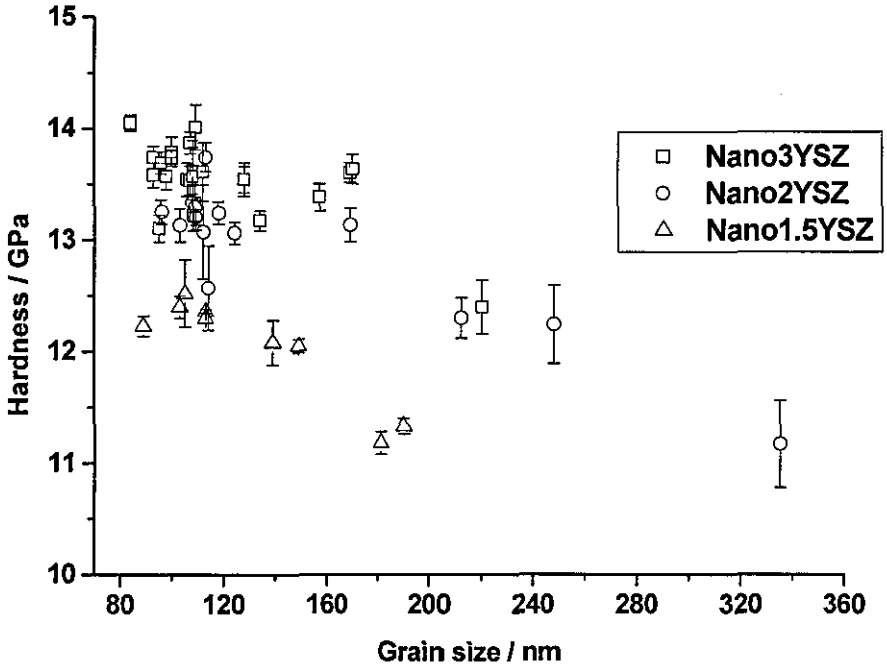

Figure 4-47 Variation in hardness with grain size for the different zirconias investigated.

The variation in indentation toughness, determined using the Anstis[86] formula, with grain size is plotted in Figure 4-48. The dependence of toughness on grain size was found to be minimal for the nano3YSZ, whilst it was very noticeable for the nano1.5YSZ. The maximum toughness obtained for the various samples with more than 99% density are summarised in Table 4-14, with the corresponding mean grain size and density values.

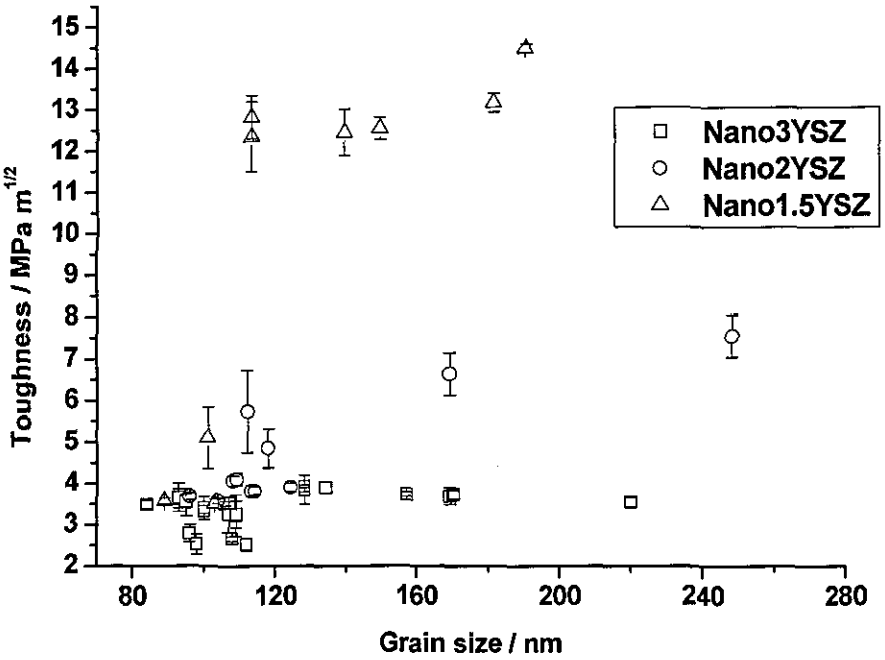

Figure 4-48 Variation in toughness with grain size for the various zirconias investigated.

The lowest toughness was observed for the nano3YSZ samples within the investigated grain size range and the maximum was obtained for the nano1.5YSZ samples. Wang et al.[84] reported similar results, with a decrease in toughness with increasing yttria content for fine grained zirconia ceramics.

Table 4-14 Maximum toughness values obtained for various compositions.

Sample	Toughness / MPa $m^{1/2}$	Avg. gs / nm	Density / %theor.
Nano1.5YSZ	14.50	190	99.9
Nano2YSZ	7.56	248	99.5
Nano3YSZ	3.92	128	99.8
Tosoh	4.57	520	99.8

The effect of grain size on strength and toughness of ceramics involving transformation toughening is very complex. The transformability of the zirconia increases with grain size, which in turn, will affect the strength and toughness. Also the grain size will decide the type of crack propagation, i.e. whether it is transgranular

or intergranular. Also as the grain size increases, the size of the Griffith flaw size increases (all other factors remaining the same), reducing the strength and toughness. For nanoceramics the development of porosity due to desintering is also a major factor determining the toughness at high densities. The transformability is also dependent on the yttria content, with the transformability decreasing with increasing yttria content. From Table 4-14 it can be observed that the toughness of the YSZ samples are highly dependent on the yttria content and the maximum toughness was obtained for nano1.5YSZ. This variation in toughness could be due to the different amounts of stress induced phase transformation taking place under indentation depending on the amount of stabiliser. This was investigated with the help of micro-Raman spectroscopy and is discussed in Section 4.9. The cracks developed on various samples after indentation are also shown in the same section.

Comparing the grain sizes of the samples that produced maximum toughness, nano2YSZ samples with higher toughness have got a larger grain size than the nano1.5YSZ with maximum toughness. This could be due to the higher amount of transformation taking place for the sample with higher stabiliser content at a higher grain size. But this is not true for the nano3YSZ sample as it showed its highest toughness at a lower grain size compared to the nano2YSZ and nano1.5YSZ. Hence it can be assumed that the optimum grain size for nano3YSZ to produce maximum toughness lies above the investigated grain size range in the present study. This is in line with the results previously reported in literature for 3YSZ. Cottom and Mayo[75] reported maximum toughness for a 3YSZ sample at a mean grain size >1 μm. Wang et al.[84] observed the highest toughness for a 3YSZ sample with a 1.4 μm mean grain size, which was larger than that of a 2.5YSZ sample where the maximum toughness was observed at 1.22 μm within their investigation range (0.6 μm to 2.0 μm). Note, however, that it is very difficult to produce fully dense 3YSZ samples with such grain sizes when utilising nanopowders because of desintering issues.

The crack propagation in the nano and submicron samples was studied using FEGSEM and found to be different. For the submicron sample, the crack propagation was trans-granular whilst for the nanosample it was inter-granular, as shown in Figure 4-49.

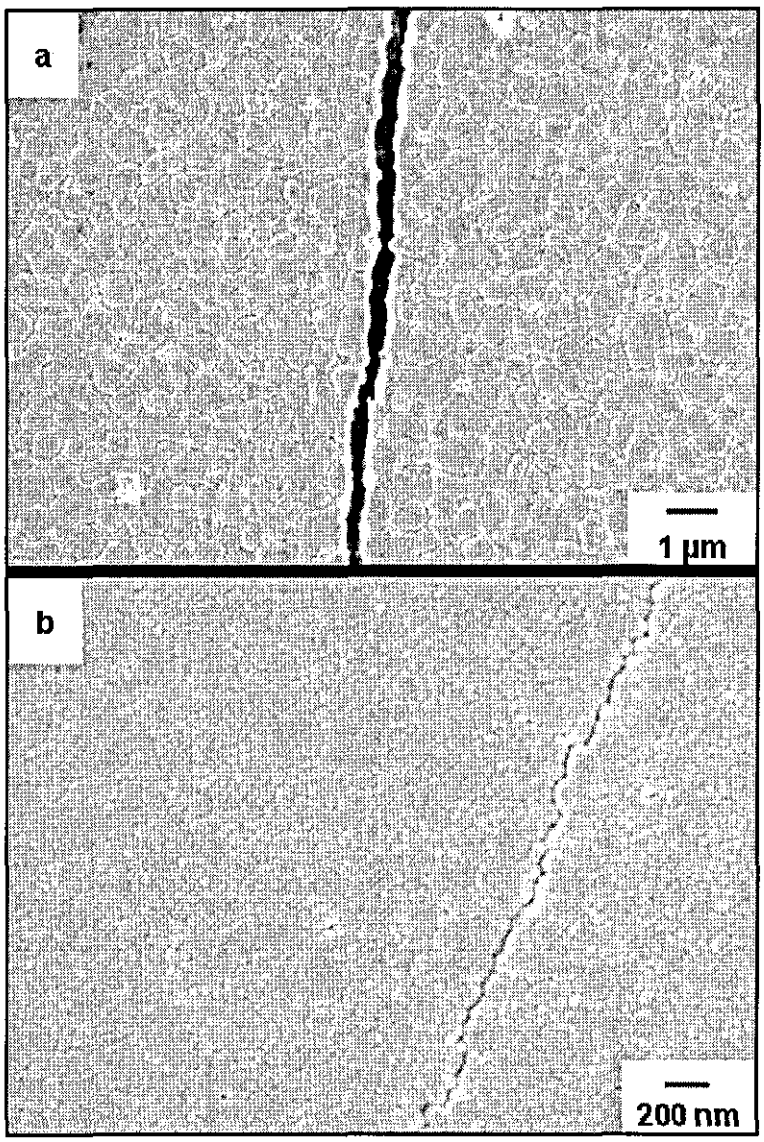

Figure 4-49 Crack propagation in submicron and nanosample, (a) transgranular crack propagation for the submicron sample and (b) intergranular crack propagation for the nano sample.

When the crack propagation was in the intergranular mode there will be crack deflections at the grain boundaries resulting in less stress concentration at the grains. This will reduce the amount of stress induced phase transformation and crack annihilation, resulting in reduced toughness values. The crack propagation is not always intergranular in the case of nanosamples, however. A non-uniform grain size distribution achieved early in the research resulted in transgranular fracture of the large grains, Figure 4-50.

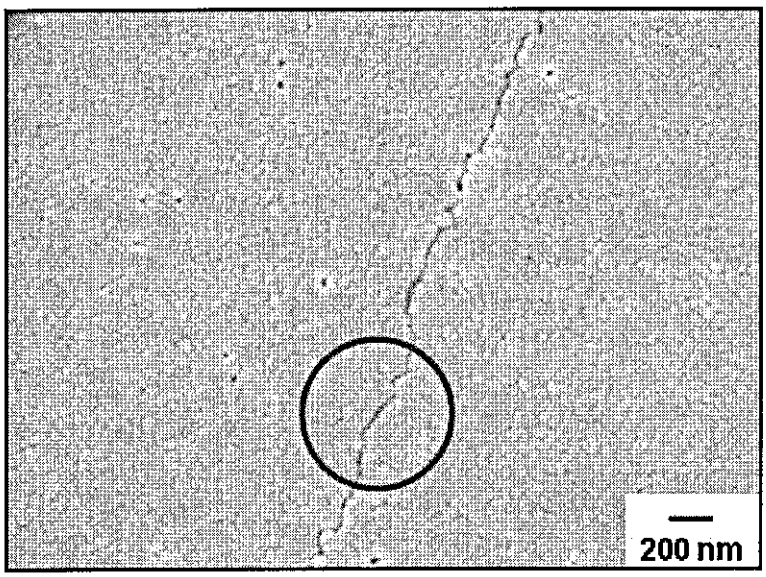

Figure 4-50 Image showing transgranular crack propagation for a nanozirconia sample with few larger grains.

4.9 Micro-Raman study of indentation induced phase transformation

Micro-Raman spectroscopy was used as an effective technique to study the spatial distribution of indentation induced phase transformations in nanozirconia with different yttria content. Raman spectra were recorded with spatial resolutions of ~1μm. The results were compared with those obtained from the benchmark Tosoh sample. It is possible to make quantitative phase calculations using micro-Raman,[252,253,254] but here it is used as a qualitative technique simply to indicate the extent of phase transformation. The idea behind this study was to investigate the grain size dependent overstabilisation of nanozirconia and the effect of grain size and crack propagation on the phase transformation for samples with different yttria content.

The 10 kg indents on the Tosoh sample and a nano1.5YSZ sample are shown in Figure 4-51. For the Tosoh sample it can be observed that cracks were propagated from all four corners of the indent. Similar cracks were formed on the nano0YSZ, nano2YSZ and nano3YSZ samples at 10 kg load even though the crack lengths were different. The behaviour of the nano1.5YSZ at the 10 kg load was found to be different from that of the other samples in that no cracks developed at this load.

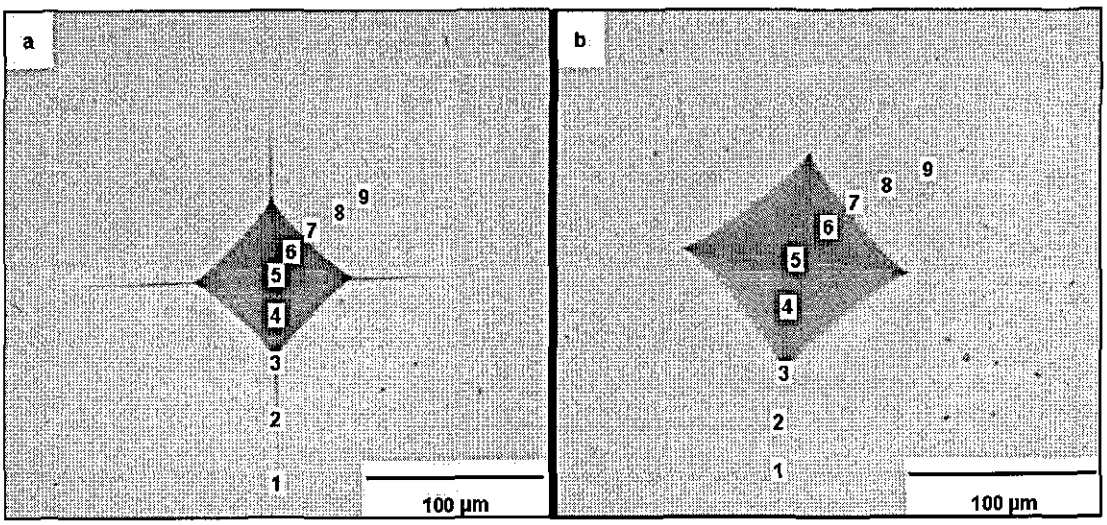

Figure 4-51 Optical microscopic image of the indent created on (a) Tosoh and (b) nano1.5YSZ at 10 kg load. The locations from where the micro-Raman spectra were taken are also highlighted. Note that no cracks were formed on the nano1.5YSZ sample at this load.

The micro-Raman spectra were recorded from the crack corner, half way through the crack, indent corner, indent edge and a number of other locations as indicated in Figure 4-51. The micro-Raman spectra of the Tosoh, nano0YSZ, nano3YSZ and nano0YSZ are shown in Figure 4-52. The distance between points 7, 8 and 9 are ~20 µm each.

All the peaks in the micro-Raman spectra of the nano0YSZ correspond to the monoclinic phase. From the XRD pattern of the same sample it was found that it contained 12.1 vol% tetragonal phase, however, as mentioned earlier, the absence of any tetragonal peaks is because the Raman doublet at 181 cm^{-1} and 192 cm^{-1} for the monoclinic peaks are ~30 times stronger than the 264 cm^{-1} peak for the tetragonal phase. This increase in intensity of the monoclinic peaks hides the tetragonal peaks.[249] Hence this technique cannot be used as a reliable tool to quantify the presence of tetragonal phases in monoclinic rich samples.

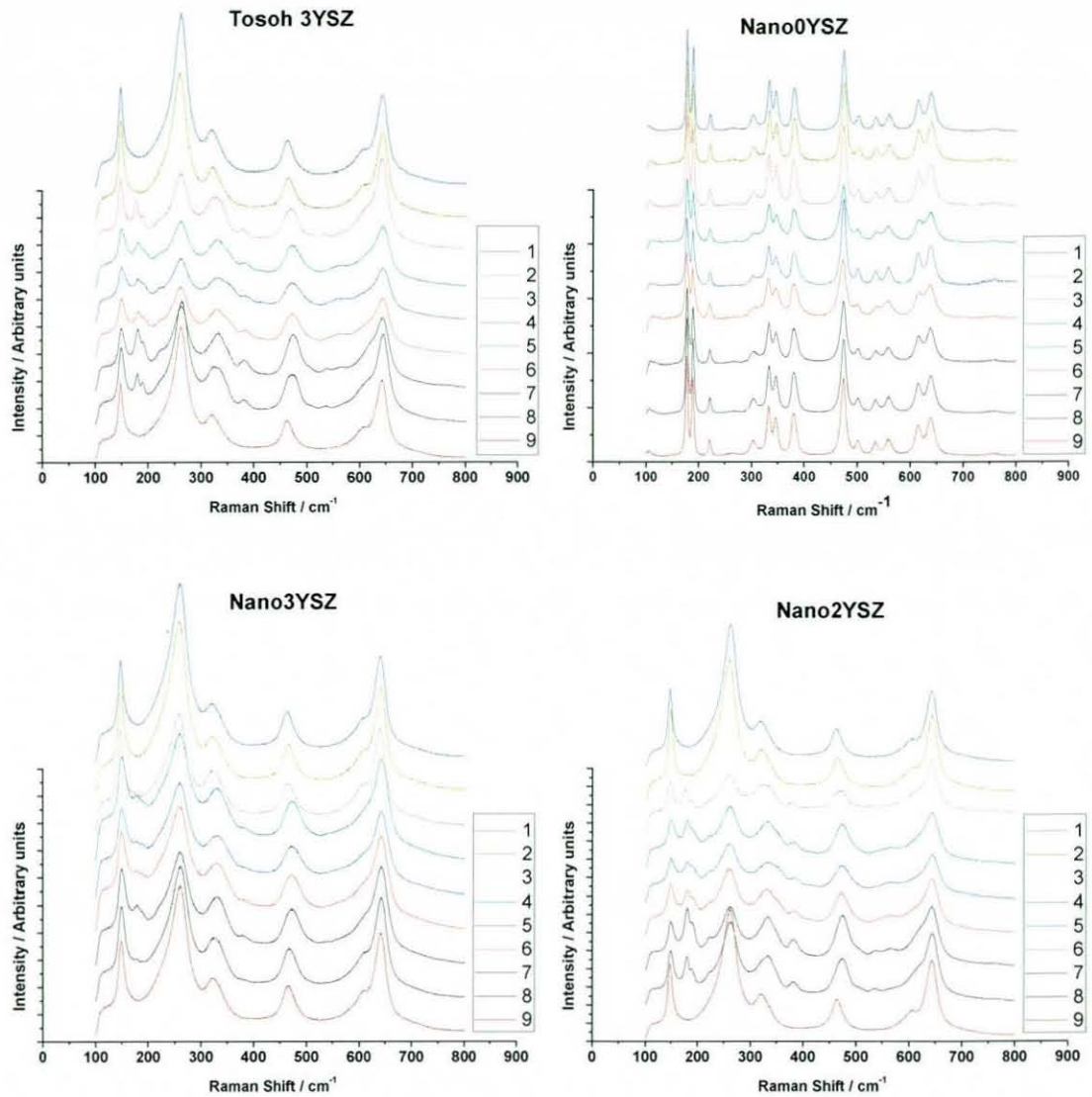

Figure 4-52 Micro-Raman spectra recorded from positions 1-9 for Tosoh, nano0YSZ, nano3YSZ and nano2YSZ samples. All the indents were created by applying 10 kg loads.

The absence of transformation for nano0YSZ resulted in very low toughness values for this material, as reported in Section 4.8. The micro-Raman spectra of the Tosoh sample mainly shows the peaks corresponding to tetragonal zirconia, but monoclinic peaks were also observed in locations 3 to 8. From the micro-Raman spectra of the benchmark Tosoh samples it can be observed that the maximum phase transformation has occurred at the indent corners and near the indent edges. The phase transformation at the crack tip and halfway through the crack were negligible and there was no monoclinic content away from the indent.

Comparing the micro-Raman spectra of the nano3YSZ with the submicron sample it is very clear that the intensity of the monoclinic peaks were much less for the nano3YSZ sample. This evidently shows that there is less transformation taking place in the case of the nano3YSZ sample and this difference is due to the variation in grain size as the yttria contents are the same for both the samples. The reduced transformation lowers the ability for crack suppression and causes less transformation toughening. Again the phase transformation was minimal at the crack tip and around the crack. This explains the lower toughness values obtained for nano3YSZ compared to Tosoh.

In the case of the nano2YSZ, more phase transformation occurred compared to the nano3YSZ and the monoclinic peak intensities were similar to those of the submicron zirconia, Figure 4-52. This resulted in better crack propagation resistance for the nano2YSZ compared to the nano3YSZ because of the presence of an increased amount of transformable tetragonal phase. This is believed to be the reason for the increased toughness of nano2YSZ compared to the nano3YSZ and Tosoh. Again no monoclinic content was observed at locations away from the indent.

From Figure 4-51 (b) it was observed that the nano1.5YSZ was not showing any cracks at the 10 kg load and hence the indentation load was increased to 20 kg. No cracks were generated here either and hence the load was increased further to 30 kg when cracks were developed at the indent corners, though they were very small in comparison to samples with other yttria contents, Figure 4-53. This image was recorded using the optical microscope with differential interference contrast to highlight the stress patterns. As reported by Kaliszewski et al.,[82] the indentation induced martensitic transformation occurs in a localised zone around the indentation, giving rise to stress fields in the surrounding material resulting from volume misfit. The slightly projected lines surrounding the indentation area are thought to be the lines of maximum shear stress. As they are visible even after the removal of the indenter, it can be assumed that the indentation induced deformation is accommodated by a permanent, non-elastic mechanism. Bravo-Leon et al.[77] also reported similar indentation behaviour for their nano1.5YSZ.

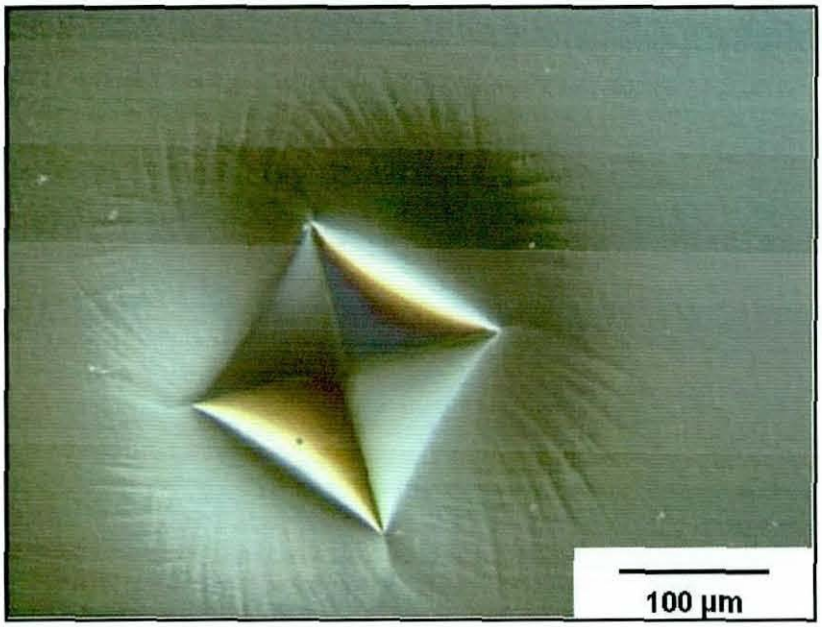

Figure 4-53 Differential interference contrast (DIC) microscopic image of an indent on the nano1.5YSZ sample. The indentation load was 30 kg.

Micro-Raman spectra were recorded for the nano1.5YSZ sample indented at different loads and the spectra for the 10 and 30 kg loads are shown in Figure 4-54.

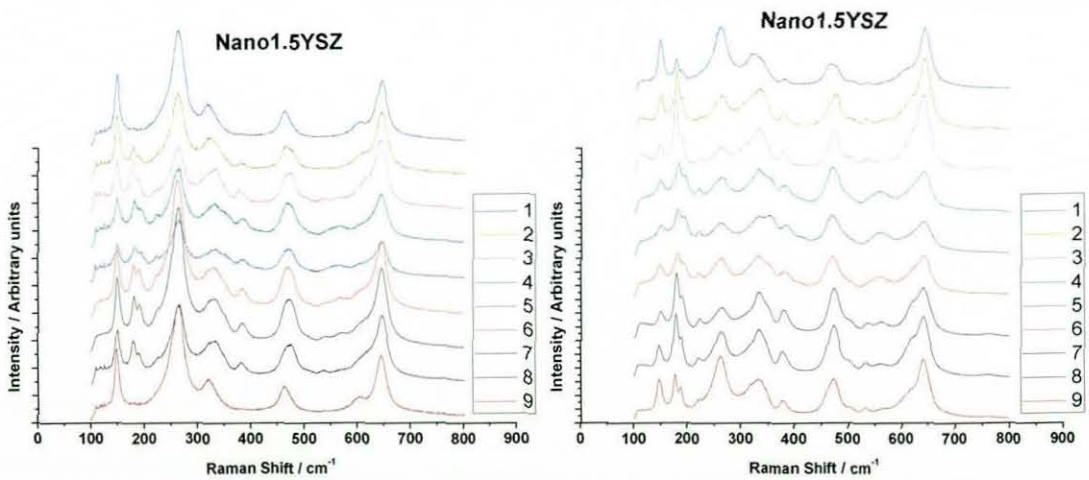

Figure 4-54 Micro-Raman spectra of the nano1.5YSZ sample after indentation (left) 10 kg load and (right) 30 kg load.

From the micro-Raman spectra of the nano1.5YSZ at 10 kg load, it can be observed that the intensities of the monoclinic peaks were higher than those of all other yttria containing samples reported before, at the same load, indicating a higher amount of phase transformation. This increased phase transformation prevented the generation of

any visible cracks at this load. The amount of transformation was found to increase with indentation load.

Considering the micro-Raman spectra obtained for the nano1.5YSZ at the 30 kg load, it was observed that there was at least some monoclinic phase at all 9 points in and around the indent as all the spectra were located within the indentation stress zone. The same result was observed for the 20 kg load even though cracks did not form. This clearly illustrated the increased phase transformation that occurred with increased loads and an increase in the size of the transformation zone. Once the volume changes due to phase transformation were not enough to contain the stresses due to the applied load, cracks propagated from the indent corners, where the stress concentration was a maximum. As long as the applied stresses are below the limit the phase transformation can accommodate, there will be no cracking. As the crack propagates, there will be more transformation along the crack tip which prevents further crack propagation.

In order to map the phase transformations around the indent, the nano1.5YSZ sample with 30 kg indent was mapped, Figure 4-55. The image represents the monoclinic (181,192) / tetragonal (264) intensity ratio; areas rich in monoclinic phase are indicated by the green colour.

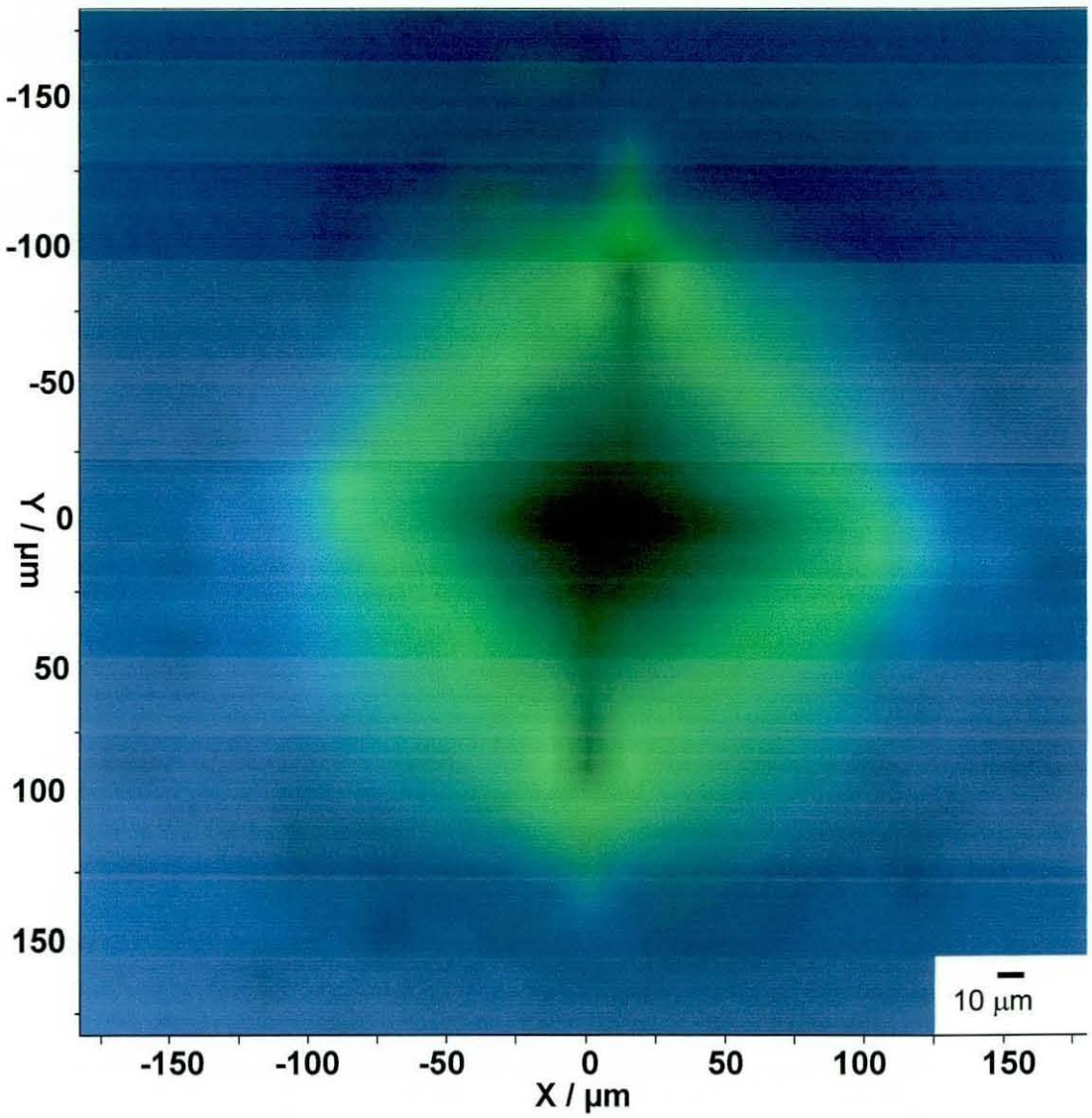

Figure 4-55 Micro-Raman mapping of the indentation induced phase transformation for a nano1.5YSZ sample. The indent was generated with 30 kg applied load. Green colour represents the presence of monoclinic phase.

From Figure 4-55 it can be observed that there is a considerable amount of phase transformation in and around the indent. The presence of monoclinic phase close to the propagating cracks is also distinguishable. Thus micro-Raman spectroscopy is a very powerful tool to study the area specific phase information, which other techniques such as XRD cannot accomplish. The resolution obtained is also high.

The amount of phase transformation observed for the various samples are reflected in their indentation toughness values also. The samples with no transformation (nano0YSZ) showed minimum toughness, because of the absence of any toughening

mechanism. The toughness of the other samples increased in proportion to the amount of transformation undergone by the samples with nano1.5YSZ showing maximum transformation and hence maximum indentation toughness. The increase in toughness observed for the nano1.5YSZ sample is not associated with an increase in the indentation crack length and hence it can be assumed that the increase in toughness is not an artefact due to R-curve behaviour, but is a genuine property of these classes of materials because of their increased transformability at the specific grain size.

4.10 Flexural strength and fracture toughness results from NPL

The average strength and toughness of the representative zirconia samples determined at NPL using standard test methods are summarised in Table 4-15.

Table 4-15 4-point bend strength and SCF toughness of selected ceramics measured at NPL

Sample code	Flexural strength / MPa	Toughness / MPa $m^{1/2}$
Tosoh	1040 ± 257	5.2 ± 0.6
Nano1.5YSZ	1088 ± 153	4.8 ± 0.3
Nano3YSZ	922 ± 155	5.3 ± 0.3

The flexural strength values are the average of 10 samples. From Table 4-15, comparing the strength values of the nano samples with differing yttria content, it can be observed that the strength of the nano1.5YSZ is higher than that of the nano3YSZ and benchmark commercial submicron 3YSZ, though the scatter is very high for all the samples. This is an interesting result that highlights the potential for nanozirconia ceramics. The strength of the nano3YSZ was found to be slightly lower than that of the submicron 3YSZ.

The flexural strengths of the samples were plotted against their probability of failure at different loads as shown in Figure 4-56. As seen from the plot nano1.5YSZ has shown minimum probability of failure at high loads up to 1200 MPa, though it should be noted that only 10 samples were measured for each grade; 20 is usually considered the minimum for this type of analysis.

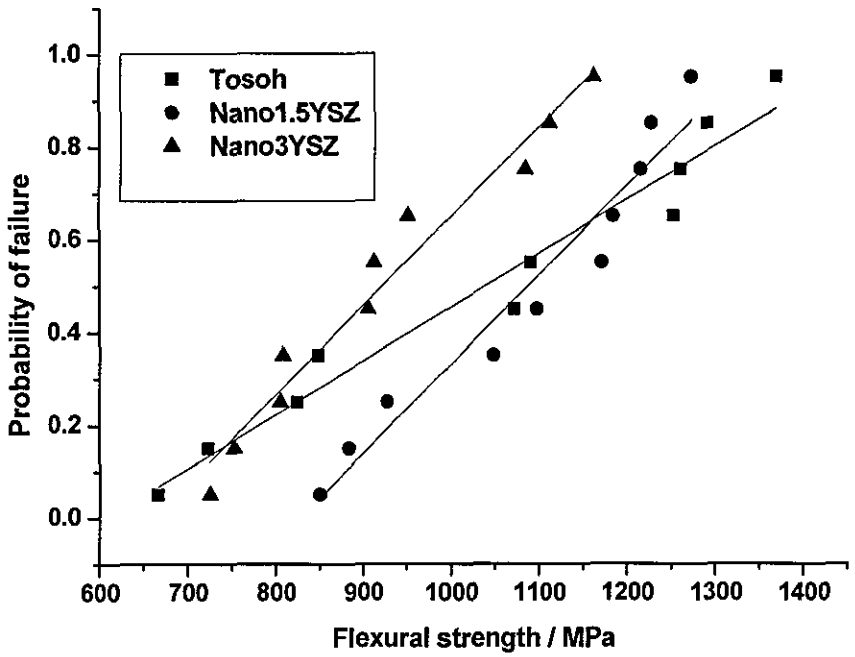

Figure 4-56 Flexural strength vs. probability of failure for the various zirconia samples.

The fracture surface of the samples were characterised using FEGSEM. The fracture mode was found to be intergranular for the nanosamples whereas it was transgranular for the submicron sample, as shown in Figure 4-57.

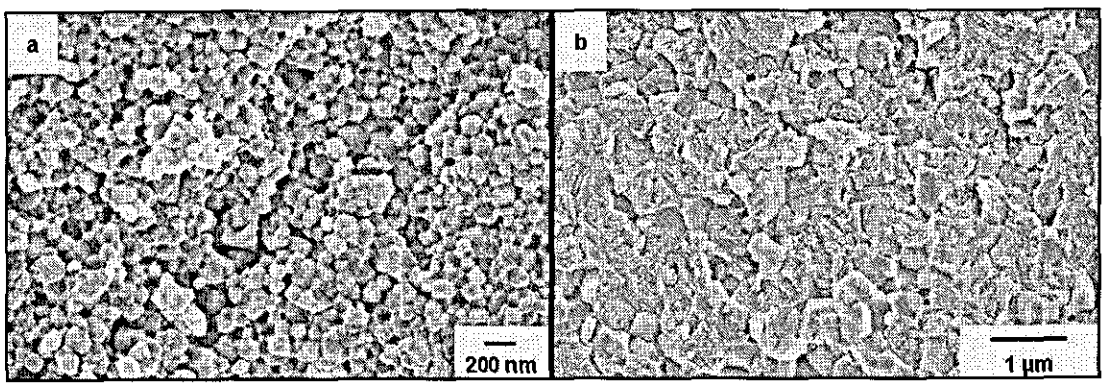

Figure 4-57 Fracture surface of samples after strength measurement (a) Nano1.5YSZ showing intergranular fracture and (b) Tosoh showing transgranular fracture.

From the fracture origin analysis, it was found that the nano samples that displayed minimum strength values failed from surface connected or near-surface defects, as shown in Figure 4-58. These defects were thought to arise from processing. This

suggests that the strength of the nanozirconia can be improved further by improving the processing and hence eliminating the defects.

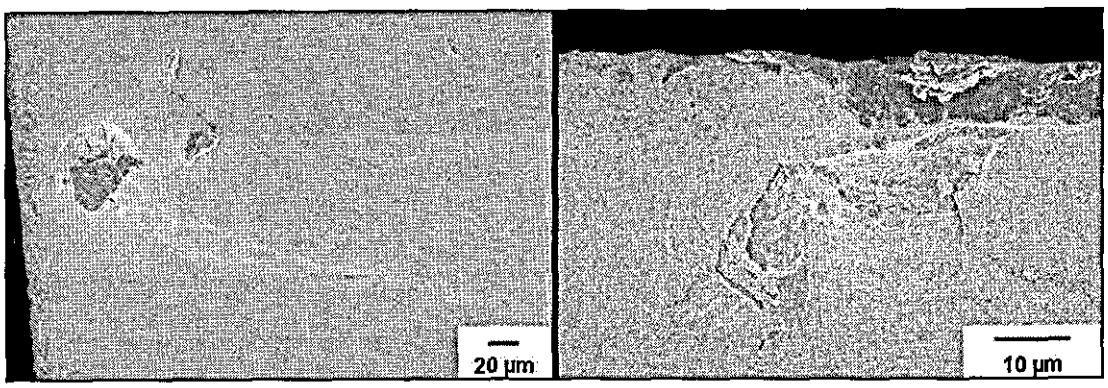

Figure 4-58 Processing-related defects observed in two nanozirconia ceramics which showed low strength values.

The flexural strength is also expected to be related to the amount of phase transformation undergone during testing and this was evaluated with micro-Raman spectroscopy on the fracture surfaces as shown in Figure 4-59.

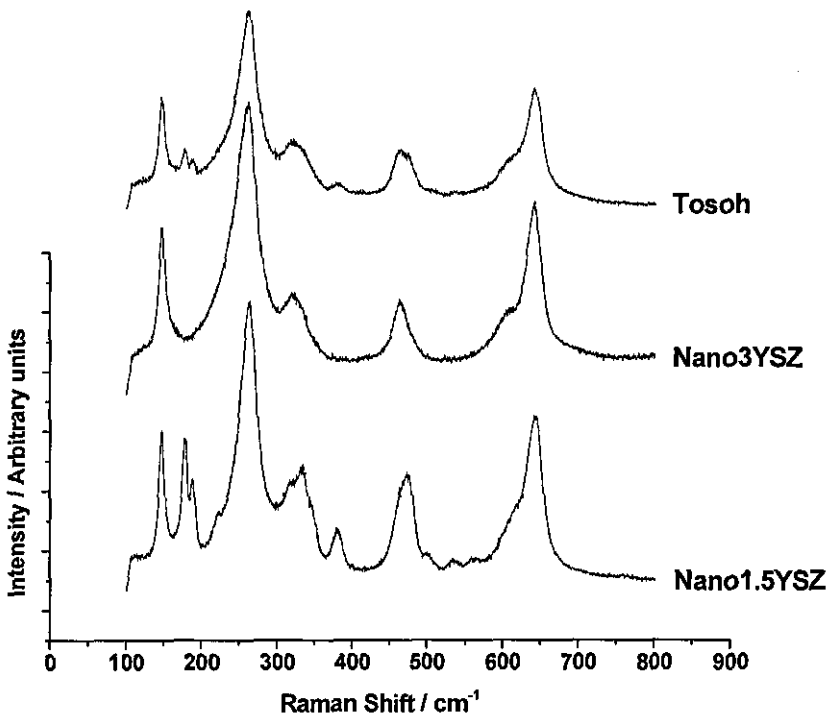

Figure 4-59 Micro-Raman spectrum on the fracture surfaces after strength measurement.

A considerable amount of t-m phase transformation was observed for the nano1.5YSZ sample and the benchmark Tosoh whereas no detectable phase transformation was observed for the nano3YSZ sample after micro-Raman spectroscopy. This trend in the amount of phase transformation was reflected in the strength values also with the nano1.5YSZ showing the highest average strength whilst the nano3YSZ showing the lowest value. According to Swain,[255] if the toughness of the material is below about 8 MPa $m^{1/2}$, the strength is flaw size limited, whilst above this value it is transformation limited. This means that the transformation stress is lower than the fracture stress so that transformation occurs preferentially and carries on until no more t-phase is available for transformation, in which event the material becomes flaw size limited again. The indentation toughness of the nano1.5YSZ samples used for strength measurements was well above 8 MPa $m^{1/2}$ and a considerable amount of transformation has been observed in the micro-Raman spectroscopy study. So if Swain is correct, it can be concluded that phase transformation contributed significantly to the strength values of the nano1.5YSZ. Hence by careful control of the yttria content and grain size, the strength of the YSZ ceramics can be maximised by optimising the transformability.

The fracture toughness of the ceramics was measured using the surface crack in flexure technique and the results obtained are also given in Table 4-15. The indents on the samples were created using a standard Vickers diamond indenter at 40 kg load after canting the sample by 5° and tilting the sample by 2°. The indent generated on one of the test specimens is shown below.

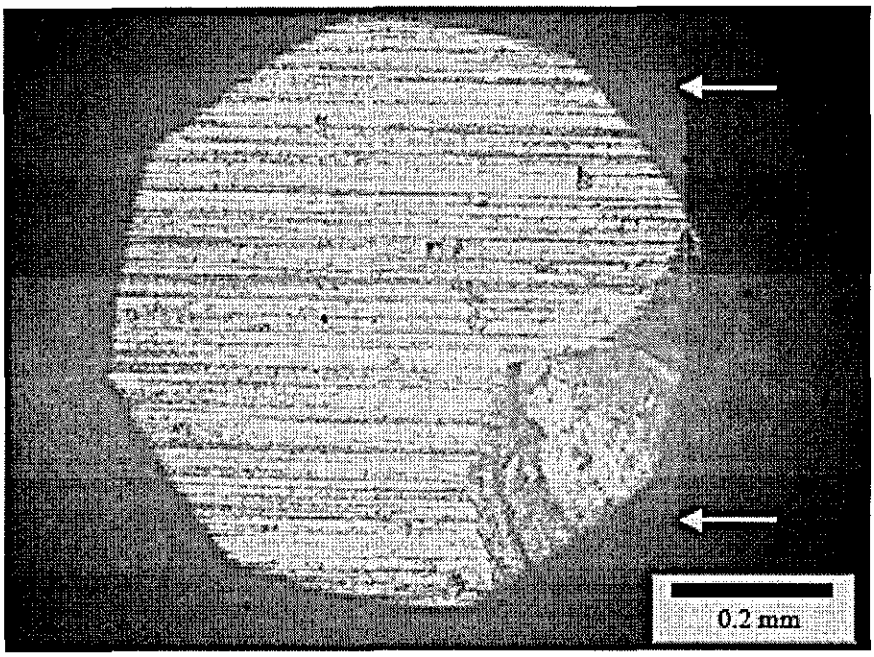

Figure 4-60 Canted HV40 indentation in one of the flexural strength specimens viewed in scattered illumination outside the aperture region, showing asymmetric surface cracks. 'Uphill' side to the top. Arrows indicate the ends of the crack.

Figure 4-61 shows an example from the nano1.5YSZ sample before and after removal of indentation damage.

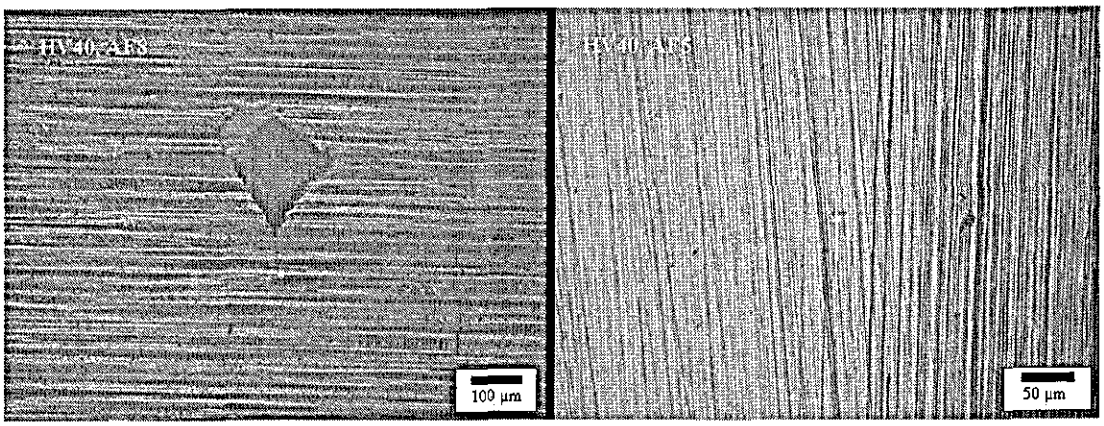

Figure 4-61 (Left) HV 40 indentation in nano1.5YSZ sample canted by 5°, the 'uphill' side being to the bottom of the image, (right) remaining pre-crack after removal of an HV40 canted indentation in another nano1.5YSZ test piece.

From the toughness values in Table 4-15, it can be observed that the toughnesses of the Tosoh and nano3YSZ samples are very similar and the toughness of the nano1.5YSZ sample is slightly lower. These values are also not in agreement with the indentation toughness values reported in Section 4.8.

The fracture surfaces of the various samples were analysed by NPL as shown in Figure 4-62, Figure 4-63 and Figure 4-64. The fracture toughness measurements were highly complicated because of the wide differences in crack formation of the samples.

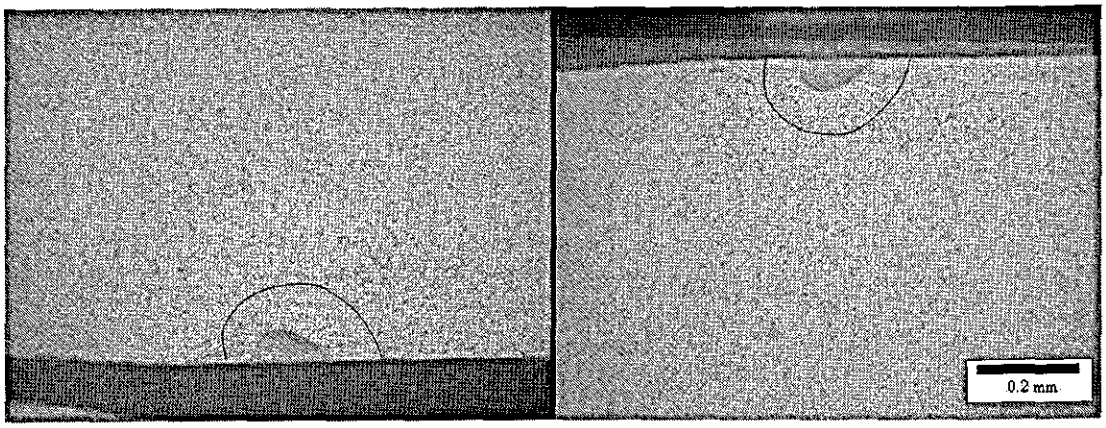

Figure 4-62 Matched fracture surface of a Tosoh test-piece showing pre-crack (dark region) and suspected subcritical growth zone (solid line).

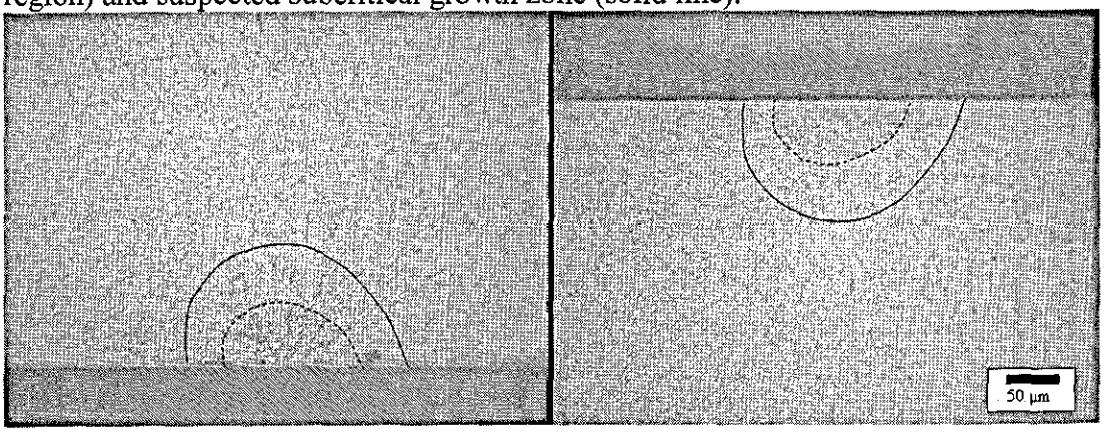

Figure 4-63 Matched fracture surface of a nano1.5YSZ test-piece showing pre-crack (dashed line) and suspected subcritical growth zone (solid line).

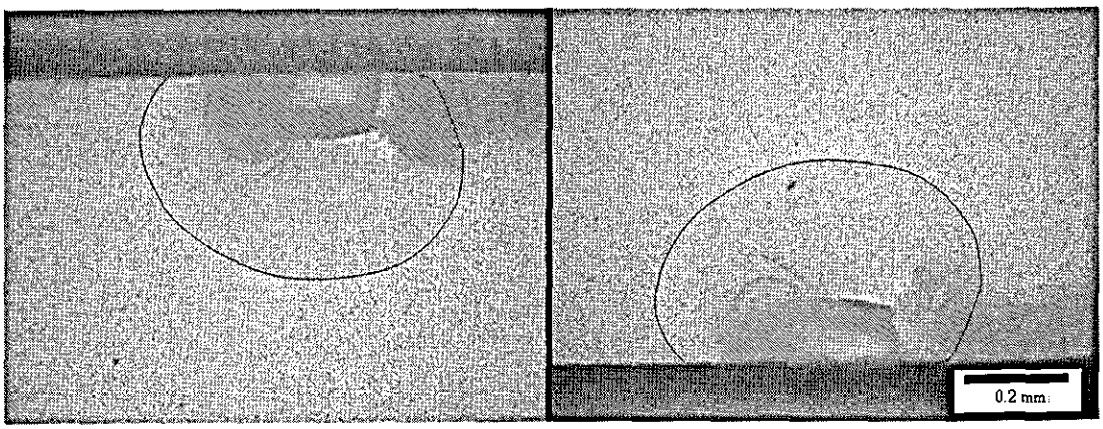

Figure 4-64 Matched fracture surface of a nano3YSZ test-piece showing a very clear subcritical growth zone (solid line), but a damaged unmeasurable pre-crack (dark region).

Comparing the fracture surfaces of the three different types of samples it can be observed that the pre-crack is not very well defined in the case of the nano1.5YSZ sample whereas they are for the benchmark sample. The size of the pre-crack is also very small for the nano1.5YSZ, indicating a better resistance to damage due to indentation. The subcritical crack growth boundaries were not that clearly defined especially for the nano1.5YSZ and benchmark, and hence led to a certain degree of uncertainty in the results. Fracture origins were principally internal defects in the materials.

Comparing the indentation toughness values with the SCF toughness values, it can be observed that there is a large difference in toughness for the nano1.5YSZ determined by the two different techniques, whilst the difference for the benchmark Tosoh and nano3YSZ were much smaller. The results obtained using the two methods are not directly comparable. As the radial crack is too short for the nano1.5YSZ compared to all other samples, it is not possible to convincingly define the indentation fracture mode; and is, therefore, difficult to make any sensible direct comparison of the Kic measured for nano1.5YSZ with those for other samples. Equally, SCF method might have had only a short crack propagation before catastrophic fracture due to the chosen testing condition, i.e. small sample size and small initial crack size. This could have resulted in measuring Kic values before reaching the plateau of the curve of cracking resistance vs the crack propagation, i.e. the R-curve. Based on the micro-Raman spectra on the fracture surfaces, the nano1.5YSZ has a much larger stress-induced transformation zone in the wake of propagating crack, compared to the other YSZs. This means nano1.5YSZ requires a longer crack propagation before the Kic reach the plateau value. Therefore, among all the samples analysed, the Kic for nano1.5YSZ is very likely underestimated by SCF method; the values for other YSZs are likely much closer to the real value, because shorter crack propagation is need to reach the plateau of the R-curve due to much smaller transformation zone in the wake of propagating crack. Therefore, further characterisation of the Kic is needed, particularly for nanosized 1.5YSZ.

The samples after the SCF toughness measurements were also analysed using micro-Raman spectroscopy. Raman spectra were recorded from three different locations

from the fracture surface; one from the pre-crack zone, one from the suspected subcritical crack growth zone and a third region, far enough away from the pre-crack and subcritical crack growth zone to be looking at the straight fracture surface.

The micro-Raman spectra taken from three different locations on the nano1.5YSZ sample are shown in Figure 4-65. Comparing the ratio of the intensities of the monoclinic to tetragonal peaks, Im(181) / It(264), it can be observed that the transformation is greatest in the pre-crack zone, slightly less in the subcritical crack growth zone and is lowest at the location far from the crack zone as expected. Micro-Raman spectroscopy detected very little transformation for the benchmark 3YSZ as shown in Figure 4-66, and no transformation was detected for the nano3YSZ, Figure 4-67.

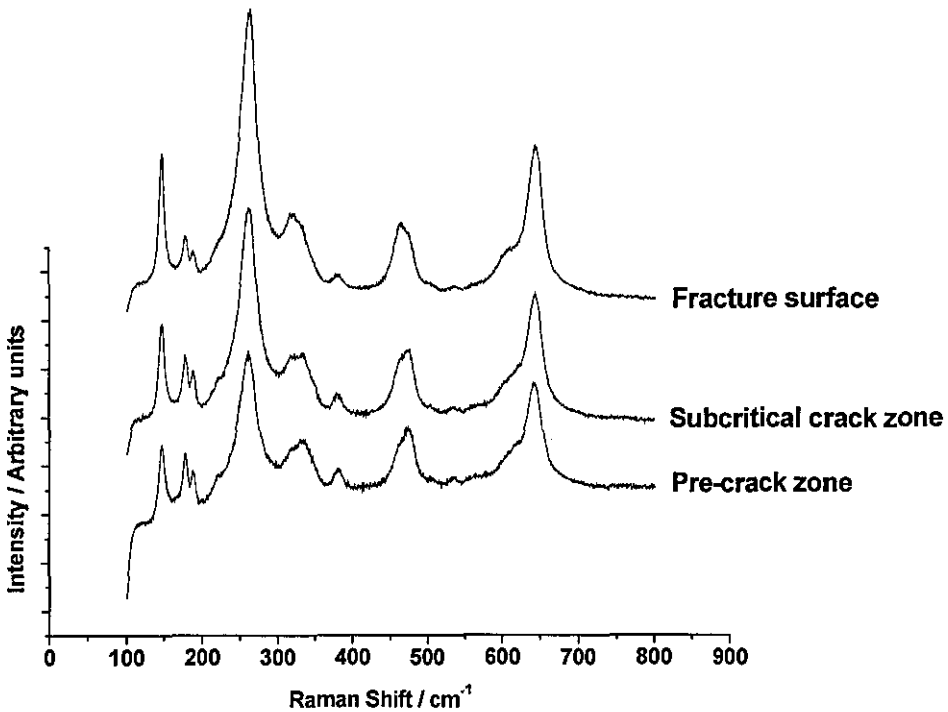

Figure 4-65 Micro-Raman spectra recorded from three different regions of the fracture surface of the nano1.5YSZ sample.

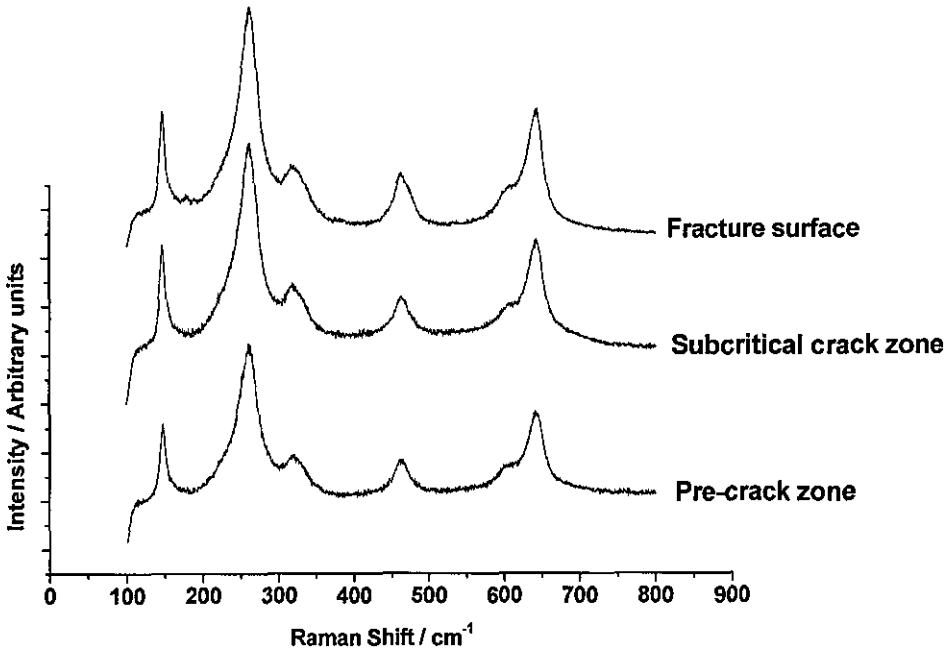

Figure 4-66 Micro-Raman spectra recorded from three different regions of the fracture surface of the benchmark Tosoh sample.

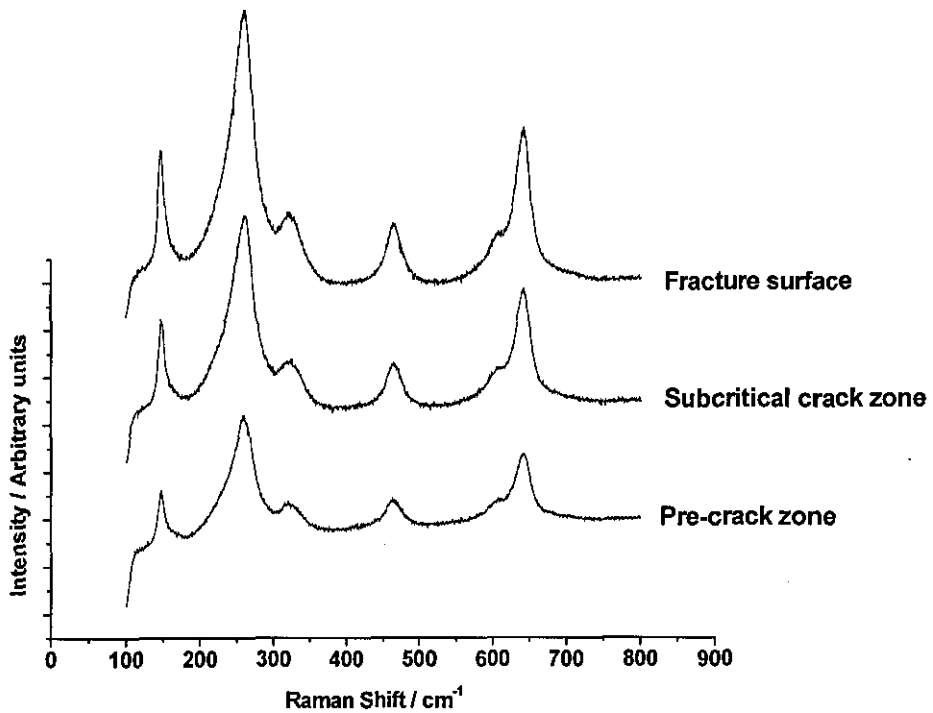

Figure 4-67 Micro-Raman spectra recorded from three different regions of the fracture surface of the nano3YSZ sample.

4.11 Determination of wear properties

The average surface roughness values were found to be 30 nm for nano3YSZ and 32 nm for benchmark Tosoh prior to wear test, which were quite comparable. The results of the various wear tests are summarised in Table 4-16

Table 4-16 Wear testing results.

Sample name	No of cycles	Applied load / N	Wear conditions	Wear volume / mm^3
Tosoh	100,000	20	Dry	1.07
Nano3YSZ	100,000	20	Dry	0.80
Tosoh	100,000	20	Wet	1.05
Nano3YSZ	100,000	20	Wet	0.64

Comparing the wear volume for the samples after dry wear it may be observed that the wear volume was higher for the benchmark Tosoh sample indicating more wear (or less wear resistance) compared to the nano3YSZ sample. Both He et al.[96] and Yan et al.[97] also reported a similar increase in wear resistance with decreasing grain size. The wear rate was not calculated since the contact area between the specimen and ball changed with time.

The wet wear test was performed using a similar experimental set up, but the samples were immersed in deionised water throughout the test. Comparing the wear volume with dry wear, there was no significant difference for the Tosoh sample whereas the volume loss decreased considerably for the nano3YSZ sample. A decrease in wear rate was anticipated in wet wear for all the samples because of a possible reduction in friction due to water lubrication. But this was clearly not the case for the benchmark Tosoh sample. Lee et al.[95] reported that there is no decrease in frictional coefficients due to the presence of water, compared to dry sliding in the case of zirconia.

4.11.1 Wear morphology

FEGSEM images of the worn surfaces were taken after the wear tests to determine the wear mechanism for the Tosoh and nano3YSZ samples. The microstructure of the polished surfaces before wear tests was similar for all of the samples. Figure 4-68

shows the FEGSEM of the turn point area of the samples after dry wear, the wear morphology was found to be different for the nano and submicron samples.

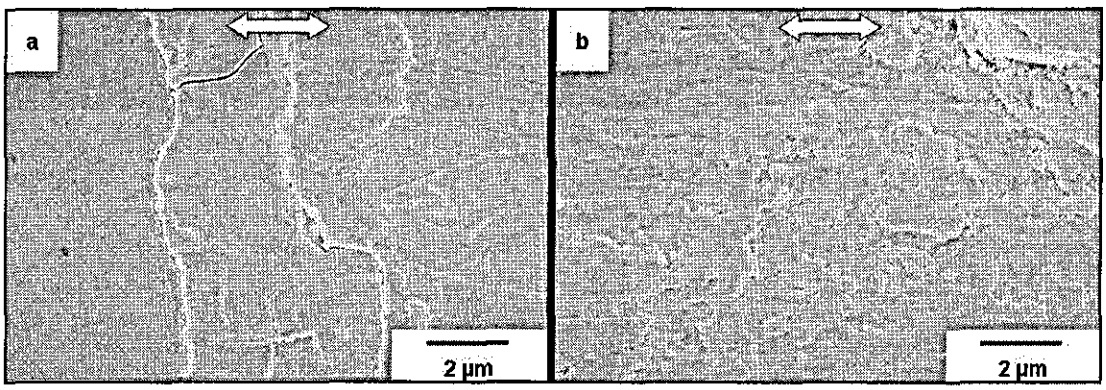

Figure 4-68 Wear morphology at the turn point area after dry wear (a) benchmark Tosoh and (b) nano3YSZ. Double headed arrows indicate the sliding direction.

From Figure 4-68 (a) it is possible to identify the development of cracks for the benchmark sample whereas in Figure 4-68 (b) the wear morphology for the nano3YSZ shows mainly fish scale pattern formation and some plastic deformation. A similar plastic deformation and transcrystalline shear fracture of the individual grains for fine grain zirconia has been reported by Zum Gahr et al.[102] Crack formation leads to subsurface damage and could cause premature failure of the material.

The wear morphology at the middle of the wear scar is shown in Figure 4-69.

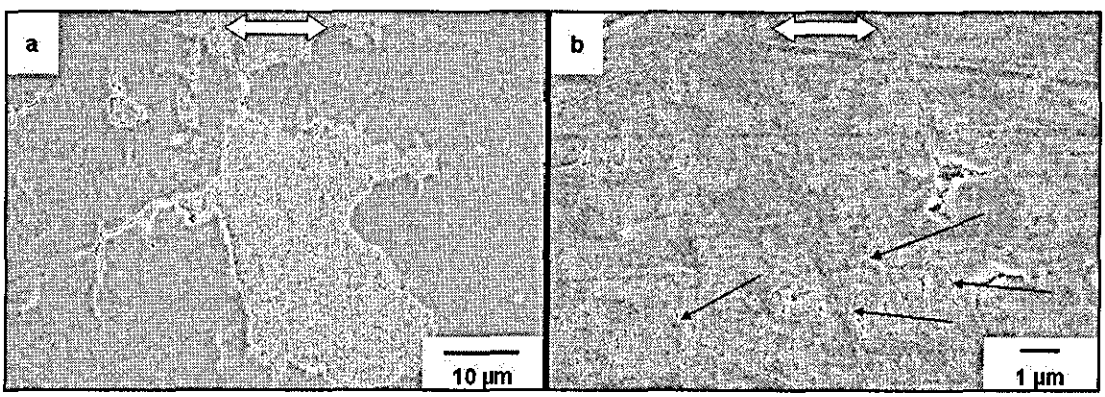

Figure 4-69 Wear morphology at the scar middle after dry wear (a) benchmark Tosoh and (b) nano3YSZ. Double headed arrows indicate the sliding direction.

The wear mechanism was quite different at the middle of the wear scar compared to the turn point region. The benchmark sample showed delamination and detachment of a surface layer after wear. This will have lead to the formation of wear debris and pits

and both will have increased the wear by increasing the friction and surface roughness. In real applications, if the wear system involves two moving surfaces moving in different directions or at different speeds, the presence of wear debris can accelerate the wear by getting in between the moving surfaces. The nano3YSZ sample showed the formation of microcracks perpendicular to the sliding direction. Similar microcracking has been reported for a 5.7 mol% YSZ with 180 nm grain size.[96] The same authors reported that no microcracks were formed for samples with larger grain sizes. This was true for the benchmark Tosoh samples from the present study. The absence of microcracks is ascribed to a shear induced phase transformation and resulting volume increase, which prevented the formation of microcracks. As a result of this transformation, a compressive layer was formed at the worn surface. Hence the formation and propagation of microcracks will have been prevented and any cracks formed will have been healed. The microcracks in the nano3YSZ sample may be due to grain sliding or strain incompatibility or could be due to lack of transformation.

Figure 4-70 is an image of the wear scar below the surface detached area on the benchmark Tosoh sample. This image shows the development of microcracks and the damage to the grains. Because of the phase transformation of the surface layer, a tensile stress can develop beneath the compressive layer, forming internal stresses in local areas. These local stresses promote microcrack nucleation at pores and grain boundaries.[96] These cracks in turn mechanically weaken the parts and could lead to premature failure of the components.

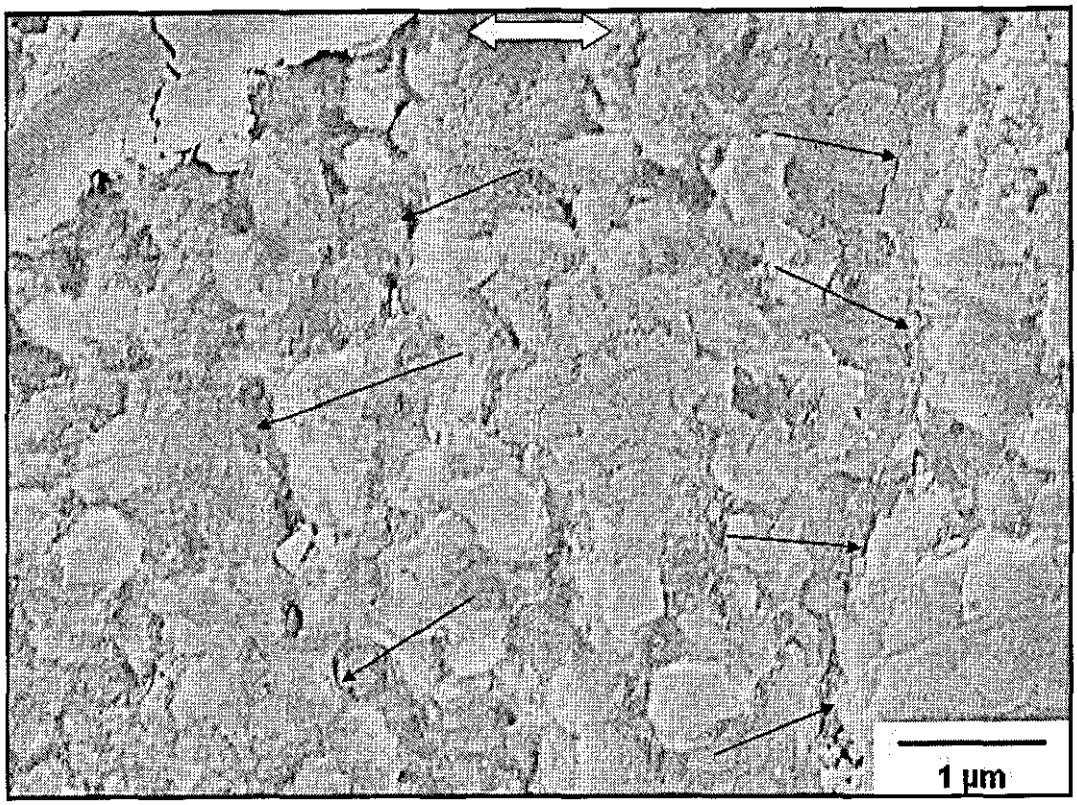

Figure 4-70 Wear morphology below the detached area on the benchmark Tosoh sample at higher magnification. Arrows indicate the cracks.

The wear morphology after wet wear is shown in Figure 4-71. It is clear that in the benchmark Tosoh sample, Figure 4-71 a, the surface detachment has taken place over a larger area after wet wear compared to dry wear. The surface damage to the nano3YSZ sample after wet wear was less severe and mainly it showed a fish scale pattern formation, Figure 4-71 b.

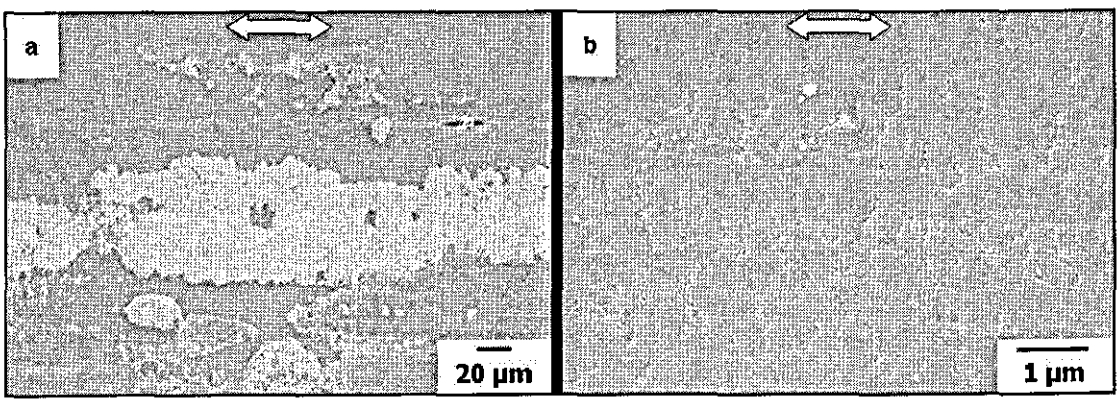

Figure 4-71 Wear morphology after wet wear (a) benchmark Tosoh and (b) nano3YSZ. Double headed arrows indicate the sliding direction.

In order to confirm the reasons for delamination, the XRD patterns recorded from the wear scar after dry and wet wear test are shown in Figure 4-72 and Figure 4-73.

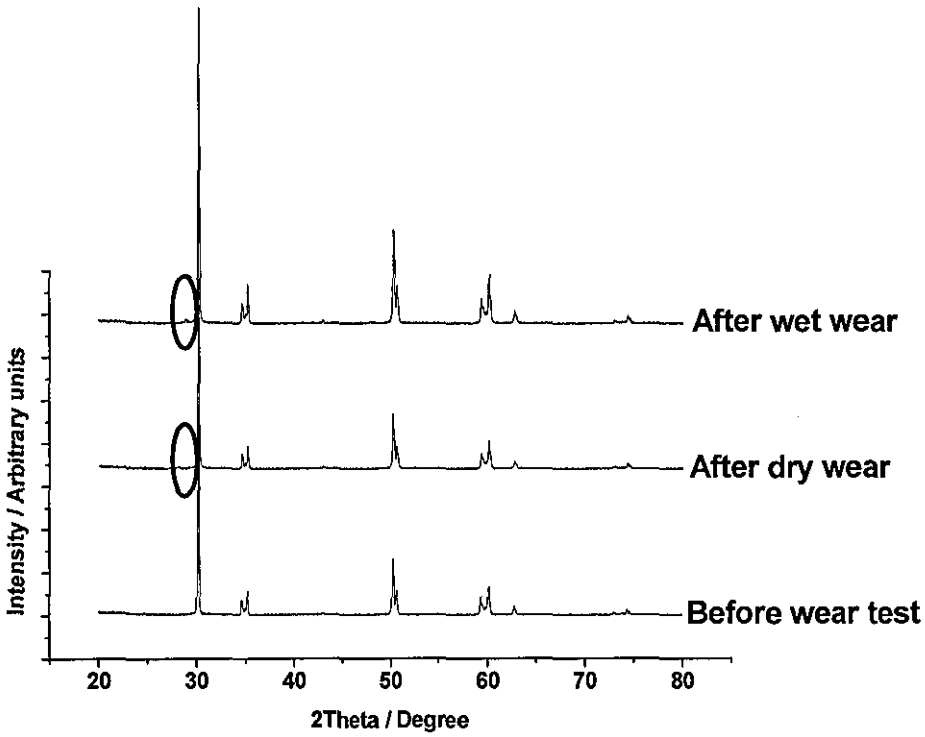

Figure 4-72 XRD pattern of the wear scar for the benchmark samples.

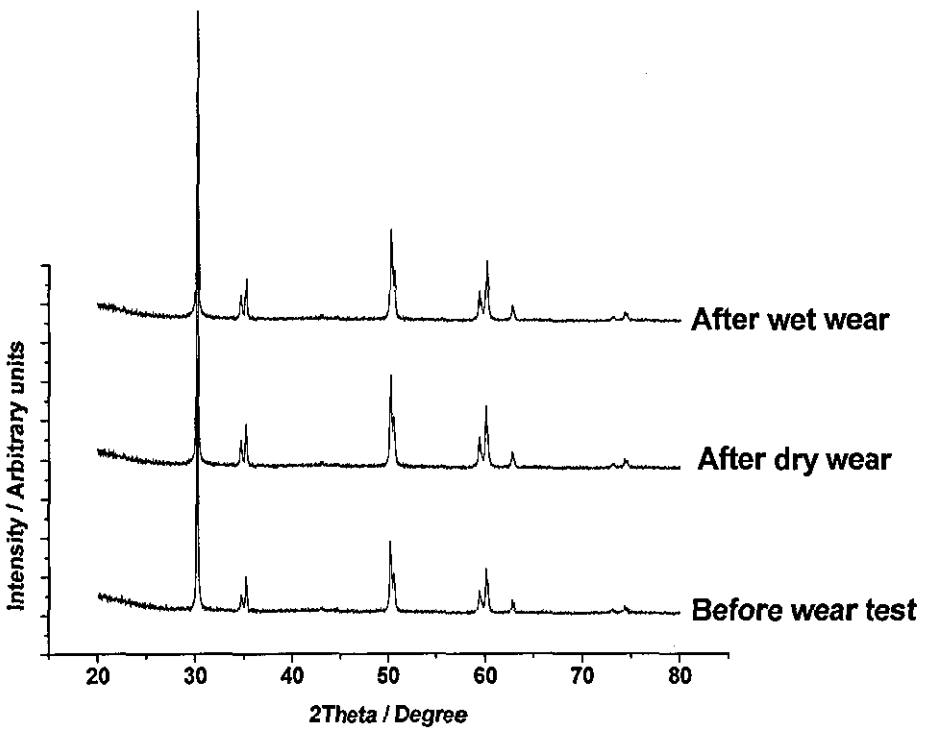

Figure 4-73 XRD pattern of the wear scar for the nano3YSZ samples.

The development of a very small peak at ~28.3°, corresponding to the monoclinic phase, was observed for the benchmark sample after wear testing. The peak intensity was very small as it was difficult to focus the X-rays perfectly on the wear scar. No monoclinic peaks, however, were observed for the nano3YSZ sample. The amount of monoclinic phase formed for the benchmark ceramic was calculated to be 2.4 vol% after dry wear and 8.1 vol% after wet wear. According to He et al.,[96] if the mean grain size is less than 700 nm there will be no phase transformation on wear testing. Based on our results for the benchmark sample, however, we can confirm that there can be some phase transformation even with a mean grain size as fine as 520 nm, albeit <10%. Similar results were obtained for a similar material with a 700 nm mean grain size after dry wear, though no monoclinic content was observed for samples with a finer grain size.[97] An increase in phase transformation with grain size has also been reported by Zum Gahr et al.[102]

Micro-Raman spectroscopy was employed to obtain more detailed information about the monoclinic conversion since it can collect data from very small areas with micrometer precision. Micro-Raman spectra were recorded from three different locations on the benchmark and nano3YSZ samples after wet wear testing, Figure 4-74 and Figure 4-75.

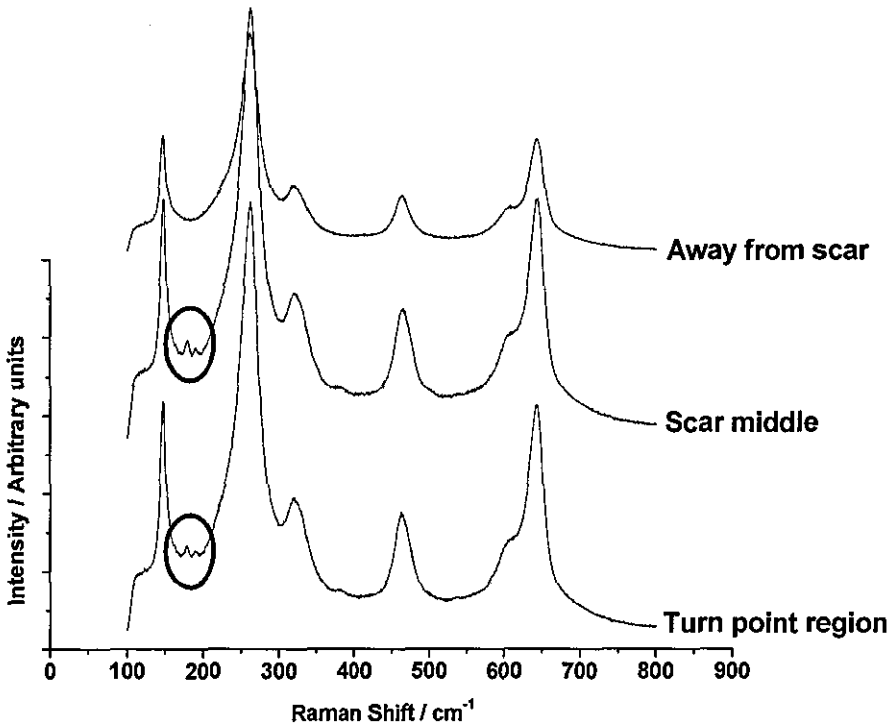

Figure 4-74 Micro-Raman spectra on the benchmark sample after wet wear testing.

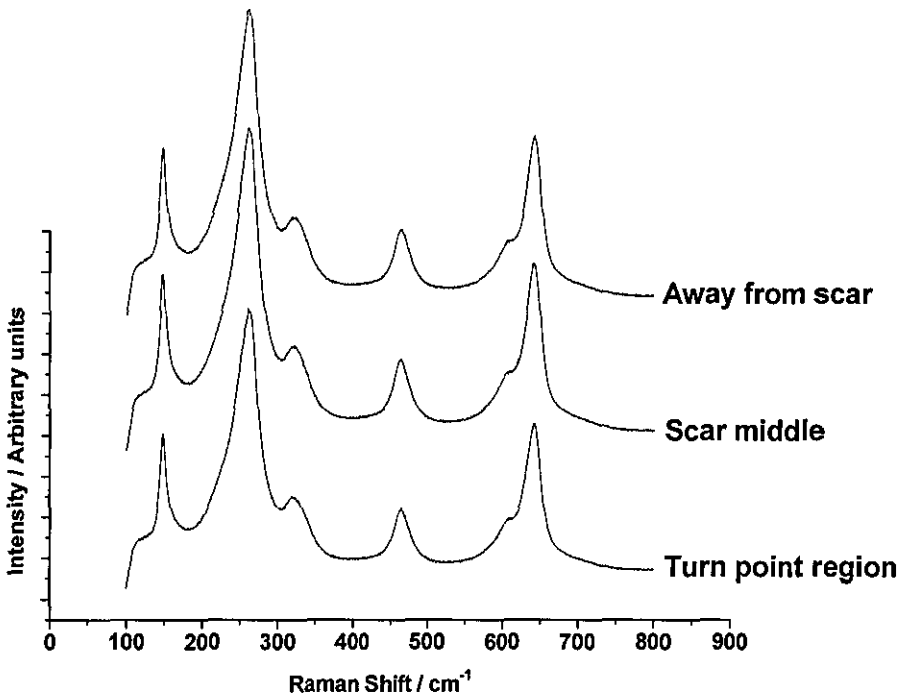

Figure 4-75 Micro-Raman spectra on the nano3YSZ sample after wet wear testing.

The presence of monoclinic peaks is very clearly identifiable for the benchmark sample. This phase transformation is due to the hydrothermal degradation of the

zirconia in the presence of water and is responsible for the detachment of the surface layer; when the latter underwent the phase transformation to monoclinic, its volume will have increased causing fracture from the material beneath and consequent detachment after further wear. There was no monoclinic phase transformation for the nano3YSZ sample and hence no surface detachment.

A detailed discussion of the hydrothermal ageing of zirconia is given in Section 4.12. Even if the wet wear is carried out at room temperature, the temperature may go up by several hundred degrees for very short period of time because of the sliding friction between the ball and the specimen, this flash temperature accelerating the phase transformation. The presence of such local 'hot spots' during unidirectional sliding wear has been reported by Zum Gahr et al.[102] It is also reported in the literature that the flash temperature for self-mated Y-TZP could rise up to 500-800°C depending on the sliding speed and load.[95] In our case, a WC-Co ball was used. With its good thermal conductivity it can be assumed that the flash temperatures were much lower than 800°C.

Based on our wear results for the benchmark and nano3YSZ samples, it can be concluded that the latter has significantly better wear resistance; however, it is difficult to assign this improvement just to grain size. The wear properties in general are dependent on a number of factors including material properties such as hardness, strength, toughness, thermal conductivity, thermal expansion, friction coefficients and microstructure. None of the above is the same for the two YSZ grades and hence a more detailed analysis is required to determine the exact relation of each of these parameters to wear resistance.

4.12 Hydrothermal ageing studies

Yttria stabilised zirconia is well known for its strength, hardness and toughness, but it suffers from a major draw back; in the presence of water or water vapour it undergoes a phase transformation from tetragonal to monoclinic, which degrades its properties severely. Kobayashi et al.[256] was the first to report this ageing transformation. Hydrothermal degradation is accelerated at elevated temperatures and is a major concern in applications such as bio-implants, e.g. femoral heads, knee implants and

dental implants; surgical tools; wear applications where moisture is involved; ferrules; thermal barrier coatings and solid oxide fuel cell (SOFC) components.

The initial hydrothermal ageing experiments used in the present study were designed to simulate conditions similar to those experienced by biomedical grade zirconias. According to Chevalier et al.,[227] 1 h of ageing at 134°C and 2 bar is equivalent to 4 years *in vivo* ageing. The XRD patterns of the benchmark samples aged at 140°C and 4 bar for up to 168 h (7 days) are given in Figure 4-76 and Figure 4-77; the arrow highlights the development of one of the major monoclinic peaks with ageing. The sample disintegrated after ageing for 14 days and hence the XRD pattern could not be recorded.

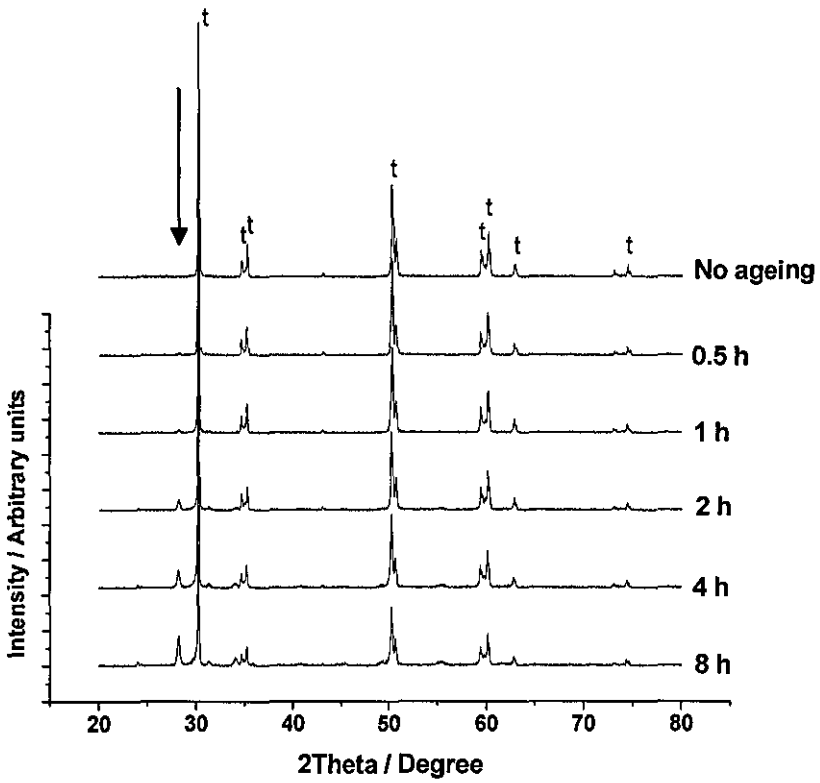

Figure 4-76 XRD pattern of benchmark Tosoh samples aged for up to 8 h at 140°C and 4 bar. Unlabelled peaks correspond to monoclinic zirconia and the arrow indicates the development of the major monoclinic peak with ageing.

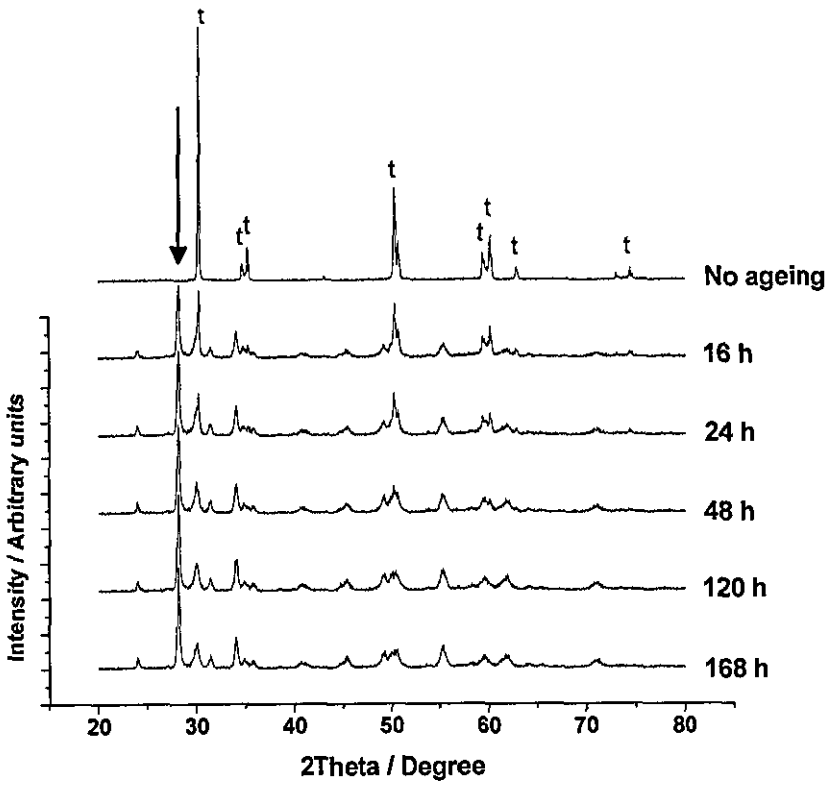

Figure 4-77 XRD pattern of benchmark Tosoh samples aged for up to 168 h at 140°C and 4 bar. Unlabelled peaks correspond to monoclinic zirconia and the arrow indicates the development of the major monoclinic peak with ageing.

Although there was no detectable monoclinic in the unaged material, phase transformation can be seen to initiate after ageing for just 30 min.; after 16 h ageing, the largest peak corresponds to the monoclinic phase zirconia. According to a number of authors, the hydrothermal degradation of zirconia shows an initiation-propagation type of kinetics. Chevalier et al.[257] reported an initiation period of up to 1 h at 130°C and ~10 h at 100°C within which no monoclinic phase transformation was observed.

The phase transformation was also verified using micro-Raman spectroscopy, as shown in Figure 4-78.

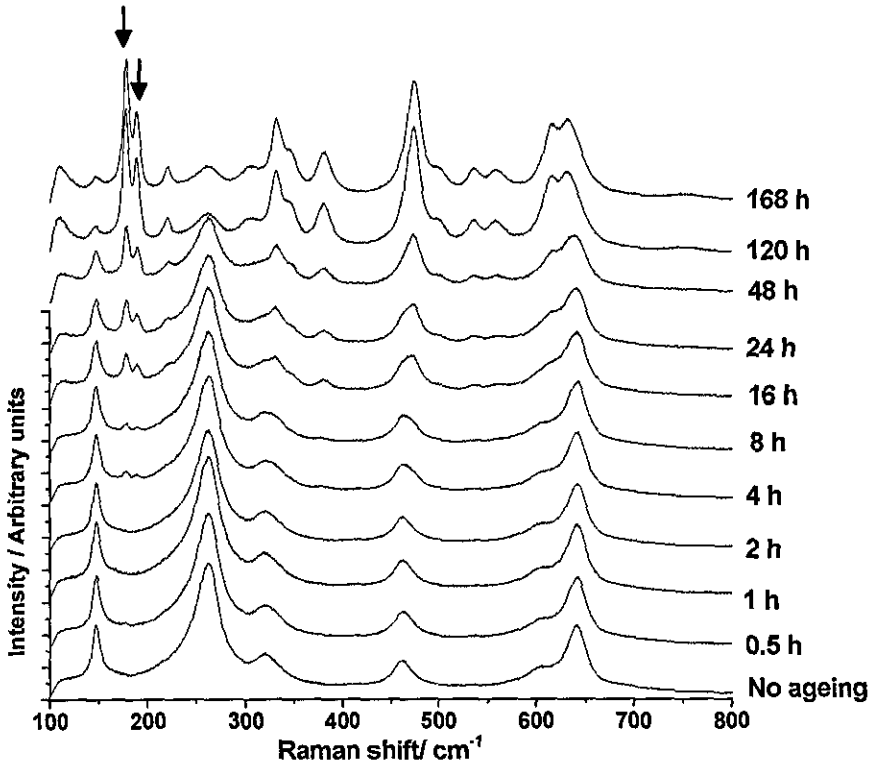

Figure 4-78 Micro-Raman spectra of the benchmark Tosoh samples aged for up to 168 h at 140°C and 4 bar. The development of the major monoclinic peaks are indicated with the arrows.

The increase in intensity of the characteristic monoclinic doublet at 181 cm^{-1} and 192 cm^{-1} can be clearly seen in the micro-Raman spectra.

The XRD pattern of the nano3YSZ sample after ageing for up to 14 days at 140°C was recorded and no monoclinic phase was detected. Since it was practically difficult to keep the samples for long periods of time, it was decided to increase the ageing temperature and pressure instead, therefore the temperature was increased to 200°C and then to 245°C. The upper temperature was limited by the temperature capability of the PTFE liner of the autoclave, whilst Sato et al.[258] suggested that the ageing is maximum at about 200°C. Only long term ageing, 7 days and 14 days, were performed to see whether there was any phase transformation for the nano3YSZ at these extremely severe conditions. Benchmark samples were also aged under the same conditions, although the outcome was known; the samples disintegrated into powder after just 30 min. The XRD patterns of the nano3YSZ samples after ageing at 140, 200 and 245°C for 14 days are shown in Figure 4-79.

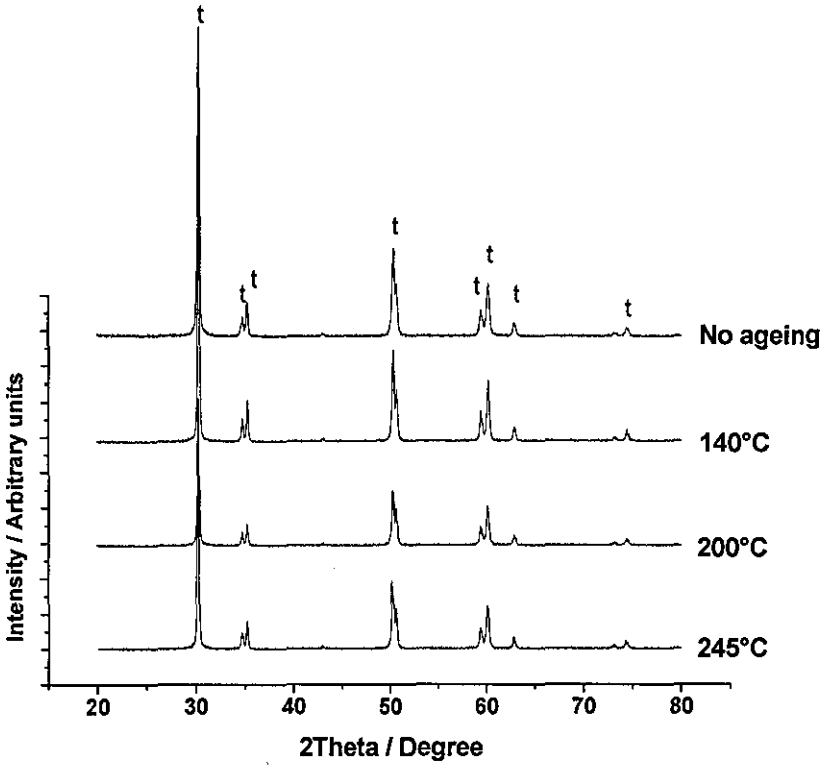

Figure 4-79 XRD pattern of nano3YSZ aged for 14 days at different temperatures.

No monoclinic phase was observed for any of the samples, even after 14 days at 245°C. The results of these ageing experiments are very interesting considering the biomedical application of zirconia; 14 days at 140°C and 4 bar is equivalent to more than 1300 years *in vivo* ageing.[227] This implies that there will be no ageing at all for a zirconia implant if it is prepared using nano3YSZ. According to Chevalier et al.[109] the ageing of nano3YSZ can be slowed down, but it is not possible to suppress it completely. However in our study no ageing at all was observed for the nano3YSZ under the conditions investigated. This increased stability is probably a result of the overstabilisation of the YSZ caused by the grain size effect.

Micro-Raman spectroscopy has also been employed to validate the presence of the different phases after hydrothermal ageing of the nano3YSZ sample, Figure 4-80, and the results correlated with that of the XRD observations. No monoclinic peaks were observed under any conditions.

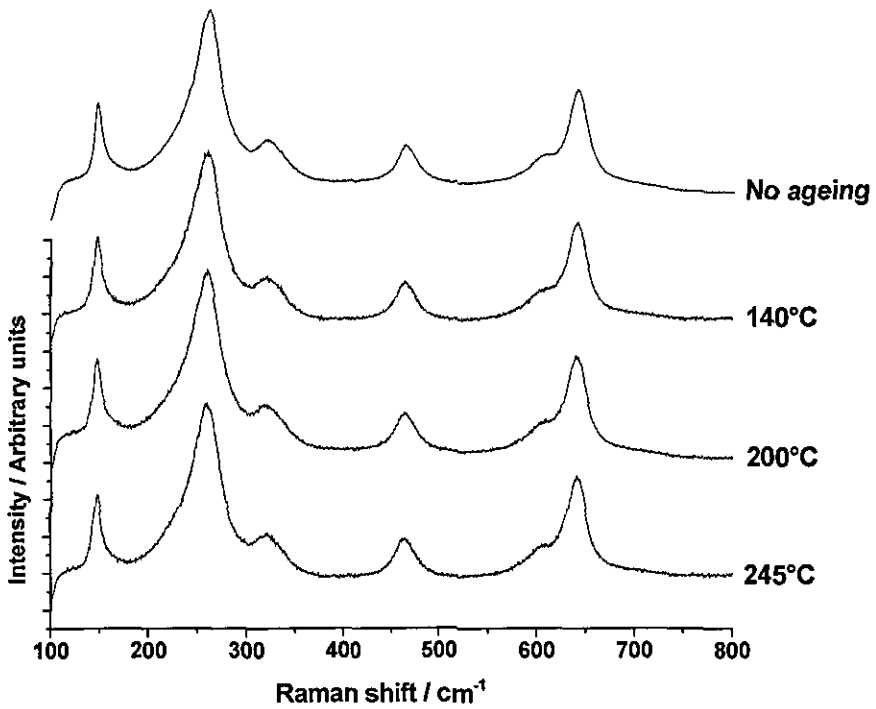

Figure 4-80 Micro-Raman spectra of the nano3YSZ aged for 14 days at different temperatures. All the peaks correspond to the tetragonal phase.

There is no single universally accepted mechanism to describe the hydrothermal degradation of zirconia, but it is generally believed that water preferentially attacks regions of low yttria content. The hydrothermal ageing of Tosoh 3YSZ can be assigned to a grain boundary segregation induced phase transformation (GBSIPT)[259,260] after sintering at temperatures similar to those used for the sintering of the same ceramic in the present study. According to this theory, when the Tosoh 3YSZ is sintered at <1300°C the yttria distribution remains uniform and all of the grains are tetragonal. However, at sintering temperatures ≥1500°C a heterogeneous distribution of yttria forms at the grain boundaries and triple points leading to the formation of some cubic grains. The yttria content has been observed to vary from ~6 mol% at the grain boundaries to ~2 mol% at the grain interiors for a tetragonal-tetragonal grain boundary, and from ~1 mol% to ~8 mol% from tetragonal grain to cubic grain across a tetragonal-cubic grain boundary, with ~6 mol% at the grain boundary itself. Based on these results it is assumed that water preferentially attacks the yttria depleted grains converting them into the monoclinic phase.

The crystalline phase in 2.9Y-TZP after sintering was reported to be 100% tetragonal at 1200°C, whilst at 1300°C 10.4 mass% of the cubic phase appeared which increased to 18.5 mass% by 1650°C.[261] A similar GBSIPT has also been observed for 2Y-TZP sintered above 1300°C, with a reported cubic fraction of 6.8 mass%.[262] For the 2Y-TZP, cubic phase regions with high yttria concentrations were formed in extremely narrow regions near the grain boundaries and triple junctions. For 8YSZ, however, the segregation was reported to be much less and all the grains were cubic.[262]

The nano3YSZ samples in the present work were sintered at temperatures much lower than 1300°C, it can be assumed that there is no GBSIPT and hence no yttria gradients. This may be one of the reasons for the hydrothermal ageing resistance of the nano3YSZ. According to Saldana et al.,[119] the critical grain size is 0.36 μm for a fully dense 3YSZ below which no transformation is observed.

The increase in monoclinic content with ageing for the benchmark Tosoh sample is plotted in Figure 4-81; ~70 % content was reached after 48 h at 140°C. Beyond this time there was only a small increase in monoclinic content; the maximum monoclinic content was ~73.6% after 168 h. This is in reasonable agreement with the maximum transformation of 76.3 % reported by Yamashita et al.[263] for the ageing of Tosoh 3YSZ at 140°C and the maximum transformation calculated by Thompson et al.[110] for a 3YSZ based on the activation energy for water induced transformation. The limiting factor which determines the maximum transformation is the fraction of yttria rich grains present in the sample after sintering.

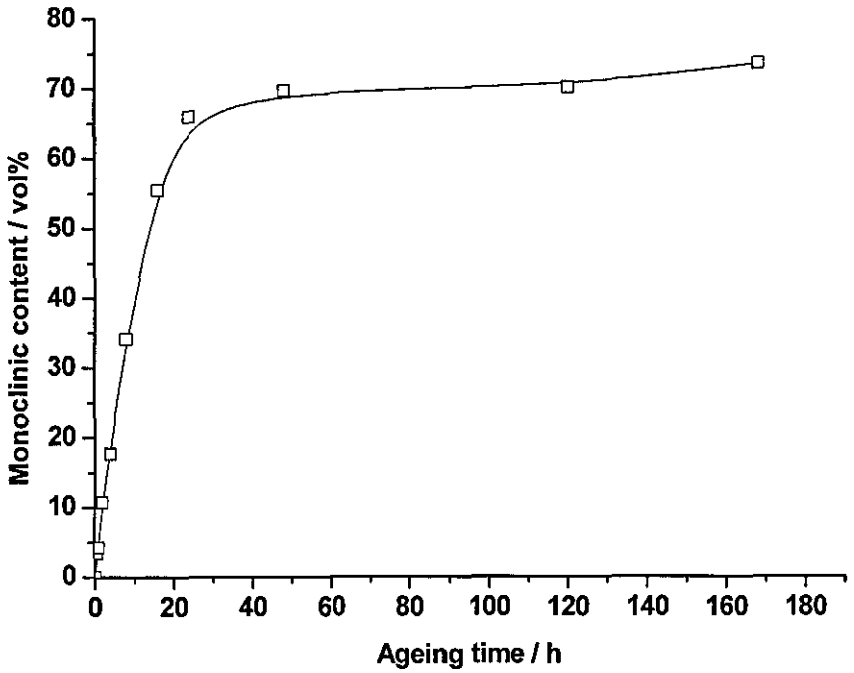

Figure 4-81 Increase in monoclinic content with ageing for the benchmark Tosoh sample at 140°C and 4 bar.

Several authors have reported the formation of cracks in zirconia after hydrothermal degradation.[118,258] In order to find whether the benchmark samples developed any cracks, they were analysed using the FEGSEM; no cracks were observed in any of the samples after ageing for up to 7 days at 140°C, though they shattered after 14 days at the same temperature. Lange et al.[116] and Eichler et al.[93] observed similar results after ageing studies on 3YSZ. Lange et al. reported that the volume expansion and shear strain associated with the transformed surface grain will produce a microcrack only if the size of the grain is greater than a critical value after studying 2 to 3YSZ with 0.3 μm grain size at 250°C. The grain size of the benchmark sample in the present study was ~0.5 μm which is comparable to that reported by Lange et al.

A benchmark sample aged for 5 days at 140°C was analysed to find the thickness of the transformed monoclinic layer; a cross section was taken, polished cleaned and analysed under the FEGSEM. A porous surface layer of monoclinic zirconia was clearly visible, as shown in Figure 4-82.

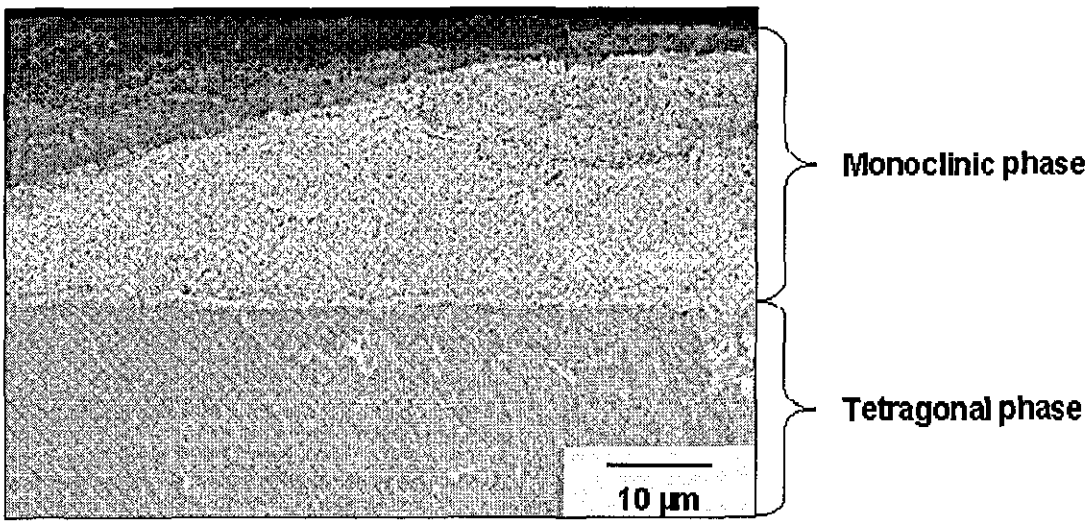

Figure 4-82 FEGSEM image of the monoclinic layer formed by hydrothermal ageing.

The thickness of the layer was found to be ~25 µm after 5 days at 140°C and 4 bar and the transformed area was very rough. Castkova et al.[264] reported a transformed layer thickness of 15 µm after ageing for 10 h at 180°C with 54.3 wt% monoclinic conversion for a similar Tosoh 3YSZ.

The correlation between accelerated ageing and actual *in vivo* ageing may not be 100% reliable; hence a zirconia showing no hint of any transformation, such as the nano3YSZ in the present study, is preferable for biomedical applications.[265] However, further work is still required. For example, it is important to carryout the ageing studies in Ringer's solution; to determine the ageing characteristics in simulated body fluids. In addition, it would be interesting to perform ageing studies at much higher temperatures than those used in the present work to determine the conditions under which the nano3YSZ will age. This could be useful for applications such as SOFCs, where the operating temperatures are above 700°C.

The hydrothermal ageing studies were not only limited to nano3YSZ, but both nano1.5YSZ and nano2YSZ samples were also subjected to the same ageing tests. Unlike the nano3YSZ, the as-sintered nano1.5YSZ was found to contain ~37 vol% monoclinic phase, hence there was no need for an initiation degradation step in this case. The ageing studies were performed to find whether there is any grain size effect which prevents the growth of the monoclinic content initially present. After 8 h at 140°C and 4 bar, the nano1.5YSZ started to disintegrate and after 16 h it was fully

disintegrated with only powder left. The XRD patterns and micro-Raman spectra were recorded after ageing as shown in Figure 4-83 and Figure 4-84 respectively.

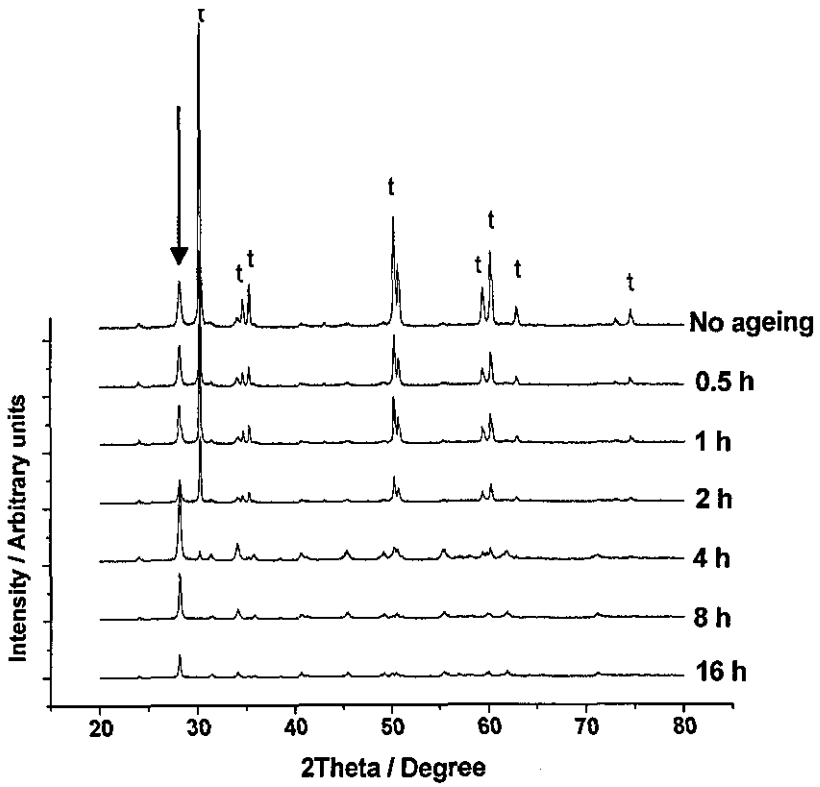

Figure 4-83 XRD pattern of nano1.5YSZ samples aged for up to 16 h at 140°C and 4 bar. Unmarked peaks correspond to monoclinic zirconia and the arrow indicates the increase in intensity of the major monoclinic peak with ageing.

From the XRD patterns it can be observed that the intensity of the monoclinic peaks increased with ageing time and it was the major peak after ageing for just 4 h at this temperature. Only monoclinic peaks were observed for the samples aged for ≥8 h. Similar results were observed from the micro-Raman spectra also.

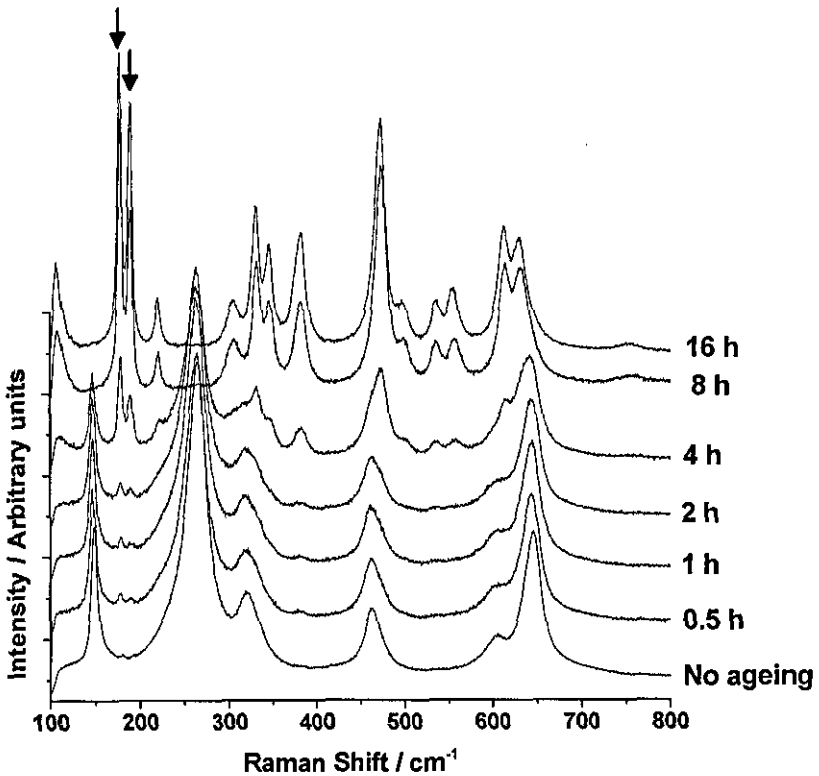

Figure 4-84 Micro-Raman spectra of nano1.5YSZ samples aged for up to 16 h at 140°C and 4 bar. The increases in intensity of the major monoclinic peaks are indicated with the arrows.

Ageing studies were also performed at 200°C and 5.7 bar; the ageing was much faster and the samples disintegrated after just 4 h. The XRD patterns and micro-Raman spectra of the samples are shown in Figure 4-85 and Figure 4-86 respectively.

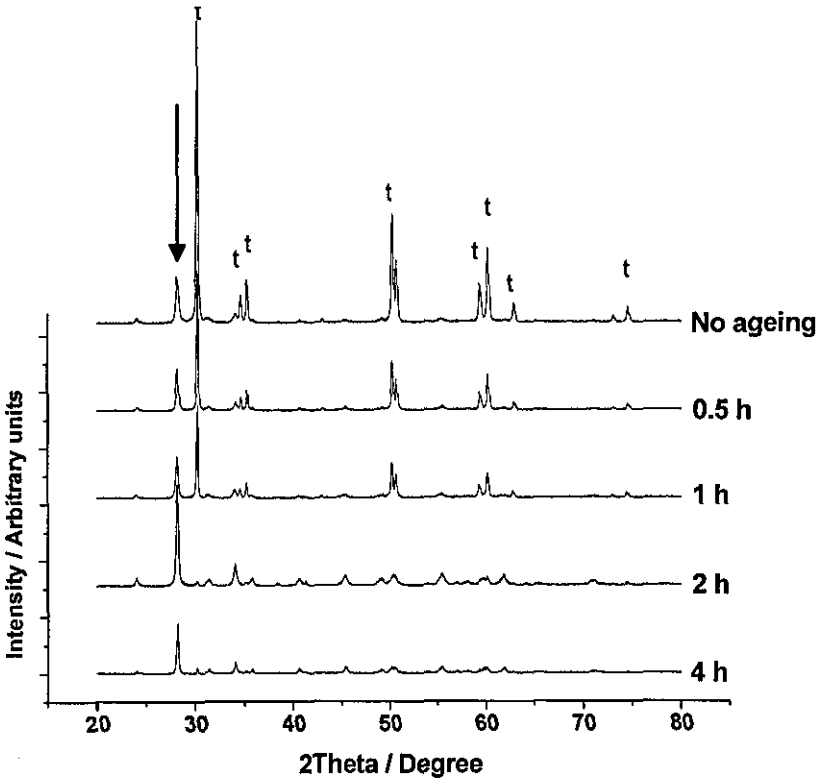

Figure 4-85 XRD pattern of nano1.5YSZ samples aged for up to 4 h at 200°C and 5.7 bar. Unmarked peaks correspond to monoclinic zirconia and the arrow indicates the increase in intensity of the major monoclinic peak with ageing.

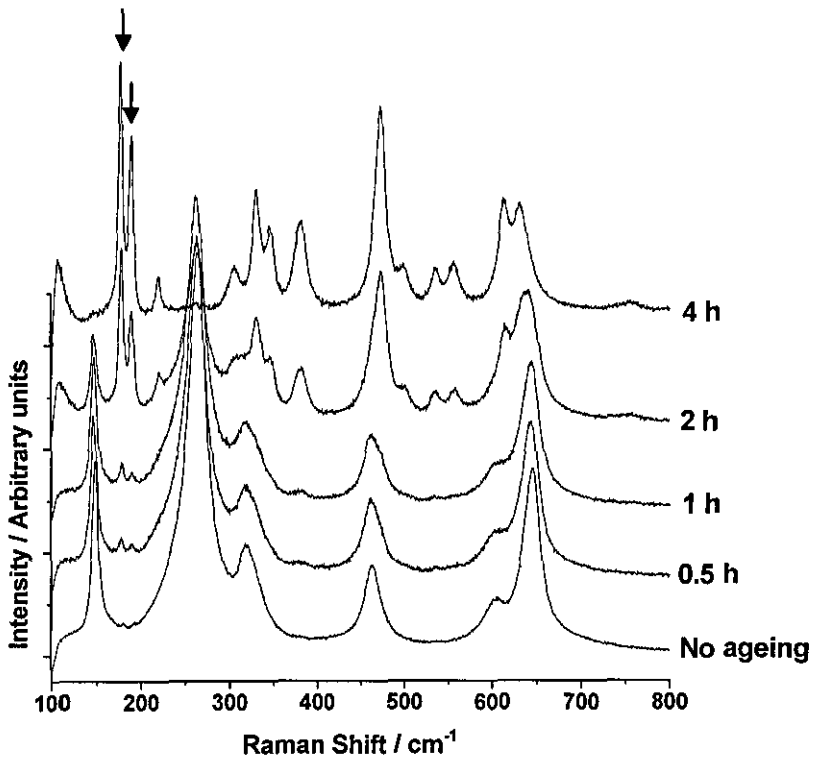

Figure 4-86 Micro-Raman spectra of nano1.5YSZ samples aged for up to 4 h at 200°C and 5.7 bar. The increases in intensity of the major monoclinic peaks are indicated with the arrows.

The monoclinic content of the nano1.5YSZ samples after ageing at 140°C and 200°C was calculated from the XRD data and is plotted in Figure 4-87.

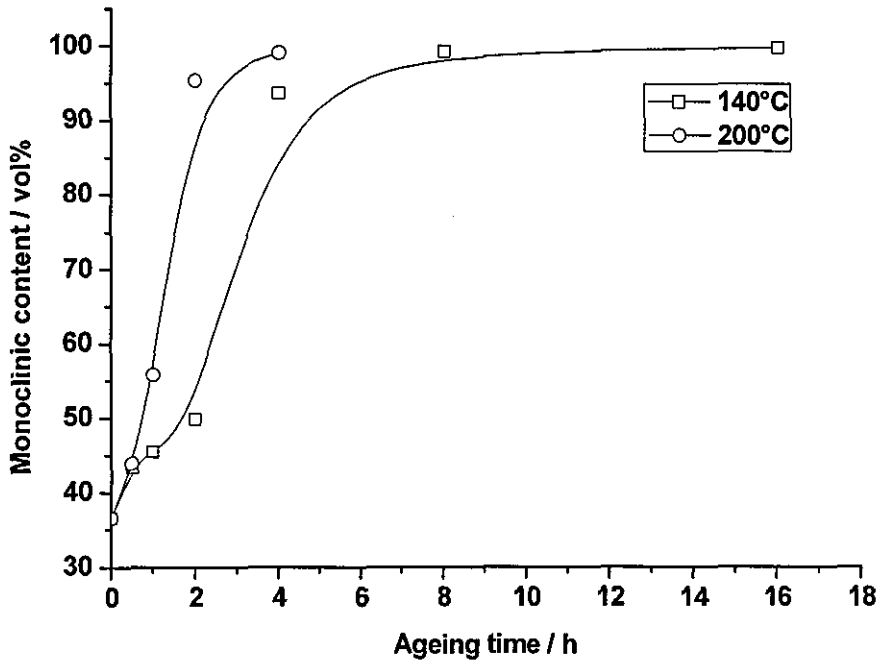

Figure 4-87 Increase in monoclinic content with ageing for the nano1.5YSZ sample at 140°C and 200°C.

From Figure 4-87 it can be observed that the monoclinic content reached more than 99% within just 4 h; a similar result was reported by Hernandez et al.[117] after the ageing studies of 2, 2.5 and 3 mol% YSZ. They reported that when the Y_2O_3 concentration was less than 2.5 mol%, the tetragonal zirconia would completely transform to the monoclinic phase. For 3YSZ they reported that saturation was reached at ~80% monoclinic conversion.

To determine the effect of yttria on the ageing of a nanosample with no initial monoclinic content, nano2YSZ samples were subjected to ageing. Two samples were aged at 140°C for 24 h and 120 h and analysed using XRD, the results are shown in Figure 4-88. The samples were found to undergo ageing, but at a much reduced rate compared to either the benchmark or nano1.5YSZ.

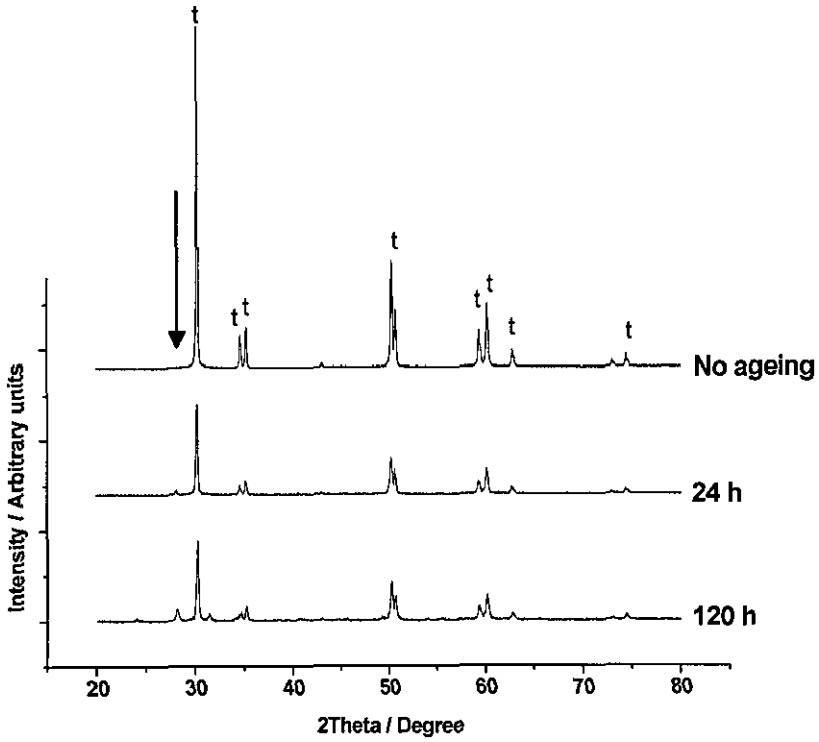

Figure 4-88 XRD pattern of nano2YSZ samples aged for 24h and 120 h at 140°C. Unmarked peaks correspond to monoclinic zirconia and the arrow indicates the development of the major monoclinic peak with ageing.

The amount of monoclinic phase formed after ageing was calculated from XRD and was found to be 12.7 vol% and 22.2 vol% respectively after 24 h and 120 h. These are much lower than the values for the benchmark sample (66 vol% and 70 vol% respectively) after similar ageing times. This increased ageing resistance of the nano2YSZ, even with the reduced amount of yttria content, is believed to be due to the increased stability provided by the reduced grain size. Hence the reduction of grain size can be used as an effective technique to increase the hydrothermal ageing resistance of zirconia ceramics.

The hardness of the benchmark Tosoh, nano3YSZ and nano1.5YSZ samples was measured before and after ageing for different periods of time. No decrease in hardness was observed for the nano3YSZ sample even after ageing for 14 days, but the hardness of the benchmark sample was found to decrease slowly with ageing at 140°C, Figure 4-89.

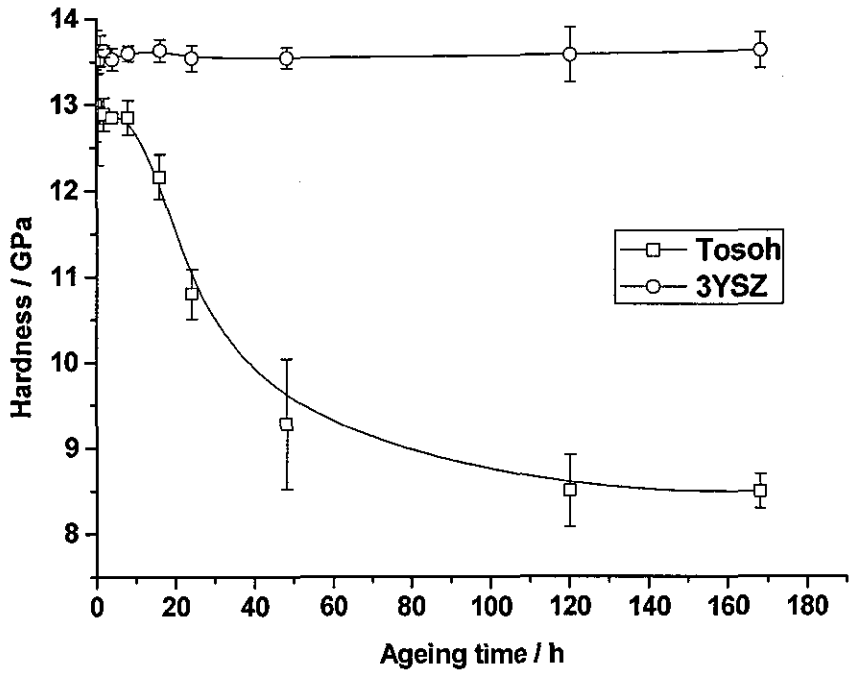

Figure 4-89 Effect of hydrothermal ageing on hardness for nano3YSZ and benchmark Tosoh at 140°C.

The hardness of the benchmark samples reached a constant value of ~8.5 GPa after 120 h at 140°C. This value is comparable to that of the monoclinic samples discussed in Section 4.8. For the benchmark samples aged for short periods of time (≤10 h), it can be assumed that the Vickers indenter penetrated through the transformed layer to the tetragonal layer below and hence yielded hardness values comparable to those of the unaged sample. With increased ageing time, the thickness of the transformed layer increased and, hence, after longer ageing times, the hardness will have been determined by the transformed monoclinic layer. This reduction in hardness clearly illustrates the detrimental effect of hydrothermal degradation and resulting phase transformation on the properties of zirconia ceramics.

As there was no decrease in hardness for nano3YSZ after ageing for 7 days (168 h) at 140°C, the hardness of the samples aged for 14 days at 140°C, 200°C and 245°C were measured, again no decrease in hardness was observed. This together with XRD and micro-Raman results clearly proves that nano3YSZ is resistant to hydrothermal ageing for at least up to 14 days at 245°C, without significant loss of mechanical performance.

The variation in hardness with ageing for the nano1.5YSZ samples at 140°C and 200°C are plotted in Figure 4-90. The hardness decreased very rapidly with ageing and the decrease in hardness was more for the samples aged at higher temperature and reached very low values, tying in with the phase evaluation results discussed above.

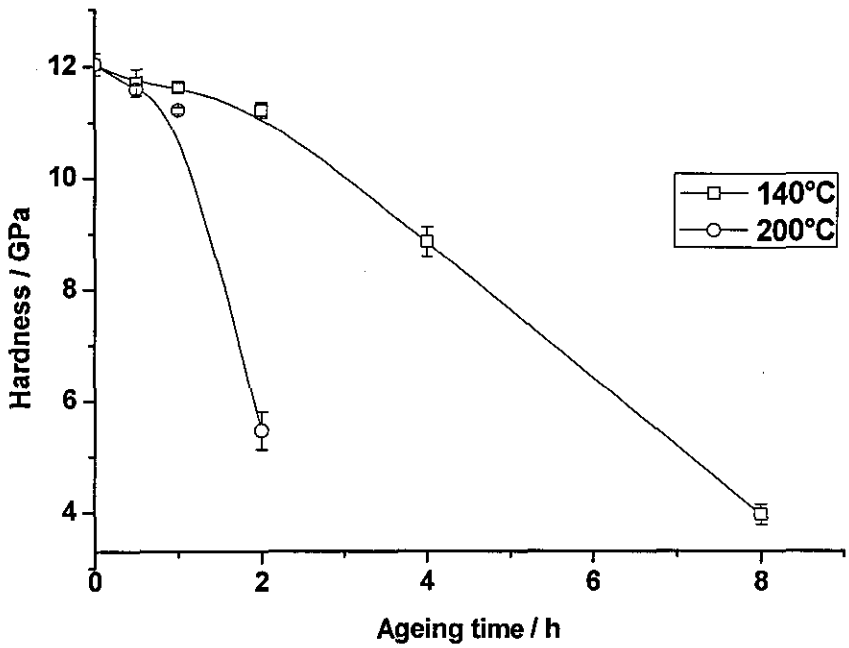

Figure 4-90 Effect of hydrothermal ageing on hardness for nano1.5YSZ at 140°C and 200°C.

Chapter 5

5 Conclusions

The main aim of the research was to determine the mechanical properties of nanozirconia ceramics with different yttria contents. The experiments were started with dry pressed green bodies and hybrid sintering. After the initial experiments, it was concluded that dry pressing was not a viable route for preparing nanozirconia ceramics using oven dried powder, because of the presence of hard agglomerates. These agglomerates, and the resulting inter-agglomerates pores, prevented the samples from reaching theoretical density.

Slip casting parameters were optimised for the preparation of green bodies from high solid content, low viscosity, zirconia suspensions. The optimum solid content was found to be ~55 wt% and it was the same for 0, 1.5, 2, and 3 mol% yttria containing suspensions. The density of the green bodies were found to be ~52% of theoretical, which was lower than that of the samples prepared by dry pressing at 480 MPa, but the green microstructure was more uniform. The biggest samples prepared by slip casting were approximately 40 mm in diameter and ~4.5 mm thickness after sintering.

Both single step and two-step sintering experiments were conducted to find the optimum sintering conditions to get >99% density and, in the case of two-step sintering, with minimum grain size. The same single step sintering cycle was found to be optimum for the sintering of nano1.5YSZ, nano2YSZ and nano3YSZ samples with respect to obtain ≥99% density, but the resulting grain sizes were different with a decrease in grain size with increasing yttria content. Compared to the sintering temperatures required for a submicron ceramic, much lower temperatures were found to be sufficient for the sintering of nanozirconia. Sintering temperatures higher than the optimum resulted in abnormal grain growth and a decrease in density due to desintering. The lower sintering temperature is a real benefit for nanoceramics considering the possibility for energy savings. The optimum sintering temperatures for the nanosamples were approximately 400°C lower than those of the submicron benchmark samples.

The optimum two-step sintering cycles to prepare fully dense (>99% theoretical) samples with nanograin size (<100 nm) was found to be different for samples with different yttria content. Lower temperatures were found to be sufficient for the nano1.5YSZ samples compared to the other yttria contents with the nano3YSZ requiring the highest temperature.

Both conventional and hybrid two-step sintering cycles were useful to prepare nanozirconia with >98% theoretical density. Microwave assisted heating was found to yield higher densities for the same time-temperature profile, with the density increasing with microwave power. This clearly illustrated the "microwave effect" and the ability to use higher heating rates and shorter sintering durations. Conventional two-step sintering provided better control over grain growth. It also enabled the sintering of samples with different green density and mass. The finest possible grain size for ≥99% dense samples obtained after conventional two-step sintering was ~90 nm; further reduction in grain size might be possible by increasing the green density or by optimising the hybrid approach for slip cast bodies. More trials are required to avoid sample cracking with higher solid content suspensions to achieve the former.

The attempts to prepare fully dense 0YSZ ceramics starting with nano0YSZ powder were not successful. Maximum density obtained after single step sintering was 98.4% and the attempts to increase density by increasing the sintering temperature resulted in shattering of the samples. The maximum density obtained after two-step sintering was only 96.4% of theoretical. The grain sizes of the nano0YSZ samples were not measured as the final densities were lower.

From the micro-hardness measurements it was found that both nano3YSZ and nano2YSZ samples were harder than benchmark submicron sample, whereas nano1.5YSZ was less hard. The hardness of the nano0YSZ samples were the lowest. The hardness increased linearly with density for all the samples, and no variation with grain size was observed below 160 nm.

After the indentation toughness measurements, it was found that the toughness was highly dependent on the yttria content. The maximum toughness was observed for the

nano1.5YSZ sample; approximately 3 times the toughness of benchmark submicron sample. The toughness of the former was highly dependent on the density and grain size and this was due to the grain size dependent variation in transformability of the tetragonal phase. The lower toughness of nano3YSZ was due to the overstabilisation of nanozirconia. The optimum grain sizes to get maximum indentation toughness were also identified for each composition. Thus, grain size control can be used as an effective technique to prepare toughness tailored zirconia ceramics. The toughness determined by the SCF technique showed minimum toughness for the nano1.5YSZ sample. This was expected to be due to the generation of a monoclinic-rich weak zone around the pre-crack. The SCF toughness values obtained for the other samples were comparable to those determined using the indentation technique. Combining the indentation and SCF results indicate that the nano1.5YSZ ceramics may be best viewed as crack, or damage, initiation resistant rather than crack propagation resistant.

The strength of the sintered nanostructured ceramics has been found to be very similar to that of conventional submicron ceramics, viz. ~1GPa. Interestingly, the fracture mechanism is different; the nanostructured ceramics all failure via an intergranular fracture mode whilst it was transgranular for the benchmark, submicron ceramics. It is believed that it may be possible to achieve even greater strength for the nanostructured ceramics once processing and the mean grain size have been optimised further.

From the micro-Raman spectroscopic study of the indentation induced phase transformations, it was found that nano1.5YSZ underwent maximum transformation and this increased with indentation load. The phase transformation was found to be minimum for the nano3YSZ sample of all the compositions investigated, which showed minimum indentation toughness. Thus micro-Raman spectroscopy can be used as a very effective technique to study the indentation induced phase transformation in zirconia ceramics.

The wear performance of the nano3YSZ sample was found to be superior to that of the benchmark Tosoh sample under both wet and dry conditions. The wear mechanism of nano3YSZ was controlled by plastic deformation and microcracking whereas for the submicron Tosoh sample it was due to phase transformation and

delamination. The presence of water during wear testing was found to accelerate the phase transformation, reducing the wear resistance.

From the hydrothermal ageing studies it was found that nano3YSZ is extremely resistant to ageing induced phase transformation, showing no hint of transformation even after ageing for 14 days at 245°C. In comparison, the benchmark Tosoh samples disintegrated after 7 days at 140°C. This ageing resistance of nano3YSZ is potentially very exciting. The ban for zirconia femoral heads and other body implant materials is due to the poor hydrothermal ageing resistance of submicron and micron zirconia. The superior ageing resistance properties of nano3YSZ, combined with its better wear resistance and finer surface finish, make it an ideal material for producing femoral heads and other body implant materials. Nano2YSZ and nano1.5YSZ both underwent phase transformation during hydrothermal ageing, although, the ageing resistance of the nano2YSZ was better than that of benchmark 3YSZ even with its lower yttria content. This superior ageing resistance of nanozirconia ceramics is clearly due to their smaller grain size and hence enhanced stabilisation.

So overall it can be concluded that nanozirconia ceramics can be sintered to full density using a pressureless two-step sintering cycle. They display unique properties not observed with submicron or micron grain sized ceramics. By judicious selection of the yttria content and grain size, ceramics with superior mechanical, and/or ageing properties can be produced from nanozirconia suspensions.

Chapter 6

6 Future work

From the room temperature and high temperature XRD diffraction data it was found that the phase composition of the nanoYSZ powders is different from that of the samples with larger particle sizes. The current phase diagrams of YSZ have not taken the grain size effect into consideration. So it is logical to construct a phase diagram for YSZ which takes grain size into consideration. This will be a three dimensional plot with grain size as the third axis. This will help to predict the phase composition of a particular yttria stabilised zirconia composition for a particular grain size. This work will involve a large number of high temperature XRD and high temperature DSC studies for different compositions with different grain sizes.

From the conventional two-step sintering studies, it was found that the mean grain size can be retained below 100 nm, whilst achieving densities $\geq$ 99.0% of theoretical, though, they are close to 100 nm. Further reduction in grain size should be possible by increasing the green density of the samples. Two different approaches can be followed to accomplish this; one is to increase the solid content of the suspensions used for slip casting, the other is to prepare flowable, crushable powders using the nanopowders by techniques such as spray freeze drying. Initial slip casting studies with high solid content suspensions led to cracking of the samples. This could be avoided by selecting the proper grades of PoP and also by varying the PoP/water ratio to prepare the moulds. Weak, flowable powders can be prepared by the addition of carefully chosen additives to the nanosuspensions prior to spray freeze drying and also by optimising the solid content of the suspension.

From the hybrid two-step sintering of slip cast nano3YSZ samples with 10 mm diameter; it was found that this technique can be successfully employed to prepare fully dense samples within a much shorter period of time compared to conventional two-step sintering. So it will be interesting to optimise the sintering cycles for different sample mass, size, density and yttria content. This would enable a considerable reduction in sintering time. Further reduction in grain size might also be achieved, particularly if the green density can be increased, see above.

The attempts to prepare fully dense pure monoclinic zirconia were not successful because of the slow phase transformation to tetragonal zirconia at sintering temperatures. It could be possible to lower the sintering temperatures by using a MW assisted sintering schedule. Trials needed to be done in this direction.

So far only a small range of nanoYSZ samples were characterised for strength and toughness; it is essential to conduct similar measurements for all samples with different yttria content and grain size to obtain a clear picture of the dependence of these properties on these parameters. This will require the preparation and testing of a large number of samples. Further characterisation of the Kic values of nano1.5YSZ has to be carried out considering the small size of the pre-crack.

Ceramics with <500 nm grain size have the potential for displaying superplasticity. The nanoceramics from the present study have got grain sizes of the order of 100 nm; they can be tested for superplasticity.

Another potentially useful experiment will be to measure the ionic conductivity of the various nanoceramics with differing yttria content. From the mechanical property measurements, a grain size dependent shift in properties was observed. If there is such a shift in ionic conductivity, it could be possible to use 5-6 mol% YSZ for applications such as solid oxide fuel cells, instead of the 8YSZ which is commonly used now. This will result in a potential cost reduction as yttria is very expensive (provided the cost of the nanopowders does not undo the cost benefit gained). Also lower yttria content zirconia sinters at lower temperatures, resulting in energy savings. The lower sintering temperatures also enable co-sintering with metals, potentially making the whole process of preparing SOFCs much easier.

From the ageing studies it was found that nano3YSZ and nano2YSZ offers better ageing resistance compared to submicron3YSZ, with nano3YSZ showing no degradation even at 245°C. This combined with better surface finish makes nano3YSZ an ideal material for making body implants such as femoral heads. However, the ageing resistance has to be evaluated in Ringer's solution and clinical trials have to be carried out before making any actual implants.

7 Appendix

Standard powder diffraction data file

78-1807 Quality: C
CAS Number:
Molecular Weight: 123.22
Volume[CD]: 140.88
Dx: 5.809 Dm:
Sys: Monoclinic
Lattice: Primitive
S.G.: P2$_1$/c (14)
Cell Parameters:
a 5.150 b 5.211 c 5.317
α β 99.230 γ
I/Icor: 4.82
Rad: CuKa1
Lambda: 1.54060
Filter:
d-sp: calculated
ICSD #: 062993

Zr O2
Zirconium Oxide
Ref: Calculated from ICSD using POWD-12++, (1997)
Ref: Howard, C.J., Hill, R.J., Reichert, B.E., Acta Crystallogr., Sec. B: Structural Science, 44, 116 (1988)

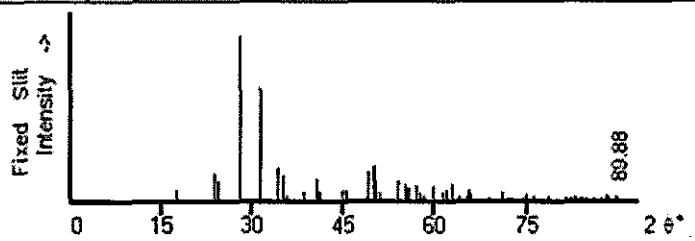

2θ	Int-f	h	k	l	2θ	Int-f	h	k	l	2θ	Int-f	h	k	l
17.430	64	1	0	0	50.090	212	2	2	0	64.054	13	0	2	3
24.044	168	0	1	1	50.540	122	$\bar{1}$	2	2	64.252	29	$\bar{0}$	3	2
24.440	118	$\bar{1}$	1	0	51.168	53	$\bar{2}$	2	1	64.252	29	$\bar{1}$	2	3
28.166	999 *	$\bar{1}$	1	1	54.059	116	2	0	2	64.968	8	$\bar{2}$	3	0
31.455	678	1	1	1	54.059	116	3	0	0	65.349	23	$\bar{1}$	3	2
34.138	201	0	0	2	54.657	7	1	2	2	65.657	65	2	2	2
34.387	130	0	2	0	55.252	50	2	2	1	65.657	65	$\bar{3}$	2	0
35.280	149	$\bar{2}$	0	0	55.347	98	0	1	3	65.884	40	$\bar{2}$	3	1
35.874	31	$\bar{1}$	0	2	55.564	74	$\bar{1}$	1	3	68.898	21	1	3	2
38.541	53	0	2	1	55.687	38	0	3	1	69.585	8	1	2	3
39.407	10	$\bar{2}$	1	0	55.884	75	1	3	0	70.155	5	$\bar{2}$	2	3
39.949	5	$\bar{1}$	1	2	57.125	80	$\bar{3}$	1	0	71.017	22	$\bar{3}$	2	1
40.702	128	$\bar{2}$	1	1	57.125	80	$\bar{3}$	1	1	71.017	22	$\bar{3}$	2	2
41.129	50	1	0	2	57.855	50	$\bar{1}$	3	1	71.223	48	$\bar{1}$	0	4
41.365	48	$\bar{1}$	2	1	58.242	34	$\bar{2}$	2	2	71.897	9	0	0	4
43.782	1	1	2	1	59.767	87	1	3	1	72.069	15	$\bar{2}$	3	2
44.802	64	1	1	2	59.996	80	$\bar{3}$	0	2	72.485	13	0	4	0
45.485	67	$\bar{2}$	0	2	61.322	55	1	1	3	72.582	12	2	1	3
45.485	67	2	1	1	61.931	64	$\bar{2}$	1	3	73.514	4	$\bar{3}$	1	3
48.898	21	$\bar{2}$	1	2	62.793	96	$\bar{3}$	1	1	74.611	18	4	0	0
49.238	171	0	2	2	62.793	96	$\bar{3}$	1	2	75.056	42	0	4	1

PDF no 781807

79-1769 Quality: C
CAS Number:
Molecular Weight: 123.22
Volume[CD]: 67.04
Dx: 6.104 Dm:
Sys: Tetragonal
Lattice: Primitive
S.G.: P4$_2$/nmc (137)
Cell Parameters:
a 3.595 b c 5.185
α β γ
I/Icor: 9.87
Rad: CuKa1
Lambda: 1.54060
Filter:
d-sp: calculated
ICSD #: 066787

Zr O2
Zirconium Oxide
Ref: Calculated from ICSD using POWD-12++, (1997)
Ref: Bondars, B et al., J. Mater. Sci., 30, 1621 (1995)

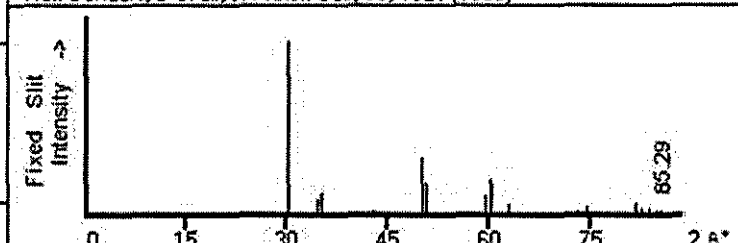

2θ	Int-f	h	k	l	2θ	Int-f	h	k	l	2θ	Int-f	h	k	l
30.222	999 *	1	0	1	59.272	106	1	0	3	81.731	64	2	1	3
34.569	81	0	0	2	60.202	200	2	1	1	82.541	31	3	0	1
35.271	124	1	1	0	62.851	47	2	0	2	83.673	24	1	1	4
42.974	14	1	0	2	68.621	3	2	1	2	84.883	17	2	2	2
50.218	320	1	1	2	72.917	15	0	0	4	85.287	15	3	1	0
50.738	171	2	0	0	74.589	37	2	2	0					
53.933	1	2	0	1	78.347	3	1	0	4					

PDF no 791769

References

1 R. Feynman,"There's Plenty of Room at the Bottom" (reprint from speech given at annual meeting of the West of the American Physical Society), Eng. Sci., 23, 22–36, 1960

2 B. Bhushan (Ed.), Handbook of Nanotechnology. Springer, Chapter 1, 2004

3 K.E.Drexler, C. Peterson and G. Pergamit, Unbounding the Future.William Morrow, New York, 1991., B. Bhushan (Ed.), Handbook of Nanotechnology. Chapter 10, Springer, 2004

4 R. W. Whatmore and J. Corbett, "Nanotechnology in the Marketplace," Comput.Control J., [June] 105–107, 1995

5 W. I. Atkinson, Nanocosm— Nanotechnology and the Big Changes Coming from the Inconceivably Small; pp. 36–39.AMACOM

6 C. P. Poole and F.J.Owens, Introduction to Nanotechnology. Wiley, New York, 1-7, 2003

7 S. Falder, Science in Parliament, Vol. 61, no 1 spring, 12-13, 2004

8 G. Smith, Science in Parliament, Vol.61, no 1, Spring, 10-11, 2004

9 K. Sobolev and M. F. Gutierrez, Am.Ceram.Soc.Bullet., 84(10) 14-18

10 K. J. Klabunde (Ed.), Nanoscale Materials in Chemistry.Wiley, New York, 1-13, 2001

11 W.-X. Zhang, C.-B. Wang and H.-L. Lien, Catal.Today, 40, 387–95, 1998

12 W. C. W. Chan, D. J. Maxwell, X. Gao, R. E. Bailey, M. Han and S. Nie, Curr.Opin. Biotechnol., 13, 40–46, 2002

13 T. Watanabe, E. Kojima, K. Norimoto, T.Kimura, M.Machida, M. Hayakawa, A.Kitamura, M. Chikuni,Y. Saeki,T. Kuga and Y. Nakashima,"Multi-functional Material with Photocatalytic Functions and Method of Manufacturing Same." U.S. Pat. No. 6 294 247, 2001

14 Super-Hydrophilic Photocatalyst and Its Applications, http://www.toto.co.jp hydro_e/index.htm., Pilkington Activ™ Self-cleaning Glass, http://www.pilkington.com /international+ products/activ/usa/english/default.htm

15 Q. Zhang, J. Wang and S. Cheng, J. Funct. Polym., 15 (3) 271–75, 2002

16 B. J. Bauer, D. Liu, C.L. Jackson, et al., Polym.Adv.Technol., 7, 333–39, 1996

17 M. C. Roco, R.S. Williams and P. Alivisatos (Eds.),"Vision for Nanotechnology R&D in the Next Decade," IWGN Report on Nanotechnology Research Directions,National Science and Technology Council, Committee on Technology, 1999

18 K. J. Klabunde (Ed.), Nanoscale Materials in Chemistry.Wiley, New York, 2001., H. Somekawa, T.Tanaka, H. Sasaki, K. Kita, A. Inoue and K. Higashi, Acta Mater., 52 (4) 1051–59, 2004

19 M. Wilson, K. K. G. Smith, M. Simmons and B. Raguse, Nanotechnology—Basic Science and Emerging Technologies. Chapman and Hall/CRC, 2000

20 J. M. Calderon-Moreno, M. Schehl and M. Popa, Acta Mater., 50 (16) 3973–83 2002

21 M. J. Mayo, Int. Mater. Rev., 41, 85-115, 1996

22 F. Wakai, S. Sakaguchi, and Y. Matsuno., Adv. Ceram. Mater., 1, 259-263 1986.

23 J. Karch and R. Birringer, Ceram. Int. 16, 291-294, 1990

24 H. Hahn and R. S. Averback, J. Am. Ceram. Soc., 74, 2918-2921, 1991

25 T. H. Cross and M. J. Mayo, Nanostructured Mater., 3, 163-168, 1993

26 W. E. Kuhn, in Ultrafine particles (ed. W. E. Kuhn), Wiley New York, 41-103, 1963

27 I. Kosacki, T. Suzuki, V. Petrovsky, H. U, Anderson., Solid State Ionics, 136-137, 1225-1233, 2000

28 J. Karch, R. Birringer and H. Gleiter, Nature, 330, 556-558, 1987

29 M. J. Mayo, R. W. Seigel, A. Narayanasamy and W. D. Nix, J. Mater. Res., 5, 1073-1082, 1990

30 J. R. Groza and R. J. Dowding, Nanostruct. Mater., 7, 749- 768, 1996

31 J. D. Hansen, R. P. Rusin, M. H. Teng and D. L. Johnson, J. Am. Ceram. Soc., 75 (5), 1129-1135, 1992

32 www.accuratus.com/zirc.html

33 www.morganadvancedceramics.com/materials/zo.htm

34 http://www.zircoa.com/e_home/products/fine_grain/dies/tube.intl.reprint.html

35 H. G. Scott, J. Mater. Sci., 10 (1), 527-535, 1975

36 M. N. Rahaman, A. Yao, B. Sonny Bal, J. P. Garino and M. D. Ries, J. Am. Ceram. Soc., 90 (7), 1965-1988, 2007

37 A. H. Heuer, N. Claussen, W. M. Kriven and M. Ruhle, J. Am. Ceram. Soc., 65, 642-650, 1982

38 I. W. Chen and Y. H. Chiao, Acta. Metall, 31 (10), 1627-1638, 1983

39 X. M. Wang, G. Lorimer and P. Xiao., J. Am. Ceram. Soc., 88, 809-816, 2005

40 P. Duran, M. Villegas, F. Capel, P. Recio and C. Moure, J. Eur. Ceram. Soc., 16, 945-952, 1996

41 L. Zych and K. Haberko, J. Eur. Ceram. Soc., 26, 373-378, 2006

42 U. Popp, R. Herbig, G. Michel, E. Muller and Ch. Oestreich, J. Eur. Ceram. Soc., 18, 1153-1160, 1998

43 R. E. Juarez, D. G. Lamas, G. E. Lascalea and N. E. Walsoe de Reca, J. Eur. Ceram. Soc., 20, 133-138, 2000

44 M. Bhagwat and V. Ramaswamy, Mater. Res. Bull., 39, 1627-1640, 2004

45 K. Maca, M. Trunec, P. Dobsak and J. Svejcar, Rev.Adv.Mater.Sci., 5, 183-186, 2003

46 S. Ran, L. Winnubst, W. Wiratha and D. H. A. Blank, J. Eur. Ceram. Soc., 26, 391-396, 2006

47 F. C. M. Woundenberg, W. F. C. Sager, J. E. ten Elshof and H. Verweig, J. Am. Ceram. Soc., 87, 1430- 1435, 2004

48 F. Bondioli, C. Leonelli, T. Manfredini, A. M. Ferrari, M. C. Caracoche, P. C. Rivas and A. M. Rodriguez, J. Am. Ceram. Soc., 88, 633-638, 2005

49 Y. L. Song, S. C. Tsai, C. Y. Chen, T. K. Tseng, C. S. Tsai, J. W. Chen and Y. D. Yao, J. Am. Ceram. Soc., 87, 1864-1871, 2004

50 R. Mueller, R. Jossen, S. E. Pratsinis, M. Watson and M. K. Akhtar, J. Am. Ceram. Soc., 87, 197-202, 2004

51 C. Huang, R. Guo, Z. Tang and Z. Zhang, J. Am. Ceram. Soc., 88, 1651-1654, 2005

52 E. O. Hall, Proc. Phys. Soc. B., 64:747,1951

53 N. J. Petch, J. Iron Steel Inst., 174:25, 1953

54 R. Wurschum, S. Herth, U. Brossmann, Adv. Eng. Mater., 5, 365-372, 2003

55 P. Mondal, A. Klein, W. Jaegermann and H. Hahn, Solid State Ionics, 118, 331-339, 1999

56 C. Demetry and X. Shi, Solid State Ionics, 118, 271-279, 1999

57 F. Wakai, S. Sakaguchi, and Y. Matsuno, Adv. Ceram. Mater., 1, 259-63, 1 986

58 L. A. Xue, X. Wu and I-W. Chen., J. Am. Ceram. Soc., 74, 842-45, 1991

59 F. Wakai, Y. Kodama, S. Sakaguchi, N. Murayama and K. Niihara., Nature, 344, 421-423, 1990

60 T. Rouxel, F. Wakai and K. Izaki., J. Am. Ceram. Soc., 75, 2363-2372, 1992

61 Y. Shinoda, T. Nagano and H. Gu., J. Am. Ceram. Soc., 82, 2916-18, 1990

62 F Wakai, Y. Kodama, S. Sakaguchi, and T. Nonami, J. Am. Ceram. Soc.. 73, 457-60, 1990

63 J. Yun, Y. T. Chou and M. P. Harmer, J. Am. Ceram. Soc., 85, 1190–96, 2002

64 F. Wakai and H. Kato, Adv Ceram. Mater., 3, 71-76, 1988

65 C. K. Yoon and I-W. Chen, J. Am. Ceram Soc., 73, 555-65, 1990

66 F. Wakai, Y. Kodama, S. Sakaguchi, N. Murayama. K. Izaki, and K. Nihara, Nature (London), 344, 421 -23, 1990

67 A. J. A. Winnubst, M. M. R. Boutz, Y.J. He, A. J. Burggraaf, H. Verweij, Ceram. Int., 23, 215–21, 1997

68 U. Betz, H. Hahn, Nanostruct. Mater., 12, 911–4, 1999

69 W. Strek, D. Hreniak, P. Mazur, W. Lojkowski, J. Hanuza, A. Bednarkiewicz, R. Fedyk, G. Boulon, Proceedings of the Ninth Asia Pacific Physics Conference (9th APPC), Hanoi, Vietnam, October 25-31, 2004

70 T. C. Lu, X. H. Chang, J. Q. Qi, X. J. Luo, Q. M. Wei, S. Zhu, K. Sun, J. Lian, and L. M.Wang, Appl. Phy. Lett., 88, 213120, 2006

71 M.A. Meyers, A. Mishra and D. J. Benson, Progress in Mater. Sci., 51, 427-556, 2006

72 R. C. Garvie, J. Phy. Chem., 69 (4), 1238-1243, 1965

73 S. Sukla and R. Seal, Int. Mater. Rev., 50 (1), 45-64, 2005

74 E. Medvedovski and P. Sarkar, J. Am. Ceram. Soc.Bull., 9201-9213, 2003

75 B. A. Cottom and M. J. Mayo, Scripta Materialia, 809-814, 1996

76 R. Chaim and M. Hefetz, J. Mater. Sci., 3057-3061, 2004

77 A. Bravo-Leon, Y. Morikawa, M. Kawahara and M. J. Mayo, Acta Materialia, 4555-4562, 2002

78 O. Vasylkiv, Y. Sakka and V. V. Skorokhod, J. Am. Ceram. Soc., 86 (2) 299-304, 2003

79 C. B. Ponton and R. D. Rawlings, Mater. Sci and Tech, 865-871, 1989

80 C. B. Ponton and R. D. Rawlings, Mater. Sci and Tech., 961-976, 1989

81 R. F. Cook and G. M. Pharr, J. Am. Ceram. Soc., 787-817, 1990

82 M. S. Kaliszewski, G. Behrens, A. H. Heuer et al., J. Am. Ceram. Soc., 1185-1193, 1994

83 G. W. Dransmann, R. W. Steinbrech, A. Pajares et al., J. Am. Ceram. Soc., 1194-1201, 1994

84 J. Wang, M. Rainforth and R. Stevens, Br. Ceram. Trans. J., 1-6, 1988

85 B. Basu, J. Vleugel and O. Van der Biest, Mater. Sci. Eng., 215-221, 2004

86 G. R. Anstis, P. Chantikul, B. R. Lawn and D. B. Marshall, J. Am. Ceram. Soc., 533-538, 1981

87 K. Niihara, R. Morena and D. P. H. Hasselman, J. Matter. Sci. Lett., 13-16, 1982

88 K. Niihara, J. Mater. Sci. Lett., 221-223, 1983

89 J. Eichler, M. Hoffman, U. Eisele and J. Rodel, J. Eur. Ceram.Soc., 3575-3582, 2006

90 J. Eichler, U. Eisele and J. Rodel, J. Am. Ceram. Soc., 1401-1403, 2004

91 G. D. Quinn and R. Morrell, J. Am. Ceram. Soc., 2037-2066, 1991

92 G. D. Quinn J. Am. Ceram. Soc., 2374-2384, 1990

93 J. Eichler, J. Rodel, U. Eisele and M. Hoffman, J. Am. Ceram. Soc., 90 (9) 2830-2836, 2007

94 T. E. Fisher, M. P. Anderson and S. Jahanmir, J. Am. Ceram. Soc., 75 (2), 252-257, 1989

95 S. W. Lee, S. M. Hsu and M. C. Shen, J. Am. Ceram. Soc., 76 (8),1937-1947, 1993

96 Y. He, L. Winnubst, A. J. Burggraaf, H. Verweij, , P. G. Th. Van der Varst and B. de With., J. Am. Ceram. Soc., 80 (2), 377-380, 1997

97 C. T. Yang and W. J. Wei, Wear, 97-104, 2000

98 B. Basu, J. Vleugels and O. Van Der Biest, J. Eur. Ceram. Soc., 24, 2031-2040, 2004

99 B. Basu, J-H. Lee and D-Y. Kim, J. Am. Ceram. Soc., 1771-1774, 2004

100 J. D. B. S. Sanchez and W. M. Rainforth, J. Am. Ceram. Soc., 82 (6), 1483-1491, 1999

101 Y. He, L. Winnubst, A. J. Burggraff, H. Verweij, P. G. Th. van der Varst and B. de With, J. Am. Ceram. Soc., 79 (12), 3090-3096, 1996

102 K. H. Zum Gahr, W. Bundschuh and B. Zimmerlin, Wear, 162-164, 269-279, 1993

103 K. Kobayashi, H. Kuwajima and T. Masaki, Solid State Ionics, 3/4, 489-493, 1981

104 U.K. Medical Devices Agency, Adverse Incidents Centre. Safety Notice MDA SN 9617, "Zirconia Ceramic Heads for Modular Total Hip Femoral Components: Advice to Users on Re-Sterilization", 1997

105 US Food and Drug Administration, Steam Re-Sterilization Causes Deterioration of Zirconia Ceramic Heads of Total Hip Prostheses, 1997, http://www.fda.gov/cdrh/steamst.html

106 US Food and Drug Administration, Medical Device Recalls Recall of Zirconia Ceramic Femoral Heads for Hip Implants, 2001, http://www.fda.gov/cdrh/recalls/zirconiahip.html

107 W. Rieger, World Tribology Forum in Arthroplasty, © Hans Huber, Bern, 2001

108 I. C. Clarke, M. Manaka, D. D. Green, P. Williams, G. Pezzotti, Y. H. Kim, M. Ries, N. Sugano, L. Sedel, C. Delauney, B. Ben Nissan, T. Donaldson and G. A. Gustafson, J. Bone Joint Surg. Am., 85, 73-84, 2003

109 J. Chevalier, L. Gremillard and S. Deville, Annu. Rev. Mater. Sci., 37, 1-32, 2007

110 I. Thompson and R. D. Rawlings, Biomaterials, 11, 505-508, 1990

111 K. Haraguchi, N. Sugano, T. Niishi, H. Miki, K. Oka and H. Yoshikawa, J. Bone Joint Surg. B 83, 996–1000, 2001

112 M. Yoshimura, T. Noma, K. Kawabata and S. Somiya, J. Mater. Sci. Lett., 6, 465-467, 1987

113 M. Yoshimura, Am. Ceram. Soc. Bull., 67 (12) 1950-1955, 1988

114 S. Lawson, J. Eur. Ceram. Soc., 15, 485-502, 1995

115 T. Sato and M. Shimada, J. Am. Ceram. Soc., 68 (6), 356-359, 1985

116 F. F. Lange, G. L . Dunlop and B. I. Davis, J. Am. Ceram. Soc., 69 (3), 237-240, 1986

117 M. T. Hernandez, J. R. Jurado, P. Duran and J. L. G. Fierro, J. Am. Ceram. Soc., 74 (6), 1254-1258, 1991

118 X. Guo, J. Mater. Sci., 36, 3737-3744, 2001

119 J. M. Saldana, H. B. Ramirez, D. J. Vigueras, T. Iga and G. A. Schneider, J. Mater. Res., 18 (10), 2415-2426, 2003

120 J. Chevalier, Biomaterials, 27, 535-543, 2006

121 R. Birringer, H. Gleiter, H. P. Klein and P. Marquardt, Phy. Lett., 102A, 365-369, 1984

122 M. J. Mayo, R. W. Seigel, Y. X. Liao and W. D Nix, J. Mater. Res., 7 (4), 973-979, 1992

123 J. Eastman and R. W. Seigel, Res. Dev., 31, 56-60, 1989

124 R. W. Seigel, S. Ramasamy, H. Hahn, Z. Zonghuan and L. Ting., J. Mater. Res., 3, 1367, 1988

125 H. Hahn, J. Logas and R. S. Averback., J. Mater. Res., 5, 609-614, 1990

126 J. L Shi, J. H. Gao, Z. X. Lin and T. S. Yen, J. Am. Ceram. Soc., 74, 994-997, 1991

127 A. Roosen and H. Hausner in 'Scinece and Technology of Zirconia 2' , Adv. in Ceram. Vol. 12, 714-726, 1985

128 A. O. Boschi and E. Gilbart, in 'Advanced Ceramic Processing and Technology 1' (Ed. J. G. P. Binner), Park Ridge, NJ, 73-93, 1990

129 W. H. Rhodes, J. Am. Ceram. Soc., 64, 19-22, 1981

130 A. Pechenik, G. J Piermarini and S.C. Danforth., J. Am. Ceram. Soc., 75, 3283-3288, 1992

131 O. L. Khasanov and E. S. Dvilis, Adv. Appl. Ceram., 107 (3), 135-141, 2008

132 J. A. Lewis, J. Am. Ceram. Soc., 83 (10), 2341-2359, 2000

133 B. E. Novich and D. H. Pyatt, J. Am. Ceram. Soc., 73 (2), 207-212, 1990

134 http://www.keram.se/eng/pdf/slip_casting.pdf

135 D. W. Richerson, Modern Ceramic Engineering, 422-441, Marcel Dekker.

136 M. N. Rahaman, Ceramic processing and sintering, Marcel Dekker Inc., 302-306, 1995

137 H. H. D. Lee, J. Am. Ceram. Soc., 73 (8), 2309-2315, 1990

138 F. Shojai, A. B. A. Pettersson, T. Mantyla and J. B. Rosenholm, J. Eur. Ceram. Soc., 20, 277-283, 2000

139 T. Fengqiu, H. Xiaoxian, Z. Yufeng and G. Jingkun, Ceram. Int., 26, 93-97, 2000

140 Y. H. wang, X. Q. Liu and G. Y. Meng, Ceram. Intl., 33, 1025-1031, 2007

141 G. Suarez, M. P. Albano, L. B. Garrido and E. F. Aglietti, Ceram. Intl., 33, 925-929, 2007

142 J. Wang and L. Gao, Nanostructured Mater., 11 (4), 451-457, 1999

143 C. Duran, Y. Jia, K. Sato and K. Watari, J. Mater. Res., Vol. 20, No. 5, 1348-1355, 2005 (check for cross ref in nano synthesis)

144 Q. Tan, Z. Zhang, Z. Tang, S. Luo and K. Fang, Mater. Chem. Phy., 80, 615-619, 2003

145 B. Jachimska and Z. Adamczyk, J. Eur. Ceram. Soc., 27, 2209-2215, 2007

146 C. Renger, P. Kuschel, A. Kristoffersson, B. Clauss, W. Oppermann and W. Sigmund, J. Eur. Ceram. Soc., 27, 2361-2367, 2007

147 L. Chera, E. Palcevskis, M. Berzins, A. Lipe and I. Jansone, Funct. Mater. And Nanotech., 93, 1-5, 2007

148 I. Santacruz, K. Annapoorani and J. Binner, J. Am. Ceram. Soc., 91 (2), 398-405, 2008

149 J. G. P. Binner, I. Santacruz and K. Annapoorani, International Patent Application Publication . No. WO 2006/136780 A2, 2006

150 S. J. L. Kang, Sintering: Densification, Grain growth and Microstructure., Elsevier Butterworth Heinemann, 5-60, 2005

151 http://www.keramverband.de/brevier_engl

152 J. E. Burke and D. Turnbull, Prog. Met. Phy., 3, 220-292, 1952

153 J. E. Burke and J. H. Rosolowski, "Sintering" in the Treatise on Solid State Chemistry, Vol 4. 1976

154 M. N. Rahaman, Ceramic processing and sintering, Marcel Dekker Inc., Chapter 7,8 and 9, From page 331,1995

155 R. L. Coble, J. Appl. Phys., 32, 789 – 792, 1961

156 G. C. Nocholson, J. Am. Ceram. Soc., 48, 214, 1965

157 Y. Iida, J. Am. Ceram. Soc., 41, 397, 1958

158 C. W. Park and D. Y. Yoon, J. Am. Ceram. Soc., 85, 1585-1593, 2002

159 J. R. Groza, Int. J. Powd. Met., 35, 59-67, 1999

160 M. P. Harmer and R. J. Brook, J. Br. Ceram. Soc., 80,147-149, 1981

161 H. Mostaghaci and R. J. Brook, J. Mater. Sci., 21, 3575-3580, 1986

162 D. W. Richerson, Modern Ceramic Engineering, Pages 552-565, 1991

163 C. Pithan, Y. Shiratori, R. Waser, J. Dornseiffer and F. H. Haegel, J. Am. Ceram. Soc., 89, 2908-2916, 2006

164 T. C. Lu, X. H. Chang, J. Q. Qi, X. J.Luo, Q. M. Wei, S. Zhu, K. Sun, J. Lian, and L. M. Wang, Appl. Phys. Lett., 88, 213120 1-3, 2006

165 M. M. R. Boutz, L. Winnubst, A. J. Burggraaf, M. Nauer and C. Carry, J. Am. Ceram. Soc., 78, 121-128,1995

166 G. D. Zhan, J. Kuntz, J. Wan, J. Garay and A. K. Mukherjee, J. Am. Ceram. Soc., 86 (1), 200-202, 2002

167 K. R. Venkatachari and R. Raj, J. Am. Ceram. Soc., 70, 514-520, 1987

168 Y. Shinoda, T. Nagano and F. Wakai, J. Am. Ceram. Soc., 82 (3), 771-773, 1999

169 I. W. Chen and X. H. Wang., Nature., 404, 168-171, 2000

170 X. H Wang, P. L. Chen and I. W. Chen., J. Am. Ceram. Soc., 89, 431-437, 2006

171 Y. I. Lee, Y. W. Kim, M. Mitomo and D. Y. Kim., J. Am. Ceram. Soc., 86 (10), 1803-805, 2003

172 H. T. Kim, Y. H. Han, Ceram. Int., 30, 1719-1723, 2004

173 X. H. Wang, X. Y. Deng, H. L. Bai, H. Zhou, W. G. Qu, L. T. Li and I. W. Chen., J. Am. Ceram. Soc., 89, 438-443, 2006

174 A. Palotai, K. Breece, E. Dickey, C. Randall and A. Ragulya, J. Am. Ceram.Soc., 88 (11), 3008-3012, 2005

175 P. Duran, J. Tartaj and C. Moure, J. Am. Ceram. Soc., 86 (8), 1326-1329, 2003

176 M. Mazaheri, A. M. Zahedi and S. K. Sadrnezhaadt, J. Am. Ceram. Soc.,

177 T. Zou, X. Wang, W. Zhao and L. Li, J. Am. Ceram. Soc., 91 (1), 121-126, 2008

178 P. C. Yu, Q. F. Li, J. Y. H. Fuh, T. Li and L. Lu, J. Mater. Proc. Tech., 192-193, 312-318, 2007

179 J.Li and Y. Ye, J. Am. Ceram. Soc., 89 (1), 139-143, 2006

180 K. Bodisova, P. Sajgalik, D. Galusek and P. Svancarek, J. Am. Ceram. Soc., 90 (1), 330-332, 2007

181 A. Polotai, K. Breece, E. Dickey, C. Randall and A. Ragulya, J. Am. Ceram. Soc., 88 (11), 3008-3012, 2005

182 W. H. Sutton, Ceram. Bullet., 68, 376-386, 1989

183 Y. V. Bykov, K. I. Rybakov and V. E. Semenov, J.Phys.D: Appl.Phys., 34, R55-R75, 2001

184 M. A. Janney and H. D. Kimrey, Microwave Processing of Materials II (Materials Research Society Symp. Proc. vol 189) ed W B Snyder et al (Pittsburgh, PA: Materials Research Society) pp 215–27,1990

185 J. J. Thomas et. al. Microwave Processing of Materials III (Materials Research Society Symp. Proc. vol 269) ed M. A. Janney et al (Pittsburgh, PA: Materials Research Society) pp 277–83, 1992

186 D. Jaglin, J. Binner and B. Vaidhyanathan, C. Prentice, B. Shatwell and D. Grant, J. Am. Ceram. Soc., 89 (9), 2710-2717, 2006

187 J. Wang. ' Evidence of Microwave Effect during Hybrid Sintering and Annealing of Ceramics', PhD Thesis, Loughborough University, 2005

188 J. Aguilar, Z. Valdez, U. Ortiz., J. of microwave power and electromagnetic energy, Vol. 39, 191- 196, 2004

189 J. G. P. Binner, B. Vaidhyanathan and J. Wang, Ampere 9, International conference on Microwaves, Loughborough University, 2003

190 J. Wang, J. Binner, B. Vaidhyanathan, N. Joomun, J. Kilner and G. Dimitrakis et al., J. Am. Ceram. Soc., 89 (6), 1977-1984, 2006

191 D. Beruto, R. Botter and A. W. Searcy, J. Am. Ceram. Soc., 72, 232-235, 1989

192 R. M. Young and R. McPherson, J. Am. Ceram. Soc., 72, 1080-1081,1989

193 K. Y. Lee, P. H. Dearhouse and E. D. Case, J. Mater. Synth. Proc., 7, 159-166, 1999

194 M. Mizuno, S. Obata, S. Takayam, S. Ito, N. Kato, T. Hirai and M. Sato, J. Eur. Ceram. Soc., 24, 387-391, 2004

195 P. Piluso, L. Gaillard, N. Lequeux and P. Boch, J. Eur. Ceram. Soc., 16, 121-125, 1996

196 K. Y. Lee and E. D. Case, J. Matter. Sci. Lett., 18, 201-203, 1999

197 C. Y. Hsieh, C. N. Lin, S. L. Chung, J. Cheng and D. K. Agarwal, J. Eur. Cer. Soc.,27, 343-350, 2007

198 T. T. Meek, C. E. Holcombe and N. Dykes, J. Mater. Sci. Lett., 6, 1060-1062, 1987

199 Z. Xie, J. Li, Y. Huang and X. Kong, J. Matter. Sci. Lett., 15, 1158-1160, 1996

200 A. Goldstein, N. Travitzky, A. Singurindy and M. Kravchik. J. Eur. Cer. Soc., 19, 2067-2072, 1999

201 D. D. Upadhyaya, A. Ghosh, G. K. Dey, R. Prasad and A. K .Suri, J. Mater. Sci., 36, 4707-4710, 2001

202 C. G. Ganan, J. J. M. Martinez, D. G. Garzia and A. D. Rodriguez, J. Mater. Sci., 41, 5231-5234, 2006

203 S.G. Huang, L. Li, O. Van der Biest and J. Vleugels, J. Eur. Cer. Soc., 27, 689-693, 2007

204 S. Nath, S. Bajaj and B. Basu, Int. J. Appl. Ceram. Technol., 5, 49-62, 2008

205 K. Bai and H. G. Kim, J. Matter. Sci. Lett., 13, 806-809, 1994

206 V. P. Paranosenkov, Yu. V. Bykov, V. V. Kholoptsev, A. A. Chikina, I. L. Shkarupa and A. V. Merkulova, Refrac. and Ind. Ceram., 38, 13-15, 1997

207 G. Xu, H. Zhuang, W. Li and F. Wu, J. Eur. Cer. Soc., 17, 977-981, 1997

208 Yu. V. Bykov, O. I. Get,man, V. V. Panichkina, I. V. Plotnikov, V. V. Skorokhod and V. V. Kholoptsev, Powd. Metall. And Met. Ceram., 40, 112-120, 2001

209 M. I. Jones, M. C. Valecillos, K. Hirao and Y. Yamauchi, J. Eur. Cer. Soc., 22, 2981-2988, 2002

210 J. G. Fisher, S. K. Woo, K. Bai, I. S. Han, K. S. Lee, K. S. Hong and D. W. Seo, J. Eur. Cer. Soc., 23, 791-799, 2003

211 A. Goldstein, W. D. Kaplan and A. Singurindi, J. Eur. Cer. Soc., 22, 1891-1896, 2002

212 G. F. Xu, H. R. Zhuang, F. Y. Wu and W. L. Li, J. Eur. Cer. Soc., 17, 675-680, 1997

213 J. Wilson and S. M. Kunz, J. Am. Ceram. Soc., 71, C40-C41, 1988

214 J. Lasri, P. D. Ramesh and L. Schachter, J. Am. Ceram.Soc., 83, 1465-68, 2000

215 M. A. Janney, C. L. Calhoun and H. D. Kimrey, J.Am.Ceram.Soc., 75, 341-46, 1992

216 D. D. Upadhyaya, A. Ghosh, K. R. Gurumurthy and R. Prasad, Ceramics International, 27, 415-418, 2001

217 M. Moeller, L. H. Therm, H. S. Shulman, "A Novel Approach to Understanding Microwave Heating of Zirconia" Presented at the 104th Annual Meeting and Exposition of the American Ceramic Society, St. Louis, MO, April 28th to May 1st, 2002

218 P. K. Sharma, Z. Ounaies, V. V. Varadan and V. K. Varadan, Smart Mater. Struct., 10, 878-883, 2001

219 O. P. Thakur, C. Prakash and D. K. Agarwal, Mater. Sci. Eng., B96, 221-225, 2002

220 Z.Xie, J. Yang, X. Huang and Y. Huang, J. Eur. Ceram. Soc., 19, 381-387, 1999

221 C. Zhao, J. Vleugels, C. Groffils, P. J. Luypaert and O. Van Der Biest, Acta Mater., 48, 3795-3801, 2000

222 R. Peelamedu, A. Badzian, R. Roy and R. P. Martukanitz, J. Am. Ceram. Soc., 87, 1806-1809,2004

223 R. Wroe, T.Rowley, J. Mater. Sci., 31, 2019-2026, 1996

224 A. Lorenz, 'Investigation of Microwave Effect using a Dilatometer', Project Report, Loughborough University, 2006

225 G. A. Danko R. Silberglitt, P. Colombo, E. Pippel and J. Woltersdorf, J. Am Ceram. Soc., 1617-1625, 2000

226 J. Lankford, J. Mater. Sci. Lett., 1, 493-495, 1982

227 J. Chevalier, J. M. Drouin and B. Cales, Bioceramics, Volume 10, Edited by L. Sedel and C. Rey (Proceedings of the 10th International Symposium on Ceramics in Medicine, Paris, France,October 1997)

228 H. Toraya, M. Yoshimura and S. Somiya, J. Am. Ceram. Soc., 67,C 119-121, 1984

229 A. Suresh, M. J. Mayo, W. D. Porter and C. J. Rawn, J. Am. Ceram. Soc., 86, [2], 360-362, 2003

230 B. Vaidhyanathan and J. G. P. Binner, in Proc. Fourth World Congress on Microwave and Radio Frequency Applications, Ed. R. L. Schulz and D. C. Folz, Nov 2004, 192-198.

231 J. G. P. Binner and B. Vaidhyanathan, Microwave, conventional and hybrid processing of nanostructured ceramics. In Proceedings of the International Symposium on M'wave Science & its Application to Related Fields, 141–144, 2004

232 J. Binner, B. Vaidhyanathan and T. Carney, Adv. Sci. Tech., 45, 835-844, 2006

233 L. Gao, W. Li, H. Z. Wang, J. X. Zhou, Z. J. Chao and Q. Z. Zai, J. Eur. Ceram. Soc., 21, 135-138, 2001

234 M. Trunec and K. Maca, J. Am. Ceram. Soc., 90 (9), 2735-2740, 2007

235 N. R. Greenacre, "Measurement of the High Temperature Dielectric Properties of Ceramics at Microwave Frequencies" PhD Thesis, Nottingham University, Chapter 7, 1996

236 G. A. Dimitrakis, "High Temperature Dielectric Properties of Micro and Nano-scale Yttria Doped Zirconia at Microwave Frequencies", PhD Thesis, Nottingham University, Chapter 8, 2005

237 E. V. Dudnik, Z. A. Zaitseva, A. V. Shevchenko and L. M. Lopato, Powd. Metall. Met. Ceram., 34 (5, 6), 263-271, 1995

238 M. A. C. G. Van De Graaf, J. H. H. Ter Maat and A. J. Burgraaf, J. Mater. Sci., 20, 1407-1418, 1985

239 J. Binner, K. Annapoorani, A. Paul, I. Santacruz and B. Vaidhyananthan, J. Eur. Ceram. Soc., 28, 973-977, 2008

240 J. Binner, and B. Vaidhyanathan, J. Eur. Ceram. Soc., 28, 1329-1339, 2008

241 K. Matsui, K. Tanaka, T. Yamakawa, M. Uehara, N. Enomoto and J. Hojo, J. Am. Ceram. Soc., 90 (2), 443-447, 2007

242 J. Luo, D. P. Almond, and R. Stevens, J. Am. Ceram. Soc., 83 (7), 1703-1708, 2000

243 C. Herring, J. Appl. Phys., 21 (4) 301–3, 1950

244 C. Herring, The Physics of Powder Metallurgy, Edited by W. E. Kingston. McGraw-Hill, New York, 143–79 1951

245 A. V. Ragulya, Adv. Appl. Ceram., 107 (3), 118-134, 2008

246 V. G. Keramidas and W. B. White, J. Am. Ceram. Soc., 57 (1), 22-24, 1974

247 R. Fillit, P. Homerin, J. Schafer, H. Bruyas and F. Thevenot, J. Mater. Sci., 22, 3566-3570, 1987

248 G. Pezzotti and A. Porporati, J. Biomed. Opt., 9 (2), 372-384, 2004

249 M. Bowden, G. D. Dickson, D. J. Gardiner and D. J. Wood, J. Mater. Sci., 28, 1031-1036, 1993

250 R. M. McMeeking and A. G. Evans, J. Am. Ceram. Soc., 65 (5) 242-246 , 1982

251 A. Ghosh, A. K. Suri, B. T. Rao and T. R. Ramamohan., J. Am. Ceram. Soc., 2015-2023, 2007

252 D. R. Clarke and F. Adar, J. Am. Ceram. Soc., 65 (6), 284-288, 1982

253 T. Hirata, E. Asari and M. Kitajima, J. Solid State Chem., 110 201-207, 1994

254 B. K. Kim, J. W. Hahn and K. R. Han, J. Mater. Sci., 16, 669-671, 1997

255 M. V. Swain, Acta. Metall., 33 (11), 2083-2091, 1985

256 K. Kobayashi, H. Kuwajima and T. Masaki, Solid State Ionics, 3/4, 489-493, 1981

257 J. Chevalier, B. Cales and J. M. Drouin, J. Am. Ceram. Soc., 82 (8), 2150-2154, 1999

258 T. Sato, S. Ohtagi and M. Shimada, J. Mater. Sci., 20 (4), 1466-1470, 1985

259 K. Matsui, H. Horikoshi, N. Ohmichi, M. Ohgai, H. Yoshida and Y. Ikuhara, J. Am. Ceram. Soc., 86 (8), 1401-1408, 2003

260 K. Matsui,N. Ohmichi, M. Ohgai, H. Yoshida and Y. Ikuhara, J. Mater. Res., 21 (9), 2278-2289, 2006

261 K. Matsui, N. Ohmichi, M. Ohgai, H. Yoshida and Y. Ikuhara, J. Ceram. Soc. Jpn., 114 (3), 230-237, 2006

262 K. Matsui, H. Yoshida and Y. Ikuhara, Acta Mater., 56, 1315-1325, 2008

263 I. Yamashita and K. Tsukuma, J. Ceram. Soc. Jpn., 113 (8), 530-533, 2005

264 K. Castkova, H. Hadraba and J. Cihlar, Ceramics Silikaty, 48 (3), 85-92, 2004

265 C. Pecharroman, J. F. Bartolome, J. Requena, J. Moya, S. Deville, J. Chevalier, G. Fantozzi and R. Torrecillas, Adv. Mater., 15 (6), 507-511, 2003